Three-dimensional modeling of cosmic rays observed by PAMELA

II Ramokgaba

orcid.org/0000-0002-0605-1306

Dissertation accepted in fulfilment of the requirements for the degree *Master of Science in Physics* at the North-West University

Supervisor: Dr MD Ngobeni

Co-supervisor: Dr DC Ndiitwani

Graduation ceremony: July 2022

Student number: 25676237

Abstract

Simultaneous observation of galactic cosmic ray (GCR) proton and helium nuclei made by PAMELA space experiment from June 2006 to January 2016 unveiled new and interesting features in terms of how these nuclei are modulated at the same rigidity and over a long period of time. For this work, the modulation of galactic CR protons, helium-3 ($^3He_2$), helium-4 ($^4He_2$) and total helium (He) nuclei was studied with an improved three-dimensional numerical modulation model based on Parker's transport equation. The modulation was computed using the new GALPROP calculated local interstellar spectra (LIS) for almost all the species of interest to this study, together with a comprehensive set of modulation parameters, diffusion and drift coefficients. The main objective of this study was to uncover and investigate in detail how differently GCR species with dissimilar mass-to-charge ratios (A/Z) are modulated from solar minimum to maximum modulation conditions. The intensity ratios proton-to-helium-3 ($P/^3He_2$), proton-to-helium-4 ($P/^4He_2$), proton-to-total helium (P/He) and $^3He_2/^4He_2$ are also illustrated, with the aim of reproducing a selection of PAMELA P/He ratios taken between 2006 and 2013. From the computations of the GCR spectra in this study, it was found that the PAMELA spectra observed between 2006 and 2013 are better reproduced by the numerical model when the magnitude of the heliospheric magnetic field and the heliospheric current sheet tilt angles are continuously adjusted with time along with the value and rigidity slopes of the diffusion and the drift coefficients. The computed modulation for the considered species surprisingly changed differently with changing solar activity at rigidities below $\approx$ 5.0 GV mainly due to the differences in the slopes of their LIS's at low rigidities. This study also shows that to reproduce the value and shape of the PAMELA P/He ratios with a numerical model, the modulation effects of $^3He_2$ and $^4He_2$ in the heliosphere should be explicitly distinguished. This also allows for simultaneous study of the $P/^3He_2$, $P/^4He_2$ and $^3He_2/^4He_2$ ratios at the same rigidity and time. The time and rigidity dependence of the P/He, $P/^3He_2$, $P/^4He_2$ and $^3He_2/^4He_2$ ratios was found to be the consequence of how the combined interplaying modulation mechanisms in the heliosphere affect the modulated spectra based on their A/Z and particularly on their LIS's.

Keywords: Cosmic rays , heliosphere, solar modulation, solar activity, galactic protons, galactic helium nuclei, local interstellar spectra, mass-to-charge ratio.

Nomenclature

2D	Two-dimensional
3D	Three-dimensional
ACR	Anomalous cosmic ray
AU	Astronomical unit (1 AU = 1.49×10^8 km)
AMS	Alpha Magnetic Spectrometer
BS	Bow shock
CIR	Corotating interaction region
DC	Diffusion coefficient
eV	Electron volt (1 eV = 1.6×10^{-19} J)
GCR	Galactic cosmic ray
HCS	Heliospheric current sheet
HMF	Heliospheric magnetic field
HP	Heliopause
ISMF	Interstellar magnetic field
JKM	Jokipii-K'ota modification
LIS	Local interstellar spectra
LISM	Local interstellar medium
MFP	Mean free path
NLGC	nonlinear guiding centre theory
PAMELA	Payload for Antimatter Matter Exploration and Light-nuclei Astrophysics
QLT	Quasilinear theory
SBM	Smith-Bieber modification
SSN	Sunspot number
SW	Solar wind
TPE	Transport equation
TS	Termination shock

Contents

Chapter 1

Introduction

Galactic cosmic rays (GCRs) are high energetic particles originating from astrophysical sources in the galaxy that enter the heliosphere from all directions. When inside the heliosphere GCRs encounter a turbulent convective solar wind (SW) with an embedded heliospheric magnetic field (HMF). The understanding of this global interaction is currently based on four major modulation processes: convection, diffusion, adiabatic energy changes, and gradient, curvature and current sheet drifts. Combined, these interplaying processes lead to significant variations in the intensity of GCRs as a function of energy (rigidity), position and time over the Sun's 11-year solar activity cycle with respect to the level of their local interstellar spectra (LIS). This phenomenon is known as solar modulation of cosmic rays (CRs) in the heliosphere.

Simultaneous observations of GCRs proton and helium nuclei made by the Payload for Antimatter Matter Exploration and Light-nuclei Astrophysics (PAMELA) space experiment from June 2006 to January 2016 at the Earth (Adriani et al. [2011, 2013, 2017], Marcelli et al. [2020, 2022]) unveiled new and interesting features in terms of how these nuclei are modulated at the same rigidity and over a long period, extending close to $\approx$ 10 years. The observed time-dependent energy (rigidity) spectra of GCRs carry fundamental information regarding their origin and propagation, and further give insight into how the elements of the diffusion and drift tensor changed with time in the heliosphere. Similar to what other experiments observed (see Aguilar et al. [2018], Corti et al. [2019]), PAMELA observations also revealed the time and rigidity dependencies in the proton-to-helium (P/He) intensity ratios. In particular, that this observed ratio is not constant as a function of time at rigidities below $\approx$ 3 GV (also see a discussion by Song et al. [2021a]). This provides the opportunity to study in greater detail than before, using numerical models, how differently GCR species with a dissimilar mass-to-charge ratio (A/Z) are modulated down to a few GV at the Earth from the lowest level of solar activity in the A $<$ 0 magnetic cycle until periods of no well-defined polarity of the HMF. Understanding the detailed rigidity dependence of the P/He ratio from solar minimum to maximum conditions at the Earth opens up additional prospects to improve our understanding of the origin and propagation of these GCR nuclei in the galaxy and their modulation in the heliosphere.

Because the P/He ratio can be influenced by the helium-3 ($^3He_2$) and helium-4 ($^4He_2$) isotopic mixing (see a discussion by Tomassetti et al. [2019]), therefore understanding the modulation effects of the helium isotopes separately is pivotal in the understanding of exactly how the observed P/He ratios changed with rigidity and time.

Previously the numerical modeling of the heliospheric modulation of helium nuclei was done but without considering its isotopic mixing (e.g., Langner [2004], Steenberg & Moraal [1996]), similarly to a report in the past recent given by Shen et al. [2019]. In these studies the modeling effects of $^4He_2$ were simply assumed to be the same as those of total helium, which is an over simplification. This was mainly due to the lack of precise observations of the rigidity spectra of $^3He_2$ and $^4He_2$ over long periods of time, which posed a severe hindrance on the detailed modeling of these isotopes and made it difficult to put constraints on their LIS's using solar modulation modeling. Distinguishing explicitly the modeling effects of the helium isotopes allows also for the detailed simultaneous study of the P/He and $^3He_2/^4He_2$ ratios at the same rigidity and time.

In this dissertation the modulation of GCRs proton and helium nuclei (combination of both $^3He_2$ and $^4He_2$ isotopes) in the heliosphere is studied with a comprehensive, three-dimensional (3D), drift model based on the transport equation (Parker [1965]) and compared to observations by the PAMELA detector from 2006 to 2013. The modeling results are obtained using the exact same set of modulation parameters, diffusion and drift coefficients, with the A/Z values and LIS's the only differences remaining when comparing proton and helium modulation.

This dissertation is structured in the following manner:

Chapter 2 provides the relevant heliospheric physics and CR modulation concepts. This includes a brief discussion about the classification of CRs, the Sun and its variations over time, and the features this resulted in. Also provided are discussions about the SW, termination shock (TS), HMF and the heliospheric current sheet (HCS) together with the influence of the heliospheric structures on CRs over the solar cycle, as well as the dynamic heliosphere. Lastly, the chapter provides a brief description of the satellite experiments of interest, of which their observed data are compared with numerical model results for validation.

Chapter 3 gives the transport processes that determine the modulation of CRs throughout the heliosphere, as combined in the transport equation (TPE) (Parker [1965]), as well as a description of the diffusion tensor constructed by Vos [2016] used in this work. Emphasis is placed on the dependence of the diffusion tensor on the ratio of particle speed to the speed of light (β) for GCR species with different A/Z.

In **Chapter 4**, a well-established, comprehensive three-dimensional (3D) drift numerical model is applied to study the modulation of GCR proton spectra observed by PAMELA between 2006 and 2013. This is done with a new Galactic propagation model (GALPROP) calculated LIS of GCR proton described by Bisschoff et al. [2019], together with the comprehensive set of modulation parameters, diffusion and drift coefficients that are changed time dependently in order to reproduce PAMELA observations.

The very same 3D model is used in **Chapter 5** to study the modulation of GCR $^3He_2$ and $^4He_2$, using the same modulation parameters, diffusion and drift coefficients as used for the modulation of GCR proton with their LIS's and A/Z the differences that remain. This assures that the modeling parameters are not changed in an $ad\ hoc$ and inconsistent manner for the purpose of simply fitting $^3He_2$ and $^4He_2$ observational datasets. It is also illustrated in this chapter that the new precise Alpha Magnetic Spectra (AMS02) observation of $^3He_2/^4He_2$ as a function of rigidity (Aguilar et al. [2019]) indicates that the shape of the LIS of $^3He_2$ obtained from the GALPROP model, as described by Bisschoff et al. [2019], is most reasonable, but needs to be modestly adjusted at higher rigidities to reproduce the observed ratio. Lastly, the computed modulated spectra of $^3He_2$ and $^4He_2$ are added up to describe what is called the total helium modulated spectra for comparison with the observed PAMELA helium spectra.

Chapter 6 gives a comparative study of the global features of the computed modulated spectra of galactic proton, $^3He_2$, $^4He_2$ and total helium from solar minimum to maximum activity period. From this, it is shown how differently GCR species with dissimilar A/Z are modulated down to a few GV. The end result of this chapter is the detailed reproduction of P/He ratio measured by PAMELA from 2006 to 2013, displaying both qualitative and quantitative agreement with the main observed features.

Chapter 7 gives a summary of this work and all the prominent discussions and conclusions accumulated during the time of study.

Aspects of this dissertation were presented online at the following conferences:

• The 6th annual Conference of the South African Institute of Physics (SAIP) held in Potchefstroom, South Africa (July 2021).

• The 37th biannual International Cosmic Ray Conference (ICRC) held in Berlin, Germany (July 2021)

Extracts from this dissertation were published in

• Ngobeni, M.D., M.S. Potgieter, O.P.M. Aslam, D. Bisschoff, I.I. Ramokgaba, D.C. Ndiitwani. (2022) Simulations of the solar modulation of Helium isotopes constrained by observations, Advances in Space Research., 69, 2330-2341.

• Ngobeni, M.D., M.S. Potgieter, O.P.M. Aslam, D. Bisschoff, I.I. Ramokgaba, D.C. Ndiitwani. (2021) Numerical modeling of the solar modulation of Helium isotopes in the inner heliosphere, Proceedings of Science (ICRC 2021).

Chapter 2

A brief overview of the variable Sun, cosmic rays and the heliosphere

2.1 Introduction

This chapter serves to introduce concepts that are important to the study of CR modulation in general, with emphasis on the magnetic variable Sun, the SW and the TS, as well as the structure of the heliosphere and its features, the HMF, the HCS and its link to solar activity, and how it influences the CR modulation over the solar cycle. This chapter further discusses spacecraft of interest, which includes PAMELA - the main satellite experiment of which the data was most often used to validate the numerical model results of this study - Voyager, and the AMS02 missions.

2.2 Classification of cosmic rays

CRs are energetic particle species that originate outside the Earth's atmosphere and consist of both positively and negatively charged particles, together with long-lived isotopes and anti-particles (see Battiston [2020]). These charged particles have energies ranging from ≈ 1 MeV to 10^{20} eV and some propagate throughout the galaxy to reach the Earth in all directions. The first discovery of such particles of which their origin was characterized as extraterrestrial (Simpson et al. [1992]), was established in 1912 by Victor Hess during the historic balloon flights. They were found to consist of $\approx 97\%$ protons, $\approx 2\%$ electrons and positrons, and $\approx 1\%$ heavy nuclei (Longair [1990]). Various types of CRs in the heliosphere originate from different sources and include:

(i) GCRs, which originate outside our solar system and it is believed that the energy transfer processes during supernova explosions in the galaxy are probably the major sources of these particles (see Casadei & Bindi [2004], Kobayashi et al. [2004], Busching & Potgieter [2008]). This CR population reaches the heliospheric boundary almost isotropically from interstellar space.

Modeling the modulation of GCRs, in particular protons and helium nuclei, in the heliosphere and its comparison with PAMELA observations is the research topic for this study.

(ii) Solar energetic particles (SEPs) which originate from the solar flares (Smith et al. [2003]) are mainly observed at the Earth during solar maximum but only for several hours. Coronal mass ejections (CMEs) and shocks in the interplanetary medium can also produce energetic particles. These particles are disregarded for the purpose of this study. For more information on SEPs, see Dresing et al. [2014], Wei et al. [2019] and van den Berg et al. [2020].

(iii) Anomalous CRs (ACRs) enter the heliosphere as neutral interstellar atoms and become ionized near the Sun through charge-exchange or photo-ionization (Pesses et al. [1981]). These ions are then picked up by the HMF and transported to the SW termination shock to be accelerated to energies up to ≈ 100 MeV. These particles are also disregarded for the purpose of this study. For more on this CR species, see Fahr et al. [2000], Strauss & Potgieter [2010] and Marquardt et al. [2018].

(iv) Jovian electrons which originate from Jupiter's magnetosphere, regarded as the strongest source of electrons at energies ≈ 30 MeV (Simpson et al. [1974]) dominate the lowest part of the electron energy spectrum around Earth and are observed at distances within 10 AU from the Sun. Like SEPs and ACRs, Jovian electrons are also disregarded in this study. For an overview of the study on Jovian electrons, see Heber & Potgieter [2006], Nndanganeni [2016] and Vogt et al. [2018, 2020, 2022].

2.3 The variable Sun

The Sun, which is the only star by far that forms part of our solar system, is a prominent source of light that supports life on Earth. The Sun is located at a distance of about ≈ 1 AU (1.49×10^8 km) from the Earth and composed of $\approx 90\%$ of hydrogen gas, $\approx 10\%$ helium and a fragment of heavier elements. The Sun's atmosphere consists of four layers that include the photosphere, the chromosphere, the transition region and the corona. A basic structure of the Sun is given in Figure 2.1. The most visible part of the Sun observed from the Earth is called the photosphere, which emits most of the Sun's light and heat. Sunspots, discussed below, are observed on the photosphere. The next layer is the chromosphere, where the temperature increases from 4300 **K** (Kelvin) to nearly 10^4 **K**. This is followed by the corona - the upper most layer and extended plasma atmosphere of the Sun - which is less dense and has an extremely high temperature ($\approx 10^6$ **K**). The corona extends into the interplanetary space to become the SW. Apart from these layers, the Sun is not a solid body like the Earth but is made up of a hot plasma which rotates at different speeds at its equator compared to its poles. Such differences in the plasma speed (differential rotation) produces a very complex Sun day phenomena: where, at the equator, the

Sun makes a full rotation after 25 days, which takes about 36 days near the poles (Bartusiak [1994], Schou et al. [1998]).

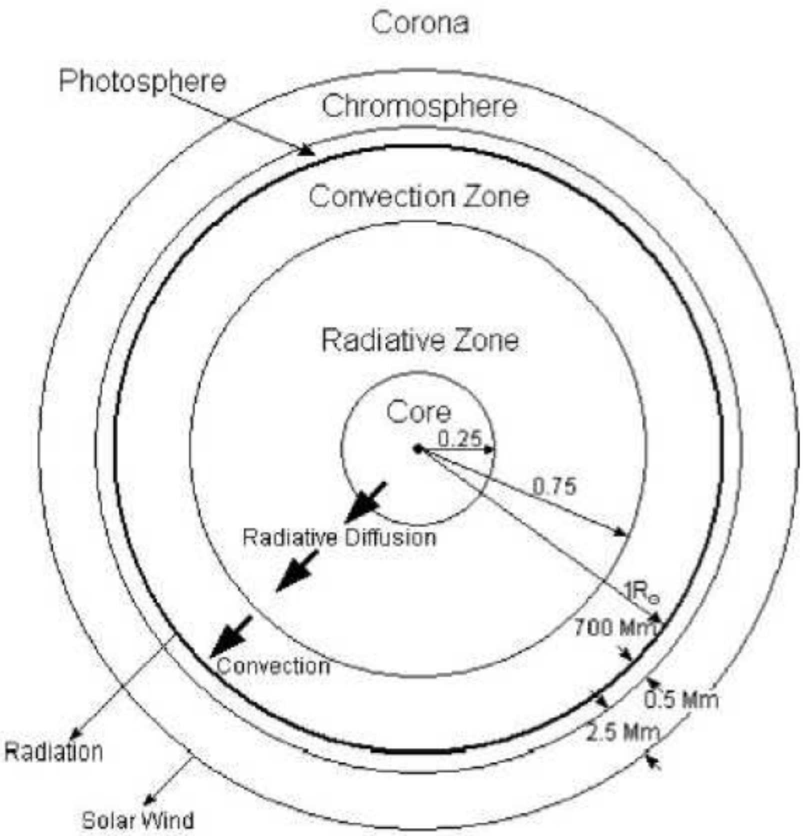

Figure 2.1: The structure of the Sun in its basic form adapted from: www.oulu.fi/spaceweb/textbook/sun.html.

The gases produced by the Sun are constantly moving and interact with the different pressures generated by the hot plasma at Earth's equator and poles to form magnetic fields with the two hemispheres, of which the polarities vary. The interaction between the gases and the magnetic field causes variations in the magnetic field that cause it to tangle, twist or stretch. Depending on the interaction between the Sun's gases and the magnetic field therein, the activities occurring in the Sun are not constant but vary both as functions of time and position, known as solar activity (e.g., Usoskin [2017]). One of the solar activity proxies that gives us valuable information about the activity occurring in the Sun, is the sunspot numbers (SSNs). Sunspots are darker regions that occur on the photosphere of the Sun (Cliver & Herbst [2018]) and possess intense magnetic fields. These regions appear darker since they are cooler compared to their surroundings. The sunspot cycle observed by WDC-SILSO Royal Observatory of Belgium confirmed that solar cycle occurs for a period of $\approx$ 11 years, during which the SSNs fluctuate from lower to higher numbers, marking the period of minimum to maximum activities referred to as solar minimum and solar maximum conditions, respectively. Apart from the SSNs observed from the surface of the Sun, other solar features like prominences, CMEs, solar flares, etc., also change as a function of time and reveal valuable information about the solar cycle. The solar features mentioned are illustrated in Figure 2.2.

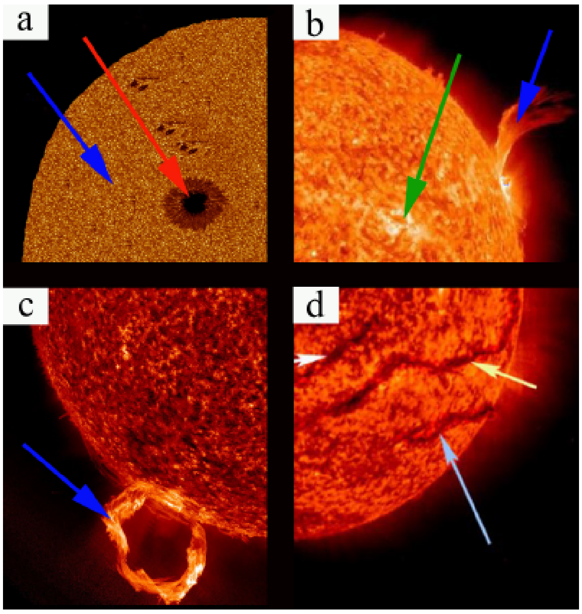

Figure 2.2: Shows different activities that occur in the Sun during minima and maxima periods divided into four panels represented by letters a to d. These panels (a to d) show a sunspot (red arrow) and solar granules (blue arrow indicated in panel a), faculae (green arrow) and a solar flare (blue arrow indicated in panel b), a prominence (blue arrow indicated in panel c), and filaments with three pointed arrows; respectively. Adapted from http://www.nasa.gov.

Figure 2.3 shows the SSNs observed from late 2009 to end of 2021 as observed and measured by the Royal Observatory of Belgium (WDC-SILSO). The measurements depicted in this figure indicate that in terms of the SSNs, the maximum and minimum solar activity periods were respectively reached at the end of 2013 and 2019. These SSNs correlate with the HMF and other solar proxies like the HCS tilt angle, α (see Soon et al. [2015] for a brief discussion). The relation of solar activity and other solar proxies mentioned are discussed in the following subsections. Additionally, the Sun's magnetic field polarity reverses (flips) at the end of every solar cycle, meaning that it will take another 11 years before both the Northern and Southern hemisphere switch back to their initial position, hence the magnetic field cycle occurs every 22 years, known as the Hale cycle (Leighton [1969]).

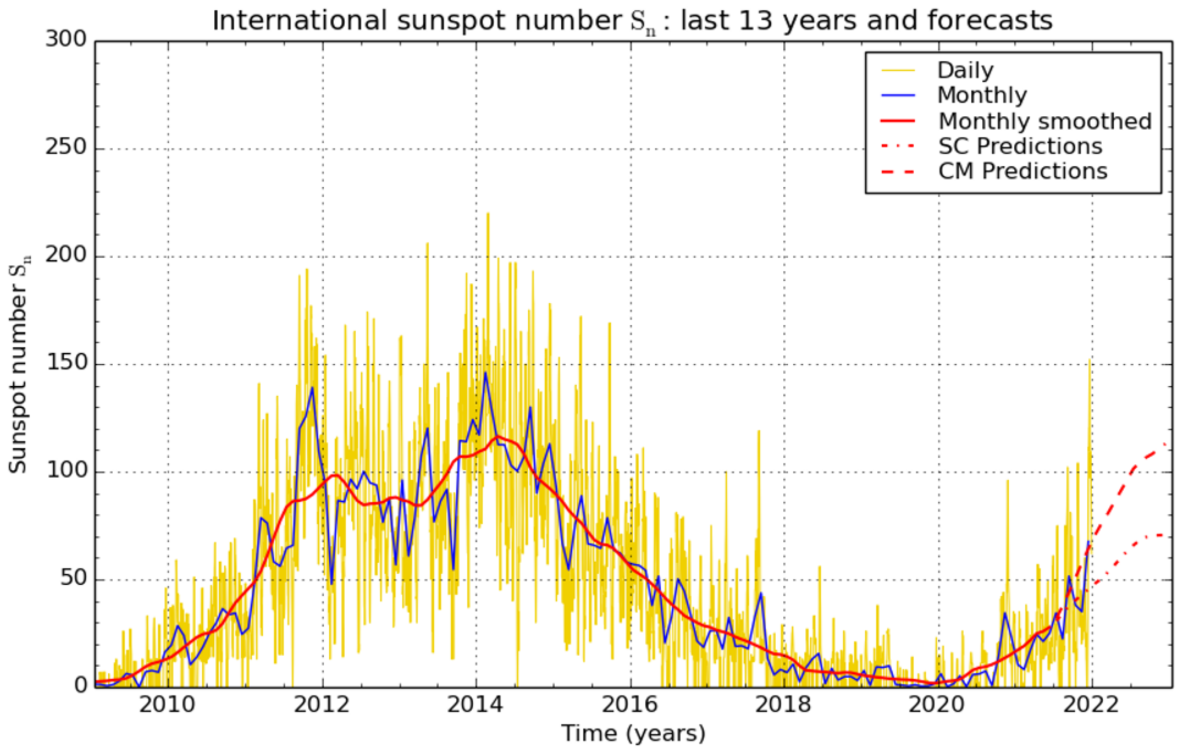

Figure 2.3: The averaged SSNs measured from late 2009 up to end of 2021 adapted from: http.sidc.be/silso.

2.4 The solar wind and termination shock

The SW was first discovered by Biermann [1951] when studying the behaviour of the tails of comets. They established that the tails of comets always pointed directly away from the Sun regardless of their position, when they were close to the Sun, and this could be understood if they were continuously bombarded by a stream of electrically charged particles emitted by the Sun (see a review by Fichtner [2001] and its references). As already mentioned, the temperature of the corona is so high that the Sun's gravity cannot hold on to it (see Hansteen & Leer [1995]). Therefore, for the Sun to maintain equilibrium, some of the solar particles contained in this region must be released. Hence, the SW is the radial outflow of particles from the Sun that flows through interplanetary space and past the Earth with a velocity of several hundred kilometers per second, carrying the Sun's magnetic field with it. The SW has a velocity that is not uniform at all latitudes - an aspect that was first observed by the Ulysses spacecraft. Similar to the magnetic field regions, the SW can also be divided into two types: the slow and fast SW streams which are classified by velocities of $\approx$ 400 km/s and $\approx$ 800 km/s at low (equatorial regions) and high latitudes (polar regions) of the Sun (e.g., Phillips et al. [1994, 1995]), respectively. The slow SW, which occurs mainly at the low heliographic latitudes, is associated with closed magnetic field line regions and results from the small coronal holes together with the large coronal hole edges (Wang [2011]), whereas the fast SW occurring at the higher heliographic latitudes is associated with open magnetic field line regions and results from large coronal holes situated at the poles of the Sun (McComas et al. [2002]). When the fast SW catches up with the earlier ejected slow SW streams, the corotating interaction region (CIR) are formed. For a detailed study on how CIRs influence GCR modulation in the heliosphere see Luo et al. [2021].

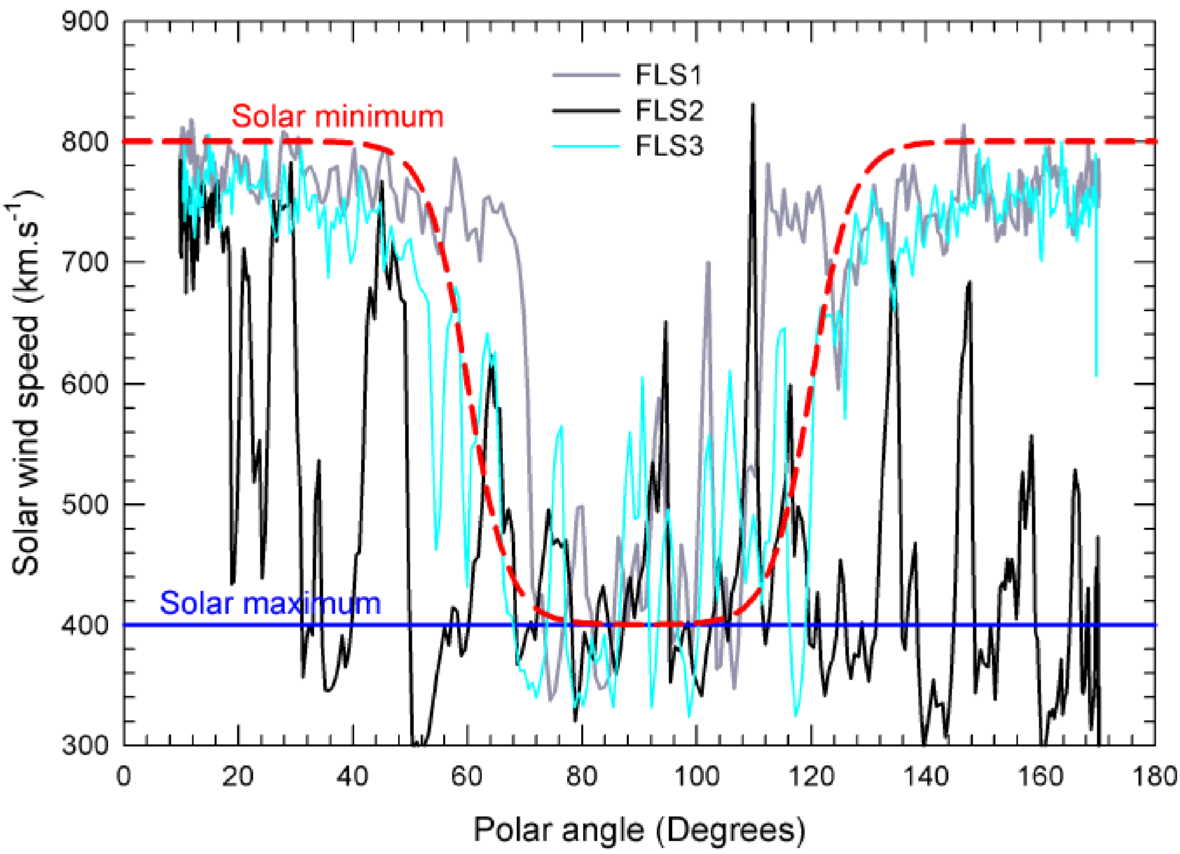

Figure 2.4: The SW speed as a function of heliolatitude with 90 degrees at the equatorial plane as measured by Ulysses during the three fast latitude scans (FLS), represented by FLS1 (grey line, July 1994 - July 1995), FLS2 (black line, October 2000 - September 2001) and FLS3 (cyan line, February 2007 - January 2008) in comparison with the modeled SW during solar minimum (red dashed line given by Equation (2.2)) and solar maximum (blue line given by Equation (2.3)). The SW data was taken from http://cohoweb.gsfc.nasa.gov.

In the numerical model used in this study, the SW velocity vector, $\mathbf{V}_{sw}$, is assumed to consist of both the radial and latitudinal dependencies given as

$$\mathbf{V}'_{sw}(r,\theta) = V'_{sw}(r,\theta)\mathbf{e}_r = V_0 V_r(r) V_\theta(\theta)\mathbf{e}_r, \tag{2.1}$$

where r, θ and $\mathbf{e}_r$ respectively represents the radial distance in AU, the polar angle and the unit vector in the radial direction with V_0 = 400 km/s. Considering solar minimum conditions, the latitude dependence of the characterized SW, $V_\theta(\theta)$, (Hattingh [1998]) is modeled as

$$V_\theta(\theta) = 1.475 \mp 0.4tanh\left[6.8\left(\theta - \frac{\pi}{2} \pm \xi\right)\right], \tag{2.2}$$

where the top and bottom signs correspond to the Northern ($0 < \theta \leq \frac{\pi}{2}$) and Southern ($\frac{\pi}{2} < \theta \leq \pi$) hemisphere respectively, and $\xi = \frac{20\pi}{180}$. In this equation ξ determines the initial polar angle where the SW velocity transition from slow SW (400 km/s) to fast SW (800 km/s). For solar maximum, no clear latitudinal dependence is assumed; hence, during this period $V_\theta(\theta)$ is modeled as,

$$V_\theta(\theta) = 1.0. \tag{2.3}$$

A similar approach in modeling the latitudinal dependence of the SW velocity during both solar minimum and solar maximum was followed in various studies (see Ferreira [2002], Langner [2004], Vos [2012], Manuel [2013], Ngobeni & Potgieter [2015], Nndanganeni [2016]).

Figure 2.4 shows the modeled latitude dependence of the SW as given by Equations (2.2) and (2.3) for solar minimum (dashed red line) and solar maximum (blue solid line) conditions respectively, in comparison with Ulysses' SW speed data measured during the three fast latitude scan (FLS) periods, represented in the figure as FLS1 (grey line), FLS2 (black line) and FLS3 (cyan line). The measurements of the magnitude of the SW velocity taken during solar minimum are represented by FLS1 and FSL3, while FLS2 represents measurements taken during solar maximum conditions. The observed latitudinal dependencies of the SW show that the slow SW lies at the equator (20^0 south and 20^0 north), while the fast SW lies at higher latitudes in the Northern and Southern hemisphere of the Sun ($> 20^0$) during solar minimum. For solar maximum conditions, the observed SW speed has no well-defined latitude dependence (e.g., Richardson et al. [2001], McComas et al. [2002]) such that the fast and slow SW streams are mixed up. Clearly, the modeled SW latitudinal profile matches the Ulysses observations showing that the magnitude of the SW velocity indeed increases from about 400 km/s in the equatorial plane to about 800 km/s towards the polar region during solar minimum, whereas the modeled SW remains constant at 400 km/s during solar maximum .

The radial dependence of the SW inside the TS, $V_r(r)$, is given as

$$V_r(r) = 1 - exp\left[\frac{40}{3}\left(\frac{r_\odot - r}{r_0}\right)\right], \tag{2.4}$$

where $r_\odot$ = 0.005 AU is the Sun's radius and r_0 = 1 AU.

The TS, which was first suggested by Parker [1961], is a region in the heliosphere at which the SW is abruptly slowed down from supersonic speed to subsonic speed in order for the SW ram pressure to match the interstellar thermal pressure. The TS can be considered as the first heliospheric boundary away from the Sun. Voyager 1 (V1) and Voyager 2 (V2) observations

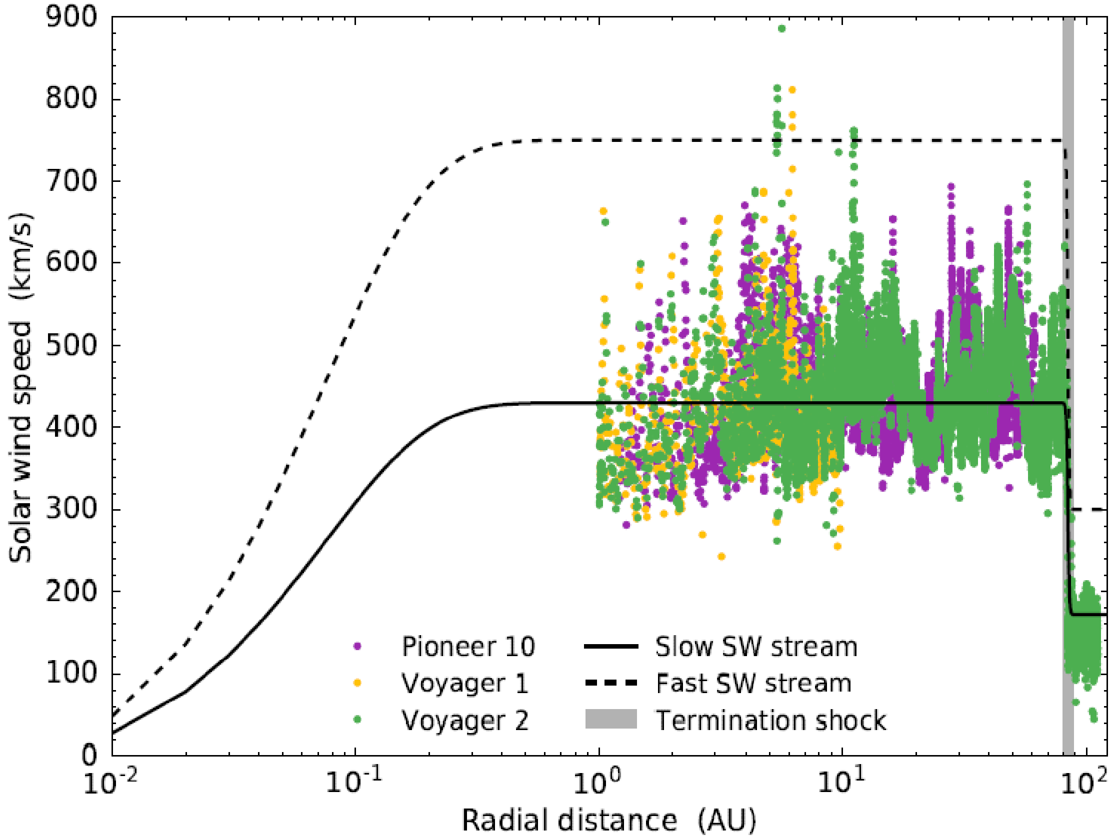

Figure 2.5: The modeled radial dependence of the SW speed representing slow and fast SW streams (solid and dashed lines given by Equation (2.5) is shown together with spacecraft measurements (coloured symbols). Three sets of SW speed measurements are shown, namely Pioneer 10 (purple symbols), Voyager 1 (orange symbols) and Voyager 2 (green symbols). The TS is kept at 84 AU, as indicated by a drop in Voyager 2 measurements. Data obtained from http://cohoweb.gsfc.nasa.gov./.

confirmed that the position of the TS is dynamic and changes with changing solar activity (see Whang et al. [2004], Decker et al. [2005], Stone et al. [2005, 2008], Burlaga et al. [2008], Richardson et al. [2008]). For details on how the TS moves in and out with solar activity and its effects on GCR modulation, see Snyman [2007] and Manuel et al. [2015].

The radial profile of the SW, $V_{sw}(r,\theta)$, including the transition at the TS is modeled as

$$V_{sw}(r,\theta) = V_{sw}^{'}(r_{TS},\theta)\frac{s+1}{2s} - V_{sw}^{'}(r_{TS},\theta)\frac{s-1}{2s}tanh\left(\frac{r-r_{TS}}{L}\right), \tag{2.5}$$

where r_{TS} is the radial position of the TS which ranges from 80 AU to 88 AU in this study, the shock scale length L = 1.2 AU (le Roux et al. [1996]), and s = 2.5 the shock compression ratio which is located beyond the shock and is defined as $s = V_1/V_2$, with V_1 and V_2 as the flow speed in the upstream and downstream regions, respectively. For a detailed study on the TS and its properties, see also Li et al. [2008] and McComas et al. [2019].

Figure 2.5 shows the modeled radial dependence of the SW speed given in Equation (2.5) representing both the slow and fast SW streams (solid and dashed lines), together with various spacecraft measurements of the SW (coloured symbols). The TS is kept at 84 AU, as indicated by a drop in V2 measurements. Take note that, in the heliosheath, the SW deviates from its original radial flow and, hence, its radial profile is expected to be different from that given by Equation (2.5).

2.5 The heliospheric magnetic field

2.5.1 Parker heliospheric magnetic field

The Sun, which consistently blows out the SW in the radial direction, rotates about an axis almost perpendicular to the equatorial plane. The SW carries the embedded (or frozen in) magnetic field with it throughout the heliosphere, which then becomes the HMF. This HMF exhibits a spiral structure referred to as the Parker spiral field (Parker [1958]).

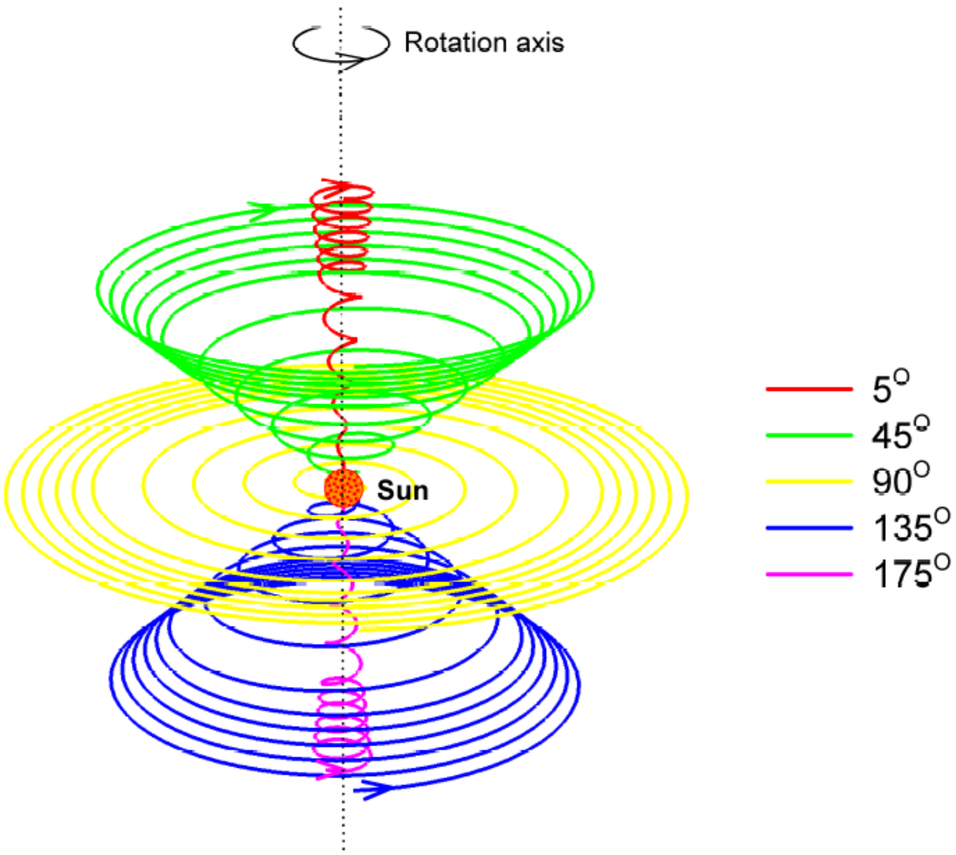

Figure 2.6: A 3D structure representation of the Parker's HMF, with field lines rotating outward at different polar angles 5^0 (red), 45^0 (green), 90^0 (yellow), 135^0 (blue) and 175^0 (purple). Also included is the Sun (orange ball like structure) located at its origin (the center), the rotation axis (dotted vertical line) and the direction of the HMF and its rotation (indicated using arrows). Taken from Manuel [2013].

The analytical expression that describes the Parker's HMF spiral, as derived by Parker [1958], is written as

$$\mathbf{B} = B_n \left(\frac{r_o}{r}\right)^2 (\mathbf{e}_r - tan\psi \mathbf{e}_\phi) \left[1 - 2H\left(\theta - \theta^{'}\right)\right], \tag{2.6}$$

where **B** is the magnetic field in nT, B_n is used to determine the HMF magnitude at the Earth (1 AU), and $\mathbf{e}_\phi$ is the unit vector in the azimuthal direction. The term $tan\psi$ is approximated as

$$tan\psi = \frac{\Omega\,(r - r\odot \sin\theta)}{V_{sw}}, \tag{2.7}$$

where the average angular rotation speed of the Sun Ω = 2.67× 10^{-6} rad/s, and ψ is the spiral angle defined as the angle between the radial direction and the direction of the average HMF at any given position. The spiral angle ψ at the Earth has a value of $\approx 45^0$ and increases to be $\approx 90^0$ at $r \geqslant 10$ AU. The term $H\left(\theta - \theta^{'}\right)$ given in Equation (2.6) is called the Heaviside step function and is given by

$$H(\theta - \theta') = \begin{cases} 0 & \text{for } \theta < \theta' \\ 1 & \text{for } \theta > \theta', \end{cases} \tag{2.8}$$

where θ' is the HCS polar position. This function determines the magnetic field polarity that causes the HMF reversal across the HCS. An example of the 3D representation of the Parker spiral taken from Manuel [2013] is shown in Figure 2.6 for the polar angles 5^0, 45^0, 90^0, 135^0 and 175^0 respectively, with the Sun at the center. The HMF lines are compressed beyond $r >$ 80 AU due to the slower SW flow in this region. Also indicated in this figure is the direction of the HMF, which is assumed to point outward in the Northern hemisphere and inward in the Southern hemisphere. The direction of the HMF is crucially important for understanding charge-sign dependent modulation because particles with different charge-sign access the heliosphere from different directions (see Vos [2016]). This will be discussed in details in the next chapter.

The magnitude of the magnetic field given in Equation (2.6), | **B** |, is written as

$$B = B_n \left(\frac{r_o}{r}\right)^2 \sqrt{1 + (tan\psi)^2}. \tag{2.9}$$

From Equation (2.9), it is easy to note that B towards the polar regions decreases as r^{-2}, leading to an over-estimation of drift effects in this region. The dynamics of the HMF, particularly at the poles, is a contentious subject (see e.g., Thomas & Smith [1980], Smith [2011], Sternal et al. [2011]). Over the years, many modifications of the Parker HMF have been proposed with varying levels of complication (see e.g., Jokipii & Kóta [1989], Moraal [1990], Smith & Bieber [1991], Fisk [1996]).

2.5.2 The Smith-Bieber modification

An interesting modification of the Parker's HMF is the Smith-Bieber modification (SBM). Smith & Bieber [1991] proposed that the magnetic field is not fully radial below the radius at which the magnetic field and solar corona rotate in phase, presumably between $10r_\odot$ and $30r_\odot$. The effect of this modification is that the average magnetic field magnitude becomes larger in the polar regions than in the regions further away from the poles. Therefore, the modification to the Parker's HMF is implemented through ψ and the expression for $tan\psi$ becomes

$$tan\psi = \frac{\Omega\left(r - b\sin\theta\right)}{V_{sw}(r,\theta)} - \frac{rV_{sw}(b,\theta)}{bV_{sw}(r,\theta)}\left(\frac{B_T(b)}{B_R(b)}\right), \tag{2.10}$$

where b = $20r_\odot$, $\frac{B_T(b)}{B_R(b)}$ is the ratio of the azimuthal to the radial magnetic field component at a position b near the solar surface. Smith & Bieber [1991] estimated B_T/B_R to be -0.02. For earlier works that implemented this modification, see Haasbroek et al. [1995], Haasbroek [1997], Vos [2016] and Raath [2020]. Similar to what was done by Vos [2016], the SBM was implemented in the numerical model used in this study and applied to model GCR species of interest from solar minimum to solar maximum conditions.

2.5.3 The Jokipii-Kóta modification

A widely implemented modification to the geometry of the Parker's magnetic field which addresses the overly large drift velocities in the polar regions was proposed by Jokipii & Kóta [1989], and known as the Jokipii-Kóta modification (JKM). This modification is such that Parker's magnitude of the HMF in Equation (2.9) becomes

$$B = B_n\left(\frac{r_o}{r}\right)^2\sqrt{1 + (tan\psi)^2 + \left(\frac{r\delta(\theta)}{r_\odot}\right)^2}. \tag{2.11}$$

The term $\delta(\theta)$ modifies the HMF in the polar direction without altering the HMF in the equatorial plane. This implies that the modification by Jokipii & Kóta [1989] varies the HMF only in the polar regions and maintains Parker's HMF in the equatorial plane. Therefore, according to this modification, $\delta(\theta) \approx 0$ in the equatorial plane .

A graphic representation of the magnetic field streamlines originating at the same colatitude of 30^0 on the source surface resulting from Parker (red line), SBM (cyan line) and JKM (blue line) is shown in Figure 2.7 taken from Shen et al. [2021]. It can be seen that the SBM mainly keeps the Parker spiral, but seems to be more tightly wound.

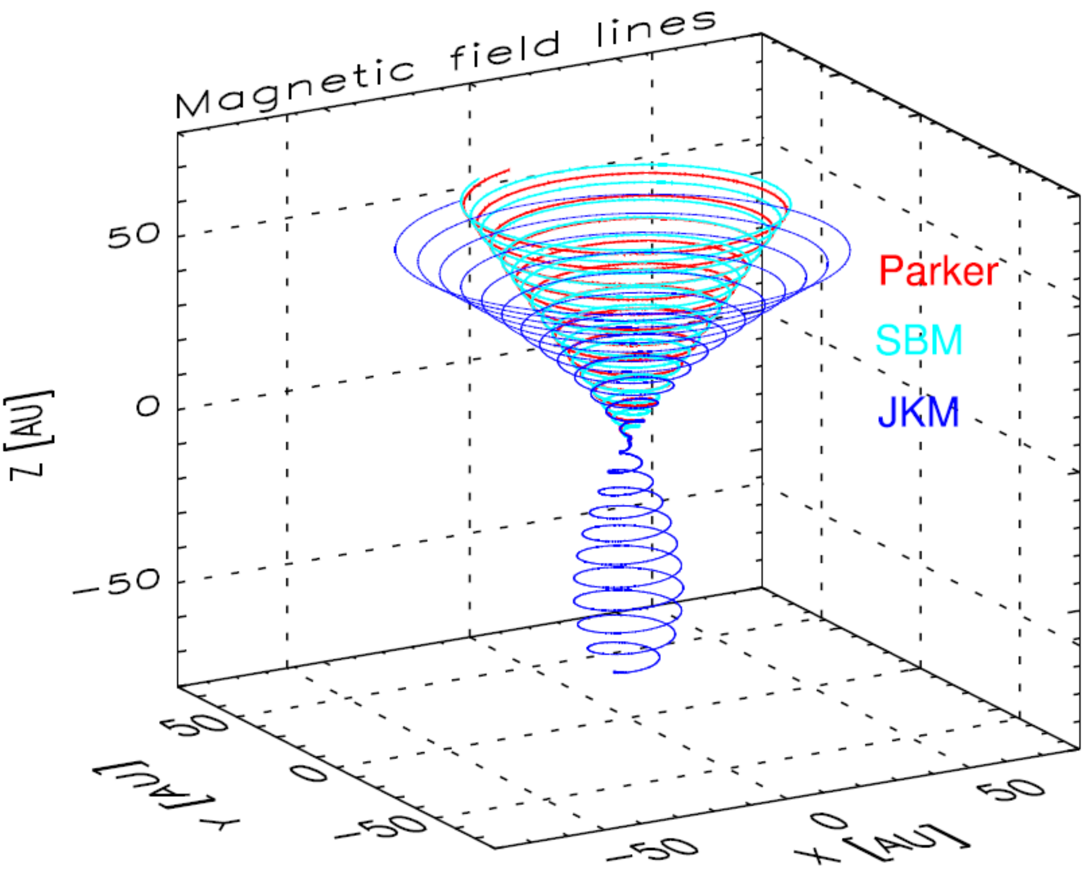

Figure 2.7: The magnetic field lines of Parker, SBM, and JKM HMF, represented by red, cyan and blue colours at 30^0 colatitude. Adapted from Shen et al. [2021].

2.5.4 Fisk type magnetic field

Apart from the Parker spiral field and its two modifications mentioned above, there exist a more complex field referred to as the Fisk field (Fisk [1996]). The Fisk field is based on the argument that the Sun does not rotate rigidly, but rather differentially with solar poles rotating $\approx$ 20 % slower than the solar equator (e.g., Snodgrass [1983]). The Fisk field includes a meridional component that is not present in the Parker field. This could account for observations from the Ulysses spacecraft of recurrent energetic particles events at higher latitudes (see Sternal et al. [2011]). Therefore, in the Fisk field, the magnetic field lines at high latitudes can be directly connected to corotating regions in the SW at lower latitudes. The implementation of this Fisk HMF lies beyond the scope of this study. However, for illustrative purposes, Figure 2.8 shows a graphic representation of both types of the complicated Fisk fields also at colatitude of 30^0 (Burger & Hattingh [2001]), clearly showing the distortion of the nicely wound Parker spiral. Furthermore, this Fisk field HMF leads to a more complicated form of transport equation (see Sternal et al. [2011]).

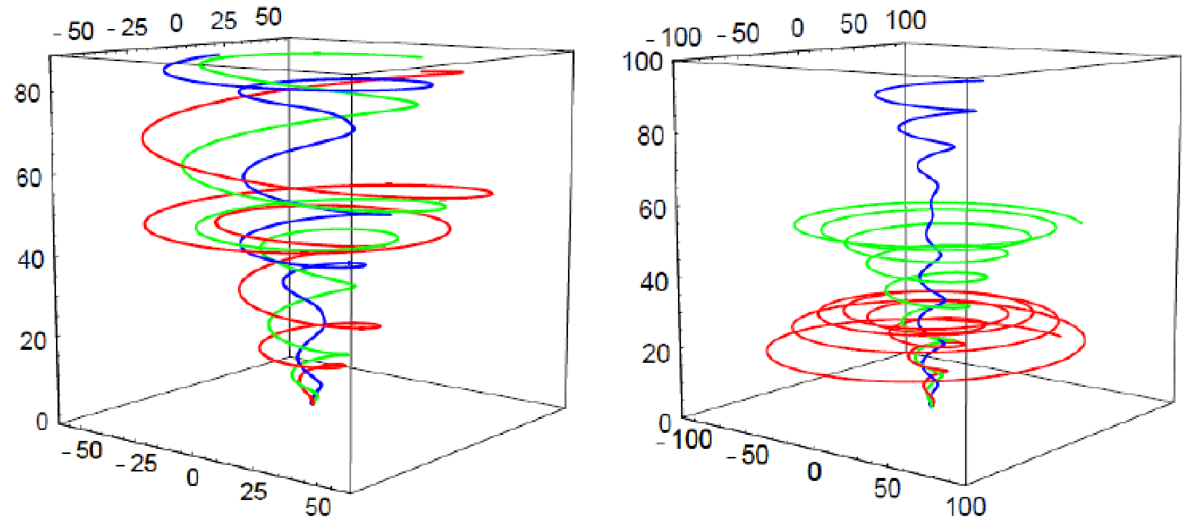

Figure 2.8: A representation of the type I (left panel) and type II Fisk HMF lines (right panel). Both HMF types are at 30^0 colatitude, but at different longitudes. Adapted from (Burger & Hattingh [2001]).

2.6 The heliospheric current sheet

The HMF changes sign across a neutral sheet, thus dividing the heliosphere into two halves, a hemisphere where the HMF is directed inward and a hemisphere where the HMF is directed outward. The transition between these hemispheres is made through the HCS, which is a 3D corotating structure of the HMF. Since the rotational and magnetic axis of the Sun are misaligned by tilt angle α, the rotation of the Sun causes the HCS to have a wavy structure instead of being flat. This waviness of the HCS then correlates with the $\approx$ 11-year solar activity period of the Sun (Hoeksema [1992]). As a consequence, α values also correlates with the changing solar activity cycle, where smaller α values (as low as 5^0) are typically observed during solar minimum conditions and larger α values (as high as 75^0) during solar maximum conditions.

The expression of the wavy HCS was derived by Jokipii & Thomas [1981] for constant and radial SW speed, and is written as

$$\theta' = \frac{\pi}{2} + \sin^{-1}\left\{\sin\alpha \sin\left[\phi + \frac{\Omega\,(r - r_\odot)}{V_{sw}}\right]\right\}, \tag{2.12}$$

where for small values of α Equation (2.12) reduces to

$$\theta' \approx \frac{\pi}{2} + \alpha \sin\left[\phi + \frac{\Omega\,(r - r_\odot)}{V_{sw}}\right]. \tag{2.13}$$

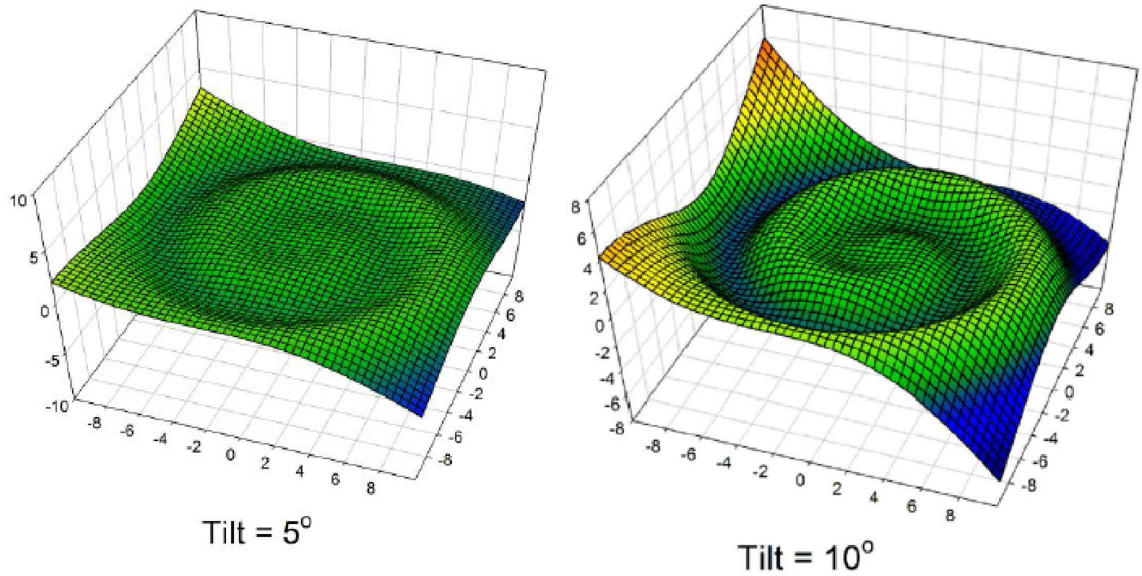

Figure 2.9: HCS simulated at α = 5^0 (left) and α = 10^0 (right). Adapted from Raath [2015].

A 3D simulation of the HCS through the first 10 AU with α of about 5^0 (left) and 10^0 (right) is illustrated in Figure 2.9. It is evident from this figure that an increase in the HCS α causes an increase in the waviness of the HCS. The existence of the HCS is also supported by measurements taken from the Wilcox Solar Observatory (http://wso.stanford.edu/) in a form of synoptic charts of the solar surface at $2.5r_\odot$ as given in Figure 2.10. These synoptic charts depict the magnetic field strength and polarities (Northern and Southern hemispheres) during the solar maximum (high solar activity) of solar cycle 24 (top panel) in December 2015, and solar minimum (low solar activity) of solar cycle 25 (bottom) in October 2021. The black bold lines separating the two regions of opposite polarity, indicated by different shades of grey, represent the HCS. The charts presented clearly show how the waviness of the HCS varies with solar activity. From Figure 2.10, it is evident that the HCS is a bit flat during lower solar activity periods, but develops more with increasing solar activity to become wavier at higher solar activity periods.

Figure 2.11 shows the tilt angle as a function of time measured in years and per Carrington rotation taken from 1975 to 2021 using the classic potential field source surface (PFSS) model (solid line) and the radial model (dashed line). In both models represented in this figure, the lowest value of the HCS tilt angle measured is $\approx 5^0$ during solar minimum conditions, while the highest is $\approx 75^0$ during solar maximum conditions, showing a correlation relationship between solar activity and the tilt angle values as mentioned already. For this study, the radial model of the HCS α is used. For a detailed review on the HCS, see Strauss et al. [2012] and

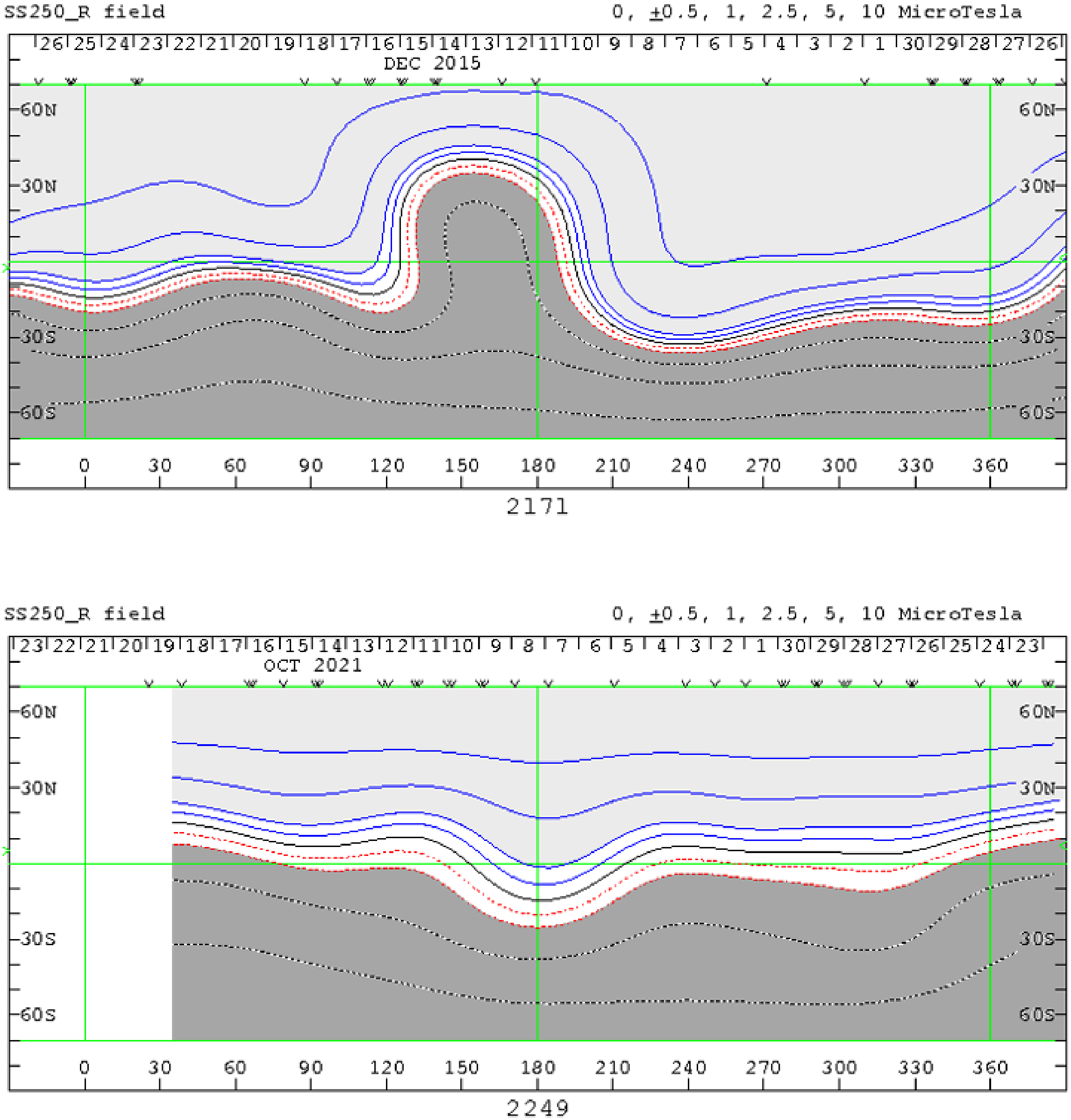

Figure 2.10: Source surface field maps measured at $2.5r_{\odot}$ showing the magnetic field strength (contour lines of various colours), opposite polarities (different shades of grey) and the HCS (black bold contour) during maximum(top panel) and minimum solar activity (bottom panel); respectively. Adapted from the Wilcox Solar Observatory at http://wso.stanford.edu/.

Khabarova et al. [2021].

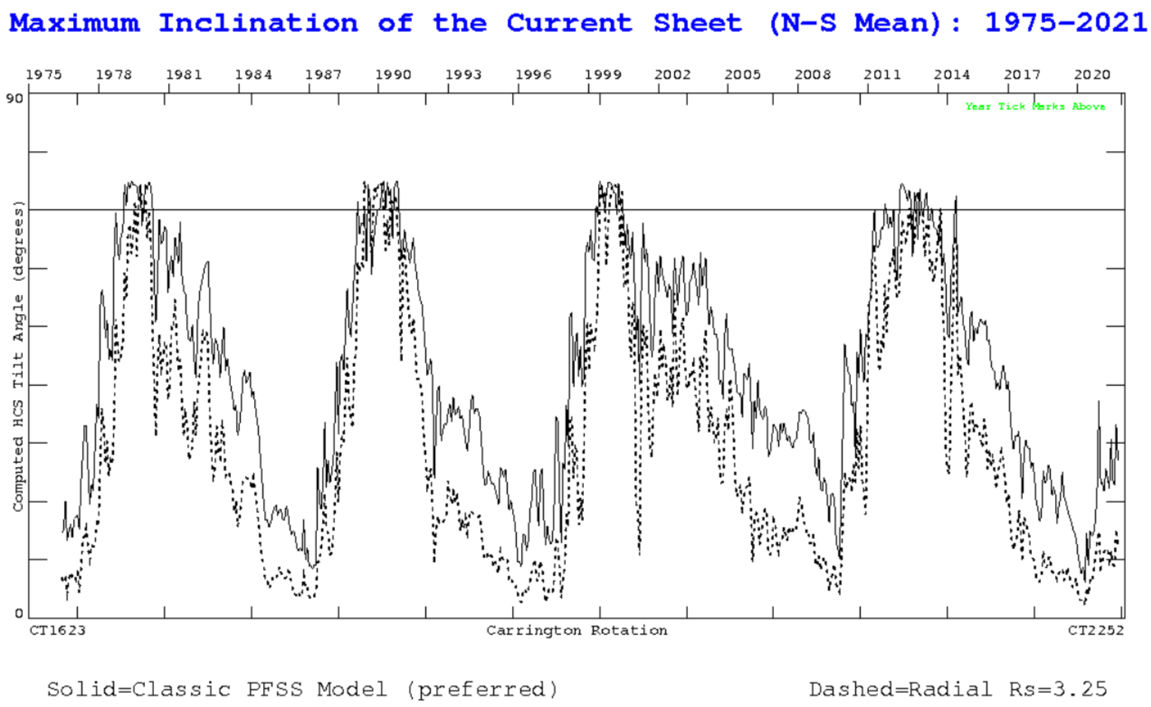

Figure 2.11: Variation in the HCS tilt angle measured from 1975 to 2021 using both the classic potential field source surface (PFSS) model (solid line) and the radial model (dashed line). Data obtained from the Wilcox Solar Observatory at http://wso.stanford.edu/.

2.7 The heliosphere

In simple terms, the heliosphere is a bubble like structure (Ruderman [2000]) that is formed in interstellar space by the interaction between the SW and the local interstellar medium (LISM) (see Opher et al. [2015]). This bubble like structure extends over the entire solar system and is filled with the SW and HMF. The SW and the HMF push back the interstellar magnetic field (ISMF) and plasma to prevent them from flowing into the heliosphere. Shown in Figure 2.12 is the schematic representation of the geometry of the heliosphere including the heliopause (HP), the TS and the bow shock (BS) positions as the main boundaries of the heliosphere. The HP serves as a boundary where the pressure from the SW is balanced by LISM, therefore implying that the SW plasma changes its direction at this region and merges with the surrounding LISM (Ruderman [2000], Pogorelov et al. [2017]). The TS, however, possesses dynamic features that vary with solar activity, the SW, interstellar wind, etc., and serves as a boundary where supersonic speeds of the SW are decreased to subsonic speeds after an encounter with the LISM (Mitchell et al. [2005], Ferreira et al. [2007]), as already mentioned. Additionally, when the SW speed is decreased in this region, there is an increase in plasma temperature and density, showing that this shock region causes discontinuity in the heliosphere (Mitchell et al. [2005]). However, as the heliosphere moves through the LISM, it becomes asymmetrical with respect to the Sun, with the tail region in Figure 2.12 much more extended than the nose region in the direction of the movement. The BS, on another hand, is a boundary formed when the SW pushes against the interstellar wind (e.g., Scherer & Fichtner [2014]). Moreover, between the TS and HP exists a region called the inner heliosheath (Ferreira et al. [2007]), while the region between the HP and the BS is referred to as the outer heliosheath (Mitchell et al. [2005]). Noteworthy is that, in most CR modulation studies, the term heliosheath is used to refer to the inner heliosheath.

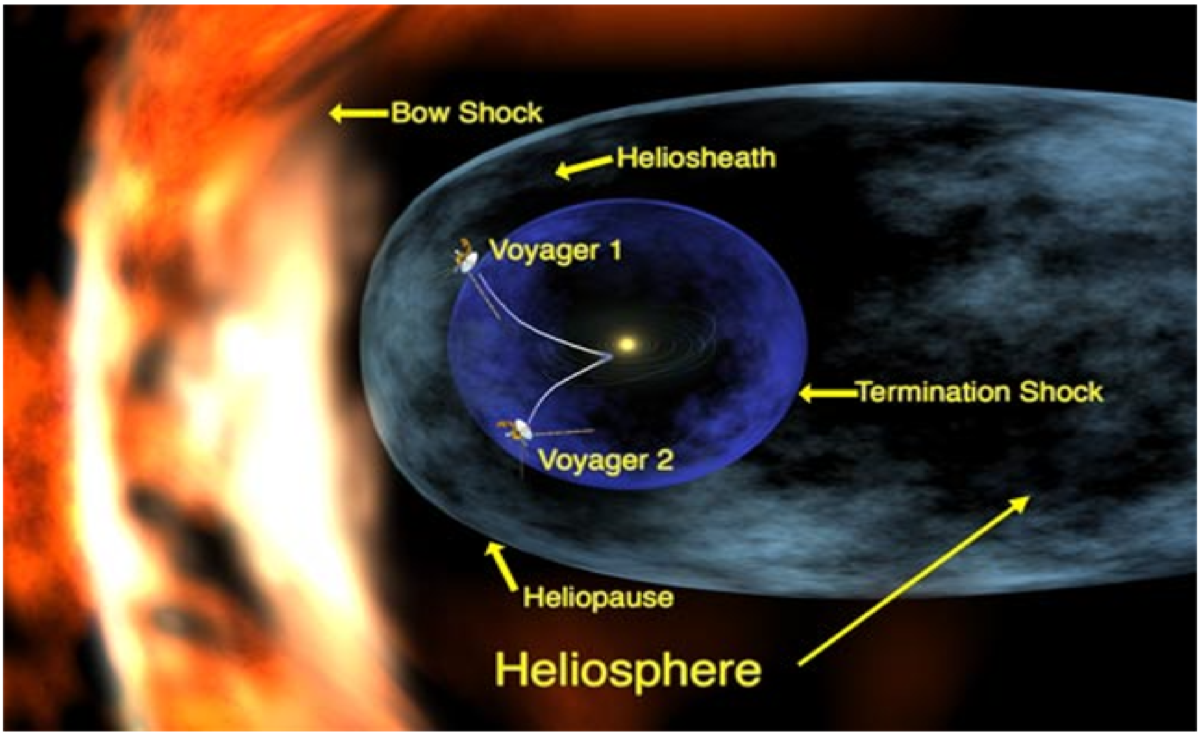

Figure 2.12: A representation of the geometry and features of the heliosphere. Taken from NASA's website:nasa.gov/missionpages/sunearth/science Heliosphere.html.

In this work the HP is assumed to be the CRs modulation boundary, where the LIS's are specified. Therefore, no boundary beyond the HP (outer heliosheath and BS) is considered.

2.8 The influence of the heliospheric structures on CRs over the solar cycle

When entering the heliosphere, GCRs are modulated as a function of position, time and energy as already mentioned in the previous sections. This modulation, however depends on solar activity and its features, e.g., HMF, HCS α, HCS waviness and SSNs. The behaviour of the CR species during different solar activity periods at the Earth are widely studied using neutron monitor (NM) counts. Figure 2.13 illustrates various measurements of heliospheric modulation parameters in panels (a) to (e) from 1960 until the end of 2014 (Strauss & Potgieter [2014a]),

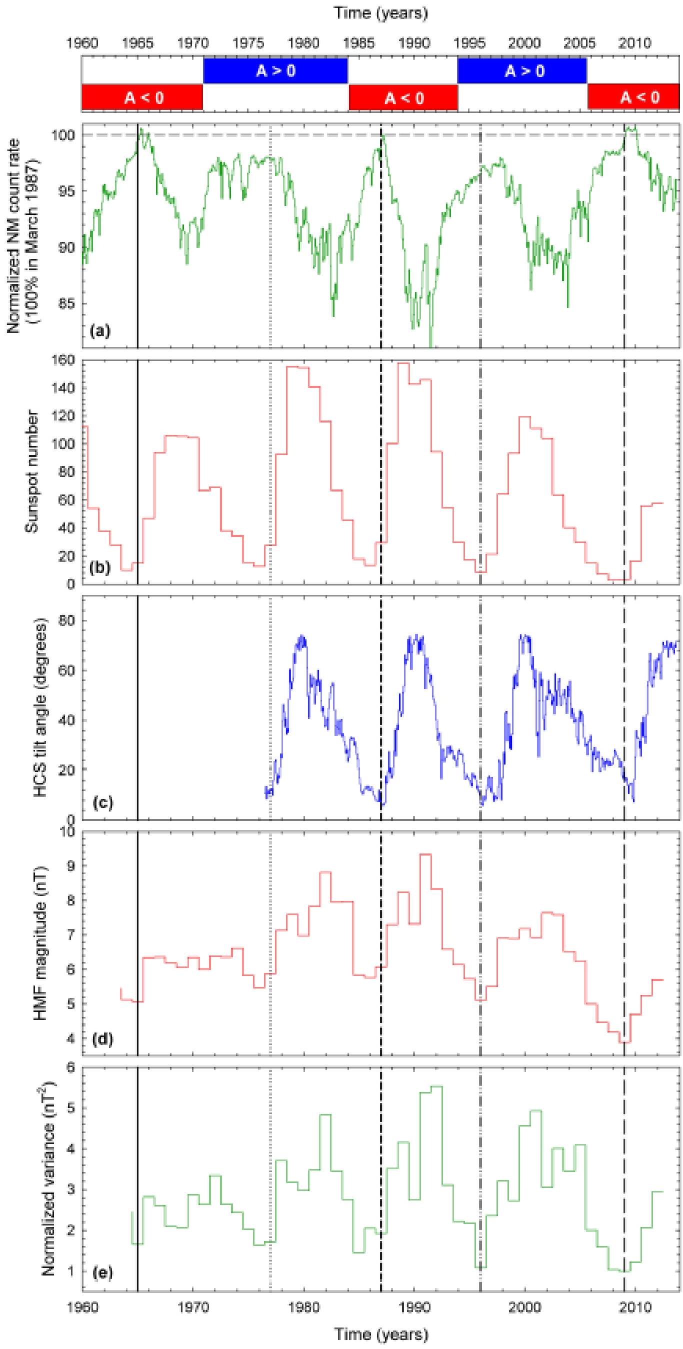

Figure 2.13: Panel (a) shows the neutron monitor (NM) counting rate, normalized to March 1987, of the Hermanus NM in South Africa; panel(b) the yearly averaged SSNs (taken from the Solar Influences Data Analysis Center: sidc.oma.be); panel (c) the highest latitudinal excursion of the HCS, as the average of the new and classical HCS models (taken from the Wilcox Solar Observatory:wso.stanford.edu); and panel (d) the HMF magnitude at Earth (taken from cohoweb.gsfc.nasa.gov). The HMF polarity cycles are indicated by A $<$ 0 and A $>$ 0, respectively. Adapted from Strauss & Potgieter [2014a].

spanning five solar-minimum and solar maximum epochs. The long-term solar modulation recorded by NM counting rate shows a clear 11-year modulation cycle. This cycle is anti-correlated with solar activity, with maximum CR intensities for solar minimum (smaller values of the SSNs, HMF, α, and the magnetic variance) and minimum intensities for solar maximum conditions (larger values of the SSNs, HMF, α, and the magnetic variance). Apart from the 11-year modulation cycle, a 22-year cycle is also evident where some periods of maximum intensity shows a plateau and some peak-like shapes. This can be described by drift effects where in an A $>$ 0 cycle positively charged particles drift inwards toward the Sun through the polar regions and are relatively insensitive to conditions in the equatorial region, e.g. like changes in the HCS, and the plateau-like pattern is observed. While for the A $<$ 0 cycle, these positive particles drift along the HCS and are very sensitive to changes in the tilt angle resulting in a peaked profile (Strauss & Potgieter [2010], Potgieter [2013], Raath [2015]). For more details on the behaviour of CRs over the solar cycle and NM measurements, see Ross & Chaplin [2019].

2.9 Spacecraft and satellite missions of interest

From the numerical modeling point of view, the accumulation of data from $in\ situ$ observations by spacecraft is one of the most important aspect in the study of the heliospheric modulation of CRs. This is so because the accumulated data contribute meaningfully to the testing, refinement and validation of the numerical models in use. In this section the PAMELA, Voyager and AMS02 space missions are briefly discussed.

2.9.1 PAMELA mission

PAMELA is a satellite-borne experiment that was designed with an aim to make long-term duration cosmic radiation near the Earth (Picozza et al. [2007], Adriani et al. [2013], Marcelli et al. [2020, 2022]). This satellite experiment was launched in June 2006 from Bajkonur cosmodrome Kazakhstan and has been collecting valuable GCRs up to January 2016, spanning almost 10 years in orbit. Though the primary scientific objective for PAMELA was to study the antimatter component of CRs (Boezio et al. [2017]), this satellite experiment with its low-energy limit, also measured CR protons and helium nuclei which is suitable for studies focusing on low-energy CRs with different mass-to-charge ratios (see Martucci et al. [2018], Marcelli et al. [2020, 2022]). PAMELA's orbit was initially elliptical with an altitude ranging between 350 km and 610 km with an inclination of about 70^0, but later in the year 2010 was set to circular at a fixed altitude of about 600 km. What is of interest to this study, and related to this satellite experiment, is the high precision CR flux data observed around the Earth together with the observed non-constant proton to helium ratio reported by Marcelli et al. [2020, 2022]. For a review of PAMELA satellite and its scientific missions, see Adriani et al. [2017] and Boezio et al. [2017]. For more information on PAMELA datasets visit: http://pamela.roma2.infn.it/.

2.9.2 Voyager mission

The National Aeronautics and Space Administration "twin" spacecraft, V1 and V2 were launched in 1977. Both V1 and V2 travel at speeds of about ≈ 3.6 AU/year and ≈ 3.1 AU/year at heliolatidues of 34.4^0 and 28.8^0 above and below the equatorial plane, respectively. On making their way out of the solar system, these spacecraft encountered planets Saturn and Jupiter, which were planets of interest and part of the mission's objective. Moreover, V2 extended the objective and encountered planets Uranus and Neptune, and is still the only spacecraft by far that has explored these outer planets. Observations made with the two Voyager spacecraft confirmed that the SW decelerates to form the heliospheric TS, with V1 crossing this TS at a radial distance of ≈ 94 AU in 2004 (Stone et al. [2005], Decker et al. [2005]), while V2 crossed it in 2007 at ≈ 84 AU but at a different heliolatitude (Stone et al. [2008], Richardson et al. [2008]). These different positions of the TS confirm the dynamic and cyclic nature of the shock's position, and that it is north-south asymmetrically shaped. The V1 and V2 missions were the first to study the outer solar system, the TS, and the heliosheath. Additionally, in August 2012, V1 made a transition through the HP at ≈ 122 AU, and, for the first time, it measured directly the unmodulated spectra for various GCR species at lower energies (Stone et al. [2013], Krimigis et al. [2013]). About 7 years later, V2 also crossed the HP in November 2018 at ≈ 119 AU. The two spacecraft are still in orbit and expected to remain there until 2025. For more information on the Voyager missions, visit http://voyager.jpl.nasa.gov/mission/intersterllar.html/.

2.9.3 AMS02

The AMS02 is another space-borne experiment that explores the composition of high-energy (rigidity) CRs with high precision and accuracy near the Earth similar to PAMELA. This spectrometer operates within the international space station and has been mounted there since May 2011. In addition to measuring CR data over a wide energy (rigidity) range, AMS02 also measures this data with different time resolution and contains an intense magnetic field formed by its superconducting magnet of about 0.87 T. Additionally, the AMS02 also has an efficient particle identification feature which, together with the superconducting magnet, enables high precision measurements extending to TeV regions. After being operational in 2011, the first ever results from this spectrometer were put out by Aguilar et al. [2013], and more soon after, including CR proton and helium flux measured between May 2011 and May 2017 (see Aguilar et al. [2018]) and CR helium isotopes (Aguilar et al. [2019]) which are of particular interest in this study.

Due to its efficient particle identification feature, AMS02 is able to separate and measure helium isotopes ($^3He_2$ and $^4He_2$) simultaneously and return their individual flux data instead of just the total helium (He). Studying these isotopes individually is of great importance to reproduce accurate numerical model results as shown by Ngobeni et al. [2022]. Therefore, AMS02 observations are used in this study only to constrain the helium isotope LIS's. For more on the achievements of the mission, visit http://www.ams02.org/.

2.10 Summary

This chapter briefly introduced concepts that are necessary for the understanding of the modulation of CR species in the heliosphere. These concepts included the: variable Sun and its observed features, SW and the TS, Parker HMF and its modifications, HCS and the geometry of the heliosphere. This was followed by a concise illustration of how these heliospheric structures influence CRs over a solar cycle. This chapter ended with a brief discussion of PAMELA, Voyager and AMS space missions.

The next chapter gives an overview of the CR transport in the heliosphere, with more emphasis placed on species with different A/Z.

Chapter 3

The transport equation and the elements of the diffusion tensor

3.1 Introduction

Once GCRs are inside the heliosphere, they interact with the radially expanding SW and its embedded turbulent magnetic field. The understanding of this interaction is based on four major modulation processes: convection, diffusion, adiabatic energy changes, and gradient, curvature and current sheet drifts. Combined, these processes cause the intensity of GCRs to change relative to their LIS's, as a function of position, time and momentum, known as CR modulation in the heliosphere. Theoretically, the four major modulation processes are described by the Parker [1965] transport equation.

In this chapter, the modulation processes in the TPE are introduced and discussed, with the aim of illustrating the spatial and rigidity dependence of the elements of the diffusion tensor. This work builds on the previous work of Vos [2016], but with more emphasis on the dependence of the diffusion and drift coefficients on the ratio of particle speed to the speed of light (β) for GCR species with different A/Z. The essence of this chapter is to provide theoretical background required in Chapters 4 - 6.

3.2 The Transport Equation

The four major modulation processes that describe the transport and modulation of CRs were first combined into one equation of CR transport by Parker [1965], thereafter redefined by Gleeson & Axford [1967]. This TPE is given by

$$\frac{\partial f}{\partial t} = -(V_{sw} + \langle v_d \rangle) \cdot \nabla f + \nabla \cdot (K_s \cdot \nabla f) + \frac{1}{3}(\nabla \cdot V_{sw}) \frac{\partial f}{\partial lnp} + Q, \tag{3.1}$$

in terms of the omni-directional CR distribution function $f = f(\overrightarrow{r}, p, t)$, with $\overrightarrow{r}$ as the position vector, p the particle momentum, t time, K_s the symmetric diffusion tensor ,and $\langle v_d \rangle$ the averaged guiding center drift velocity for a near isotropic distribution function. The terms on the right-hand side represent the outward convection of particles due to the radial outflow of the SW, drift of particles due to changes in the current-sheet, gradient and curvature of the HMF, the diffusion of CRs parallel and perpendicular to the HMF, adiabatic energy changes due to the expanding SW, and the source term which describes possible sources of CRs inside the heliosphere, respectively. Since the particles of interest in this study include only GCRs, Q in Equation (3.1) is set to zero. For an overview on CR transport and processes inside the heliosphere, see e.g., Potgieter [2013], Vos [2016], Nndanganeni [2016] and Luo et al. [2020].

For this study, the TPE is solved numerically for a steady state ($\frac{\partial f}{\partial t} = 0$) condition in 3D as a function of rigidity P in a spherical coordinate system rotating with the sun. Therefore, Equation (3.1) is rewritten as

$$
\begin{aligned}
0 \;=\; & \left[\frac{1}{r^2}\frac{\partial}{\partial r}(r^2 k_{rr}) + \frac{1}{r\sin\theta}\frac{\partial}{\partial\theta}(k_{\theta r}\sin\theta) + \frac{1}{r\sin\theta}\frac{\partial k_{\phi r}}{\partial\phi} - V\right]\frac{\partial f}{\partial r} \\
& + \left[\frac{1}{r^2}\frac{\partial}{\partial r}(r k_{r\theta}) + \frac{1}{r^2\sin\theta}\frac{\partial}{\partial\theta}(k_{\theta\theta}\sin\theta) + \frac{1}{r^2\sin\theta}\frac{\partial k_{\phi\theta}}{\partial\phi}\right]\frac{\partial f}{\partial\theta} \\
& + \left[\frac{1}{r^2\sin\theta}\frac{\partial}{\partial r}(r k_{r\phi}) + \frac{1}{r^2\sin\theta}\frac{\partial k_{\theta\phi}}{\partial\theta} + \frac{1}{r^2\sin^2\theta}\frac{\partial k_{\phi\phi}}{\partial\phi} + \Omega\right]\frac{\partial f}{\partial\phi} \\
& + k_{rr}\frac{\partial^2 f}{\partial r^2} + \frac{k_{\theta\theta}}{r^2}\frac{\partial^2 f}{\partial\theta^2} + \frac{k_{\phi\phi}}{r^2\sin^2\theta}\frac{\partial^2 f}{\partial\phi^2} + \frac{2k_{r\phi}}{r\sin\theta}\frac{\partial^2 f}{\partial r\partial\phi} \\
& + \frac{1}{3r^2}\frac{\partial}{\partial r}(r^2 V)\frac{\partial f}{\partial\ln P},
\end{aligned}
\tag{3.2}
$$

with κ_{rr}, $\kappa_{\theta r}$, $\kappa_{\phi r}$, $\kappa_{r\theta}$, $\kappa_{\theta\theta}$, $\kappa_{\phi\theta}$, $\kappa_{r\phi}$, $\kappa_{\theta\phi}$ and $\kappa_{\phi\phi}$ as the elements of the diffusion and drift tensor in spherical coordinate system. These nine elements of the 3D tensor based on a Parkerian HMF are discussed in details below. Note that κ_{rr}, $\kappa_{r\phi}$, $\kappa_{\theta\theta}$, $\kappa_{\phi r}$, $\kappa_{\phi\phi}$ describe the diffusion processes and that $\kappa_{r\theta}$, $\kappa_{\theta r}$, $\kappa_{\theta\phi}$, $\kappa_{\phi\theta}$ describe particle drifts, in most cases considered to be gradient, curvature, and current sheet drifts.

The steady-state approximation is a reasonable assumption during solar minimum, but less so during solar maximum. However, for studies of time variation of GCR intensities averaged over Carrington rotations, it is still acceptable and a good approximation (see Aslam et al. [2019]).

The relationship between P and p is given as

$$P = \frac{pc}{\mid q \mid}, \tag{3.3}$$

where c is the speed of light and $\mid q \mid = Ze$ is the charge, where Z is the number of charges or atomic number and e is the elementary charge. Considering the relationship between energy and momentum, the conversion from rigidity in Equation (3.3) to kinetic energy per nucleon, E, is defined as

$$P = \left(\frac{A}{Z}\right) \sqrt{E(E + 2E_0)}, \tag{3.4}$$

with A the mass number and E_0 as the particle's rest mass energy (see Moraal [2013] for a more detailed discussion). For GCR protons and both helium isotopes, the rest mass per nucleon $E_0 = 0.9383$ GeV is assumed, however their A/Z are different. The proton particle has $A/Z = 1$, whereas helium has $A/Z = 1.5$ or $A/Z = 2$, depending on the helium isotope of interest. The relation in Equation (3.4) is illustrated in Figure 3.1 for CR species with different A/Z. The relationship is such that for the same rigidity value, species with lower A/Z maintain higher kinetic energy/nucleon.

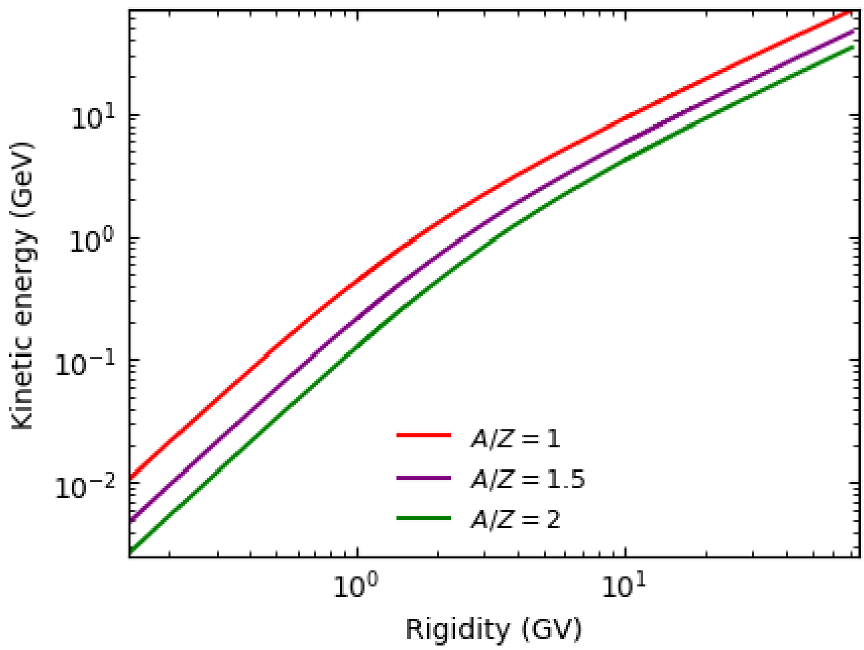

Figure 3.1: Kinetic energy/nucleon as a function of rigidity for CR species with different A/Z values (protons with $A/Z = 1$, $^3He_2$ with $A/Z = 1.5$ and $^4He_2$ with $A/Z = 2$).

It is worth noting that for each CR species of interest as given in Figure 3.1, E is proportional to P^2 and P, respectively, below and above their rest-mass energies. This can also be deduced from Equation (3.4) with the limits $E \ll E_0$ and $E \gg E_0$.

Another important quantity that can be derived from Equation (3.4) is β, which depends on A/Z and P, given as

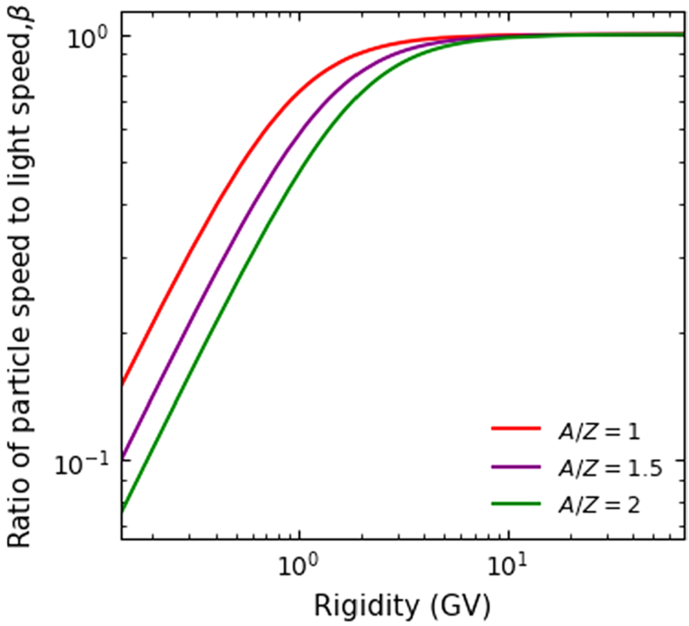

Figure 3.2: The ratio of particle speed to speed of light β as a function of rigidity for CRs species with different A/Z.

$$\beta = \frac{v}{c} = \frac{P}{\sqrt{P^2 + \left(\frac{A}{Z}\right)^2 E_0^2}}. \tag{3.5}$$

The relation in Equation (3.5) is illustrated in Figure 3.2 as a function of rigidity for CR species with different A/Z values. Note a difference in β for the three GCR species below $P \approx 5$ GV, whereas above this rigidity the three curves become similar with increasing rigidity and move towards a constant value of 1.0 as the particles become relativistic.

Since the TPE is solved in this study in terms of the distribution function, $f = f(\overrightarrow{r}, P, t)$, and the CR intensities being represented in terms of the differential intensities, $j = j(\overrightarrow{r}, P, t)$, the two are related in a form,

$$j(\overrightarrow{r}, P, t) = P^2 f(\overrightarrow{r}, P, t), \tag{3.6}$$

with units of particles / unit area / unit time/ unit solid angle / unit kinetic energy. For a derivation of this equation, see e.g., Vos [2016] and Raath [2020].

In the next section, it is illustrated how these coefficients are transformed from the magnetic field aligned to spherical coordinate system.

3.3 Diffusion tensor

The diffusion tensor in the magnetic field aligned coordinate system, necessary for the transport of charged particles in the heliosphere, is made up of a symmetrical diffusion tensor K_s as in Equation (3.1) and an asymmetrical drift tensor K_A. Therefore, the tensor in the heliosphere consists of both diffusion and drift coefficients, and is given as $K = K_s + K_A$, which can further be written as

$$K = \begin{bmatrix} \kappa_{||} & 0 & 0 \\ 0 & \kappa_{\perp\theta} & 0 \\ 0 & 0 & \kappa_{\perp r} \end{bmatrix} + \begin{bmatrix} 0 & 0 & 0 \\ 0 & 0 & \kappa_A \\ 0 & -\kappa_A & 0 \end{bmatrix} = \begin{bmatrix} \kappa_{||} & 0 & 0 \\ 0 & \kappa_{\perp\theta} & \kappa_A \\ 0 & -\kappa_A & \kappa_{\perp r} \end{bmatrix}, \tag{3.7}$$

where $\kappa_{||}$ is the diffusion coefficient (DC) parallel to the mean HMF, $\kappa_{\perp r}$ and $\kappa_{\perp\theta}$ denote the DCs perpendicular to the mean HMF in the radial and polar direction respectively, with κ_A describing that of gradient, curvature and HCS drifts encountered by particles.

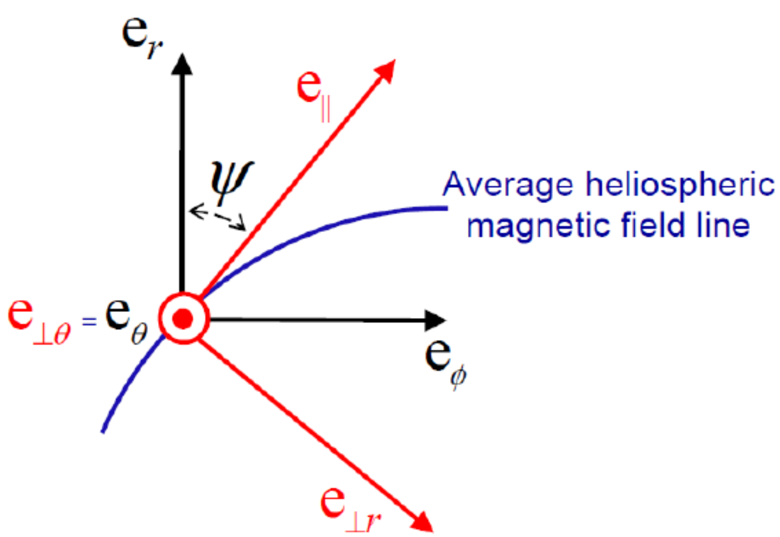

Figure 3.3: A schematic representation of the magnetic field-aligned coordinate system and its relation to the spherical coordinate system. The unit vectors parallel to the average heliospheric magnetic field line, perpendicular in the radial and polar directions are represented by $e_{||}$, $e_{\perp r}$ and $e_{\perp\theta}$, respectively; with e_r, e_θ and e_ϕ spherical polar coordinates unit vectors. Adapted from Manuel [2013].

Figure 3.3 shows a schematic representation of the HMF-aligned coordinate system and its relation to the spherical coordinate system. The unit vector parallel to the average heliospheric magnetic field line, perpendicular in the radial and polar direction are represented by $e_{||}$, $e_{\perp r}$ and $e_{\perp\theta}$, respectively, with e_r, e_θ and e_ϕ as spherical polar coordinates unit vectors. It is evident from this figure that the relation between the unit vectors in HMF-aligned and spherical coordinate systems are given as

$$
\begin{aligned}
e_{||} &= \cos\psi e_r + \sin\psi e_\phi \\
e_2 &= e_{||} \times e_1 = \sin\psi e_r + \cos\psi e_\phi \\
e_1 &= e_\theta,
\end{aligned}
\tag{3.8}
$$

where ψ is the spiral angle, defined as the angle between the parallel component ($e_{||}$) of the HMF and the radial direction (e_r) mentioned in Chapter 2. The transformation matrix between the two coordinates systems can thus be written as

$$
\mathbf{T} = \begin{bmatrix} \cos\psi & 0 & -\sin\psi \\ 0 & 1 & 0 \\ \sin\psi & 0 & \cos\psi \end{bmatrix},
\tag{3.9}
$$

so that in spherical coordinate system the diffusion tensor given in Equation (3.7) is

$$
\begin{aligned}
\begin{bmatrix} k_{rr} & k_{r\theta} & k_{r\phi} \\ k_{\theta r} & k_{\theta\theta} & k_{\theta\phi} \\ k_{\phi r} & k_{\phi\theta} & k_{\phi\phi} \end{bmatrix} &= \mathbf{TKT}^{\mathsf{T}} \qquad (3.10) \\
&= \begin{bmatrix} \cos\psi & 0 & \sin\psi \\ 0 & 1 & 0 \\ -\sin\psi & 0 & \cos\psi \end{bmatrix} \begin{bmatrix} k_{||} & 0 & 0 \\ 0 & k_{\perp\theta} & k_A \\ 0 & -k_A & k_{\perp r} \end{bmatrix} \begin{bmatrix} \cos\psi & 0 & -\sin\psi \\ 0 & 1 & 0 \\ \sin\psi & 0 & \cos\psi \end{bmatrix} \\
&= \begin{bmatrix} k_{||}\cos^2\psi + k_{\perp r}\sin^2\psi & -k_A\sin\psi & (k_{\perp r} - k_{||})\cos\psi\sin\psi \\ k_A\sin\psi & k_{\perp\theta} & k_A\cos\psi \\ (k_{\perp r} - k_{||})\cos\psi\sin\psi & -k_A\cos\psi & k_{||}\sin^2\psi + k_{\perp r}\cos^2\psi \end{bmatrix},
\end{aligned}
$$

where $\mathbf{T}^{\mathsf{T}}$ represents the transpose of matrix $\mathbf{T}$ in Equation (3.9).

Since a 3D numerical model is used in this study, all the elements of the diffusion tensor in Equation (3.10) are of interest. This way the expressions for $\kappa_{||}$, $\kappa_{\perp r}$ and $\kappa_{\perp\theta}$ must be specified, in addition to that of ψ. The expression for ψ is already given in Chapter 2 and Figure 3.4 shows for illustrative purposes the magnitudes of $\sin^2\psi$ and $\cos^2\psi$, together with $\cos\psi\sin\psi$ as a function of radial distance in the equatorial plane. From this figure it follows that both $\cos^2\psi$ and $\cos\psi\sin\psi$ decrease with increasing radial distance, with the decrease being more rapid for $\cos^2\psi$ compared to $\cos\psi\sin\psi$. These two curves show a significant decrease at the TS position, whereas $\sin^2\psi$ stays almost constant for most of the heliosphere.

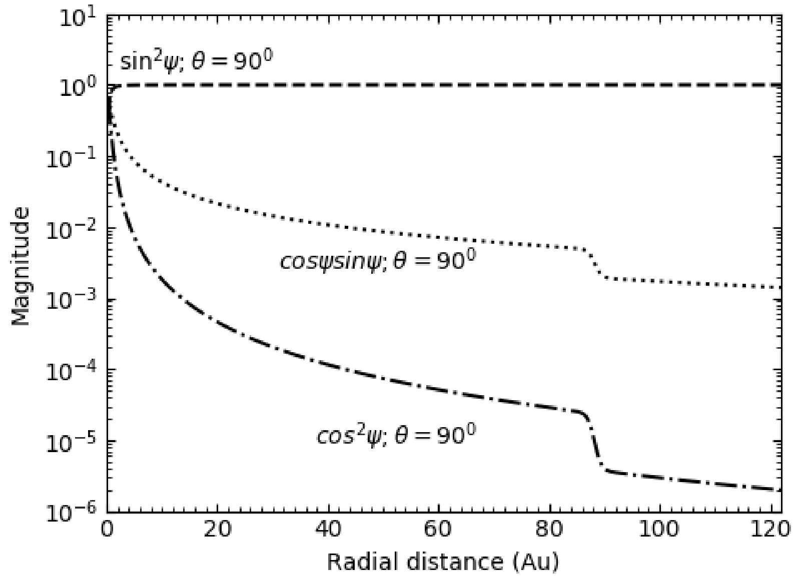

Figure 3.4: shows $\sin^2\psi$ (dashed lines), $\cos^2\psi$ (dash-dot-dash lines), and $\cos\psi\sin\psi$ (dotted lines) represented in Equation (3.10) as a function of radial distance r at the equatorial plane ($\theta = 90^0$).

3.4 Particle diffusion

The transport of CRs inside the heliosphere is mainly determined by their diffusion along and across the HMF lines, which results from the HMF irregularities and scattering. Cosmic ray diffusion is included in Equation (3.1) with the elements of diffusion, e.g., $\kappa_{\parallel}$, $\kappa_{\perp r}$ and $\kappa_{\perp\theta}$ given in Equation (3.7). These elements of the diffusion tensor are referred to as the DCs and are related to the Mean-free paths (MFPs) λ through

$$\kappa = \frac{v}{3}\lambda, \tag{3.11}$$

with the particle speed $v = \beta c$, derived from the relation given in Equation (3.5).

3.4.1 Parallel diffusion

The diffusion processes can be described by quasi-linear theory (QLT) (see e.g. Jokipii [1966], Hasselmann & Wibberenz [1970]), with the expression of $\kappa_{\parallel}$ derived from the Fokker-Planck equation using the method of [Earl, 1974] given as

$$\kappa_{\parallel} = \frac{v^2}{8}\int_{-1}^{1}\frac{(1-\mu^2)^2}{D_{\mu\mu}}d\mu, \tag{3.12}$$

where $D_{\mu\mu}$ is the Fokker Plank coefficient for pitch angle scattering and μ is the cosine of the pitch angle. In Equation (3.12), $D_{\mu\mu}$, which is essentially the rate of particle scattering, depends

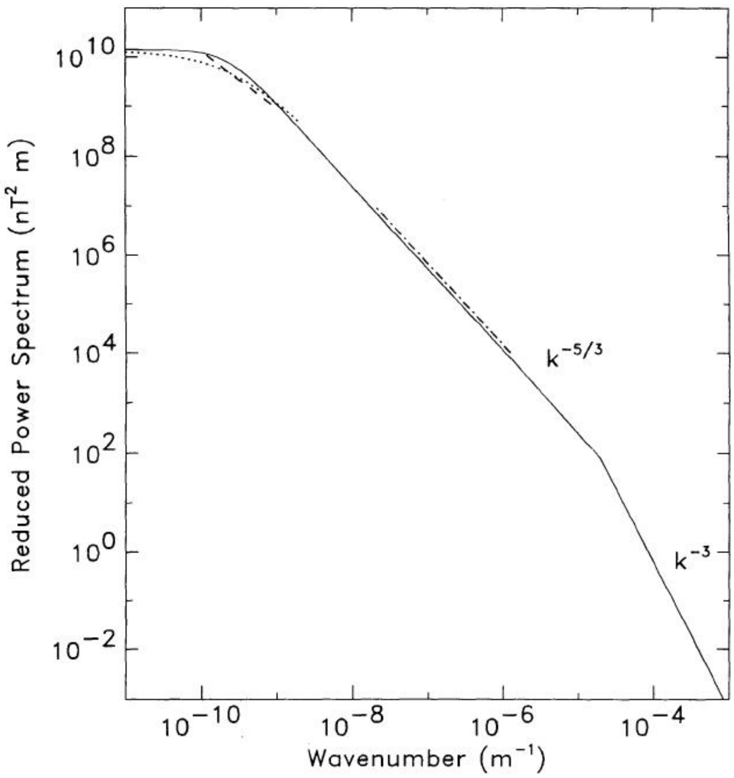

Figure 3.5: The power spectrum for slab turbulence model (solid line) for the heliosphere at Earth compared to observations (dashed and dotted lines). Adapted from Bieber et al. [2004].

on the turbulence model considered (see Teufel & Schlickeiser [2002], Teufel & Schlickeiser [2003], Shalchi & Schlickeiser [2004]).

The calculation of $\kappa_{||}$ in Equation (3.12) needs as input the power spectrum of the magnetic field fluctuations, shown in Figure 3.5, which can be divided into three ranges namely the energy range, where the power spectrum variation is independent of the wave number k, the inertial range, where it is proportional to $k^{-5/3}$, and a dissipation range where it is proportional to k^{-3} (see e.g., Bieber et al. [1994]). However, when it comes to reproducing both the observed CR kinetic energy and rigidity spectra, with unprecedented accuracy over a long period of time (e.g., PAMELA and AMS02 observations), $\kappa_{||}$ obtained from such turbulence techniques frequently cause complications. As a result, the spatial and rigidity dependence of $\kappa_{||}$ used in this study is described using a more simplified approach which is verified to be a reasonable approximation of the QLT and reproduces reasonably well Spacecraft observations for different CR species around the Earth (see Vos [2016], Nndanganeni [2016], Corti et al. [2019], Fiandrini et al. [2021], Luo et al. [2020]).

The expression for $\kappa_{||}$ assumed to study the modulation of GCR proton and the two helium isotopes in this study was originally adapted from Vos & Potgieter [2015], but due to its success in reproducing observations over a wide energy and rigidity range, it has recently found its way into the work of many researchers (see Potgieter & Vos [2017], Corti et al. [2019], Ngobeni et al. [2020], Luo et al. [2020], Fiandrini et al. [2021]). The rigidity of $\kappa_{\|}$ is approximated by two power-laws with a smooth transition of slopes, and is given by

$$\kappa_{\|} = (\kappa_{\|})_0 \beta \left(\frac{B_0}{B}\right) \left(\frac{P}{P_0}\right)^{c_1} D_{\|}(P), \tag{3.13}$$

where

$$D_{\|}(P) = \left[\frac{\left(\frac{P}{P_0}\right)^{c_3} + \left(\frac{P_k}{P_0}\right)^{c_3}}{1 + \left(\frac{P_k}{P_0}\right)^{c_3}} \right]^{\frac{c_{2\|} - c_1}{c3}}, \tag{3.14}$$

with $(\kappa_{\|})_0$ a scaling constant in units of $10^{22} cm^2 s^{-1}$, P_0 = 1 GV, B_0 = 1 nT and P_k = 4 GV as the rigidity at which the two power-laws make a transition, while c_1 gives the rigidity slope of DCs below 4 GV, $c_{2\|}$ the rigidity slope above 4 GV and c_3 controls the smoothness in the rigidity slopes before and after the transition.

Therefore, the relationship between $\lambda_{\|}$ and $\kappa_{\|}$ follows from Equation (3.11) and is given as

$$\kappa_{\|} = \frac{v}{3} \lambda_{\|}. \tag{3.15}$$

From Equation (3.15) it is notable that MFPs describe CR diffusion in the heliosphere.

3.4.1.1 Rigidity dependence of $\kappa_{\|}$

Figure 3.6 shows the computed rigidity dependence of $\kappa_{\|}$ (left panel) and $\lambda_{\|}$ (right panel) at 1 AU in the equatorial plane. This figure is obtained with the assumed dimensionless quantity $c_{2\|}$ = 1.20, $c_{2\perp}$ = 0.70$c_{2\|}$, c_1 = 0.85, and c_3 = 2.50 in Equation (3.13). The magnitude of the HMF at the Earth and the tilt, together with the position of the termination shock are kept at B = 4.95 nT, α = 16.58^0, and TS = 88 AU, respectively. These parameters may change with time, if required, in response to changing solar activity. This will be shown in detail in Chapter 4.

Below 1 GV the function $D_{||}$, given in Equation (3.14), is almost rigidity independent and approaches a constant value of $\approx$ 1.0. As a result, the shape of the rigidity dependence of $\kappa_{||}$ at these rigidities is determined by the combination of the rigidity power law index c_1 and the rigidity dependence of β as shown in Figure 3.2. Therefore, the slope of the rigidity dependence of $\lambda_{||}$ below 1 GV depends only on the power law index c_1. Consequently, $\kappa_{||}$ and $\lambda_{||}$ have different rigidity slopes as noted in Figure 3.6. However, at higher rigidities, $\beta \approx 1.0$ and the rigidity dependence of $\kappa_{||}$ and $\lambda_{||}$ is determined by a combination of the rigidity power indices c_1 and $c_{2||}$.

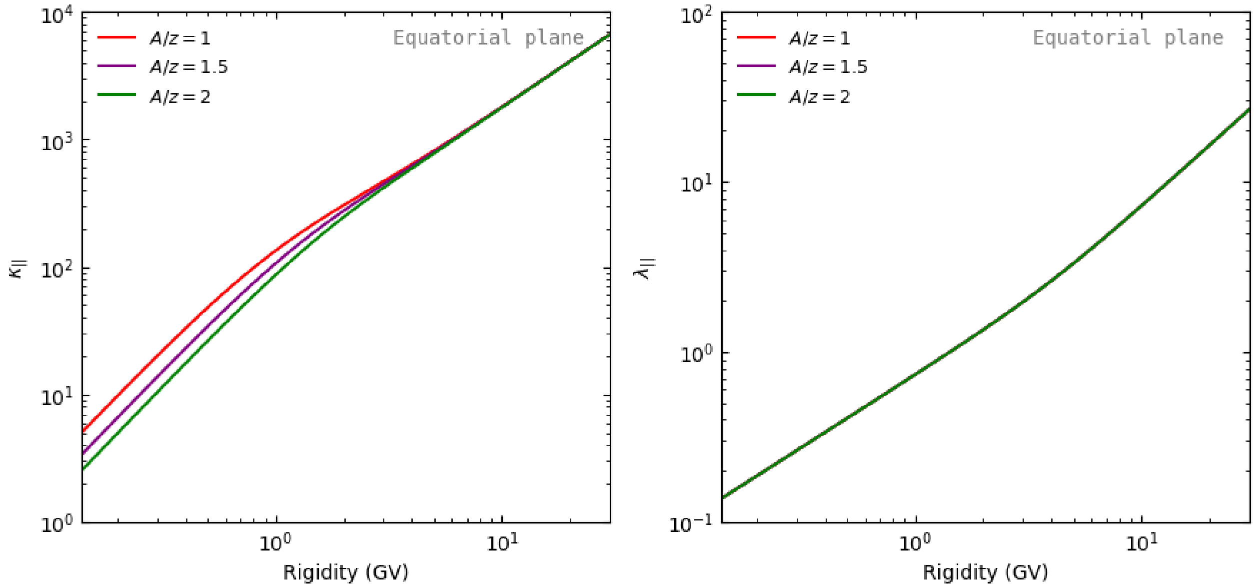

Figure 3.6: The rigidity dependence of $\kappa_{||}$ (left panel) for CR species with different A/Z values at 1 AU in the equatorial plane with the corresponding MFP $\lambda_{||}$ (right panel).

The dependence of $\kappa_{||}$ on β is clearly highlighted on the left panel of Figure 3.6. This figure indicates that $\kappa_{||}$ decreases with increasing A/Z with $P \leq 4$ GV, whereas above this rigidity it remains independent of A/Z. The right panel illustrates that as a function of rigidity, the dependence of $\lambda_{||}$ on A/Z is eliminated at all rigidities. This is taken as an indication that there is no reason to believe that there are fundamental differences between the modulation of CR species with different A/Z when inside the heliosphere, an aspect that has been emphasized by Ngobeni et al. [2020].

3.4.1.2 Spatial dependence of $\kappa_{||}$

Figure 3.7 illustrates the latitudinal (left panel) and the radial dependence (right panel) of $\kappa_{||}$. From the left panel of this figure, it is indicated that $\kappa_{||}$ is larger in the polar region and decreases towards the equatorial plane, even more significantly at $\theta \geq 50^0$. It is also evident from this figure that particles with a smaller A/Z value will have larger DCs compared to those with a larger A/Z value.

The radial dependence of $\kappa_{||}$ is indicated in the right panel of Figure 3.7. The term $\kappa_{||}$ given in Equation (3.13) scales spatially as B^{-1}, where $B \propto r^{-1}$ both in the equatorial and polar regions for the Smith-Bieber modification utilized in this study. As a result, $\kappa_{||}$ increases significantly with increasing radial distance starting from $r > 1$ AU as indicated on the right panel of Figure 3.7 until at ≈ 86 AU. Changes in the the three curves at 88 AU are due to a compression in the HMF lines. These compressions occur beyond the TS position and result in larger HMF magni-

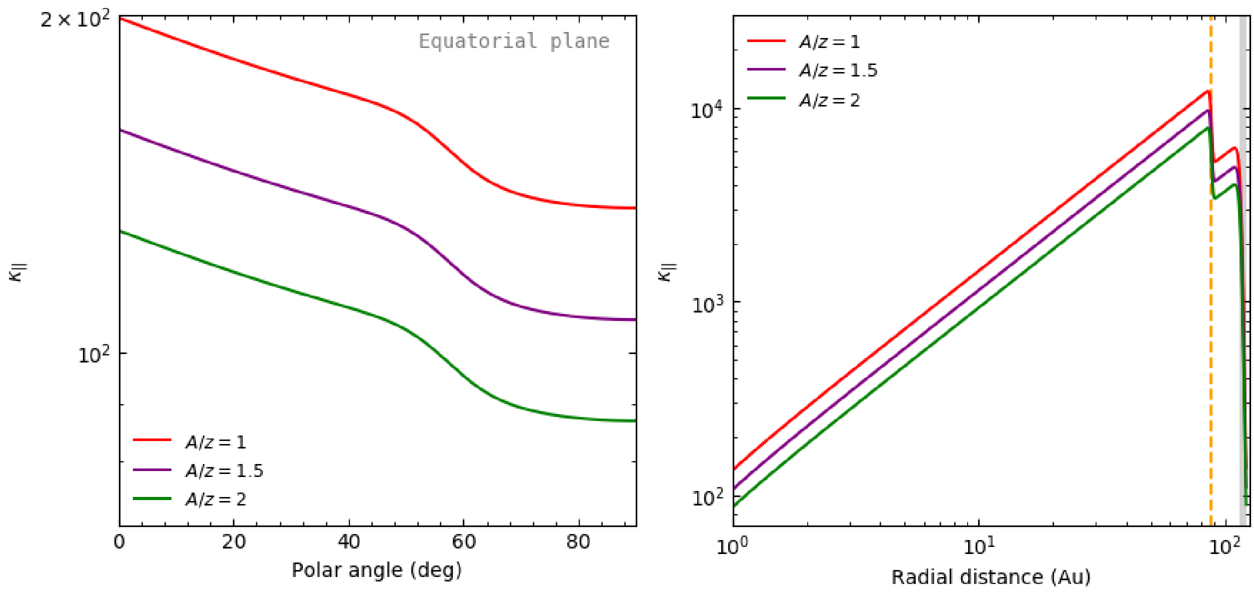

Figure 3.7: The latitudinal dependence (left panel) of $\kappa_{||}$ for 1 GV CR species with different A/Z values at 1 AU and the corresponding radial dependence (right panel) in the equatorial plane. The TS position at 88 AU indicated by the orange dashed-line and the highlighted region representing 5 AU in front of the HP which is placed at 122 AU.

tudes which therefore result in smaller DCs. Over ≈ 5 AU region in front of the HP (indicated by the shaded region), V1 measured a strong increase in GCR intensities as a precursor to entering the HP region (e.g., Krimigis et al. [2013], Gurnett et al. [2013], Burlaga et al. [2013]). This effect has been accounted for in the model by exponentially decreasing the DCs in this region to reproduce the observed increases in intensities (see Vos [2016] for a concise discussion). In Figure 3.7 this is indicated as a sharp drop in $\kappa_{||}$ starting from $r = 117$ AU.

3.4.2 Perpendicular diffusion

The scattering of GCR particles perpendicular to the HMF is caused by two fundamental processes, which include the particle gyro-centres displaced transverse to the mean HMF through scattering and the so-called random walk of the magnetic field lines (Kóta & Jokipii [1999]). The perpendicular diffusion coefficient, $\kappa_{\perp}$ - used in numerical models to account for all of these processes - is subdivided into two independent coefficients, namely $\kappa_{\perp r}$ and $\kappa_{\perp\theta}$. The significance of this diffusion coefficient in modulation has been pointed out in various studies (see e.g., Potgieter & le Roux [1992], Potgieter [2000], Ferreira et al. [2000], Burger et al. [2000]). A theory for perpendicular diffusion known as the Nonlinear Guiding Center (NLGC) has been proposed by Matthaeus et al. [2003] and extended by Shalchi [2006, 2010]. In this work, $\kappa_{\perp}$ is assumed to scale spatially as $\kappa_{||}$ as confirmed by Giacalone & Jokipii [1999] who established that the ratio of $\kappa_{\perp}$ / $\kappa_{||}$ ranges between 0.02 and 0.04.

The expressions for the perpendicular diffusion used in this study are given by

$$\kappa_{\perp r} = \kappa^0_{\perp r}\kappa_{\|}\frac{D_\perp}{D_\|}, \tag{3.16}$$

and

$$\kappa_{\perp\theta} = \kappa^0_{\perp\theta}F_{\perp\theta}\frac{D_\perp}{D_\|}\kappa_{\|} = F_{\perp\theta}\kappa_{\perp r}, \tag{3.17}$$

where $\kappa^0_{\perp r}$ = $\kappa^0_{\perp\theta}$ = 0.02 which are expressions used to define the ratio of $\kappa_\perp$ / $\kappa_\|$ and $F_{\perp\theta}$ is referred to as the enhancement function which enhances $\kappa_{\perp\theta}$ by a factor $d_{\perp\theta}$ towards the polar regions with respect to its value in the equatorial plane (the values of $d_{\perp\theta}$ are briefly discussed below). The enhancement is prompted by Ulysses measurements that showed differences in the variance of the HMF, which increased less in the radial direction compared to the transverse and normal directions of the HMF (Jokipii & Kóta [1995]). The expression for the term $D_\perp$ in Equations (3.16) and (3.17) is given as

$$D_\perp = \left[\frac{\left(\frac{P}{P_0}\right)^{c_3} + \left(\frac{P_k}{P_0}\right)^{c_3}}{1+\left(\frac{P_k}{P_0}\right)^{c_3}}\right]^{\frac{c_{2\perp}-c_1}{c3}}, \tag{3.18}$$

where $c_{2\perp}$ is a dimensionless constant of both $\kappa_{\perp r}$ and $\kappa_{\perp\theta}$ that determine the slope of their rigidity dependence above rigidity P_k. Therefore, the ratio $\frac{D_\perp}{D_\|}$ in Equations (3.16) and (3.17) is a term that modifies the rigidity dependence of $\kappa_{\perp r}$ and $\kappa_{\perp\theta}$ relative to that of $\kappa_\|$ above P_k (Ngobeni et al. [2020]).

3.4.2.1 Rigidity dependence of $\kappa_\perp$

Figure 3.8 shows the rigidity dependence of the ratio $\frac{D_\perp}{D_\|}$, with $c_{2\perp}$ = 0.70 $c_{2\|}$ assumed in Equation (3.18). It is evident that below 2 GV, the ratio of $D_\perp/D_\|$ is ≈ 1, as a result $\kappa_{\perp r}$ shown in the left panel of Figure 3.9 and $\kappa_{\perp\theta}$ (not shown) have the same rigidity dependence as $\kappa_\|$ at these rigidities. However, above this rigidity the rigidity dependence of $\kappa_{\perp r}$ and $\kappa_{\perp\theta}$ become much flatter compared to that of $\kappa_\|$ due to significant decreases in the ratio $D_\perp/D_\|$ with increasing rigidity, reaching minimum values at the highest rigidity considered. The dependence of $\kappa_{\perp r}$ on the ratio $D_\perp/D_\|$ and β is clearly illustrated on the left panel of Figure 3.9, indicating that $\kappa_\perp$ also decreases as A/Z increases with $P \leq 4$ GV, whereas above this rigidity it remains independent of A/Z. On the other hand, the right panel of Figure 3.9 illustrates that, as a function of rigidity, the dependence of $\lambda_{\perp r}$ on A/Z is eliminated at all rigidities, similar to that of $\lambda_{||}$, with $\lambda_{\perp r}$ being much flatter throughout the entire rigidity range as compared to $\lambda_\|$.

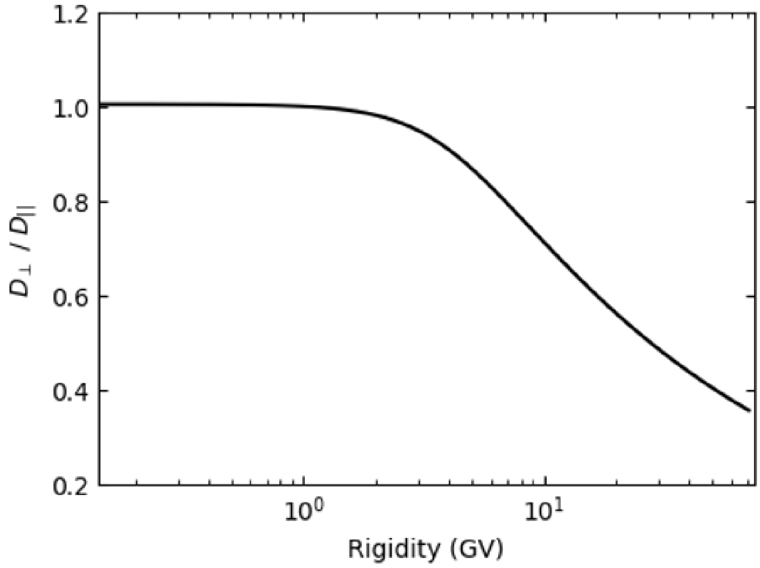

Figure 3.8: The rigidity dependence of $D_\perp/D_\|$.

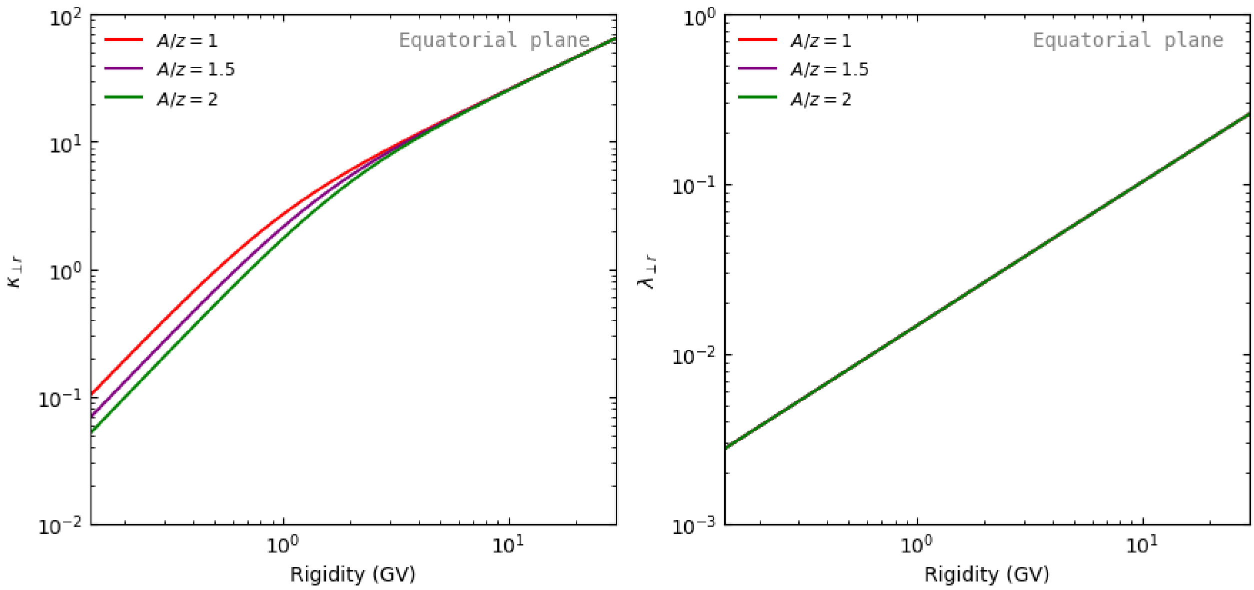

Figure 3.9: The rigidity dependence of $\kappa_{\perp r}$ (left panel) for CR species with different A/Z values at 1 AU in the equatorial plane with the corresponding MFP $\lambda_{\perp r}$ (right panel).

3.4.2.2 Spatial dependence of $\kappa_\perp$

The radial dependence of both $\kappa_{\perp r}$ and $\kappa_{\perp \theta}$ is similar to that of $\kappa_{||}$ and, hence, not shown. What is of interest is the enhancement of $\kappa_{\perp \theta}$ in the polar direction, represented by the enhancement function $F_{\perp \theta}$ given as

$$F_{\perp\theta} = A^{+} \mp A^{-} tanh\left[8(\theta_A - 90^0 \pm \theta_F)\right], \tag{3.19}$$

where $A^{\mp} = \frac{1}{2}(d_{\perp\theta} \mp 1)$ and for $\theta \leq 90^0$, $\theta_A = \theta$ with $\theta_F = 35^0$, while for $\theta \geq 90^0$, $\theta_A = 180^0 - \theta$ and $\theta_F = -35^0$. The function $F_{\perp\theta}$ is illustrated in the left panel of Figure 3.10 as a function of polar angle with $d_{\perp\theta} = 6$. Several studies have shown that the enhancement of the latitudinal transport is required to produce the correct magnitude and rigidity dependence of the observed latitudinal gradient of GCR in the heliosphere. For motivations on this enhancement, see e.g., Burger et al. [2000], Potgieter [2000] and Heber & Potgieter [2006].

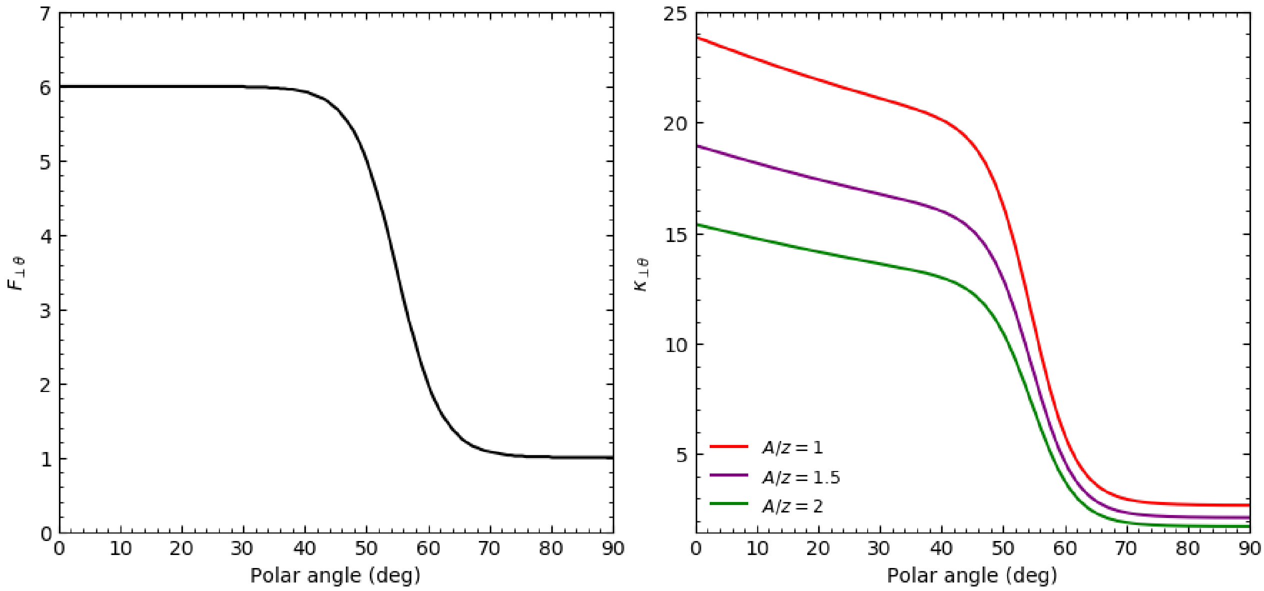

Figure 3.10: Shows $F_{\perp\theta}$ (left panel) in Equation (3.17) as a function of polar angle θ with $d_{\perp\theta} = 6$ and $\kappa_{\perp\theta}$ (right panel) as a function of polar angle at 1 AU for 1 GV CR species with different A/Z values.

The right panel of Figure 3.10 shows $\kappa_{\perp\theta}$ as a function of polar angle at 1 AU for 1 GV CR species. From this panel, it follows that $F_{\perp\theta}$ enhances $\kappa_{\perp\theta}$ with respect to $\kappa_{\perp r}$ by a factor of $d_{\perp\theta}$ over the polar regions. Therefore, in the equatorial plane $\kappa_{\perp\theta} = \kappa_{\perp r}$, whereas $\kappa_{\perp\theta} > \kappa_{\perp r}$ over the poles. The dependence of $\kappa_{\perp\theta}$ on β is clearly highlighted on this panel, where the differences in $\kappa_{\perp\theta}$ as a function of polar angle between CR species with different A/Z are notable. In general, the assumed perpendicular DCs are smaller in the equatorial plane and increase towards the polar region.

3.4.3 The effective diffusion coefficients in the radial and azimuthal directions

The effective DCs in the radial κ_{rr} and azimuthal directions $\kappa_{\phi\phi}$ in Equation (3.10) are respectively given as

$$\kappa_{rr} = \kappa_{\parallel} \cos^2 \psi + \kappa_{\perp r} \sin^2 \psi, \tag{3.20}$$

and

$$\kappa_{\phi\phi} = \kappa_{\perp r} \cos^2 \psi + \kappa_{\parallel} \sin^2 \psi, \tag{3.21}$$

where $\sin^2 \psi$ and $\cos^2 \psi$ modify $\kappa_{\parallel}$ and $\kappa_{\perp r}$ throughout the entire heliosphere. Equations (3.20) and (3.21) explicitly indicate that κ_{rr} is a linear combination of $\kappa_{\parallel} \cos^2 \psi$ and $\kappa_{\perp r} \sin^2 \psi$, whereas $\kappa_{\phi\phi}$ is made up of a linear combination of $\kappa_{\parallel} \sin^2 \psi$ and $\kappa_{\perp r} \cos^2 \psi$. In addition to κ_{rr} and $\kappa_{\phi\phi}$, the DC in the ϕr direction known as a correction term that marginally reduces the radial and azimuthal gradients of CRs (see Nkosi [2006], Nndanganeni [2012, 2016]) is given as

$$\kappa_{\phi r} = (\kappa_{\perp r} - \kappa_{\parallel}) \sin \psi \cos \psi = \kappa_{r\phi}, \tag{3.22}$$

with $\sin \psi \cos \psi$ as the modification therein.

3.4.3.1 Rigidity dependence of $\kappa_{\phi\phi}$ and κ_{rr}

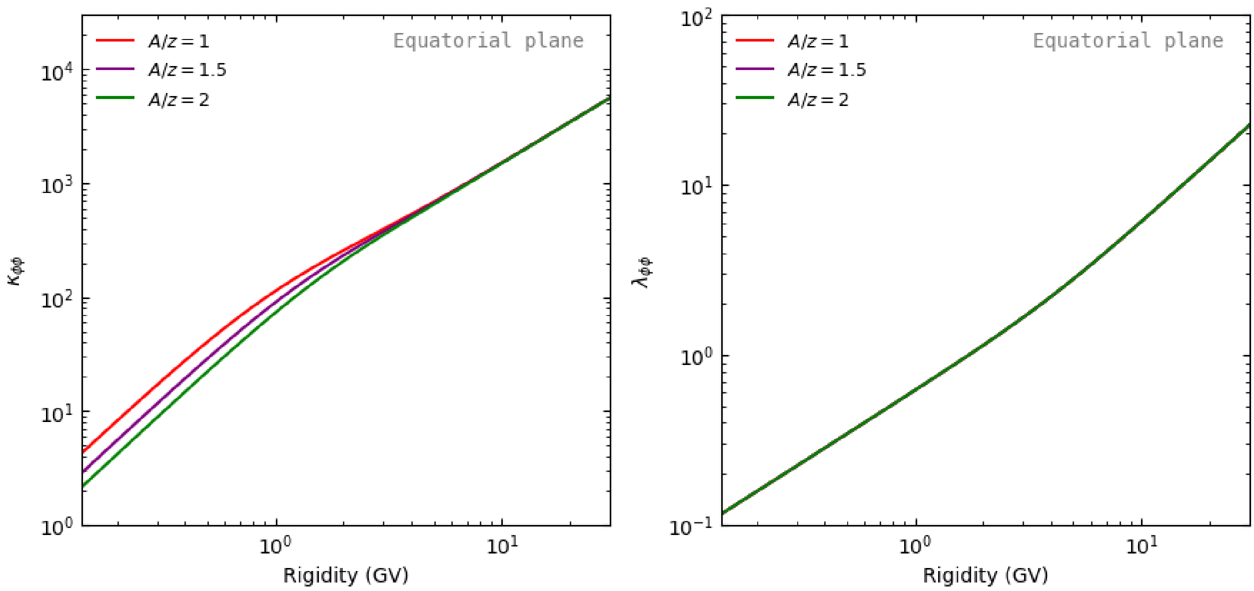

Figure 3.11: The rigidity dependence of $\kappa_{\phi\phi}$ (left panel) for CR species with different A/Z values at 1 AU in the equatorial plane together with the corresponding MFP $\lambda_{\phi\phi}$ (right panel).

Shown in Figure 3.11 is the rigidity dependence of $\kappa_{\phi\phi}$ (left panel) and the corresponding MFP $\lambda_{\phi\phi}$ (right panel) at 1 AU in the equatorial plane. The rigidity dependence of $\kappa_{\phi\phi}$ follows from that of $\kappa_{\parallel}$ since $\kappa_{\phi\phi}$ is dominated by $\kappa_{\parallel} \sin^2 \psi$ throughout the heliosphere in the equatorial region as mentioned before. As a result, the rigidity dependence of $\lambda_{\phi\phi}$ is similar to that of $\lambda_{\parallel}$.

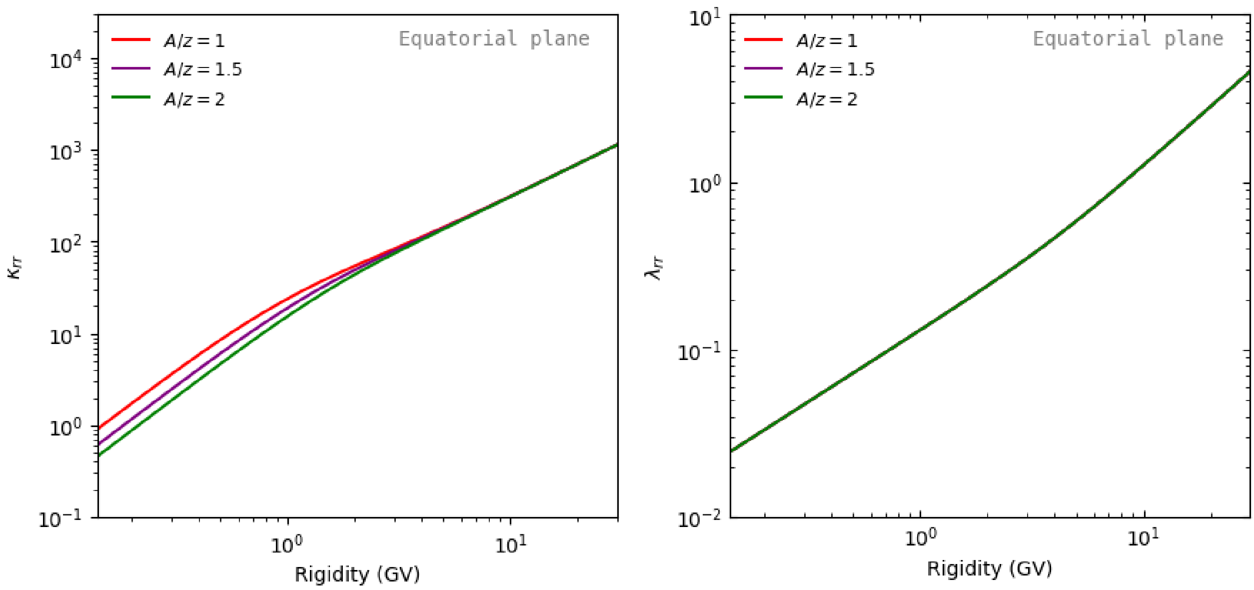

Figure 3.12: The rigidity dependence of κ_{rr} (left panel) for CR species with different A/Z values at 1 AU in the equatorial plane with the corresponding λ_{rr} (right panel).

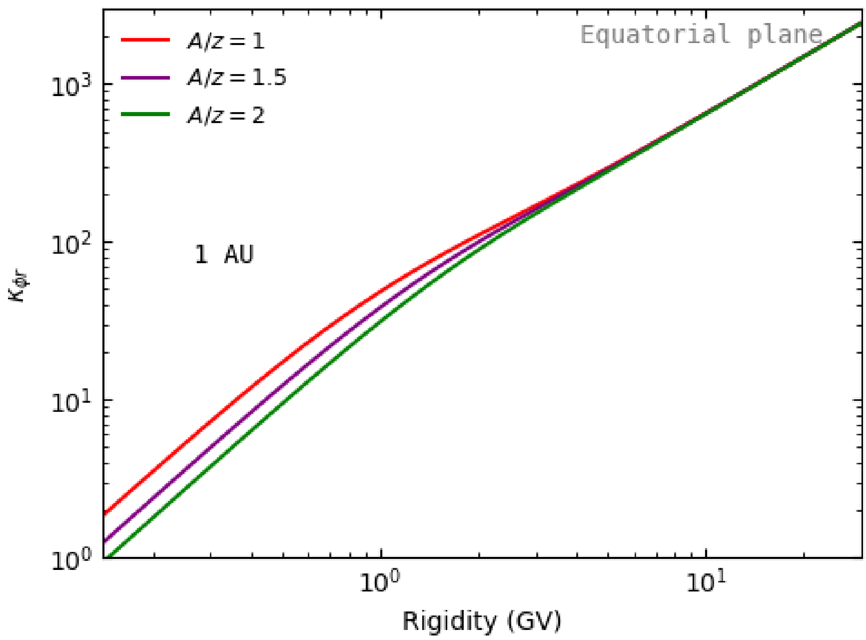

Figure 3.13: The rigidity dependence of $\kappa_{\phi r}$ for CR species with different A/Z values.

Figure 3.12 depicts the rigidity dependence of κ_{rr} (left panel) and the corresponding MFP λ_{rr} (right panel) at 1 AU in the equatorial plane. At Earth (1 AU), the rigidity dependence of κ_{rr}

is also determined by the rigidity dependence of $\kappa_{||}$ - as expected; at $r < 10$ AU in the inner heliosphere, κ_{rr} is dominated by $\kappa_{||}\cos^2\psi$ and the rigidity dependence of λ_{rr} also follows from that of $\lambda_{||}$. Therefore, the assumed rigidity dependences of both κ_{rr} and $\kappa_{\phi\phi}$ are similar at the Earth.

The rigidity dependence of -($\kappa_{\phi r} = \kappa_{r\phi}$) at 1 AU in the equatorial plane for the same CR species of interest is indicated in Figure 3.13. It follows from this figure that rigidity dependence of $\kappa_{\phi r}$ is similar to that of $\kappa_{||}$ as well.

3.4.3.2 Spatial dependence of $\kappa_{\phi\phi}$ and κ_{rr}

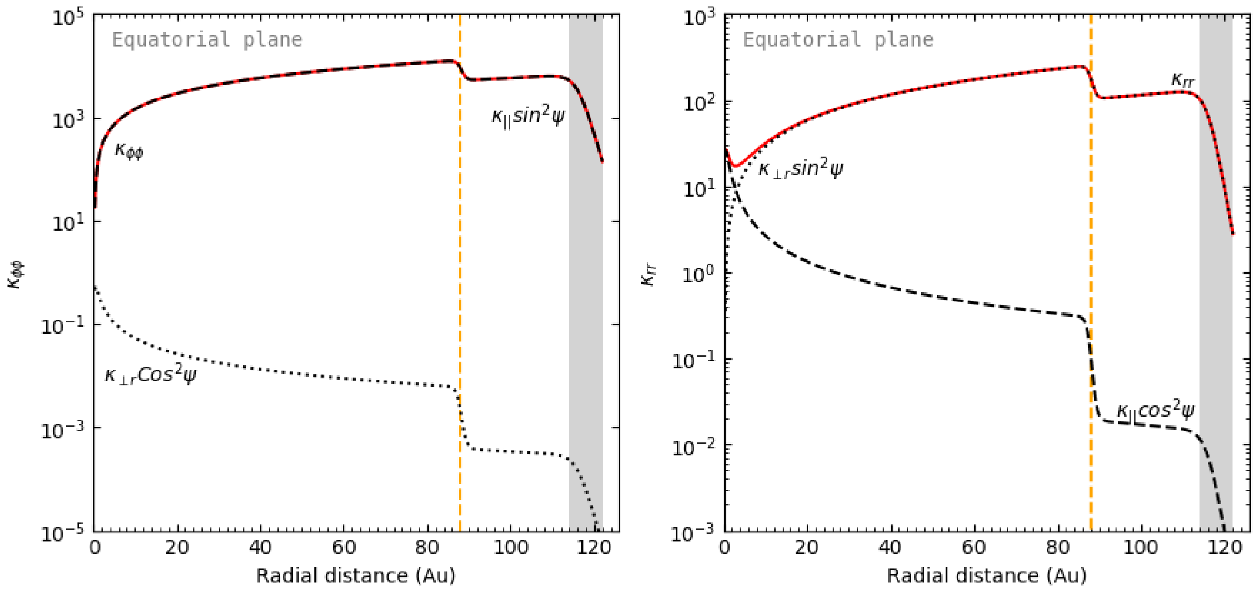

Figure 3.14: The radial dependence of $\kappa_{\phi\phi}$ (solid red line) and κ_{rr} (solid red line) in the equatorial plane for 1 GV protons, with the contribution of terms given in Figure 3.4. The dotted and dashed lines respectively represent the modification of $\kappa_{\perp}$ and $\kappa_{||}$. The TS position at 88 AU indicated by the orange dashed-line and the the highlighted region representing 5 AU region in front of the HP which is placed at 122 AU.

Figure 3.14 shows the radial dependence of $\kappa_{\phi\phi}$ (left panel) and κ_{rr}(right panel) in the equatorial plane together with their linear combinations as given in Equations (3.21) and (3.20) respectively. The main purpose of this figure is to show how $sin^2\psi$ and $cos^2\psi$ modify both $\kappa_{||}$ and $\kappa_{\perp r}$. It is clearly indicated in the left panel of this figure that $\kappa_{||}$ dominates $\kappa_{\phi\phi}$ throughout the heliosphere in the equatorial plane. Furthermore, as shown on the right panel of this figure, κ_{rr} is dominated by $\kappa_{||}$ only in the inner heliosphere, where $r < 10$ AU; in the outer heliosphere, κ_{rr} is dominated by $\kappa_{\perp r}$. It is notable that at $r > 10$ AU, both κ_{rr} and $\kappa_{\phi\phi}$ have similar radial dependences, while below 10 AU their differences in the radial dependence are caused by the effects of $sin^2\psi$ and $cos^2\psi$.

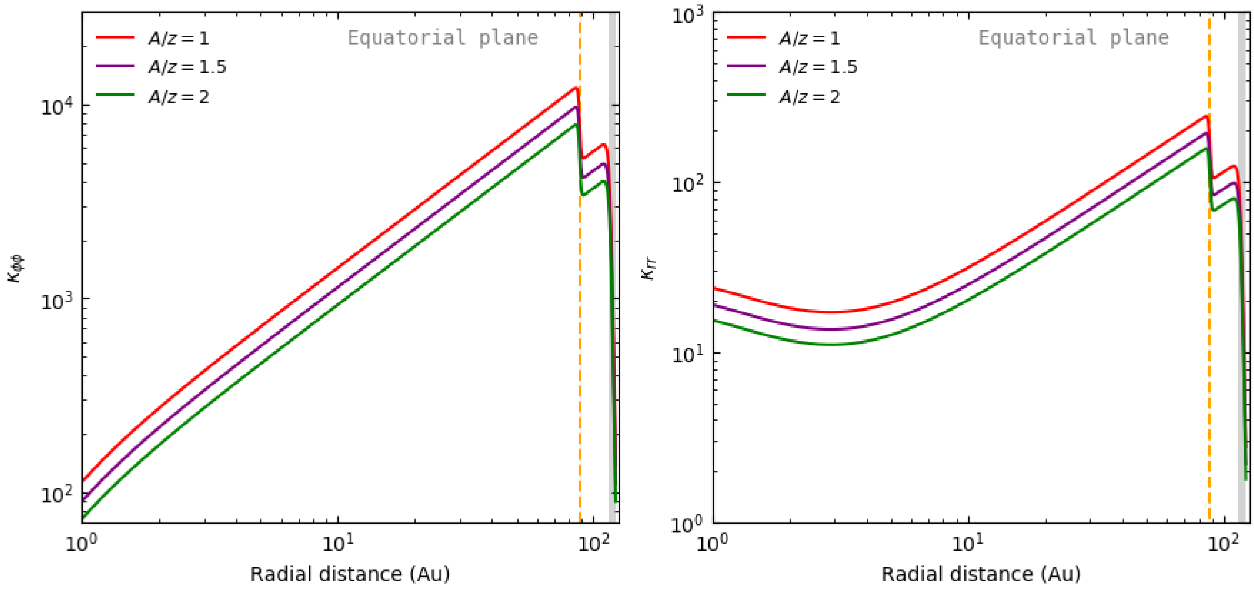

Figure 3.15: The radial dependence of $\kappa_{\phi\phi}$ (left panel) and κ_{rr} (right panel) in the equatorial plane for 1 GV CR species with different A/Z values. The TS position at 88 AU indicated by the orange dashed-line and the the highlighted region representing 5 AU region in front of the HP which is placed at 122 AU.

Figure 3.15 shows the radial dependence of both $\kappa_{\phi\phi}$ (left panel) and κ_{rr} (right panel) at 1 GV in the equatorial plane but now depicted for species with different A/Z. Similar to $\kappa_{\|}$ and $\kappa_{\perp r}$, CR species with different A/Z also have different κ_{rr} and $\kappa_{\phi\phi}$ at this rigidity. Moreover, from the two panels, it is evident that $\kappa_{\phi\phi}$ is notably larger than κ_{rr} throughout most of the equatorial region of the heliosphere and that its radial dependence is mainly $\approx \kappa_{\|} \sin^2 \psi$. In 2D approximation, usually in r and θ directions, $\kappa_{\|}$ only dominates very close to the Sun when most of the modulation has already taken place; an obvious limitation of the 2D approximation.

The radial dependence of $\kappa_{\phi r}$ is shown in Figure 3.16. Clearly $\kappa_{\phi r}$ increases slightly with radial distance at $r \leq 10$ AU and becomes almost constant with increasing radial distance until the TS position is reached. Thereafter, $\kappa_{\phi r}$ decreases abruptly in a similar way to $\kappa_{\|}$ and $\kappa_{\perp r}$.

Figure 3.17 illustrates the latitudinal dependence of $\kappa_{\phi\phi}$ (left panel) and κ_{rr} (right panel) at 1 AU for 1 GV CR species with different A/Z. The left panel indicates that the latitudinal dependence of $\kappa_{\phi\phi}$ is almost similar to that of κ_{rr}, with both coefficients being small in the equatorial plane and increasing towards the poles.

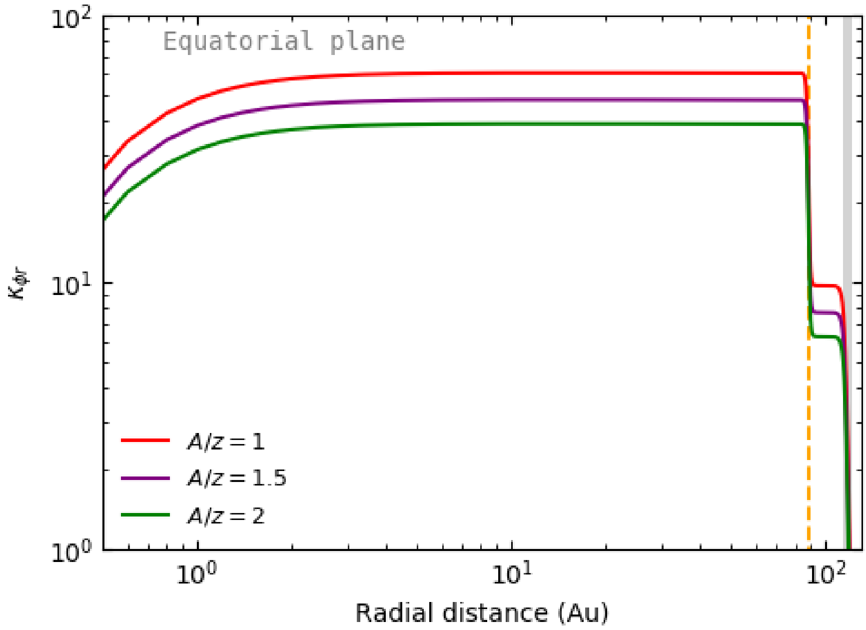

Figure 3.16: Simillar to Figure 3.15 but the radial dependence of $\kappa_{\phi r}$ is shown.

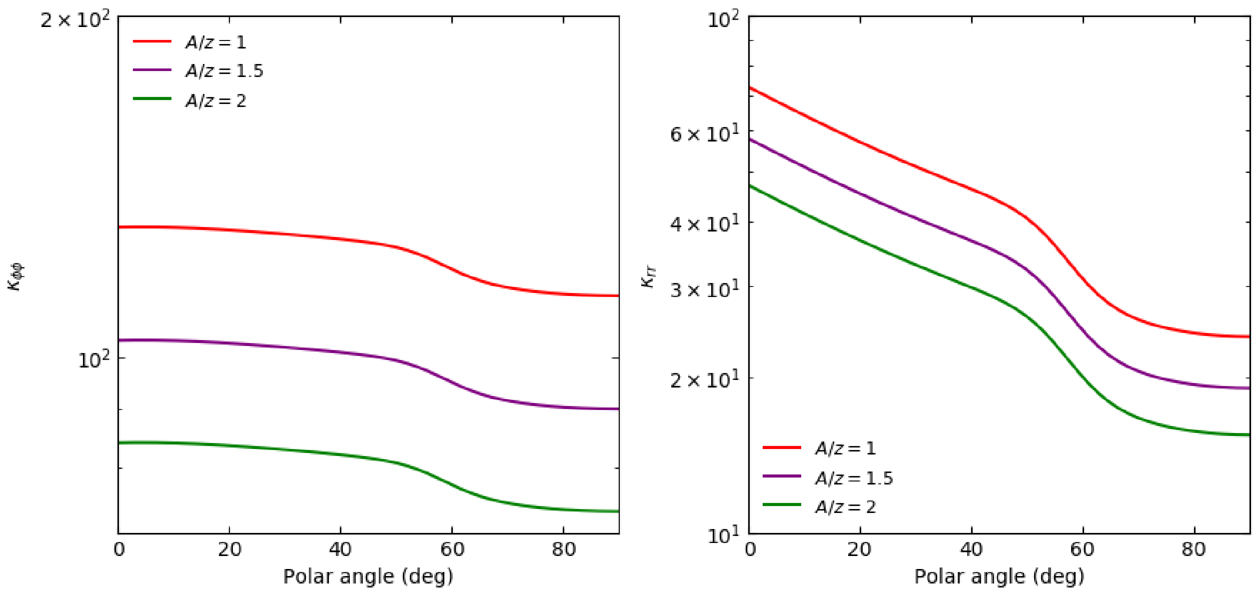

Figure 3.17: $\kappa_{\phi\phi}$ (left panel) and κ_{rr} (right panel) at 1 AU for 1 GV for CR species with different A/Z values as a function polar angle.

3.5 Particle Drifts

Out of the four major modulation processes considered in modulation studies, particle drifts were overlooked in previous studies until Jokipii et al. [1977] pointed out that they could influence the modulation of charged particles in the heliosphere. The drift directions of CRs in the heliosphere depends on their charge and the polarity of the HMF, leading to a charge-sign asymmetry between oppositely charged CRs. When the HMF is directed outward (inward) from the Sun in the Northern polar region and inward (outward) in the Southern polar region, positively charged particles are expected to drift into the inner heliosphere mainly over the solar poles (along the HCS) and out along the HCS (solar poles). This period is known as the $A > 0$ ($A < 0$) magnetic polarity epoch. In this phase of the solar cycle, the drift pattern of negatively charged particles is in the opposite direction. This drift pattern is shown in Figure 3.18.

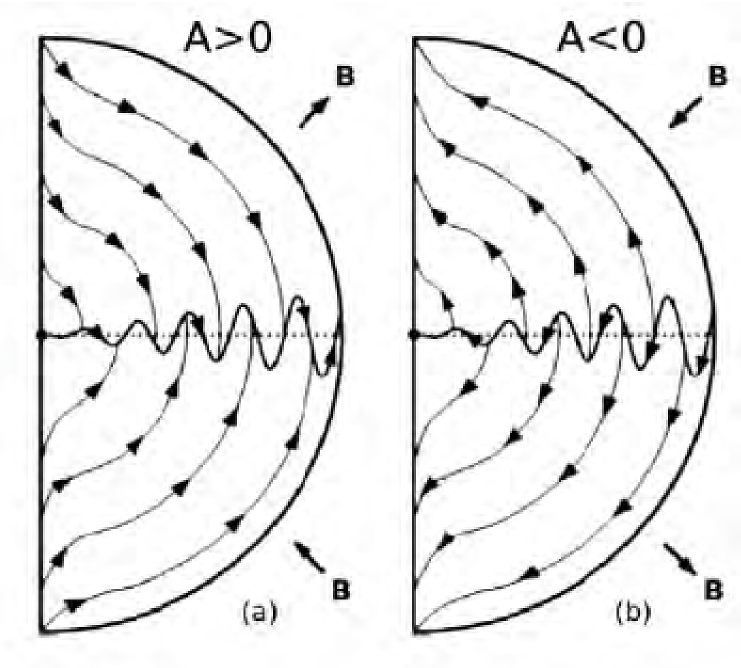

Figure 3.18: The global drift patterns including current sheet drifts for positively charged particles are during $A > 0$ and $A < 0$ magnetic polarity cycles. Adapted from Heber & Potgieter [2006].

The average drift velocity in the HMF is given by

$$\langle v_d \rangle = \nabla \times k_A \mathbf{e}_B, \tag{3.23}$$

with $\mathbf{e}_B = \dfrac{\mathbf{B}}{B}$ a unit vector in the direction of magnetic field $\mathbf{B}$ and κ_A is the generalized drift coefficient (also known as κ_D in some studies).

To highlight HCS drifts, Equation (3.23) is written as

$$\langle v_d \rangle = \nabla \times k_A \mathbf{e}_B (1 - 2H(\theta - \theta')) + 2\delta_d(\theta - \theta') k_A \mathbf{e}_B \times \nabla(\theta - \theta'), \tag{3.24}$$

where the first term on the right represents gradient and curvature drifts, and the second term represents HCS drifts; H is the Heaviside step function with δ_d as the Dirac-Delta function given by

$$\delta_d(\theta - \theta') = \begin{cases} 0 & \text{if } \theta \neq \theta' \\ \infty & \text{if } \theta = \theta'. \end{cases} \tag{3.25}$$

From Equation (3.24), the geometry of the HMF, as well as what is assumed for κ_A, is crucial for evaluating drift effects when studying the modulation of CRs in the heliosphere.

A general expression of κ_A in Equation (3.24) is given as

$$\kappa_A = \frac{\beta P}{3B} f_s = \frac{\beta P}{3B} \left[\frac{(\omega\tau)^2}{1 + (\omega\tau)^2} \right], \tag{3.26}$$

with

$$f_s = \left[\frac{(\omega\tau)^2}{1 + (\omega\tau)^2} \right], \tag{3.27}$$

where f_s is the drift reduction factor due to diffusive scattering, ω the particle's gyro-frequency and τ some time scale defined by scattering. It is not yet established how $\omega\tau$ should change as a function of rigidity and time throughout the heliosphere. It follows from Equation (3.26) that when f_s = 0, the κ_A and $\langle v_d \rangle$ given in Equation (3.24) become zero, meaning that drift effects will cancel out from the numerical model. However, when f_s = 1 drifts reach a maximum value (see Ngobeni & Potgieter [2015] for a concise discussion).

The function f_s can be utilized to adjust the drift coefficient κ_A at lower rigidities with the assumption that $\omega\tau \propto P$, and this modification is given as

$$\kappa_A = \frac{\beta P}{3B_m} f_s = \kappa_{A0} \frac{\beta P}{3B_m} \frac{\left(\frac{P}{P_{A0}}\right)^2}{1 + \left(\frac{P}{P_{A0}}\right)^2}, \tag{3.28}$$

where B_m is the Parker's modified HMF and κ_{A0} is a dimensionless constant that ranges from 0 to 1.0 with P_{A0} = 0.90. If κ_{A0} = 0, this is referred to as 0 % drifts (no drifts) and κ_{A0} = 1, implies 100 % (full drifts). This modification is found to be the most efficient and direct way to suppress drift effects at low rigidities (Burger et al. [2000], Nndanganeni & Potgieter [2016], Ngobeni & Potgieter [2015]).

When f_s = 1, meaning $\omega\tau \gg 1$ in Equation (3.27), k_A is reduced to its most basic form,

$$\kappa_A^{ws} = \frac{\beta P}{3B}, \tag{3.29}$$

known as weak scattering drift coefficient. When Equation (3.29) is applied in numerical models, very large and dominant drift effects as originally obtained by Jokipii & Thomas [1981] and Kóta & Jokipii [1983], are produced.

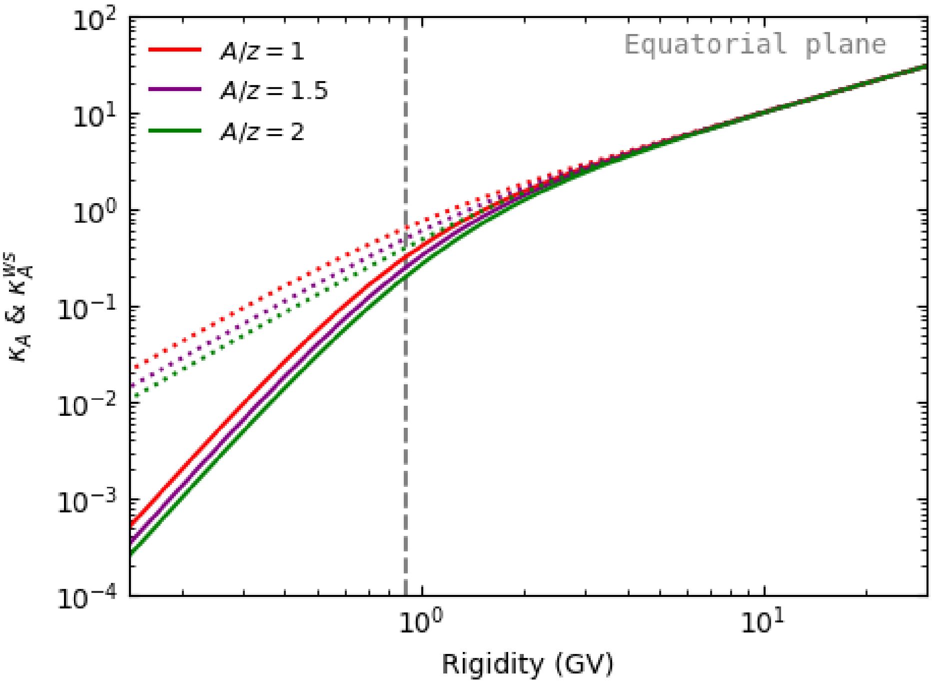

Figure 3.19: The rigidity dependence of κ_A as used in this study (solid lines) and κ_A^{ws} (dotted lines) for CR species with different A/Z values at 1 AU in the equatorial plane. The dashed gray line represent $P_{A0} = 0.90$ and below this line is were drifts are modified.

Figure 3.19 shows the weak scattering drift coefficient, κ_A^{ws} in Equation (3.29), indicated as dotted lines and the solid lines depict the modified κ_A, in Equation (3.28) as used in this work, as a function of rigidity at 1 AU in the equatorial plane for CR species with different A/Z indicated as different colours. The assumed value of κ_{A0} in Equation (3.28) is 1.0 to obtain maximum drifts. The essence of Figure 3.19 is that below P_{A0} drifts are reduced with respect to the weak scattering case in Equation (3.29). This drift adjustment is necessary in order to reproduce a comprehensive set of CR observations (Potgieter & Vos [2017], Aslam et al. [2021], Ngobeni et al. [2021b, 2022] and references therein).

The drift coefficient is related to the drift scale through

$$\lambda_A = \frac{3}{v}\kappa_A, \tag{3.30}$$

whereas for the weak scattering phenomena, the drift scale $\lambda_A^{ws} = r_L$, with r_L as the Larmor radius and given by $r_L = P/Bc$.

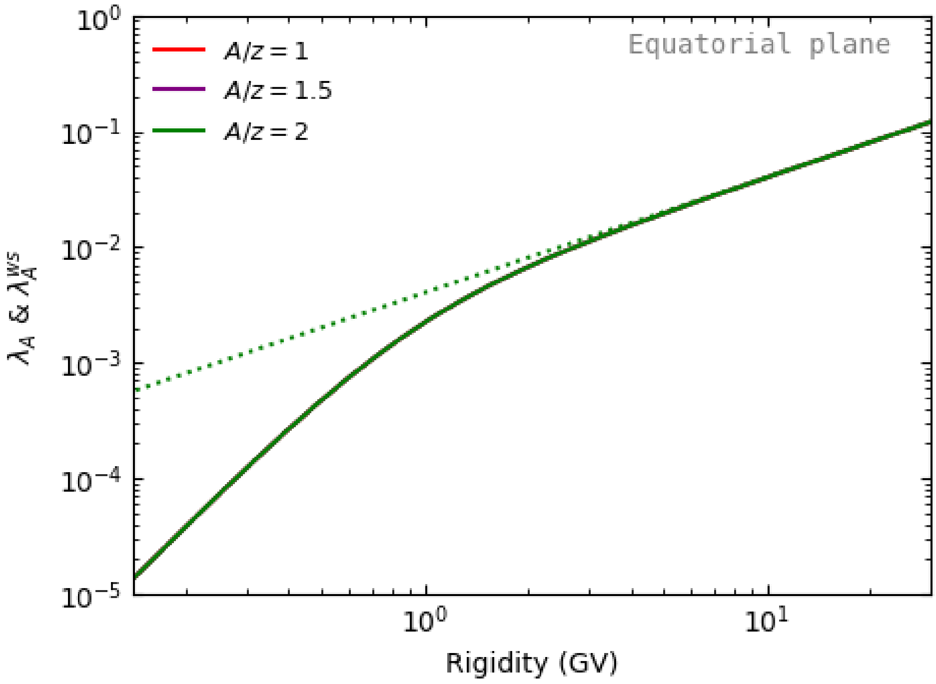

Figure 3.20: The rigidity dependence of λ_A as used in this study (solid lines) and λ_A^{ws} (dotted-lines) for CR species with different A/Z values at 1 AU in the equatorial plane.

Figure 3.20 shows the rigidity dependence of the drift scale as used in this study represented by solid-lines and the weak scattering drift scale represented by dotted-lines. The rigidity dependence of λ_A is different to that of κ_A in Figure (3.19) and also its dependence on A/Z is eliminated at all rigidities.

3.6 Summary and conclusion

In this chapter, the TPE and its modulation processes were given, together with the diffusion tensor in both HMF-aligned and spherical coordinate systems. The spatial and rigidity dependence of all the elements of the diffusion tensor were illustrated, including those in the ϕr and $\phi\phi$ directions which are overlooked in the 2D numerical model due to the model's limitations. It was shown that $\kappa_{\phi\phi}$ is dominated by $\kappa_{||}$ $sin^2\psi$ throughout most of the heliosphere in the equatorial plane while κ_{rr} is dominated by $\kappa_{||}$ $cos^2\psi$ and $\kappa_{\perp r}$ $sin^2\psi$ in the inner heliosphere and outer heliosphere, respectively. Furthermore, it was established that the DCs in the ϕr and $r\phi$ directions have the same rigidity and spatial dependencies, hence it is considered that $\kappa_{\phi r}$ = $\kappa_{\phi r}$. A basic theory on drifts was also given in this chapter, with expressions of gradient and curvature drifts together with HCS drifts given in Equations (3.23) and (3.24). The weak scattering and modified drift phenomenons were also presented. From the illustrated rigidity and spatial dependence of DCs it is evident that particles with smaller A/Z values result in larger DCs compared to particles with larger A/Z values due to their dependence on β.

The next chapter focuses on the modulation of CR proton related to observation by PAMELA experiment.

Chapter 4

Modeling of proton modulation related to PAMELA observations

4.1 Introduction

In this chapter, the 3D numerical model together with the new proton LIS as described by Bisschoff et al. [2019], and the DCs established in the previous chapter are used to study the modulation of CR protons in the heliosphere, with an aim to establish a set of modulation parameters, diffusion and drift coefficients that reproduce PAMELA proton observations at the Earth between 2006 and 2013. Firstly, the model is used to study the modulation of CR protons during solar minimum (2006-2009) conditions as done in Vos [2016] and then applied to solar maximum (2010-2013) modulation at the Earth. The results of the numerical modeling and its comparison with PAMELA proton observations give insight into how the elements of the diffusion and drift tensor changed with time from solar minimum to solar maximum conditions. In particular, it will be investigated how the rigidity slopes of the DCs influence the unfolding of the spectra of GCR proton differently with changing solar activity.

4.2 The PAMELA proton spectra from 2006 to 2013

The observations of GCR protons at the Earth had been done precisely with the PAMELA space detector and reported from July 2006 to September 2009 by Adriani et al. [2013] and from July 2010 to December 2013 by Martucci et al. [2018]. These observations span time frames from solar minimum to solar maximum activity, and revealed that the solar minimum period of 2006 to 2009 was significantly different than the previous $A < 0$ solar minimum periods. The detailed modeling of this unusual solar minimum has been given in details by Potgieter et al. [2013] and Vos & Potgieter [2015, 2016]. This section discusses the proton energy spectra measured by PAMELA from 2006 to 2013 with an aim to study the energy and time-dependent solar modulation conditions spanning this time-period.

4.2.1 Proton spectra as a function of Kinetic energy per nucleon

The left panel of Figure 4.1 outlines the proton energy spectra measured by PAMELA, averaged over a period of ≈ 27 days which corresponds to one Carrington rotation each at the end of the half-year, with different colours indicating each spectra measured from December 2006 to December 2013. The total period in energy spectra is divided into fifteen half-year periods with prefixes 'a' and 'b' representing half-year periods between 2006 and 2013: 06/11/14-06/12/12 (2006b), 07/05/24-07/06/21 (2007a), 07/12/01-07/12/29 (2007b), 08/06/09-08/07/06 (2008a), 08/11/20-08/12/17 (2008b), 09/05/30-09/06/26 (2009a), 09/08/20-10/09/16 (2009b), 10/05/30-09/06/26 (2010a), 10/08/20-10/09/16 (2010b), 11/05/20-11/06/10 (2011a), 11/11/20-11/12/16 (2011b), 12/05/27-12/06/22 (2012a), 12/12/02-12/12/28 (2012b), 13/05/13-13/06/08 (2013a), 13/11/18-13/12/14 (2013b).

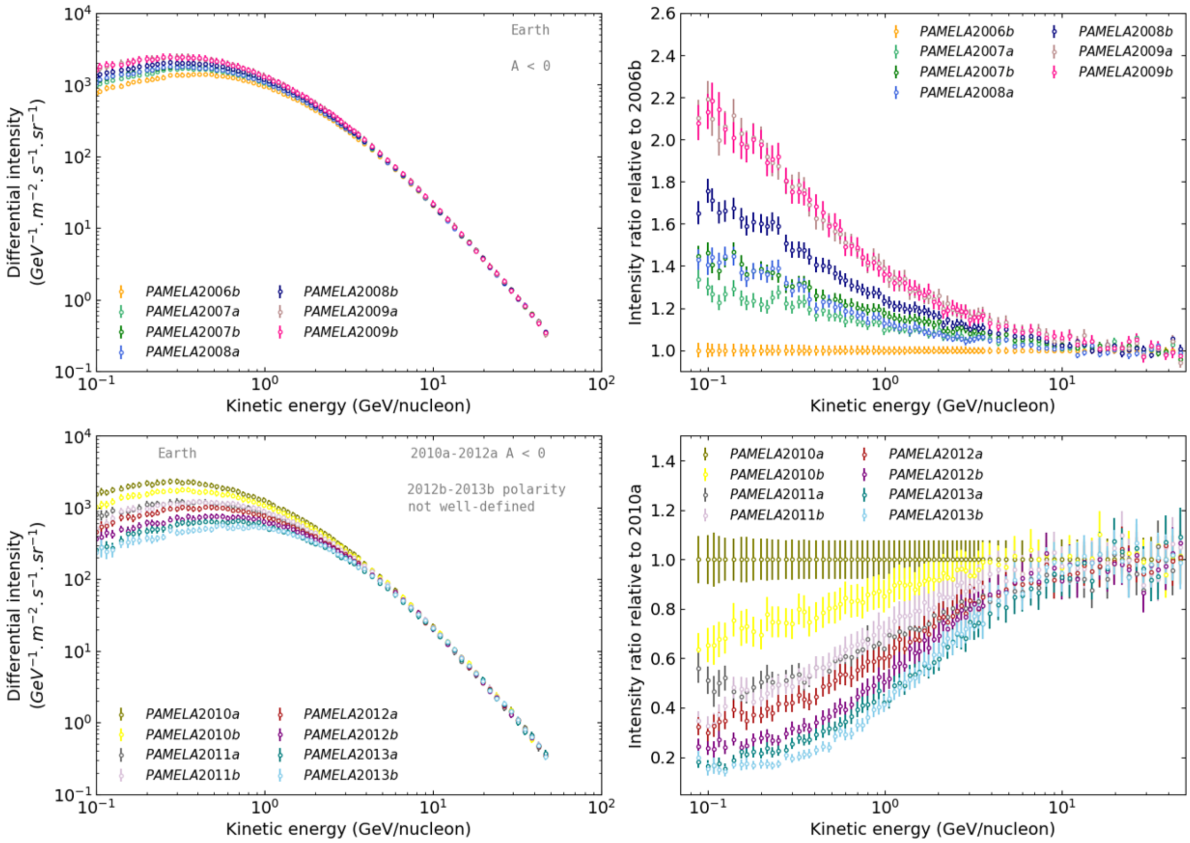

Figure 4.1: Left panel: 27-Day averaged PAMELA proton energy spectra observed between December 2006 to September 2009 (top panel) and between June 2010 to December 2013 (bottom panel) as a function of Kinetic energy/nucleon. Right panel: The corresponding intensity ratios relative to December 2006 (top panel) and June 2010 (bottom panel). The spectra in the top panel were observed at Earth in the A< 0 polarity cycle during the solar minimum of 2006 to 2009 (Adriani et al. [2013]), whereas in the bottom panel were observed during increasing solar activity period between 2010 and 2013 (Martucci et al. [2018]).

The proton spectra presented in Figure 4.1 ranges from ≈ 90 MeV/nucleon to ≈ 46 GeV/nucleon, in kinetic energy. Shown in the right panel is the corresponding intensity ratios relative to 2006b (top panel) and 2010a (bottom panel). These ratios indicate how the spectra became gradually softer towards solar minimum modulation in 2009 and harder towards the solar maximum modulation in late 2013. In 2009 solar activity decreased to its lowest level, indicated by high intensities in Figure 4.1, since the beginning of the space exploration era (see Adriani et al. [2011, 2013, 2017]). This magnetic period was characterized by a much weaker HMF and the α of HCS not decreasing as rapidly as the magnitude of the HMF at the Earth, but reaching a minimum value at the end of 2009. These two solar activity proxies will be discussed in detail below.

The effects of solar modulation in the observations shown in Figure 4.1 is clearly visible in the kinetic energy region below a few GeV/nucleon where the intensities increased from 2006 to 2009 but significantly decreased from 2010 to 2013. For example, the proton intensities measured at $\approx$ 90 MeV/nucleon increased by a factor $\approx$ 2.2 between 2006 and 2009, whereas between 2010 and 2013 these intensities decreased by $\approx$ 80%. At kinetic energies above $\approx$ 30 GeV/nucleon the ratios in the measured intensities approach a single value.

It is evident in Figure 4.1 that lower energy particles experienced larger increases in intensities from 2006-2009, whereas from 2010-2013 they experienced the largest decreases. However, for kinetic energies above 10 GeV/nucleon, the increase and decrease in intensities are less profound, while above 30 GeV/nucleon little or no modulation was observed from 2006-2013. As a result, GCR particles with kinetic energy $\geq$ 30 GeV/nucleon are considered to experience negligible modulation effects (see also Strauss & Potgieter [2014b], Vos [2016], Potgieter & Vos [2017]).

4.2.2 PAMELA proton spectra as a function of time

Figure 4.2 shows the observed GCR proton and normalized intensities relative to 2006b as a function of time at four different kinetic energies, illustrating how CR intensities evolved at different kinetic energies from 2006 to 2013 as observed by PAMELA. An interesting aspect of what the observations depict in Figure 4.2 is that lower energy CR protons have the highest increase in intensities relative to 2006b during solar minimum compared to higher energies. While towards solar maximum activity period, the intensities of the lower energy CR protons decrease faster than higher energies relative to 2006b. This general feature of long-term modulation was simulated comprehensively by le Roux & Potgieter [1992].

GCR protons are the most abundant CR species above $\approx$ 10 MeV/nucleon. Therefore, the available and precise measurements of the CR proton energy spectra by PAMELA, down to a few GeV's shown in Figure 4.1, and their time dependence from solar minimum to solar maximum conditions, shown in Figure 4.2, provide unique insights on the fundamental properties of the

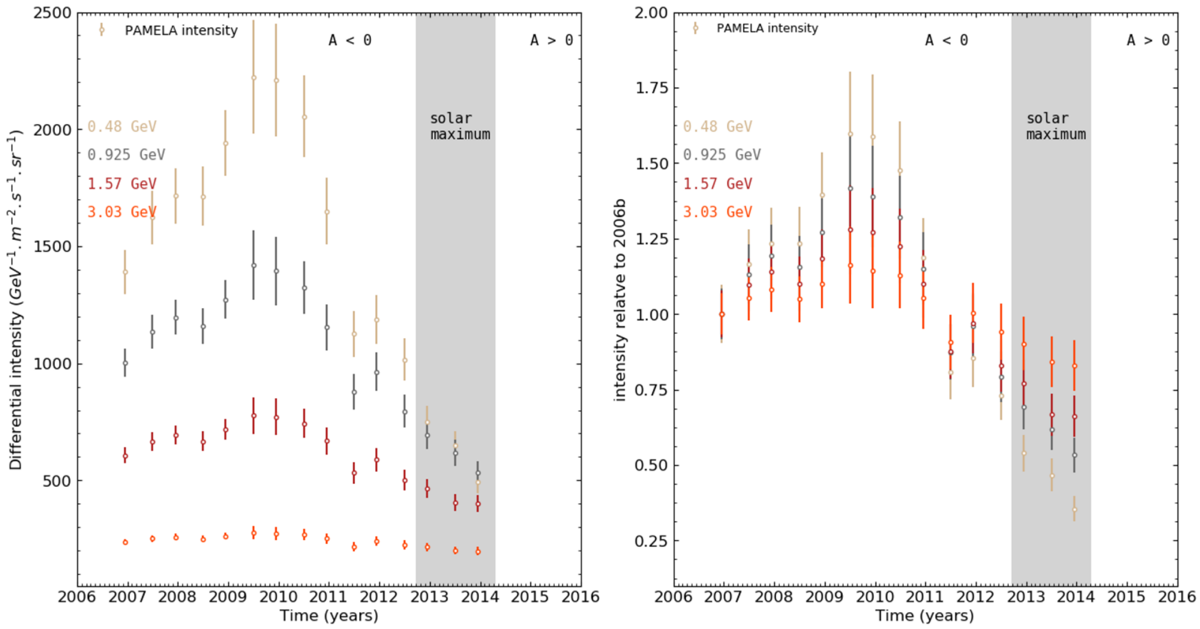

Figure 4.2: GCR proton intensities observed by PAMELA at different kinetic energies indicated by different coloured open circles (left panel) and the corresponding intensity ratios relative to 2006b (right panel) as a function of time. The shaded band indicates a period when no well-defined HMF polarity was present in the heliosphere, and also indicated is the period of the $A < 0$ and $A > 0$ HMF polarity cycles.

SW and the HMF turbulence in the heliosphere. This chapter is focused on showing how the main modulation processes in the TPE, including particle drifts and the three major diffusion coefficients, influence the energy and time-evolution of proton spectra from solar minimum to solar maximum. The end result of this chapter is the detailed reproduction of these spectra from the end of 2006 to the end of 2013 with a 3D numerical model, displaying both qualitative and quantitative agreement with the main observed features.

4.3 The proton local interstellar spectrum

When studying heliospheric modulation, it is very crucial to get the exact shape of the LIS for GCR species because they serve as initial conditions to be specified in the numerical model. These LIS's are then modulated from the HP position, taken to be around 122 AU and the boundary of the simulated heliosphere in this study, until the Earth (1 AU). In this work, the proton LIS from Bisschoff et al. [2019], based on the GALPROP model, is used. This LIS gives reasonable compatibility to V1 (Stone et al. [2013], Cummings et al. [2016]) and PAMELA (Adriani et al. [2013], Martucci et al. [2018]) observations at lower and higher energies, respectively. Figure 4.3 shows the computed proton LIS in comparison to the minimum (2013b) and maximum (2009b) intensities observed at the Earth by PAMELA indicated as open circles and V1 observations taken beyond the HP at lower energies indicated as open and closed squares.

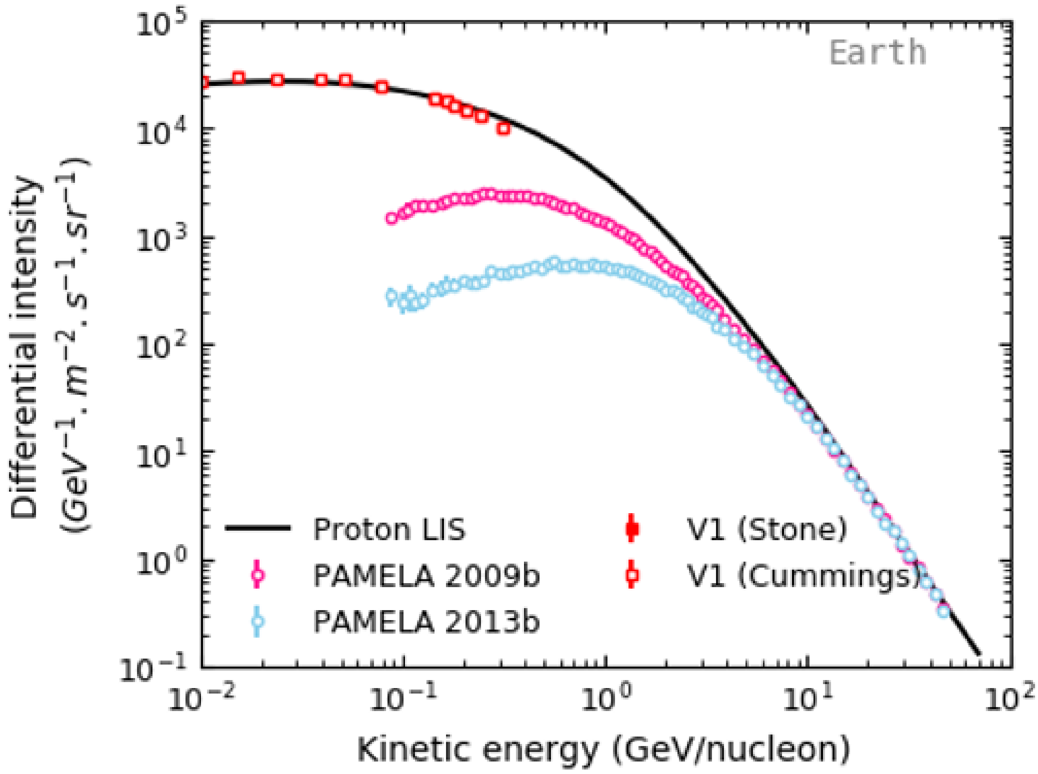

Figure 4.3: The proton LIS (black line) compared to the V1 data from Stone et al. [2013] (closed red squares) and Cummings et al. [2016] (open red squares), and PAMELA observations for the solar minimum of 2009b (pink open circles from Adriani et al. [2013]) and solar maximum of 2013b (blue open circles from Martucci et al. [2018]).

From Figure 4.3 it is evident that the computed proton LIS matches both PAMELA and V1 observations at kinetic energies of interest reasonably well. A similar approach to GCR proton LIS was discussed in details by Vos [2016]. As a result, proton modulation can be studied with a greater level of confidence during both minimum and maximum solar activity. This is done and discussed in the following sections.

The LIS from Bisschoff et al. [2019] given in Figure 4.3 can be approximated by the following expression,

$$J_P(E) = 2620.0\frac{1}{\beta^2}\left(\frac{E}{E_0}\right)^{1.1}\left(\frac{(E/E_0)^{0.98}+0.7^{0.98}}{1+0.7^{0.98}}\right)^{-4.0} + 30.0\left(\frac{E}{E_0}\right)^{2}\left(\frac{E/E_0+8.0}{9.0}\right)^{-12}, \tag{4.1}$$

where $J_P(E)$ is a function of kinetic energy, E, with units m^2.s^{-1}.sr^{-1} (GeV/nucleon)$^{-1}$ and E_0 = 1 GeV/nucleon.

4.4 Modeling the proton spectra observed by PAMELA between 2006 and 2013

4.4.1 Time-dependent changes in modulation parameters

When using a steady state numerical model, it is crucial to calculate averages of time-dependent parameters that vary consistently with solar activity, e.g., the magnitude of the HMF at Earth, and the HCS α. These parameters are incorporated in the model as moving averages in order to set realistic time-dependent modulation conditions. This approach has been found to be reasonable in establishing model compatibility with PAMELA observations as established by the numerical modeling of Vos & Potgieter [2015], Vos [2016], Aslam et al. [2019, 2021], Corti et al. [2019] and Ngobeni et al. [2020]. The HMF and HCS α are carried out from the Sun to the HP by the SW, hence the SW speed is considered when calculating the moving averages of both parameters. Because the HCS α is mostly confined in the ecliptic region (within 30^0) during minimum to moderate solar activity periods, which are associated with the slow SW speed, it takes $\approx$ 15 months for changes in the HCS α to reach the HP from the Sun to establish steady state condition in the whole heliosphere. However, the HMF is not only confined in the polar region or equatorial plane; as a result, the average time it takes both the slow and fast SW to reach the HP from the Sun is taken into consideration when calculating the HMF moving averages and the propagation time. This way the propagation time for the HMF is assumed to be $\approx$ 10 months or $\approx$ 15 months depending on the prevailing level of solar activity conditions.

Shown in Figure 4.4 is the HMF magnitude at Earth (top panel) from 2006-2016 taken from http://omniweb .gsfc.nasa.gov, together with the corresponding 10 (blue open circles) and 15 months (red open circles) moving averages, and the HCS α (bottom panel) taken from http://wso.stanford .edu with the corresponding 15 months (red open circles) moving average for the same period. The calculated moving averages are used as intrinsic parameters in the numerical model, with the magnitude of both the HMF and HCS α as good indicators of solar activity conditions where high and low values in the two parameters typically reflect maximum and minimum solar activity. It is clearly illustrated in Figure 4.4 on the top panel that the magnitude of the HMF dropped below 4 nT at the end of 2009 but recovered in mid 2010 until end of 2012 to a value of $\approx$ 5.61 nT. What is surprising and notable from this figure is the decrease in the magnitude of the HMF during the magnetic field reversal period, reaching $\approx$ 5.24 nT at the end of 2013. After the completion of the magnetic field reversal epoch, the magnitude of the HMF increases to higher values than during solar maximum conditions. For magnitudes of the HCS α, the bottom panel of Figure 4.4 shows that it reached its minimum value at the end of 2009 and increased rapidly from mid 2010 to a value of $\approx 17.28^0$ and continued to increase until 2013 where the largest value of about $\approx 65.96^0$ was reached.

In addition to changes in HMF and HCS α, the position of the TS, which also varies as a

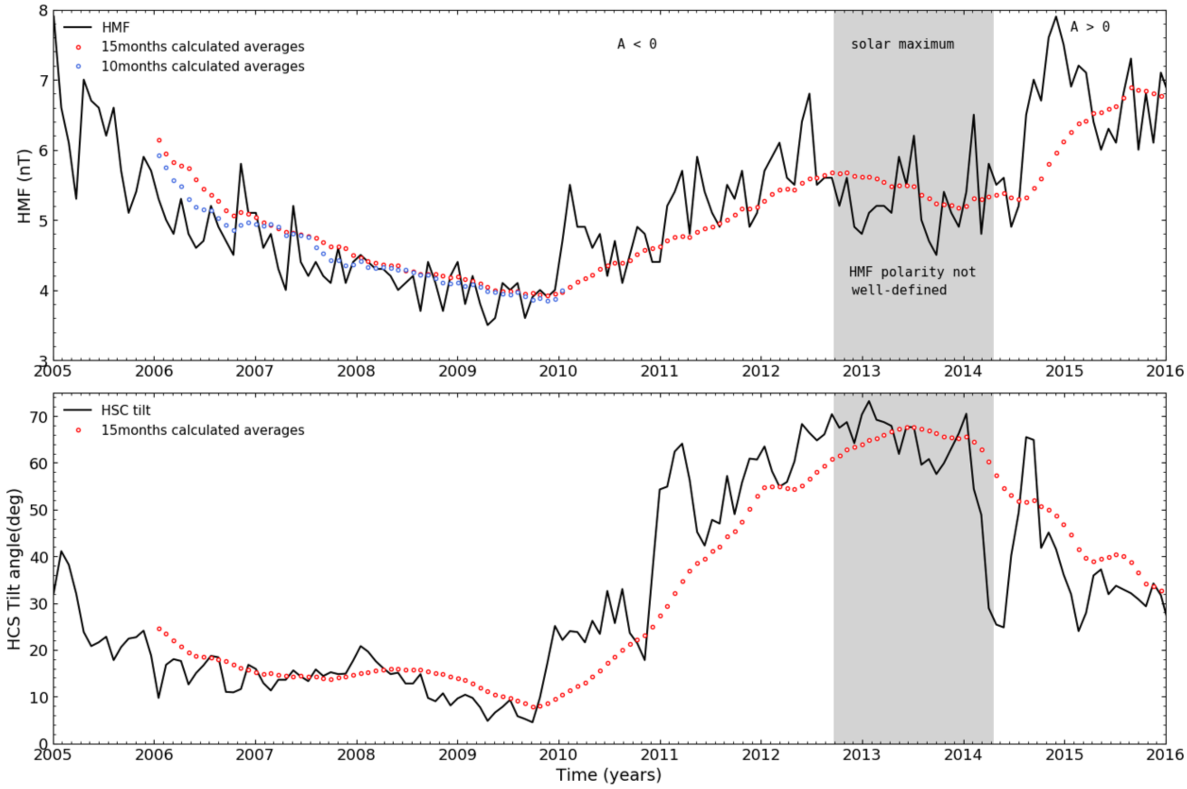

Figure 4.4: Top panel: the HMF at Earth measured during January 2005 up to December 2015, taken from **http://omniweb.gsfc.nasa.gov** which is represented by a black solid line with ≈ 15 (red open circles) and ≈ 10 (blue open circles) months moving averages. Bottom panel: tilt angle α of the HCS (black line) at the Earth for the same time period taken from **http://wso.stanford.edu** with ≈ 15 months moving averages (red open circles). The highlighted region indicates a period of the Sun's magnetic field reversal where the HMF polarity is not well-defined.

function of time, was taken into consideration, with the magnitude ranging between 80.0 AU to 88.0 AU depending on solar activity. Furthermore, to reproduce PAMELA observations at the Earth, other parameters such as $\lambda_{||}$ given in Equation (3.15), k_{A0} given in Equation (3.28), c_1 given in Equations (3.14) and (3.18), $c_{2||}$ given in Equation (3.14), $c_{2\perp}$ given in Equation (3.18), $F_{\perp\theta}$ given in Equations (3.17), and (3.19) are required to change with time. The mentioned intrinsic parameters as used in the model are summarized in Table 4.1, with $\lambda_{||}$ showing how the parallel MFP at the Earth is changing with time for CR species with rigidity 1.0 GV.

Figure 4.5 illustrates the ratio of the scaling constant, $\kappa_{||0}$ in Equation (3.13), to the magnitude of the HMF, B, as well as the rigidity dependent slopes of the MFPs (DCs) above and below 4 GV as a function of time, which indicates changes in the solar activity. The time dependences in the expressions of both $\kappa_{||}$ and $\kappa_{\perp r}$, given by Equations (3.14) and (3.18), and assumed in Figure 4.5, are necessary to reproduce PAMELA observations from 2006 to 2013. This is further discussed below. From this figure, it is evident that the rigidity slopes of the DCs below 4 GV vary with time, changing modestly between 2006 and 2011, and thereafter increasing rapidly

params	2006b	2007a	2007b	2008a	2008b	2009a	2009b	2010a	2010b	2011a	2011b	2012a	2012b	2013a	2013b
$\alpha(deg)$	16.58	14.50	14.27	15.67	14.38	10.62	9.11	17.28	21.01	35.38	45.21	55.38	61.68	65.59	65.96
B	4.95	4.77	4.35	4.27	4.11	3.98	3.91	4.26	4.52	4.84	5.11	5.50	5.61	5.54	5.24
r_{Ts} (AU)	88.0	87.0	86.0	85.0	84.0	82.0	80.0	80.0	82.0	83.0	84.0	85.0	86.0	87.0	88.0
$\lambda_{\|\|}$	0.74	0.82	0.88	0.87	0.95	1.09	1.11	0.98	0.85	0.71	0.68	0.61	0.54	0.45	0.41
κ_{A0}	0.90	0.90	0.90	0.90	0.90	0.90	0.90	0.90	0.90	0.75	0.55	0.30	0.00	0.00	0.00
$P_{A0}\ (GV)$	0.90	0.90	0.90	0.90	0.90	0.90	0.90	0.90	0.90	0.90	0.90	0.90	0.90	0.90	0.90
$\kappa^0_{\perp r}$	0.02	0.02	0.02	0.02	0.02	0.02	0.02	0.02	0.02	0.02	0.02	0.02	0.02	0.02	0.02
$\kappa^0_{\perp \theta}$	0.02	0.02	0.02	0.02	0.02	0.02	0.02	0.02	0.02	0.02	0.02	0.02	0.02	0.02	0.02
c_1	0.85	0.85	0.81	0.77	0.80	0.79	0.78	0.70	0.75	0.81	0.87	0.90	1.01	1.01	1.14
$c_{2\|\|}$	1.20	1.20	1.20	1.20	1.20	1.20	1.20	1.52	1.52	1.52	1.52	1.52	1.52	1.52	1.52
$c_{2\perp}$	0.84	0.84	0.84	0.84	0.84	0.84	0.84	0.988	0.988	0.988	0.988	0.988	0.988	0.988	0.988
c_3	2.50	2.50	2.50	2.50	2.50	2.50	2.50	2.50	2.50	2.50	2.50	2.50	2.50	2.50	2.50
$P_k\ (GV)$	4.0	4.0	4.0	4.0	4.0	4.0	4.0	4.0	4.0	4.0	4.0	4.0	4.0	4.0	4.0
$d_{\perp\theta}$	6.0	6.0	6.0	6.0	6.0	6.0	6.0	6.0	6.0	6.0	6.0	6.0	6.0	6.0	6.0

Table 4.1: Modulation parameters used to reproduce the PAMELA proton spectra.

until the end of 2013 where a maximum value is reached. This indicates that below 4 GV, the rigidity dependence of both the parallel and perpendicular DCs change in the same manner during the declining and inclining phase of solar activity. However, for the slopes of the DCs above 4 GV a constant value was assumed between 2006 and 2010, which was increased in the first half of 2010 but remained constant again between 2011 and 2013. As mentioned earlier, these time-dependencies are required in order to fit PAMELA observations. For an alternative modeling approach see Song et al. [2021b] and Fiandrini et al. [2021].

Figure 4.6 illustrates the MFPs (DCs) and drift scale, Equations (3.11), and (3.30) respectively, at the Earth (left panel) as a function of rigidity shown from 2006 to 2013. Also shown on the right panel at the same rigidity is the ratios of $\lambda_{\perp r}$ / $\lambda_{||}$ and λ_A / $\lambda_{||}$. The values used to obtain this figure are given in Table 4.1. It is clearly indicated from the left panel of this figure that MFPs (DCs) increased from 2006 to 2009 (top panel) when solar activity was decreasing and decreased from 2010 to 2013 (bottom panel). The rigidity dependence of $\lambda_{\perp r}$ ($\lambda_{\perp r}$ = $\lambda_{\perp\theta}$) is similar to that of $\lambda_{||}$ below 4 GV, whereas above this rigidity $\lambda_{\perp r}$ is much flatter compared to $\lambda_{||}$ as already mention in the previous chapter. This is clearly highlighted on the right panel when the ratio of $\lambda_{\perp r}$ / $\lambda_{||}$ is shown. The dimensionless quantity k_{A0} that adjusts the level of drifts in Equation (3.28), depending on solar activity, is given in Table 4.1. As it can be seen that no drifts were assumed during the period of HMF reversal since there was no well-defined polarity, and hence k_{A0} = 0. It can further be noted that adjusting k_{A0} influences the spread in λ_A values largely between 2010 and 2013 than between 2006 and 2009 at all rigidities. When

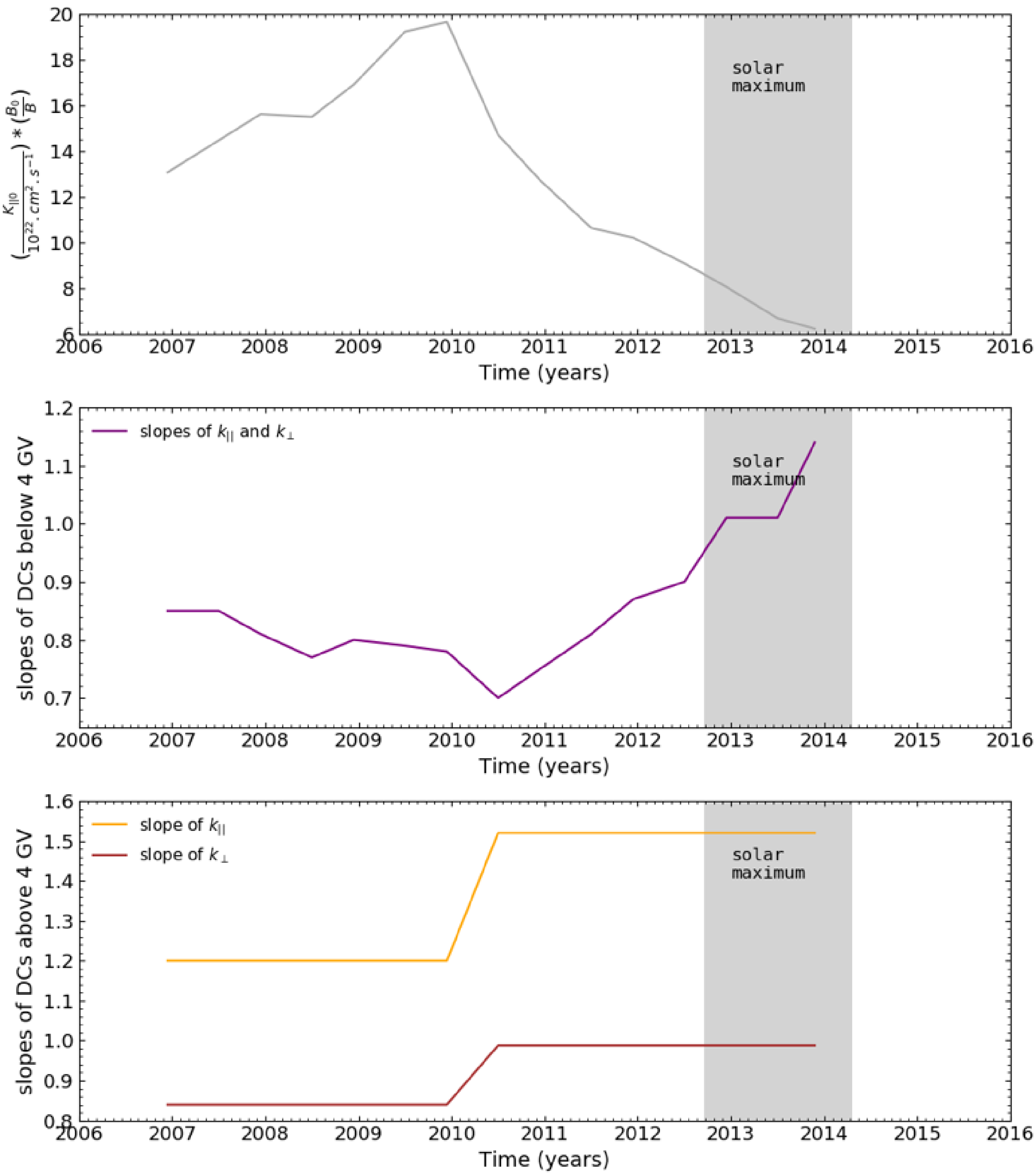

Figure 4.5: The time dependence of $k_{||_0}/B$ (top panel), slopes of DCs below (middle panel, c_1 in Equations (3.14) and (3.18)) and above 4 GV (bottom panel, $c_{2||}$ and $c_{2\perp}$ in Equations (3.13) and (3.16)), respectively.

considering the ratios of $\lambda_{\perp r}$ and λ_A to $\lambda_{||}$, it is noted that $\lambda_{\perp r}$ / $\lambda_{||}$ shows no time dependences while λ_A / $\lambda_{||}$ indicates large time dependences at all rigidities.

The MPFs, $\lambda_{||}$ and $\lambda_{\perp r}$ in Figure 4.6 are now illustrated in Figure 4.7 for four selected rigidities ranging between 1.06 GV and 3.86 GV (left panel), along with the corresponding ratios relative to 2006b as a function of time (right panel). It is shown in the left panel that $\lambda_{||}$ increases significantly from 2006 to reach a maximum at the end of 2009 and thereafter decreases gradually

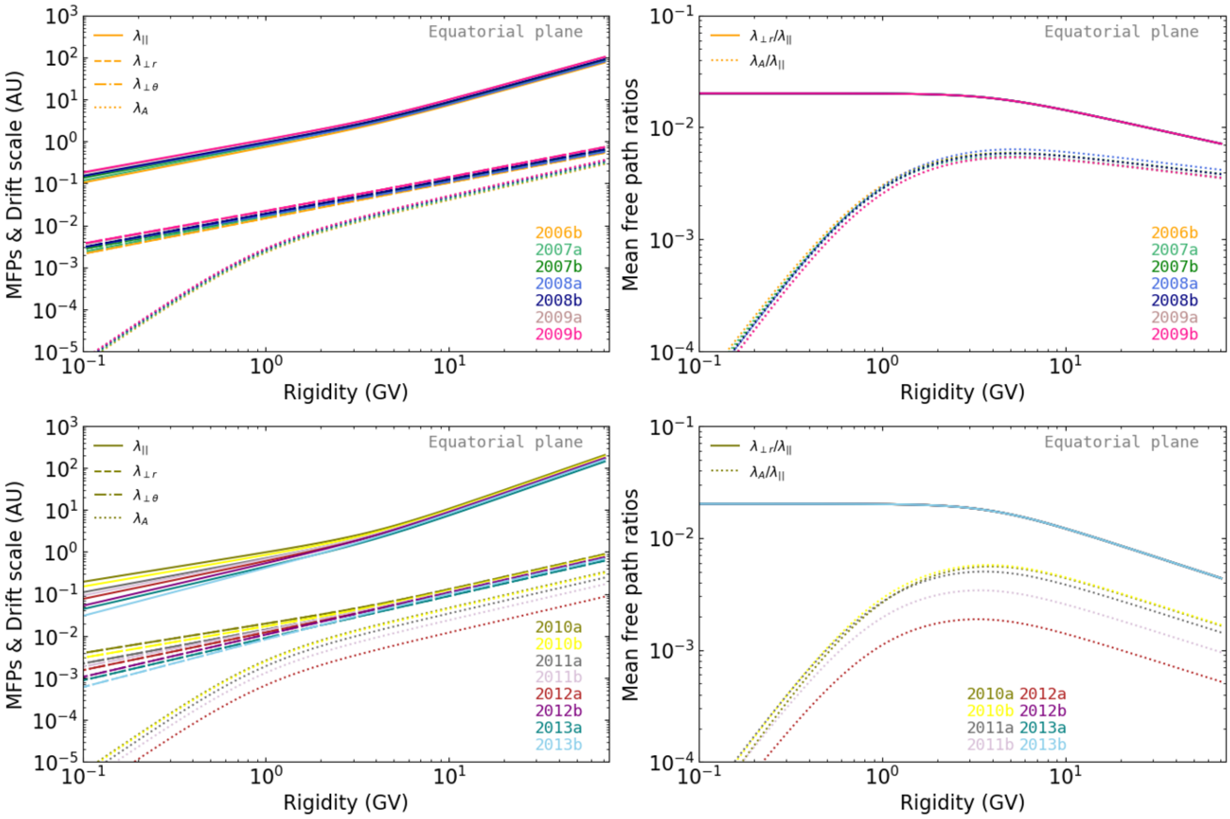

Figure 4.6: Left panel: Computed MFPs at Earth as a function of rigidity between December 2006 (top panel) and December 2013 (bottom panel) focusing on fifteen half-year periods. The solid lines represent the parallel MFPs $\lambda_{||}$, while the dashed and dashed-dotted lines represent the perpendicular MFPs in the radial ($\lambda_{\perp r}$) and polar ($\lambda_{\perp\theta}$) directions respectively and the drift scale (λ_A) is represented by the dotted lines. Right panel: The corresponding ratios of the MFPs $\lambda_{\perp r}$ / $\lambda_{||}$ (solid lines) and λ_A / $\lambda_{||}$ (dotted lines) as a function of rigidity.

towards solar maximum activity reaching minimum values in mid-2013 at rigidities $>$ 1.61 GV. From the right panel, it is notable that $\lambda_{||}$ of a lower rigidity proton compared to higher rigidity proton will increase faster during solar minimum and decrease faster towards solar maximum. It is also notable that despite the difference in magnitudes of $\lambda_{||}$ and $\lambda_{\perp r}$ as a function of time, these two MFPs evolve by the same factor relative to 2006b.

Figure 4.8 is similar to Figure 4.7 but showing λ_A together with the corresponding ratio relative to 2006b. From this figure, it is shown that λ_A increases from 2006 to reach a maximum value at the end of 2009, and thereafter decreases gradually towards solar maximum to become negligible around end of 2012 to 2013. It is notable from the left panel that lower rigidity protons assume a smaller drift scale compared to higher rigidity protons. However, the right panel shows that the drift scale for both lower and higher rigidity proton relative to 2006b required to establish compatibility with PAMELA observations changes by the same factor and in the same way between 2006 and 2013. See also Aslam et al. [2021] for a discussion.

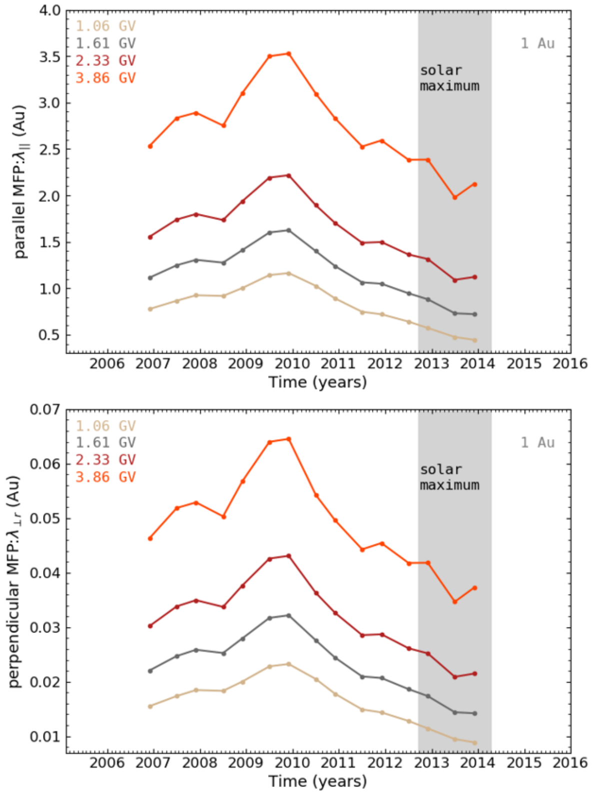

Figure 4.7: Top panel: Computed parallel MFPs, $\lambda_{||}$, as a function of time (left) at rigidities of 1.06 GV, 1.61 GV, 2.33 GV and 3.86 GV, with the corresponding ratios relative to 2006b (right). Bottom Panel: Similar to the top panel but perpendicular MFPs, $\lambda_{\perp r}$, in the radial direction is shown.

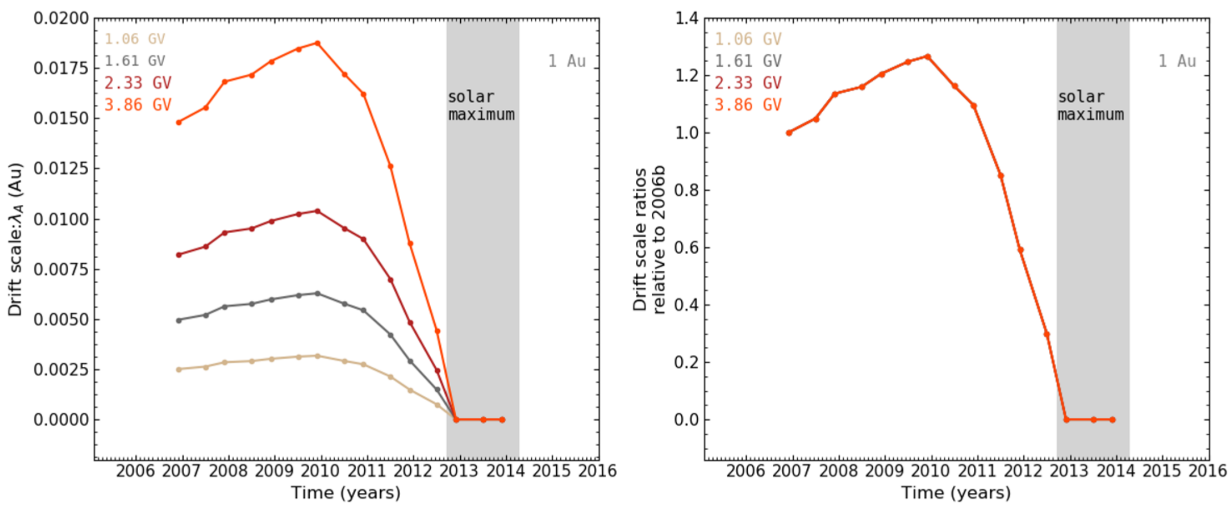

Figure 4.8: Similar to Figure 4.7 but the drift scale, λ_A, is shown.

4.4.2 Modeling PAMELA proton spectra as a function of kinetic energy

The left panel of Figure 4.9 shows the computed proton energy spectra for fifteen Carrington rotations each at the end of the half-year in comparison with the corresponding PAMELA ob-

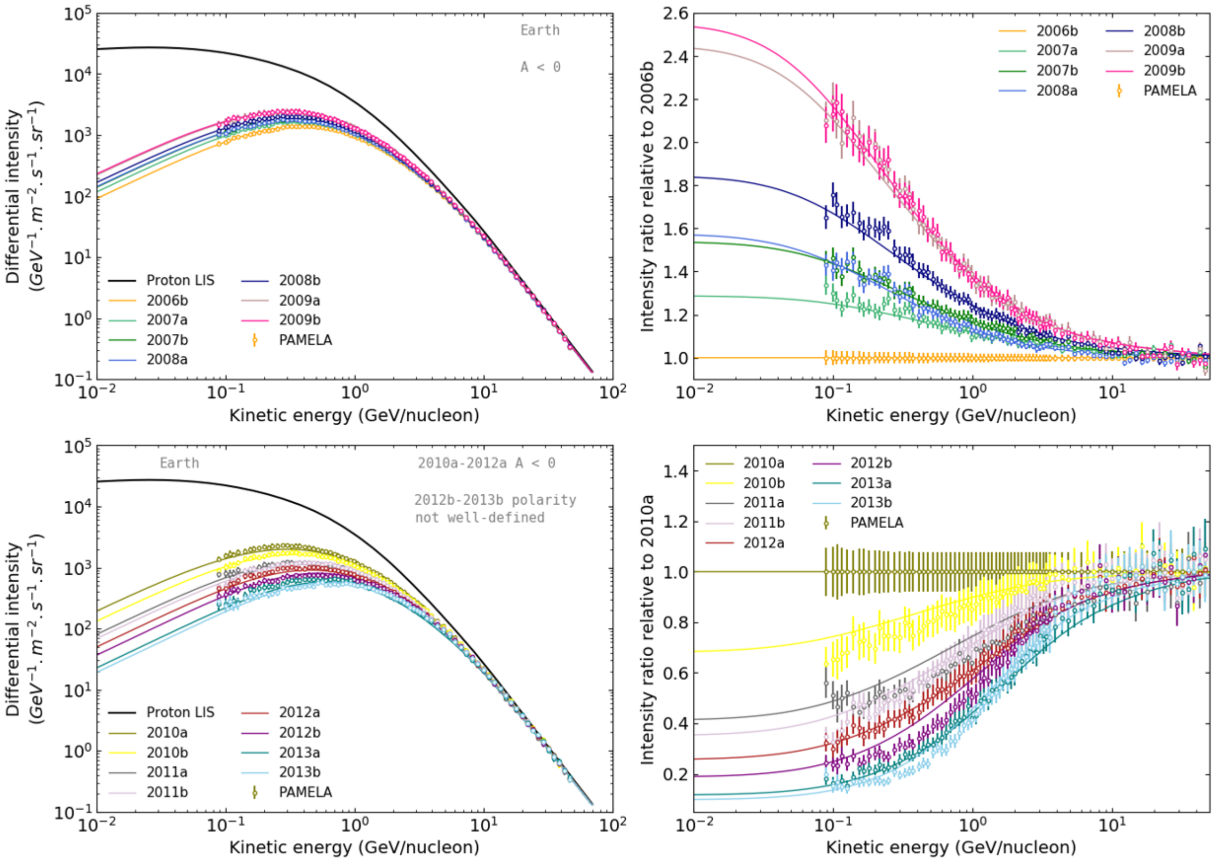

Figure 4.9: Left panel shows the LIS's for proton (black solid line) together with the modulated differential intensity computed (coloured solid lines) as a function of kinetic energy/nucleon at the Earth for the solar minimum period of 2006 to 2009 (top row) and from 2010 to 2013 (bottom row). Right panel shows the corresponding computed intensity ratios for proton (solid lines) relative to 2006b (top row) and 2010b (bottom row).

servations given already in Figure 4.1. The corresponding intensity ratios relative to 2006b (top) and 2010a (bottom), showing how adiabatic energy losses shape the spectral slopes of modulated spectra at low energies, are shown on the right panel. The numerical model reproduces PAMELA observations quite well at all energies including those above ≈ 30 GeV/nucleon where modulation is negligible. From this figure it is evident that the computed energy slope of protons below ≈ 100 MeV/nucleon is equivalent to E^1 and it is due to an effect caused by the expanding SW known as adiabatic energy cooling (losses), a modulation process already discussed in Chapter 3. This process is most effective in the inner heliosphere and dominates proton modulation at non-relativistic energies (see Ngobeni et al. [2020], Strauss et al. [2011]). On the right panel of this figure, the adiabatic energy losses consequently cause the relative intensity ratios to be almost independent of energy below ≈ 0.434 GeV/nucleon and becoming more so with decreasing energy. When looking at the modulated spectra in Figure 4.9, a characteristic peak in each spectrum is observed but shifts to higher energies with increasing solar activity. For example, in 2009b the peak is observed at ≈ 0.45 GeV/nucleon, whereas in

2013b the observed peak shifted to ≈ 1 GeV/nucleon. To reproduce these peaks with a numerical model, the rigidity slopes of the DCs below 4 GV must continually increase with time from solar minimum to solar maximum in addition to the significant change of particle drift with solar activity. The measured relative intensity ratios are also reproduced reasonably well with the numerical model, showing that at ≈ 90 MeV/nucleon they increased by a factor ≈ 2.2 between 2006 and 2009, whereas between 2010 and 2013 these intensities decreased by ≈ 80% as already mentioned. The computed relative intensity ratios also converge to a single value at energies > ≈ 15 GeV/nucleon similarly to observed ratios.

4.4.3 Modeling PAMELA proton spectra as a function of time

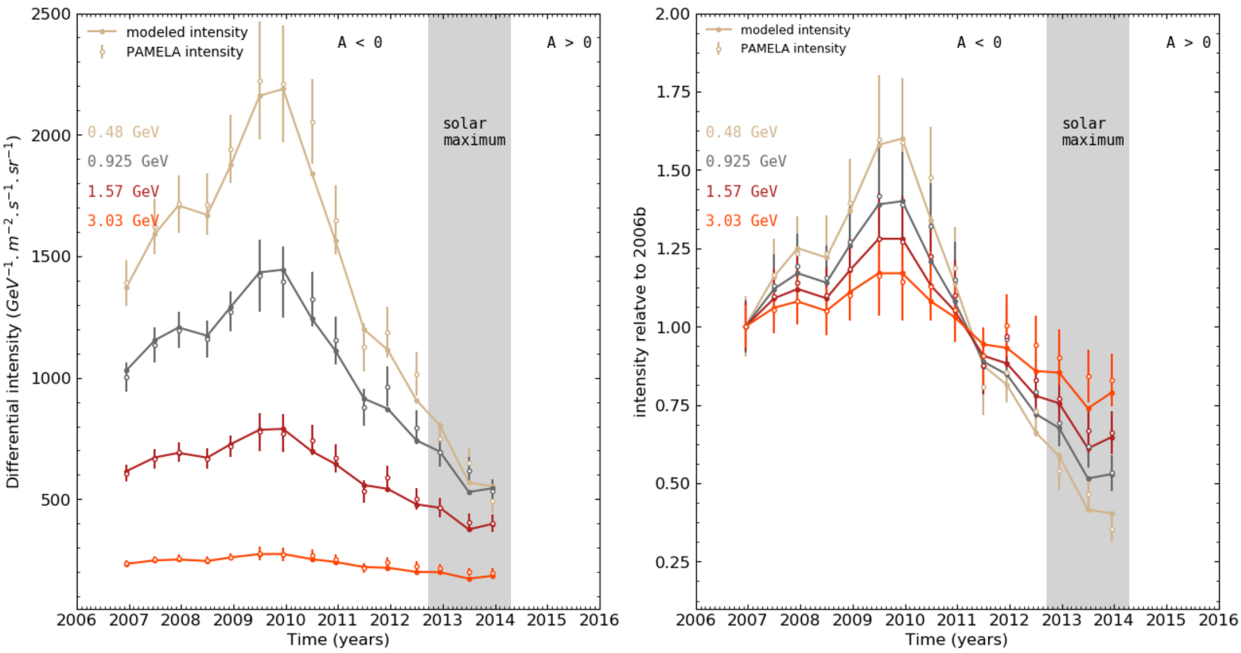

Figure 4.10: Left panel: The differential intensities as a function of time at kinetic energy ranging from 0.48 GeV to 3.03 GeV, corresponding to the selected rigidity values evaluated for the MFPs as a function of time in Figures 4.7 and 4.8. Right panel: The corresponding intensity ratios relative to 2006b.

Shown in Figure 4.10 is the computed intensities at four selected kinetic energy values as a function of time together with PAMELA observations already given in Figure 4.2. An interesting aspect of what is shown in Figures 4.7 and 4.10 is what they imply for how CR proton intensities at different kinetic energies develop during solar maximum activity periods. Because the MFPs for the higher rigidity turns around to become larger sooner than the MFPs for the lower rigidity as shown in Figure 4.7, therefore CR protons of higher kinetic energies always recover, start increasing again after minimum intensities reached during solar maximum, earlier than the lower kinetic energies. This well-known time-lag between GCRs and solar activity proxies (e.g., Tomassetti et al. [2017]) and the general features of long-term modulation are clearly depicted in Figure 4.10 (see also le Roux & Potgieter [1992]).

4.5 Effects of the rigidity slopes of the DCs on the modulated spectra

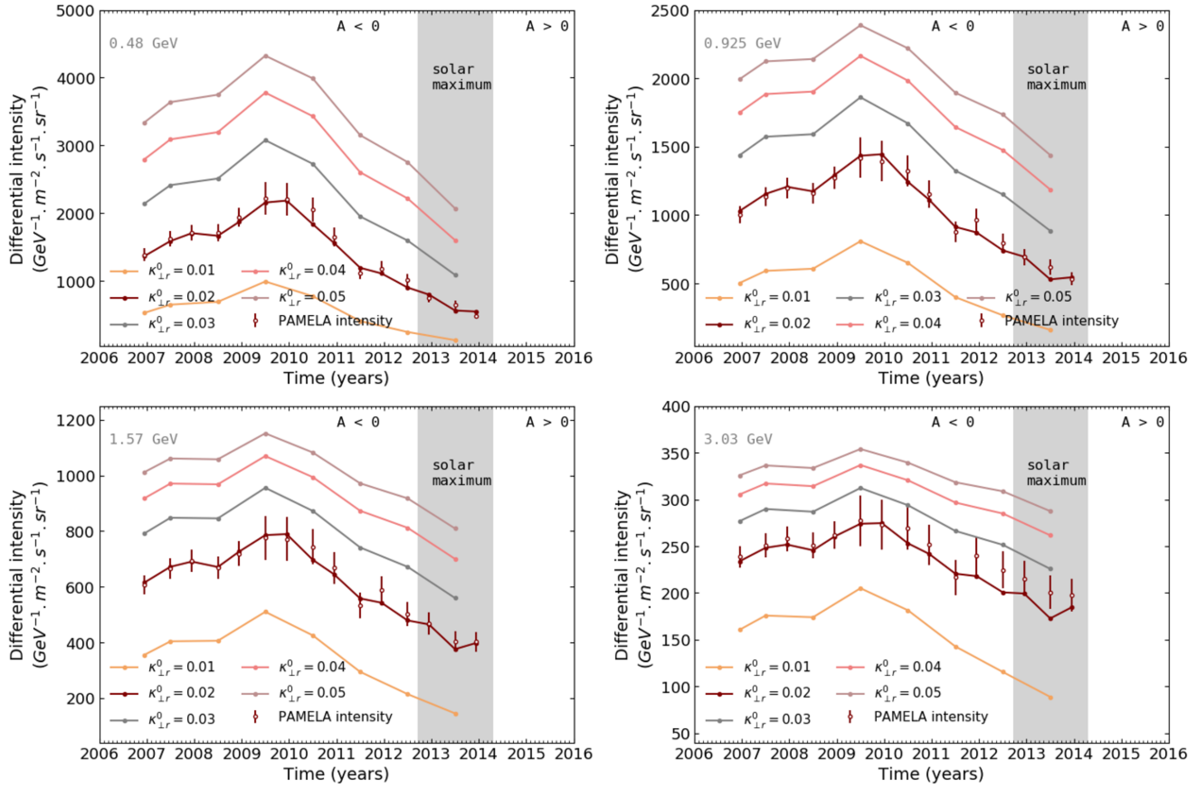

Figure 4.11: The computed differential intensity spectra as a function of time similar to figure 4.10 but with $\kappa^0_{\perp r}$ ranging from 0.01 to 0.05 indicated with different colours.

This section shows how the rigidity dependence of DCs and the magnitude of the overall scaling constant of $k_{\perp r}/k_{||}$ represented by $\kappa^0_{\perp r}$, given in Equation (3.16), used to reproduce the PAMELA proton spectra in Figures 4.9 and 4.11 were chosen. Now following what was confirmed by Giacalone & Jokipii [1999] with regards to $\kappa_{\perp}$ scaling spatially as $\kappa_{||}$, with the magnitude of $\kappa^0_{\perp r}$ ranging between 0.02 and 0.04, an investigation on the magnitude of $\kappa^0_{\perp r}$ is carried out as illustrated in Figure 4.11. Here the scaling constant is assumed to range between 0.01 and 0.05, and the computed CR proton intensities as a function of time are shown at four selected kinetic energies and compared to PAMELA observations. The maroon curves in Figure 4.11 correspond to intensities already shown in Figure 4.10. It is clearly evident in Figure 4.11 that assuming $\kappa^0_{\perp r}$ = 0.02 produces model results that are more compatible with observations from solar minimum towards solar maximum conditions at all kinetic energies. Values of $\kappa^0_{\perp r}$ lower than 0.02 produce model results that are lower than observations, while higher values produce model results that are higher than the observed intensities.

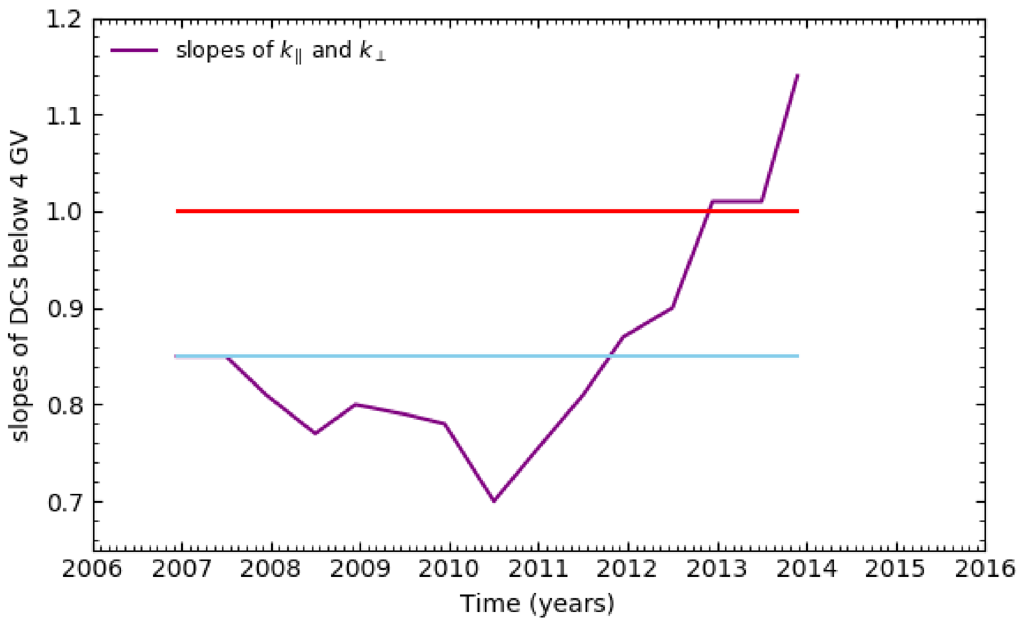

Figure 4.12: Three scenarios of the rigidity slopes of the DCs below 4 GV as a function of time at the Earth between 2006 and 2013.

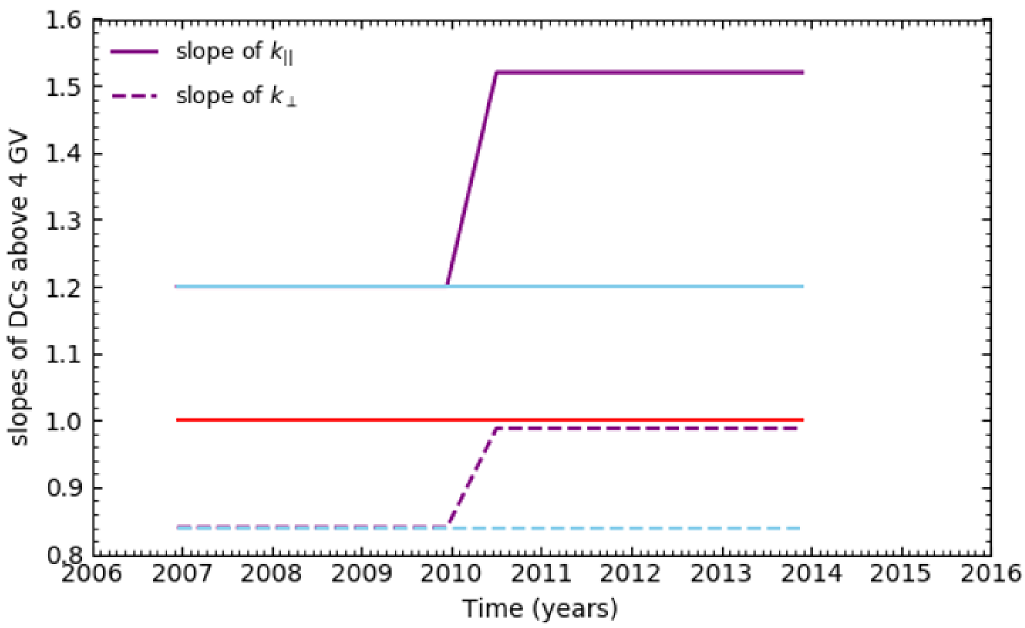

Figure 4.13: Similar to Figure 4.12 but with the rigidity slopes of the DCs above 4 GV.

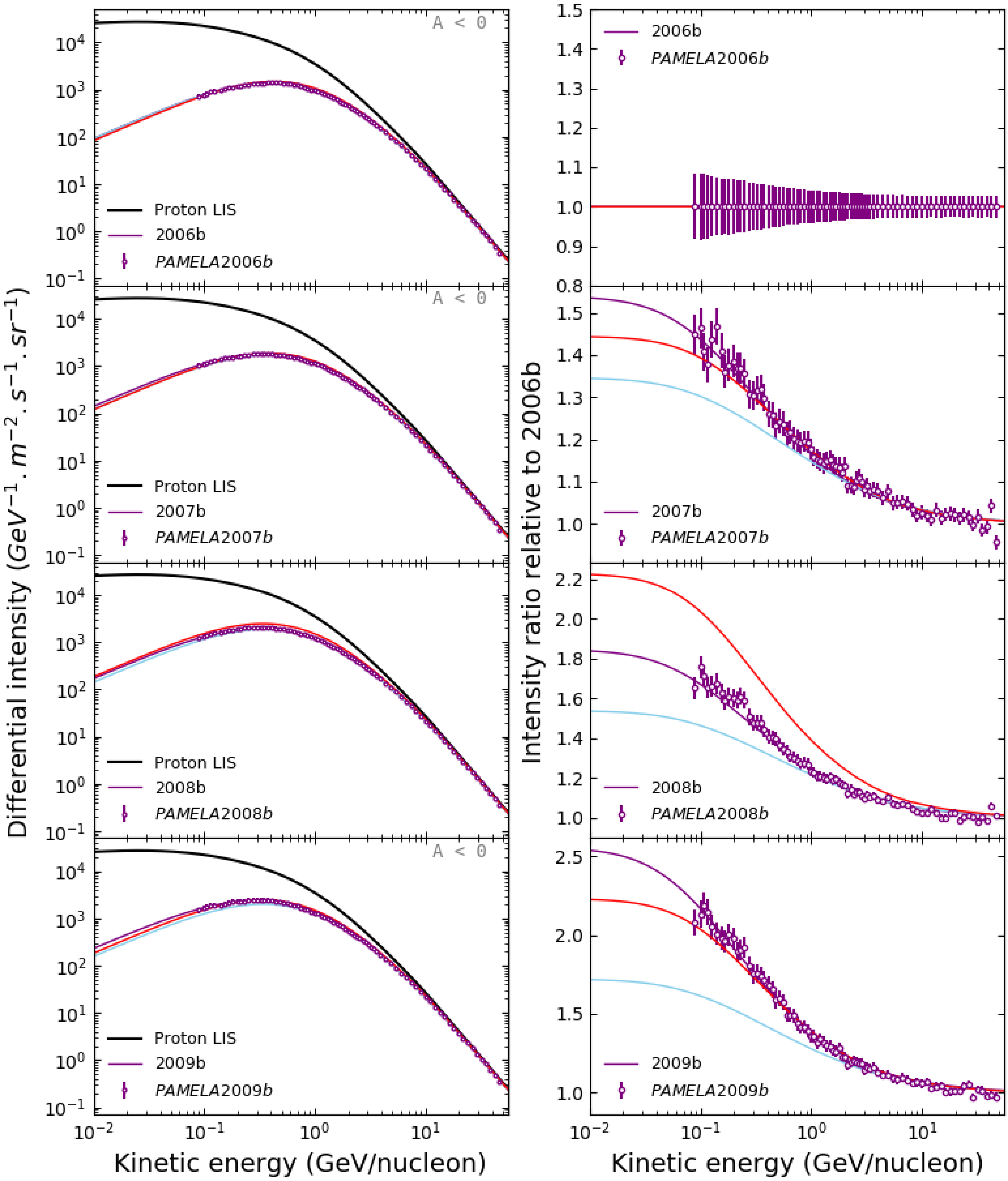

Figure 4.14: Left panel shows the LIS for GCR protons (black line) together with the modulated differential intensity computed (coloured solid lines) as a function of kinetic energy/nucleon at the Earth from 2006b to 2009b. Right panel shows the corresponding computed intensity ratios as solid lines relative to 2006b. These computed spectra are compared to PAMELA proton observations indicated by purple open circles with their errorbars. The three different spectra shown correspond to the three scenarios of the same colour of the rigidity slopes of DCs shown in Figures 4.12 and 4.13.

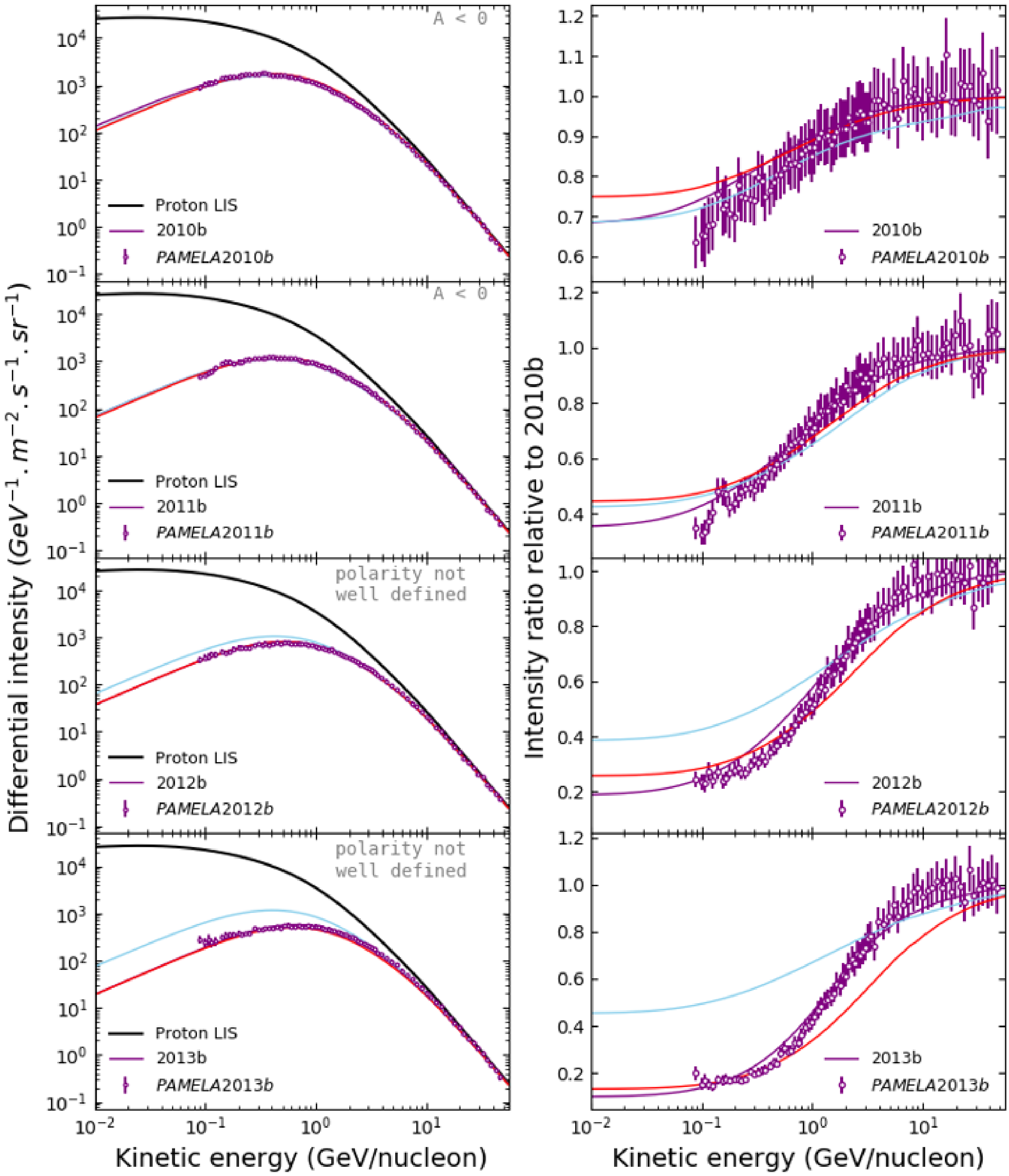

Figure 4.15: Similar to Figure 4.14 but shown from 2010b to 2013b and with ratios relative to 2010b.

Shown in Figures 4.12 and 4.13 are three scenarios of the rigidity slopes of the diffusion coefficients below (c_1 in Equations (3.13) and (3.14)) and above 4 GV ($c_{2||}$ in Equation (3.14)) as a function of time from 2006 to 2013. The purple lines in these two figures represent values of the rigidity slopes of the DCs given in Table 4.1 for the full time dependences in the model, whereas the blue lines represent the slopes of the DCs when all time dependent parameters in the model are kept constant at their 2006b values and only α and B are changed with time from 2006b to 2013b. While for the red lines the full time dependences in the model are assumed but with the DC $\approx P^1$, meaning $c_1 = c_{2||} = c_{2\perp} = 1.0$ in Equations (3.13), (3.14) and (3.18), at all rigidities and at all times keeping constant rigidity slopes of the DCs. This last scenario consequently implies that $k_\perp = 0.02k_{||}$ and the ratio of $D_\perp/D_{||} = 1$ in Equations (3.16) and (3.17) at all rigidities.

Figures 4.14 and 4.15 illustrate the computed modulation for GCR protons in comparison with PAMELA observations as a function of kinetic energy from 2006b-2009b and 2010b-2013b with their corresponding ratios relative to 2006b and 2010b, respectively. The three coloured solid lines correspond to the three model scenarios described above and given in Figures 4.12 and 4.13. Here, the effects of changing the rigidity slopes of the DCs with time are illustrated with emphasis on the resulting differences in the computed results and PAMELA observations. Both these figures, especially on the right panel, show that varying the slopes below 4 GV as given in Table 4.1 produces model results that are more compatible with observations. While on the other hand changing only the magnitude of the HMF and HCS α without changing the rigidity slopes of the DCs below 4 GV has less compatibility with observations and more so during solar maximum. Furthermore, when DCs are proportional to P^1, an assumption widely used in force-field models, the unfolding of the spectra from 2006b is not correctly reproduced at all times. See Moraal [2013], and recently Engelbrecht & Di Felice [2020] for a discussion on the limitation of the force-field model.

Figures 4.14 and 4.15 also indicate that plotting only the differential intensities as a function of kinetic energy on log-log scales may not reveal the detail unfolding of the spectra as a function of time and can easily yield misleading results as pointed out by Ngobeni et al. [2021a]. For example, the left panels of the mentioned figures suggest that the assumption that the DCs $\approx P^1$ is reasonable because it produces modulated spectra that appear to be compatible to observations, whereas the right panels tell a different story.

Evidently, allowing only B and α to change as a function of time cannot reproduce the observed spectra at all rigidities for every time interval; and also the DCs $\approx P^1$ is not a reasonable assumption when considering the time evolution of the spectra. For this reason, it is necessary to change the values of the drift and DCs and particularly the rigidity slopes of the DCs with time from 2006 to 2013.

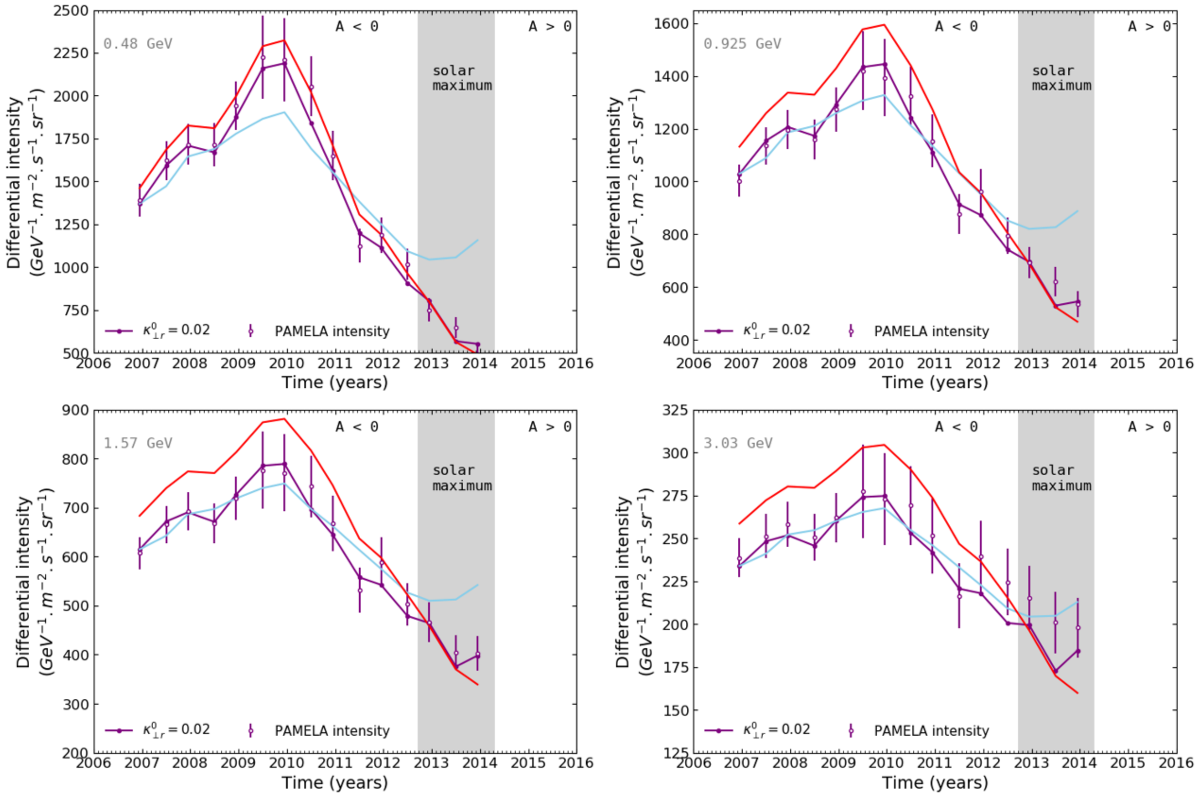

Figure 4.16: Similar to Figure 4.12 but with four selected kinetic energy values between 0.48 GeV and 3.03 GeV and the rigidity slopes of DCs as described in Figure 4.12.

The differential intensities in Figures 4.14 and 4.15 are now given in Figures 4.16 and 4.17 but as a function of time at four selected kinetic energy values including both lower and higher energies, respectively. The time-dependence of the purple lines follow the time profile of PAMELA intensities more accurately, when compared to the blue and red lines, from solar minimum and to solar maximum at all energies. Note that the blue curves produce the recovery time of CRs during solar maximum that is compatible with PAMELA observations at higher energies, whereas at lower energies the computed recovery time is much earlier than observations suggest. On the other hand, the red curves produce the recovery time at lower energies compatible with PAMELA observations, but this compatibility is lost with increasing energy. Therefore, Figures 4.16 and 4.17 further confirm that in order to reproduce PAMELA observed features with a numerical model, the assumed rigidity slopes of the DCs must be different at high and lower rigidities and should assume a significant time dependence as in this work.

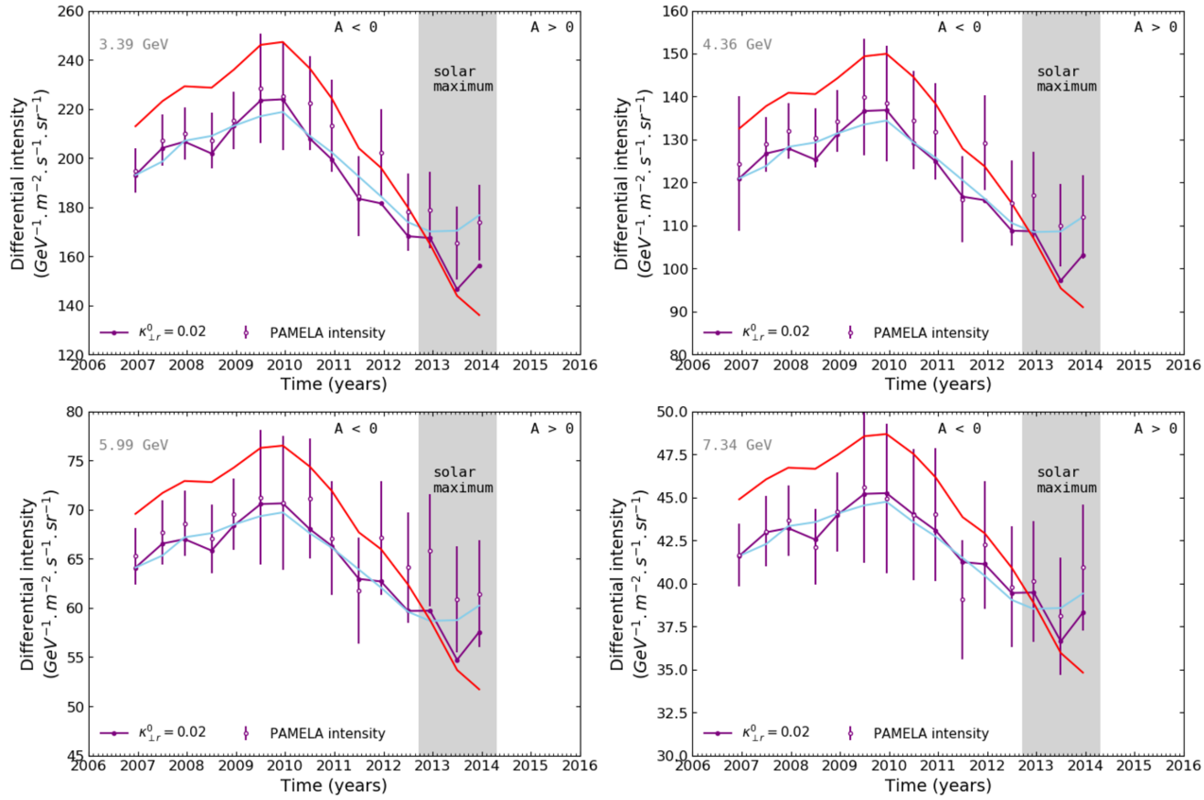

Figure 4.17: Similar to Figure 4.16 but with four selected kinetic energy values between 3.39 GeV and 7.34 GeV.

4.6 Summary and conclusion

This chapter was devoted to reproducing the PAMELA proton energy spectra from solar minimum to solar maximum. This was successfully done with the model results showing good compatibility with observations both as a function of kinetic energy and time. As expected, proton intensities increased from 2006 to 2009 and decreased from 2010 to 2013 due to the decreasing and increasing solar activity, respectively. The magnitudes of B and HCS α correlates with the changes in solar activity as indicated in Table 4.1 and the determination of their averaged values is an important part of the modeling approach in this chapter (see also Aslam et al. [2021], Kopp et al. [2021]). It was shown that to reproduce PAMELA observations, the rigidity slope of the DCs (MFPs) below 4 GV should assume a significant time dependence between 2006 and 2013, while remaining almost constant above 4 GV between 2006 - 2009 and 2010 - 2013. Therefore, this chapter established that allowing only B and HCS α to change as a function of time cannot reproduce the observed spectra at all rigidities for every selected time period; and also the assumption that DCs $\approx P^1$ is not a reasonable assumption when considering the time evolution of the spectra. For this reason, it is necessary to change the values of the drift and DCs and particularly the rigidity slopes of the DCs with time from 2006 to 2013.

The set of proton modulation parameters established in this chapter are applied in the next chapter that is devoted to the modulation of helium isotopes.

Chapter 5

Heliospheric modulation of galactic cosmic ray helium nuclei

5.1 Introduction

In the previous chapter the heliospheric modulation of galactic protons related to PAMELA observations between 2006 and 2013 was discussed. In this chapter the model is expanded to include the modulation of cosmic ray He, which is the combination of both $^3He_2$ and $^4He_2$ isotopes. This is done using the exact same set of modulation parameters, diffusion and drift coefficients discussed in Chapter 4, with their A/Z value and LIS the only differences remaining when comparing with proton modulation. Firstly, using $^3He_2/^4He_2$ ratios obtained from various observations around the Earth, it will be established that the shape of the LIS's of $^3He_2$ and $^4He_2$ obtained from the GALPROP model as described by Bisschoff et al. [2019] is most reasonable but that the LIS of $^3He_2$ needs to be modestly adjusted at higher energies in accordance with AMS02 $^3He_2/^4He_2$ observations. Secondly, these accurate LIS's are then incorporated in the 3D numerical model to study the modulation of $^3He_2$ and $^4He_2$ during solar minimum modulation period of 2006 to 2009, similar to Ngobeni et al. [2020] but also extended to periods of increasing solar activity between 2010 and 2013. The essence of separating the modulation effects of the two He isotopes when using comprehensive modeling has been given by Ngobeni et al. [2020, 2021b]. Consequently, the numerical modulation of total He (combined spectra of $^3He_2$ and $^4He_2$) and its comparison with PAMELA observations can be done with improved confidence from solar minimum to maximum activity periods (see also Song et al. [2021a]); a particular objective of this chapter. This will test the generality of the set of modulation parameters, diffusion and drift coefficients discussed in Chapter 4. Furthermore, the significance of how the slopes of the LIS's of both He isotopes combined with the rigidity slopes of the diffusion and drift coefficients influence the rigidity and time-dependence of the ratio of $^3He_2$ to $^4He_2$ with increasing solar activity is investigated in detail.

5.2 The local interstellar spectra of helium isotopes

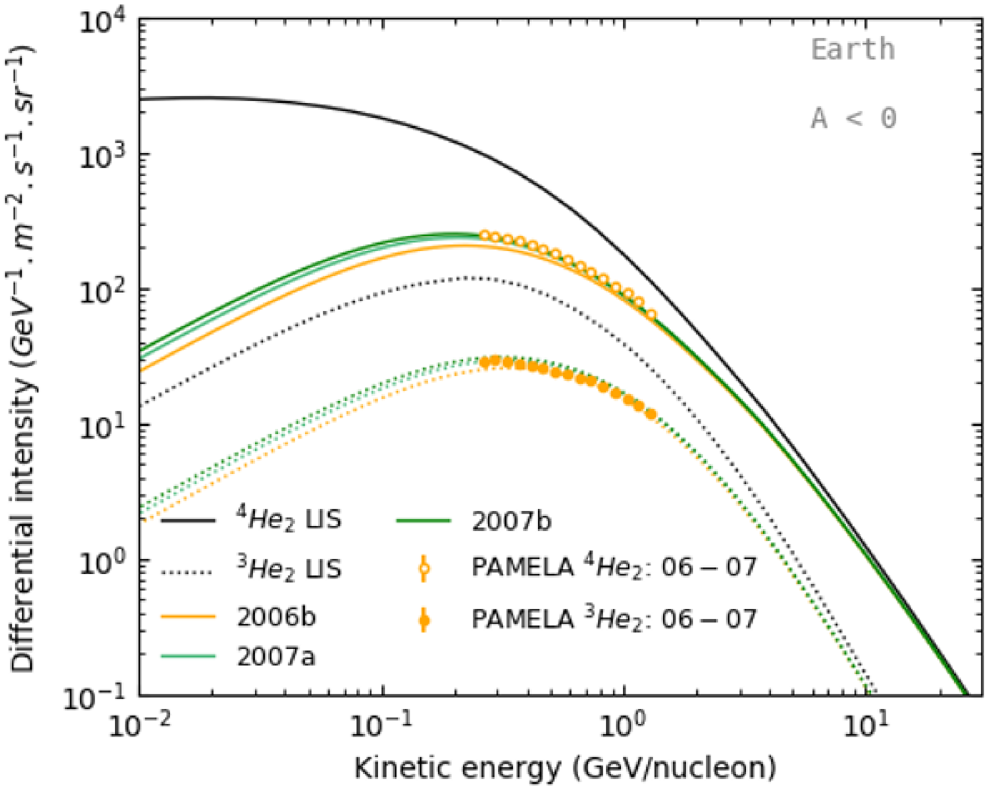

Figure 5.1: The LIS's for $^3He_2$ (black dotted lines) and $^4He_2$ (black solid lines) are shown together with the corresponding modulated differential intensities (coloured dotted and solid lines for $^3He_2$ and $^4He_2$, respectively) computed as a function of kinetic energy/nucleon at the Earth; done for three periods corresponding to the end of the year (or half-year) indicated by different colours: 2006b, 2007a and 2007b. These computed spectra are compared to PAMELA $^3He_2$ and $^4He_2$ (filled and opened orange circles respectively) taken from Adriani et al. [2016].

Galactic $^3He_2$, mainly a secondary CR species, is produced by spallation of primary $^4He_2$ when it interacts with interstellar matter during its propagation in the galaxy. It remains an important objective to determine the ratio $^3He_2/^4He_2$ (secondary-to-primary CR) in the galaxy over a wide kinetic energy/nucleon range. This ratio assists to uncover the general abundance of secondary CRs in the galaxy, and provides unique input to CR propagation models, distinctly different from the commonly studied secondary-to-primary ratios of heavier elements such as Boron-to-Carbon and Boron-to-Oxygen (see Battiston [2020], Aguilar et al. [2019], Adriani et al. [2016]).

Numerical modeling of the heliospheric modulation of He had been done in the past by various authors (e.g., Langner [2004], Steenberg & Moraal [1996]) but without considering the isotopes of He separately. The same applies to a recent report by Shen et al. [2019]. However, recently Ngobeni et al. [2020, 2021b] reported a new and fundamental approach to He modeling that considers the modulation of both isotopes separately. Separating the modeling effects of both He isotopes is important for a simultaneous explanation of the $^3He_2/^4He_2$ and proton to He ratios at the same rigidity and time.

Figure 5.1 shows the LIS's of $^3He_2$ and $^4He_2$ from Bisschoff et al. [2019], calculated with the well-known GALPROP online code, together with their corresponding computed intensities as a function of kinetic/nucleon at the Earth in comparison with the averaged PAMELA data observed between 2006 and 2007. The PAMELA observation of the He isotopes is taken from Adriani et al. [2016] and ranges from 0.26 GeV/nucleon to 1.30 GeV/nucleon. The essence of this figure is to show that the PAMELA $^3He_2$ and $^4He_2$ spectra are well reproduced by our model, though within the constraints of a limited kinetic energy range. To constrain the LIS's of both $^3He_2$ and $^4He_2$ isotopes with a numerical modulation model, their measurements together with that of their ratios at much higher kinetic energies/nucleon than 1.30 GeV/nucleon is required. Next the computed intensities obtained using the LIS's depicted in Figure 5.1 are compared to observations of $^3He_2$ and $^4He_2$, together with their ratios, taken from different detectors around the Earth.

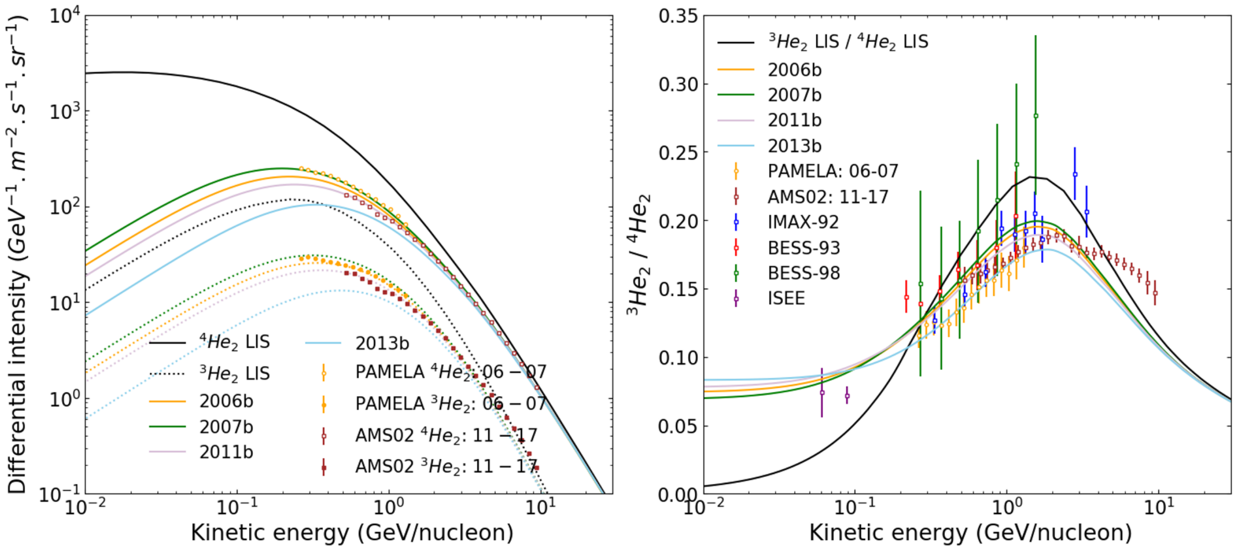

Figure 5.2: Left panel: LIS for $^3He_2$ and $^4He_2$ (dotted and solid black lines, respectively) are shown together with the corresponding modulated differential intensity (coloured dotted and solid lines for $^3He_2$ and $^4He_2$, respectively) computed as a function of kinetic energy/nucleon at the Earth; done for four periods corresponding to the end of the year indicated by different colours: 2006b, 2007b, 2011b and 2013b, respectively. Right panel: Corresponding ratios of the LIS (solid black line) and modulated spectra (solid coloured lines). Computed spectra and ratios are compared to corresponding $^3He_2$ and $^4He_2$ observations with their error bars taken from Aguilar et al. [2019] (AMS02, brown squares), Adriani et al. [2016] (PAMELA, orange circles), Myers et al. [2003] (BESS-98, green squares), Wang et al. [2002] (BESS-93, red squares), Reimer et al. [1998] (IMAX-92, blue squares), and Mewaldt [1986] (ISEE, purple squares).

Figure 5.2 illustrates the computed spectra of both $^3He_2$ and $^4He_2$ on the left panel which is similar to what is given in Figure 5.1 but now compared also with AMS02 data averaged between 2011 and 2017 as a function of kinetic energy/nucleon. The corresponding computed ratios of $^3He_2/^4He_2$ are given on the right panel of this figure and are compared to data from various spacecraft. The AMS02 data is taken from Aguilar et al. [2019] observed between May 2011 and November 2017, while other earlier experiments as indicated are taken from Myers et al. [2003], Wang et al. [2002], Reimer et al. [1998] and Mewaldt [1986]. Such an update of Figure 5.1 is required in order to put constraints on the LIS's of He isotopes using modulation models, as it is notable from the right panel of Figure 5.2 that observations of $^3He_2/^4He_2$ ratios from earlier experiments are characterized by large uncertainties. Furthermore, the observations of $^3He_2/^4He_2$ ratio by AMS02 indicate that it reaches a peak around $\approx$ 2 GeV/nucleon but then to decrease with increasing energy. It is noteworthy to point out that in terms of rigidity values, 2 GeV/nucleon corresponds to a rigidity value of about $\approx$ 4.2 GV for $^3He_2$ and $\approx$ 5.6 GV for $^4He_2$.

The left panel of Figure 5.2 indicates that the computed spectra are compatible to the observed spectra at all energies, while the right panel shows that this compatibility is lost when considering the corresponding ratios, which result in model computations falling progressively faster than observations above $\approx$ 3.4 GeV/nucleon. At these large energies, or rigidities, the effects of β on the DCs are eliminated for both isotopes, and therefore $^3He_2/\ ^4He_2$ ratio is indicative of the ratios of their LIS's. Adjusting diffusion or drifts may also improve the compatibility in this energy range but such specific adjustments were not required at all when comparing the same model with PAMELA proton observations in the previous chapter. Therefore, another option is to slightly modify the GALPROP LIS of $^3He_2$ above $\approx$ 3.4 GeV/nucleon as done next.

Overall, the LIS's of $^3He_2$ and $^4He_2$ obtained from the GALPROP model as described by Bisschoff et al. [2019] produces results that show reasonable compatibility with PAMELA observations at lower energies but at higher energies as suggested by AMS02, the LIS of $^3He_2$ needs to be adjusted for greater compatibility with observations. AMS02 ratios are used for this purpose because of their high kinetic energy/nucleon thresh-hold.

The left panel of Figure 5.3 shows the GALPROP $^3He_2$ LIS and the modified $^3He_2$ LIS as a function of kinetic energy/nucleon. The minor differences of the two LIS's at high energies can be noted, with the modified LIS slightly higher at these energies. The modified $^3He_2$ LIS is reproduced successfully by multiplying the GALPROP $^3He_2$ LIS by the function,

$$F(E) = \frac{a_1(E_1 - E) + a_2(E - E_{min})}{(E - E_{min})}, \tag{5.1}$$

where the dimensionless constants are a_1 =0.987, a_2 = 1.62 and E_1 = 17.7594, with E_{min} = 0.0046583 GeV and E_{max} = 46.3592 GeV. This modification of the LIS is appropriate to improve the model compatibility of the computed $^3He_2/^4He_2$ ratios with observations as shown in the right panel of Figure 5.3.

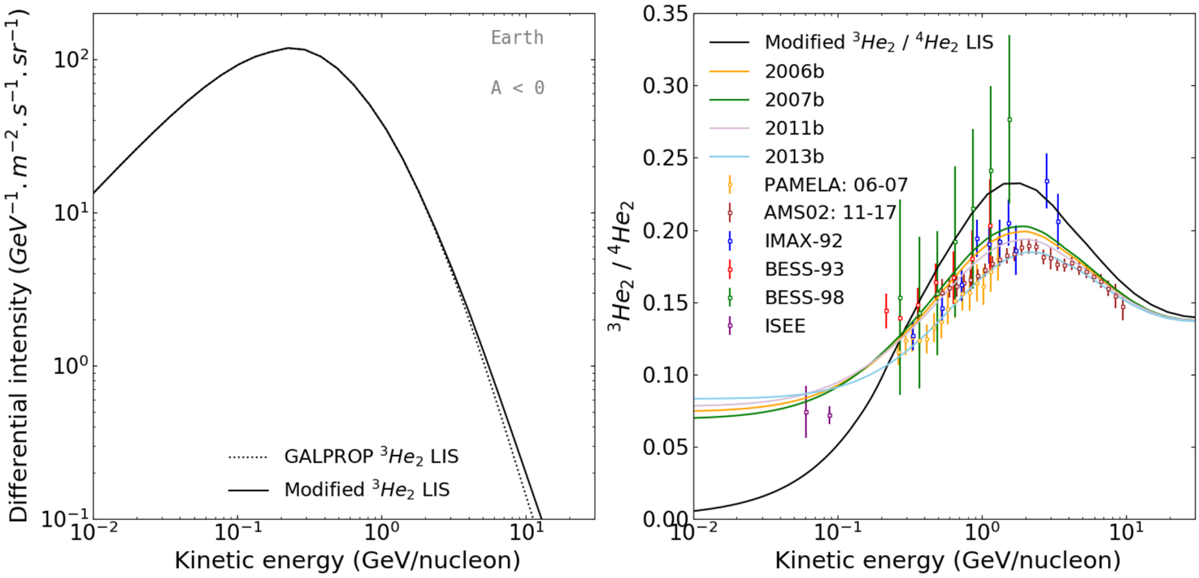

Figure 5.3: Left panel: The old (dotted line) and Modified (solid line) $^3He_2$ LIS's as a function of kinetic energy/nucleon. The right panel is similar to the right panel in Figure 5.2 but now showing the resulting computed $^3He_2$ / $^4He_2$ ratio from the modified LIS.

The approximate analytical expressions of the modified $^3He_2$ and $^4He_2$ LIS's used in this work are therefore respectively given as,

$$J_{^3He_2}(E) = \frac{29.5}{\beta^{2.1}} \left(\frac{E}{E_0}\right)^{2.085} \left(\frac{(E/E_0)^{1.105} + 0.553^{1.095}}{1 + 0.553^{1.09}}\right)^{-4.5}, \tag{5.2}$$

and

$$J_{^4He_2}(E) = \frac{130}{\beta^{2.3}} \left(\frac{E}{E_0}\right)^{1.33} \left(\frac{(E/E_0)^{0.9025} + 0.482^{0.84}}{1 + 0.482^{0.8}}\right)^{-4.51}, \tag{5.3}$$

where $J_{^3He_2}(E)$ and $J_{^4He_2}(E)$ are $^3He_2$ and $^4He_2$ LIS's, respectively, as a function of kinetic energy with units part.m^{2}s^{-1} sr^{-1} (GeV/nucleon)$^{-1}$ and E_0 = 1 GeV/nucleon.

5.3 Modeling $^3He_2$ and $^4He_2$ in the inner heliosphere

5.3.1 Modeling $^3He_2$ and $^4He_2$ spectra as a function of rigidity

Figure 5.4 illustrates the modulated $^3He_2$ (dotted lines) and $^4He_2$ (solid lines) spectra with respect to their LIS's as a function of rigidity from 2006 - 2009 and 2010 - 2013 together with their corresponding intensity ratios relative to 2006b and 2010b respectively; the time periods are according to what was shown in Figure 4.6. This figure particularly depicts the features

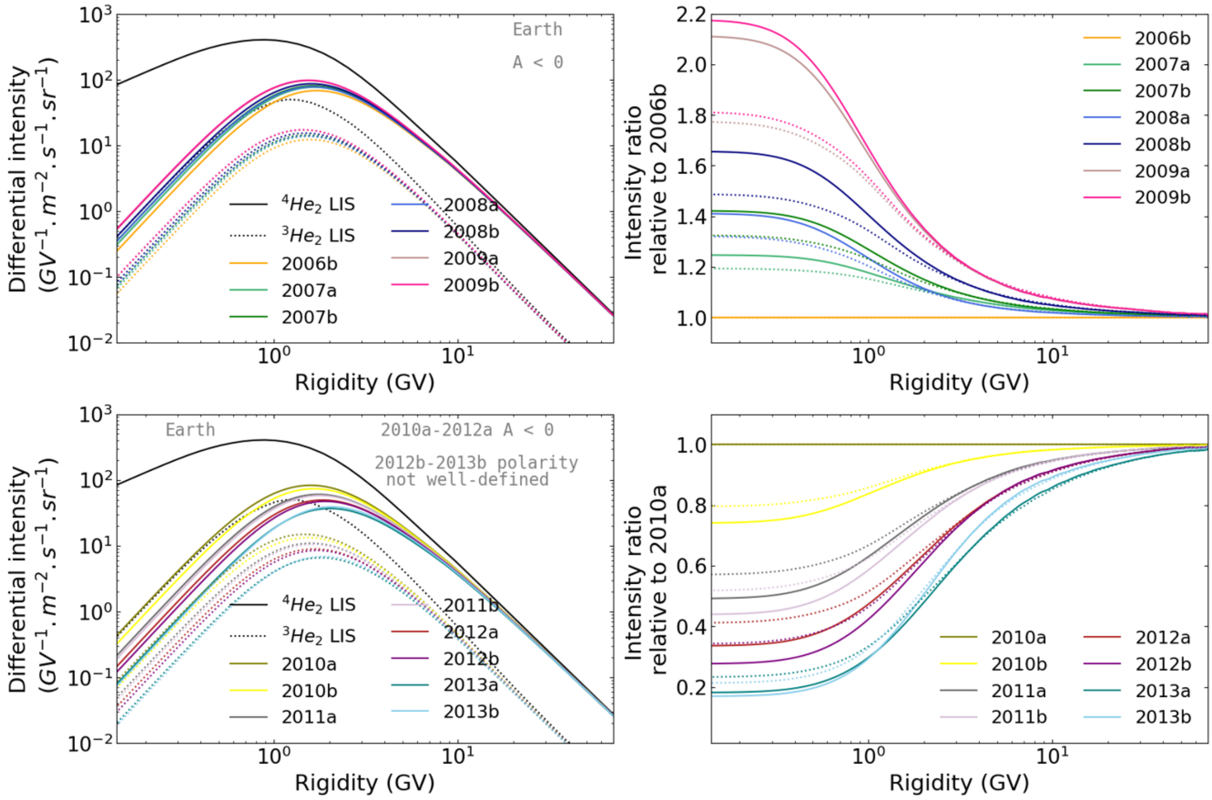

Figure 5.4: Left panel shows the LIS's for $^3He_2$ (black dotted line) and $^4He_2$(black solid line) together with the modulated differential intensity computed (coloured solid lines) as a function of rigidity at the Earth for the solar minimum period of 2006 to 2009 (top row) and from 2010 to 2013 (bottom row). Right panel shows the corresponding computed intensity ratios for $^3He_2$ (dotted lines) and $^4He_2$ (solid lines) relative to 2006b (top row) and 2010b (bottom row).

and characteristics of the modulated spectra at the Earth of species with different LIS's and A/Z. It can be seen from the left panel of this figure that apart from the large difference in the intensity levels of $^3He_2$ and $^4He_2$, the slopes of their LIS's are significantly different at low rigidities, also having spectral peaks at different rigidity values, i.e., ≈ 1.2 GV and ≈ 0.8 GV, respectively. These features greatly influence the difference in the total amount of He isotopes modulation between the HP and the Earth for a given rigidity range and also the shape of their modulated spectra at Earth. The modulated spectra for He isotopes exhibit in general a characteristic peak value for each species at a rigidity that is always higher than the rigidity of the peak in the LIS. These modulated peak values gradually decrease with increasing solar activity while shifting to higher rigidity values, and somewhat differently for $^3He_2$ and $^4He_2$, caused by the A/Z dependency of their DCs at these rigidities. The computed intensity peak in $^3He_2$ shifts from rigidity of ≈ 1.5 GV in 2009 to ≈ 2.0 GV in 2013, whereas that in $^4He_2$ shifts from ≈ 2.0 GV to ≈ 2.5 GV at the same time.

The right panel of Figure 5.4 shows how the computed intensities increased for both isotopes between 2006 and 2009 relative to 2006b and also decrease between 2010 and 2013 but relative to 2010b as function of rigidity. It is striking to note that for the same set of modulation parameters and diffusion coefficients, the $^4He_2$ computed intensities increased relatively more than $^3He_2$ below $\approx$ 3.0 GV as solar activity decreased from 2006 to 2009. Above this rigidity, the differences in relative increases are small to become negligible with increasing rigidity. While with increasing solar activity from 2010 to 2013, $^4He_2$ intensities decreased more than $^3He_2$ intensities at rigidities below $\approx$ 3.0 GV. This is a clear consequence of how adiabatic energy losses affect these He isotopes differently, with that of $^3He_2$ beginning at much higher rigidities. Evidently, the $^3He_2$ did not undergo similar spectral changes to that of $^4He_2$ from 2006 to 2009 and also from 2010 to 2013 at rigidities below $\approx$ 3.0 GV.

5.3.2 Modeling $^3He_2$ and $^4He_2$ spectra as a function of time

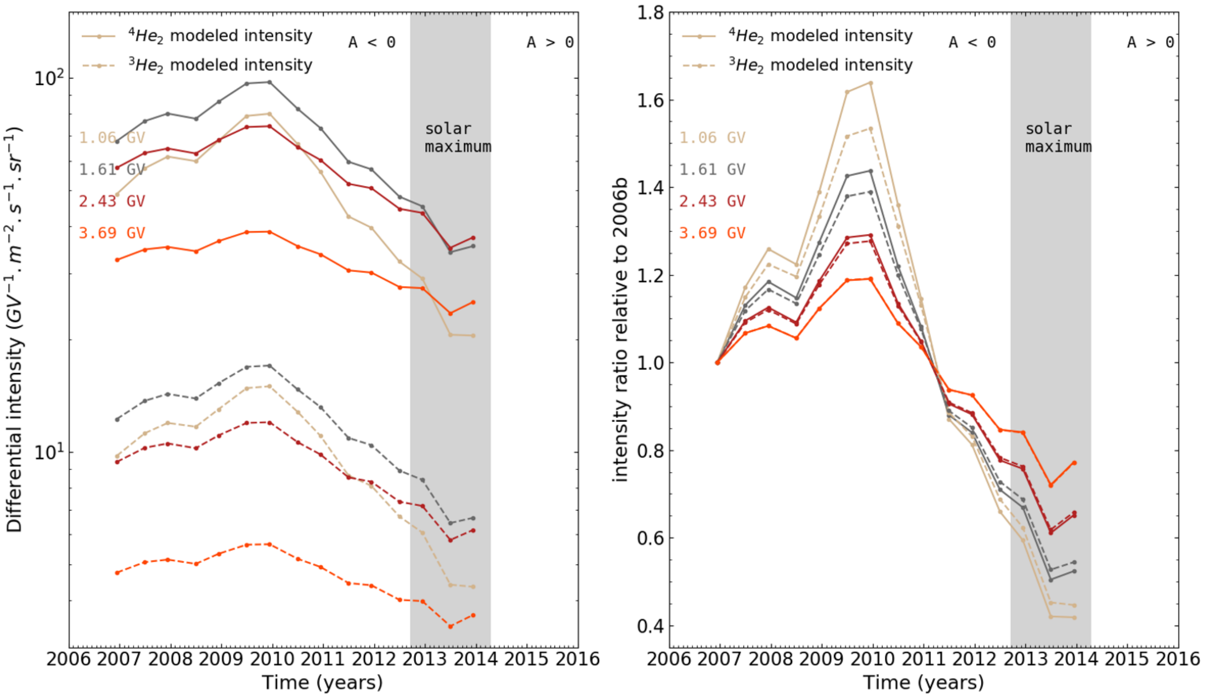

Figure 5.5: Computed $^3He_2$ (dashed-solid circle lines) and $^4He_2$ (solid circle lines) intensities as a function of time (left panel) at rigidities ranging from 1.06 GV to 3.69 GV together with the corresponding intensity ratios relative to 2006b (right panel). Also indicated is the A $<$ 0 and A $>$ 0 polarity epochs before and after the period of maximum solar activity.

Figure 5.5 displays the quantitative and qualitative time-dependent modulation of the computed $^3He_2$ and $^4He_2$ spectra at rigidity values between 1.06 GV and 3.69 GV. The corresponding intensity ratios relative to 2006b are shown in the right panel. It follows from this figure that for the displayed time scale the computed $^3He_2$ and $^4He_2$ intensities show nearly identical time dependence and relative variations in amplitude. After 2009, both $^3He_2$ and $^4He_2$ intensities started decreasing in response to increasing solar activity levels, to reach minimum values during solar maximum activity. However, a closer inspection, as displayed in the right panel of this figure, reveals that at rigidities lower than ≈ 3.69 GV, ${}^4He_2$ computed intensities changed more than that of ${}^3He_2$ with time relative to 2006b, more so the lower the rigidity as already mentioned. What is also of interest is that above this rigidity both He isotopes display the same time variation relative to 2006b. Consequently, the ${}^3He_2$ to ${}^4He_2$ ratios are expected to display interesting time dependences at lower rigidities that differ from those at higher rigidities. This issue is pursued next.

5.4 The ratio of ${}^3He_2$ to ${}^4He_2$

5.4.1 The ratio of helium isotopes as a function of rigidity

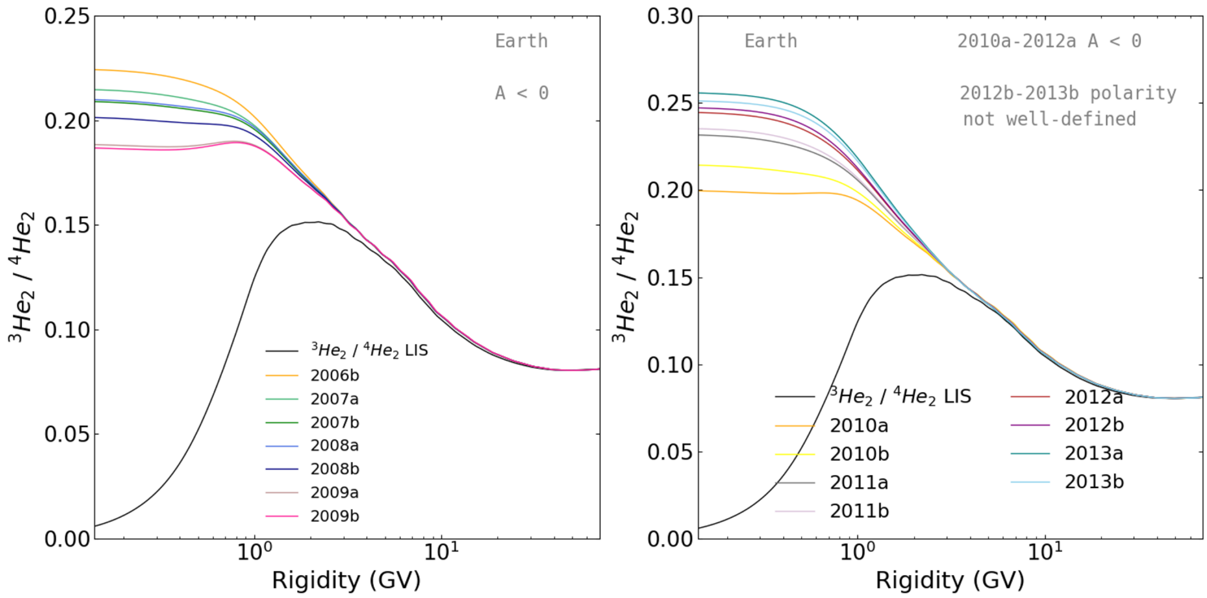

Figure 5.6: The computed intensity and LIS ratios of ${}^3He_2/{}^4He_2$ as a function of rigidity from 2006-2009 (left panel) and 2010-2013 (right panel).

Despite the importance of the rigidity and time dependence of ${}^3He_2$ and ${}^4He_2$ intensities below ≈ 2 GV as pointed out by Aguilar et al. [2019], neither their absolute fluxes nor their ratio is available as a function of rigidity at these low rigidities for comparison with numerical model calculations. However, progress is being made in this regard, as can be seen in a recent report by Lenni et al. [2021]. Therefore, the numerical modelling of ${}^3He_2/{}^4He_2$ ratio plays an essential role in understanding its rigidity and time dependence below 2 GV and what to be expected from when PAMELA observations at these rigidities are published.

Figure 5.6 illustrates the computed ${}^3He_2/{}^4He_2$ ratios from 2006 to 2009 (left panel) and from 2010 to 2013 (right panel) at the Earth relative to the ratio of their corresponding LIS's as a function of rigidity. The numerical computations predict significant time dependences of this ratio below ≈ 2 GV but to become time independent above ≈ 3 GV. It can be seen from the left panel that this ratio decreases significantly from 2006 to 2009 at these low rigidities with decreasing solar activity. However, starting from 2010 the $^3He_2/^4He_2$ ratio below 2 GV increases significantly, responding to increasing solar activity, and reaches its maximum value in 2013 during solar maximum period. Between 3 GV and 20 GV the rigidity dependence of the computed ratio is characterized by what can be described as a single rigidity power law dependence. This rigidity power law at this rigidity range has already been revealed by AMS02 measurements with good statistics (Aguilar et al. [2019]). Next the model prediction of the time variation of $^3He_2/^4He_2$ ratio at different rigidities is illustrated from the solar minimum of 2006 to 2009 up to solar maximum activity.

5.4.2 The ratio of helium isotopes as a function of time

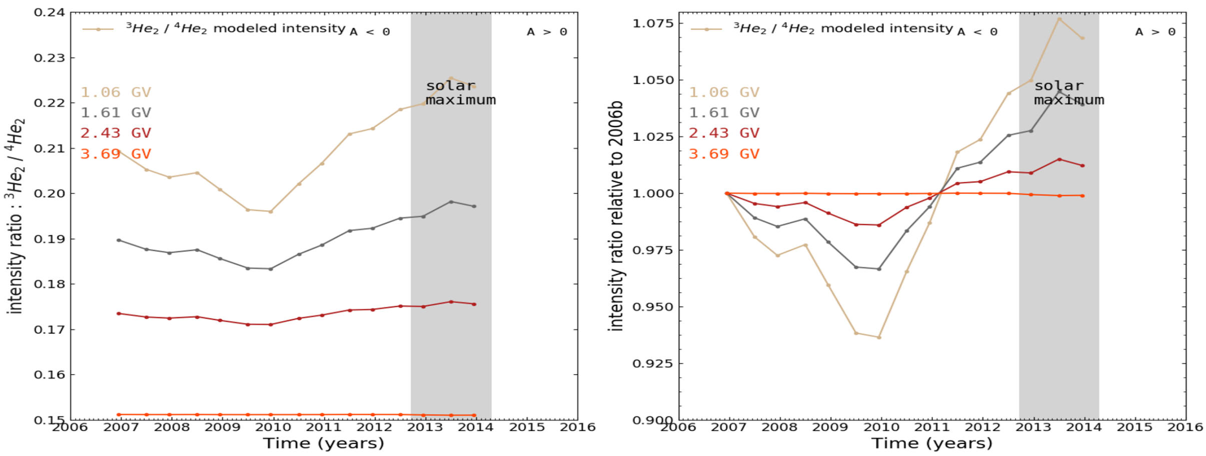

Figure 5.7: The computed intensity ratios of $^3He_2/^4He_2$ as a function of time at four selected rigidities ranging from 1.06 GV to 3.69 GV (left) together with their corresponding ratios relative to 2006b (right).

Figure 5.7 depicts the computed $^3He_2/^4He_2$ ratio as a function of time at rigidities between 1.06 GV and 3.69 GV together with their corresponding ratios relative to 2006b. It can be clearly seen from this figure that this model predicts significant time dependences of $^3He_2/^4He_2$ ratios at lower rigidities. Taking Figures 5.5 and 5.7 together, the computed $^3He_2/^4He_2$ ratio below $\approx$ 3 GV correlates with solar activity, i.e., it increases and decreases with solar activity. At these rigidities, this ratio reaches its minimum value during the end of 2009 when solar activity decreased to its lowest level since the beginning of the space exploration era (see Boezio et al. [2017] and references therein). After the end of 2009, it recovers to reach maximum values around 2013 during solar maximum. This interesting feature in the time trend of $^3He_2/^4He_2$ ratio is predicted to disappear at high rigidities, for example at rigidity 3.69 GV, causing the ratio to remain almost constant with time as solar activity increases. This aspect is clearly highlighted on the right panel of this figure when the ratio is depicted as a function of time relative to its value in 2006b. What is shown in Figure 5.7 clearly indicates that the lower the rigidity

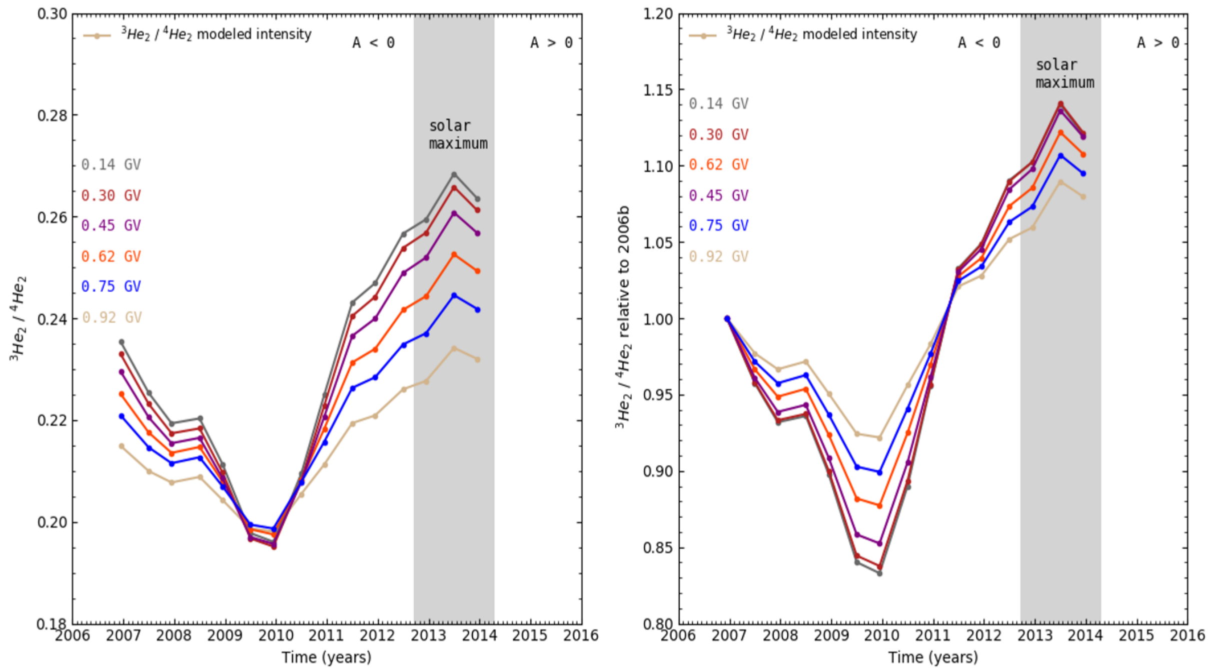

Figure 5.8: Similar to Figure 5.7 but now showing the computed $^3He_2/^4He_2$ ratios as a function of time at six selected rigidities ranging from 0.14 GV to 0.92 GV(left) together with their corresponding ratios relative to 2006b (right).

the larger the variation in $^3He_2/^4He_2$ at the Earth with solar activity.

Figure 5.8 depicts the time-dependence of the ratio of $^3He_2/^4He_2$, similarly to what is shown in Figure 5.7, but at rigidities below 1.0 GV. Clearly, the time trend in the predicted $^3He_2/^4He_2$ ratio noted in Figure 5.7 continues to the smallest rigidity value, P = 0.14 GV, under consideration in this study.

The discussions in Section 5.4, and the subsequent subsections, indicate that the modeling effects of $^3He_2$ may be small compared to $^4He_2$ when considering the differential intensities, but not negligible when $^3He_2/^4He_2$, and consequently proton to He ratios are considered. In the next section, the total He modeling is studied with the objective to reproduce PAMELA He spectra observed between 2006 and 2013.

5.5 Modulation of total He

5.5.1 PAMELA total He spectra

Figure 5.9 shows the total He spectra (left panel) measured by PAMELA from 2006 to 2013 together with the corresponding ratios (right panel) relative to 2006b (top panel) and 2010b (bottom panel) as a function of rigidity. These spectra as a function of rigidity are observed from $\approx$ 0.92 GV to $\approx$ 43 GV, covering the rigidity range as observed for protons. The PAMELA

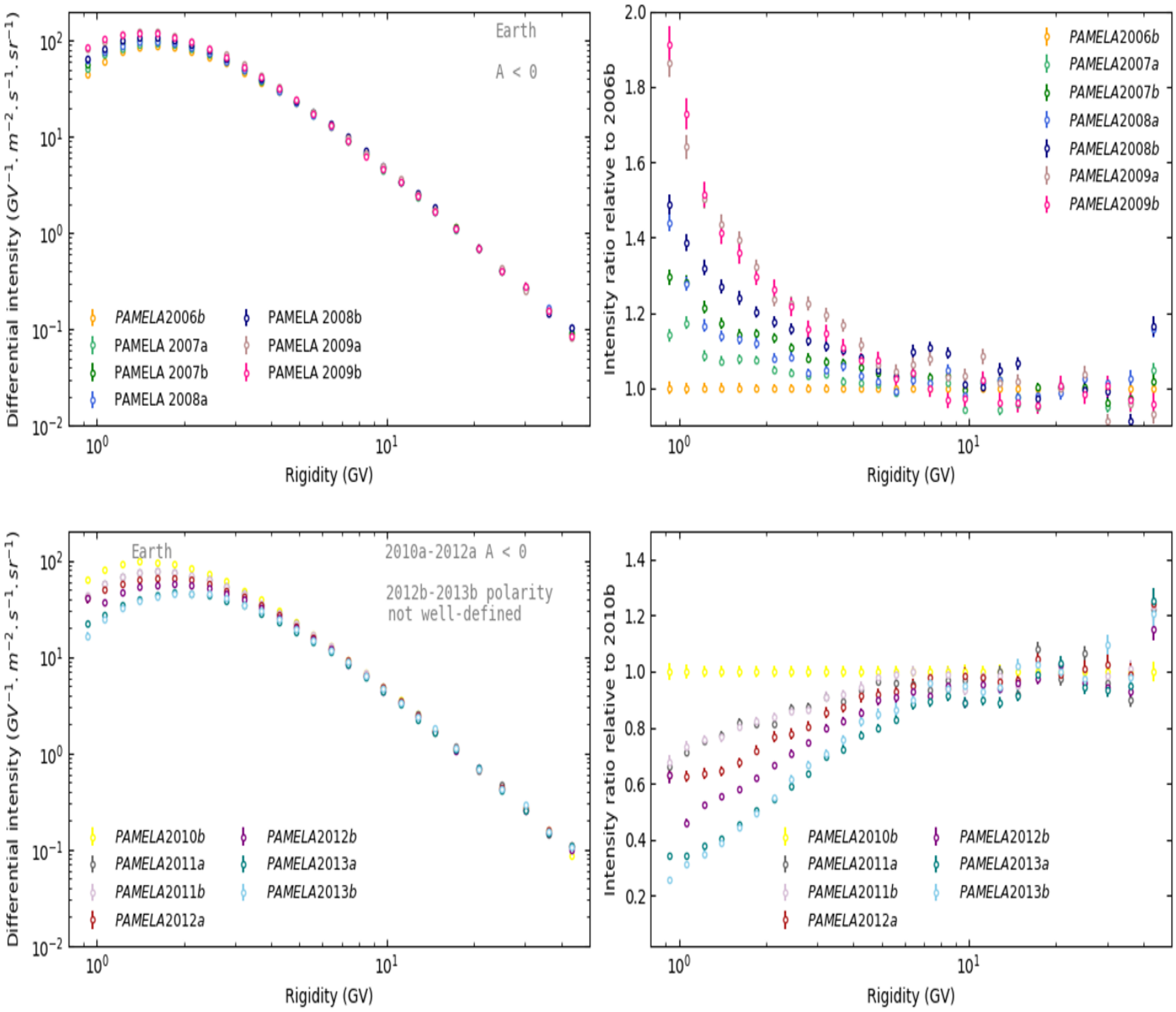

Figure 5.9: left panel: 27-Day averaged PAMELA helium energy spectra observed between December 2006 to September 2009 (top panel) and between December 2010 to December 2013 (bottom panel) as a function of rigidity. Right panel: The corresponding intensity ratios relative to December 2006 (top panel) and December 2010 (bottom panel). The spectra in the top panel observed at Earth during the A<0 solar minimum are taken from Marcelli et al. [2020], while those in the bottom panel observed during increasing solar activity are taken from Marcelli et al. [2022].

He spectra used in this study are taken from Marcelli et al. [2020, 2022] for periods from 2006 to 2009 and 2010 to 2013, respectively. It is clearly illustrated in the right panel of this figure that He intensities measured at 0.92 GV increased by a factor $\approx$ 1.98 between 2006 and 2009, whereas between 2010 and 2013 these intensities decreased by $\approx 78\%$. Similarly, to what has been observed for protons, larger increases (from 2006-2009) and decreases (from 2010-2013) in intensities are experienced by lower rigidity particles, whereas this features become less pronounce at rigidities above $\approx$ 10 GV with little to no modulation observed above $\approx$ 30 GV. The observed ratios relative to both 2006b and 2010b approach a single value at rigidities above 20 GV. As expected from modulation theory, the observed helium spectra display similar quali-

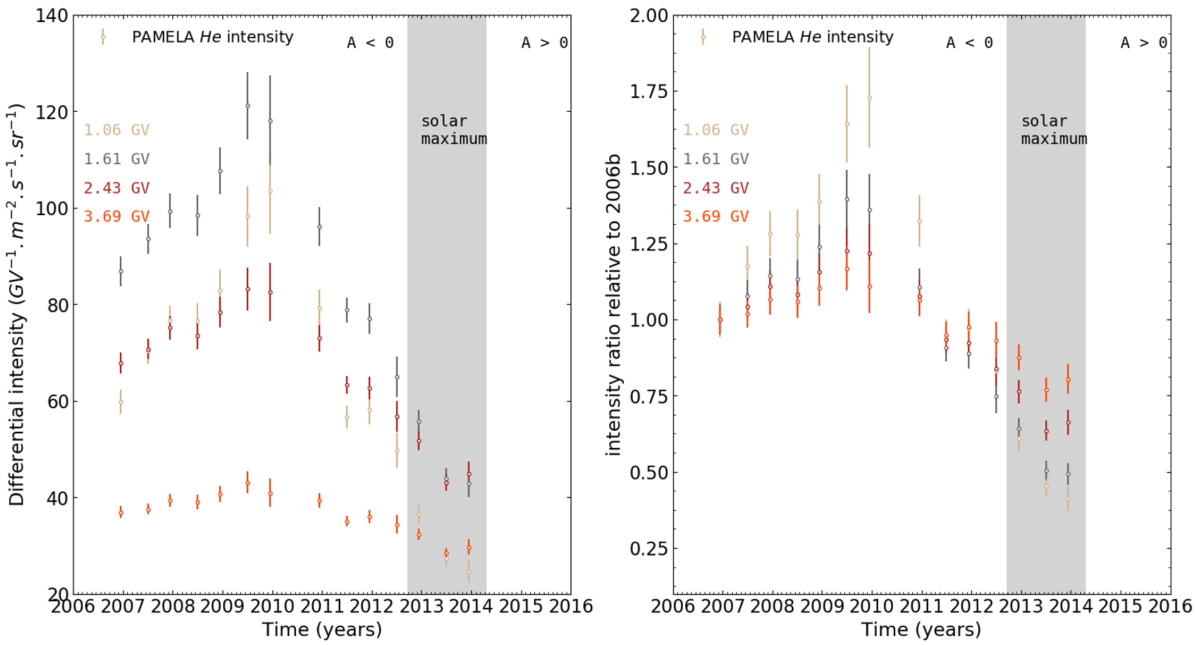

Figure 5.10: GCR helium observed by PAMELA at rigidities ranging from 1.06 GV to 3.69 GV indicated by different colored open circles (left panel) and the corresponding intensity ratios relative to 2006b (right panel) as a function of time.

tative modulation characteristics to those experienced by protons; hence there is no merit in repeating what has already been mentioned. It suffice to mention that the rigidity dependence of the spectral fall is more pronounced in proton observations than for He.

To emphasize the time-dependent modulation of GCR He observed by PAMELA, Figure 5.10 shows these intensities and normalized intensity ratios relative to 2006b as a function of time at four different rigidities. This figure displays what has already been mentioned, lower rigidity He have the highest increase in intensities relative to 2006b during solar minimum conditions compared to higher rigidities, whereas their intensities decrease faster towards solar maximum activity conditions similar to protons.

5.5.2 Modeling total He spectra

5.5.2.1 Total He LIS

To improve on the detailed reproduction of the precise observations of $^3He_2/^4He_2$ ratios, it is shown in Section 5.2 that a modest adjustment of the GALPROP $^3He_2$ LIS is required at higher rigidities. In this section the total He LIS is derived by adding the GALPROP adjusted LIS's of $^3He_2$ and $^4He_2$ established in Section 5.2, with the requirement that the sum of the two gives reasonable compatibility to V1 (Stone et al. [2013], Cummings et al. [2016]) and PAMELA (Marcelli et al. [2020]) observations at lower and higher rigidities, respectively.

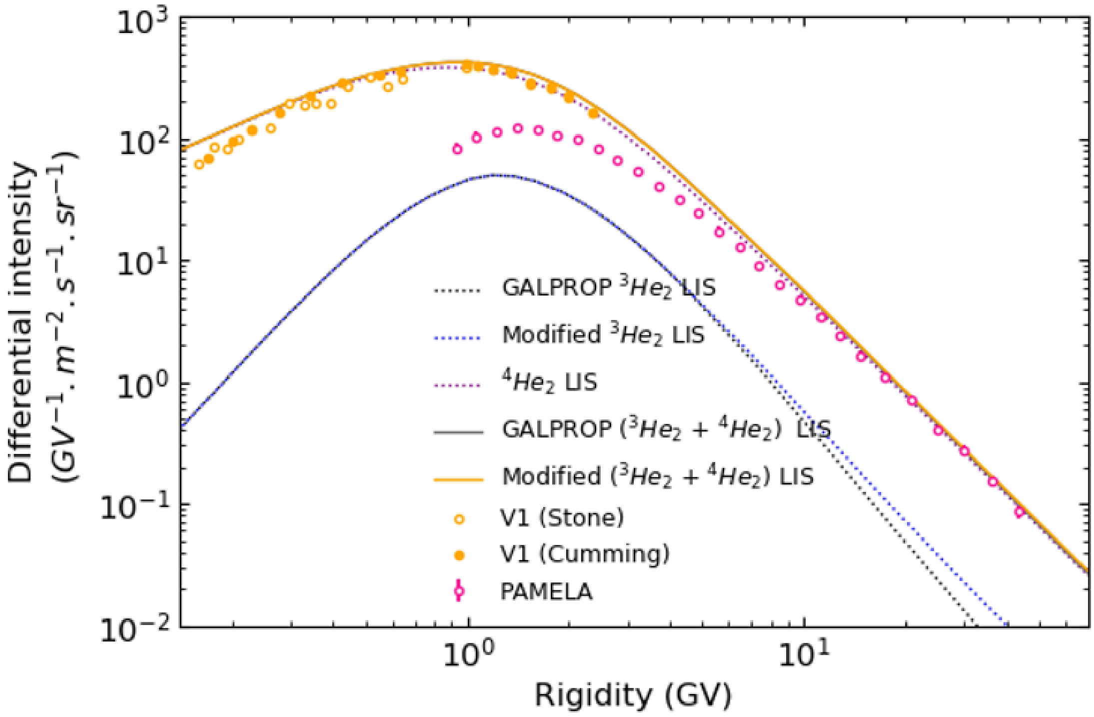

Figure 5.11: The old (dotted black line) and modified (dotted blue lines) computed $^{3}He_2$ LIS's, $^{4}He_2$ (dotted purple lines) together with the total old (solid gray line) and modified (solid yellow line) He compared to V1 observations indicated as open yellow circles from Stone et al. [2013]; closed yellow circles from Cummings et al. [2016] and PAMELA observations at the Earth during 2009b; open pink circles from Marcelli et al. [2020]. The addition of $^{3}He_2$ and $^{4}He_2$ LIS's produces the total He LIS.

Figure 5.11 depicts five LIS's, one each for $^{3}He_2$ and $^{4}He_2$ computed with GALPROP as described by Bisschoff et al. [2019], the modified $^{3}He_2$ LIS, and the corresponding GALRPROP and modified LIS's derived for total He. The total He LIS's are in comparison with V1 observations taken beyond the HP at low rigidities (Stone et al. [2013], Cummings et al. [2016]) and with PAMELA observations at high rigidities for He at the Earth taken during maximum intensity period in 2009b (Marcelli et al. [2020]). Evidently, the LIS's for He closely matches the V1 and PAMELA observations. The effects of $^{3}He_2$ LIS appear small but not negligible when considering the ratios of LIS's. This is highlighted in Figure 5.12 where the five LIS are now shown as a function of kinetic energy/nucleon together with the ratios of $^{3}He_2/^{4}He_2$ and $^{3}He_2/He$, quantitatively illustrating the contribution of ^{3}He to total He LIS. As spectra, the contribution of $^{3}He_2$ to total He appear negligible as shown in the left panel. However, the right panel of Figure 5.12, which depicts this contribution as ratios of LIS's, illustrates that the contribution of $^{3}He_2$ to total He increases with increasing energy to reach a maximum value of $\approx$18% at kinetic energies between 1-2 GeV/nucleon. Above these energies the contribution of $^{3}He_2$ to total He decreases appreciable with increasing energy. This indicates that to properly

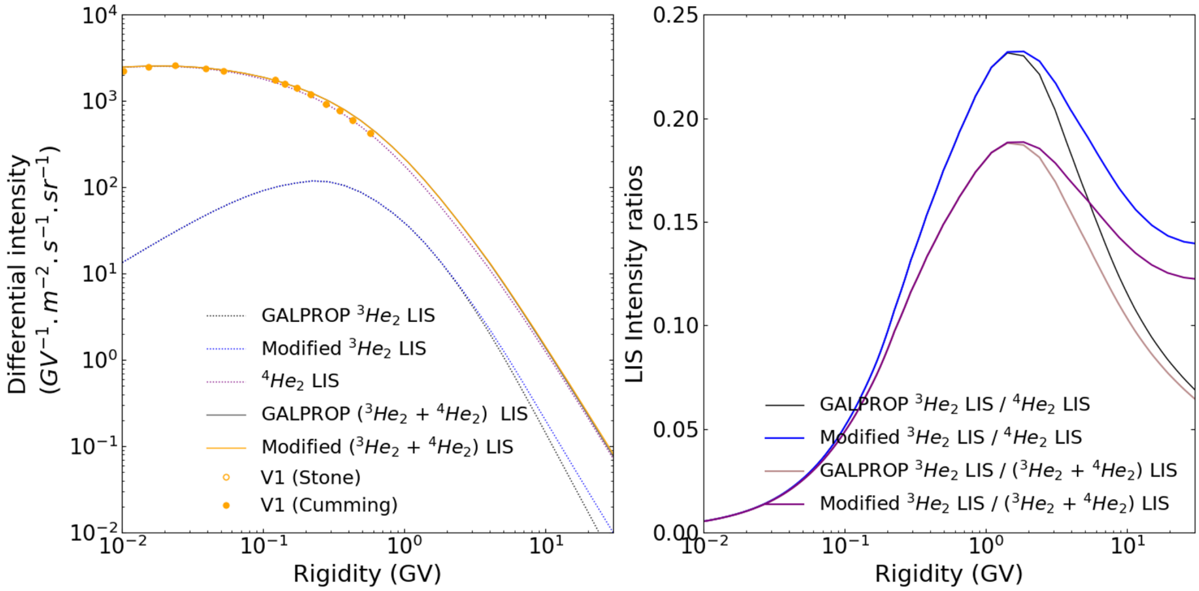

Figure 5.12: Similar to Figure 5.11 but now showing only the LIS's of total He and its two isotopes compared to V1 (Stone et al. [2013], Cummings et al. [2016]) as a function of kinetic energy/nucleon (left panel) together with their corresponding intensity ratios (right panel).

model the total He effects, the modeling effects of $^3He_2$ can not simply be neglected, especially when studying P/He and $^3He_2/^4He_2$ ratios simultaneously.

5.5.2.2 Computed He Spectra compared to PAMELA observations

The left panel of Figure 5.13 shows the computed He rigidity spectra in comparison with the PAMELA observations from 2006 to 2013 together with the corresponding ratios relative to 2006b (top) and 2010b (bottom) given on the right panel. It can be seen in the left panel of this figure that the numerical model successfully reproduces the observed characteristic peak in each spectra around 2 GV, which somewhat shifts to higher rigidities with increasing solar activity. For example, in 2009b the peak is observed at $\approx$ 1.6 GV, whereas in 2013b the peak occurs at $\approx$ 2.4 GV. The model also reproduces intensity ratios relative to 2006b and 2010b quite convincingly as illustrated in the right panel of Figure 5.13. It is further noted that the relative intensity ratios increase of a factor $\approx$ 1.8 between 2006 and 2009, and the corresponding decrease of up to 78% at 1 GV can be reasonably reproduced by the numerical model. However, for rigidities $>$ 20 GV the computed relative intensity ratios converge to a single value similar to observations. The modeled ratio relative to 2006b increases significantly with decreasing rigidity below $P \approx$ 20 GV, whereas relative to 2010b decreases with decreasing rigidity. It is evident from this figure that the model successfully reproduces the PAMELA He spectra from 2006 to 2013 using the same modulation parameters, diffusion and drift coefficients as used for protons. Furthermore, it is also worth noting that the modeled ratios gradually become

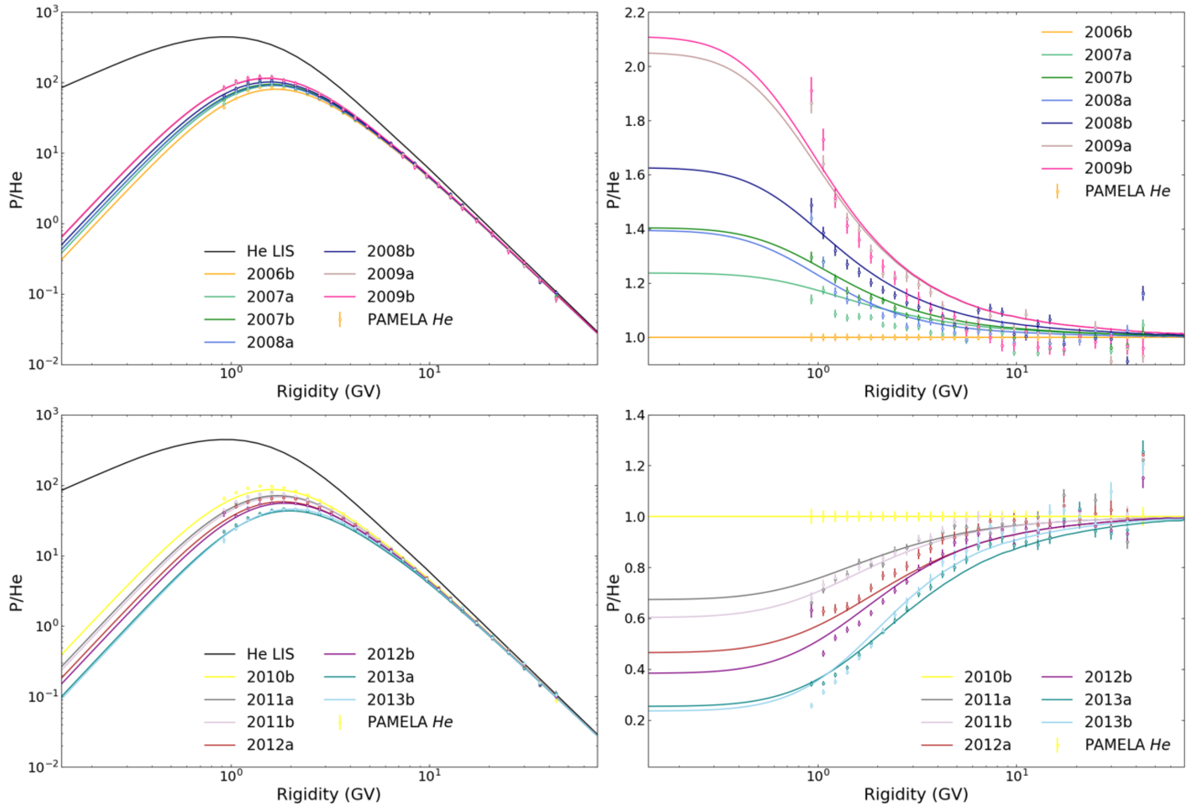

Figure 5.13: Total He spectra derived from the addition of the computed spectra in Figure 5.4 compared to PAMELA observations (left) together with the corresponding ratios (right) relative to 2006b (top) and 2010b (bottom).

flatter and move towards steady values at lower rigidities from 2006 to 2013, indicating that the modulation differences between 2006 and 2009, and also 2010 to 2013 levels off.

Figure 5.14 shows the computed He intensities at four selected rigidity values as a function of time overlaid with PAMELA observations shown in Figure 5.10. It is noted from the left panel of this figure that He exhibits a time-profile that is nearly identical to that computed for $^3He_2$ and $^4He_2$ shown in Figure 5.5 but with relative variations in amplitude, this shows that despite the amplitude variations at lower rigidities, He intensities at higher rigidities recovered earlier than those at lower rigidities, an aspect that has also been shown in Figure 5.5. The right panel of Figure 5.14 highlights the fact that the modeling of He done in this study reasonably reproduces the time variation in the PAMELA He observation relative to 2006b at different rigidities. Therefore, the modeling studies done in this chapter revealed that the modeling effects of $^4He_2$ alone are not adequate to represent the total He modeling for comparison with observations. Neglecting the modeling effects of $^3He_2$ become severe particularly when simultaneously studying $^3He_2/^4He_2$, P/He, $^4He_2/He$ and $^3He_2/He$ ratios.

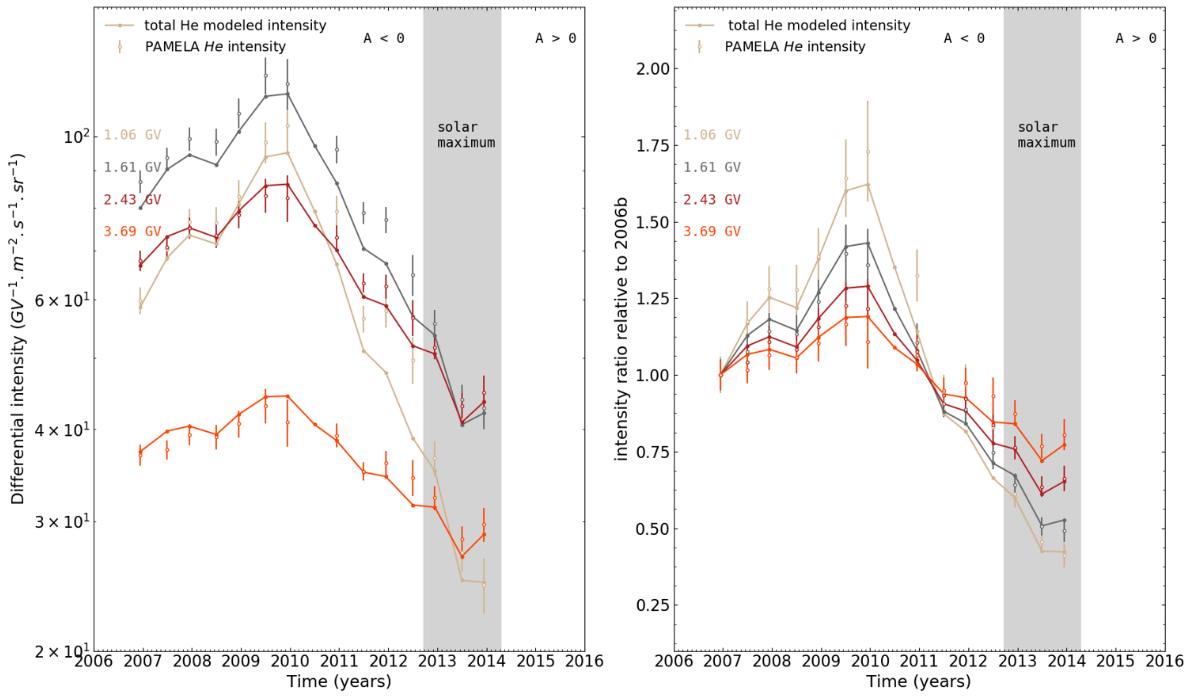

Figure 5.14: Total He as a function of time compared to PAMELA observations at rigidities between 1.06 GV and 3.69 GV (left panel) together with the corresponding ratios relative to 2006b (right panel).

5.6 Summary and conclusion

This chapter was focused on reproducing the total helium (He) spectra observed by PAMELA at the same period as protons. This was done with the same set of modulation parameters, diffusion and drift coefficients that were used to reproduce PAMELA proton observations in Chapter 4, with the only differences remaining their LIS and A/Z. Because total He has two isotopes, the modeling of these isotopes were done separately using their different LIS's as described by Bisschoff et al. [2019] but slightly modified at higher rigidities to match AMS02 ${}^3He_2/{}^4He_2$ ratios from Aguilar et al. [2019]. The modification was successfully carried out by multiplying the GALPROP ${}^3He_2$ LIS by the function given in Equation (5.1). The approximate parameterized expressions of the LIS's of both ${}^3He_2$ and ${}^4He_2$ are given as a function of kinetic energy/nucleon in Equations (5.2) and (5.3), respectively. Comparing the computed intensities of ${}^3He_2$ and ${}^4He_2$, it was established that at lower rigidities ${}^4He_2$ intensities responds more to solar activity changes than ${}^3He_2$. This is a clear consequence of how adiabatic energy losses affect these species differently, with that of ${}^3He_2$ beginning at much higher rigidities. Consequently, ${}^3He_2$ did not undergo similar spectral changes to that of ${}^4He_2$ from 2006 to 2009 and also from 2010 to 2013 at rigidities below 3.0 GV. This result in the ${}^3He_2/{}^4He_2$ ratio at these rigidities to correlate with solar activity, such that it reaches minimum values during solar minimum conditions and maximum values during solar maximum.

To obtain the numerical modulation of total He for comparison with PAMELA He observations, the computed spectra of the two helium isotopes are summed up together as shown and discussed in Figure 5.14. This figure tests the generality of the assumed transport coefficients, and reveals that indeed the numerical model reproduces PAMELA He observations reasonably well using the same set of modulation parameters that were used for protons. This is taken as an indication that GRC protons and He are not modulated differently inside the heliosphere, an aspect that has already been pointed out by Ngobeni et al. [2020]. Furthermore, this figure indicates that to properly model the total He effects in the heliosphere, the modeling effects of $^3He_2$ cannot simply be neglected, especially when studying proton to He and $^3He_2/^4He_2$ ratios simultaneously.

The next chapter focuses on effectively studying the P/He ratio observed by PAMELA detector both as a function of time and rigidity.

Chapter 6

Simultaneous modulation of galactic proton and helium isotopes

6.1 Introduction

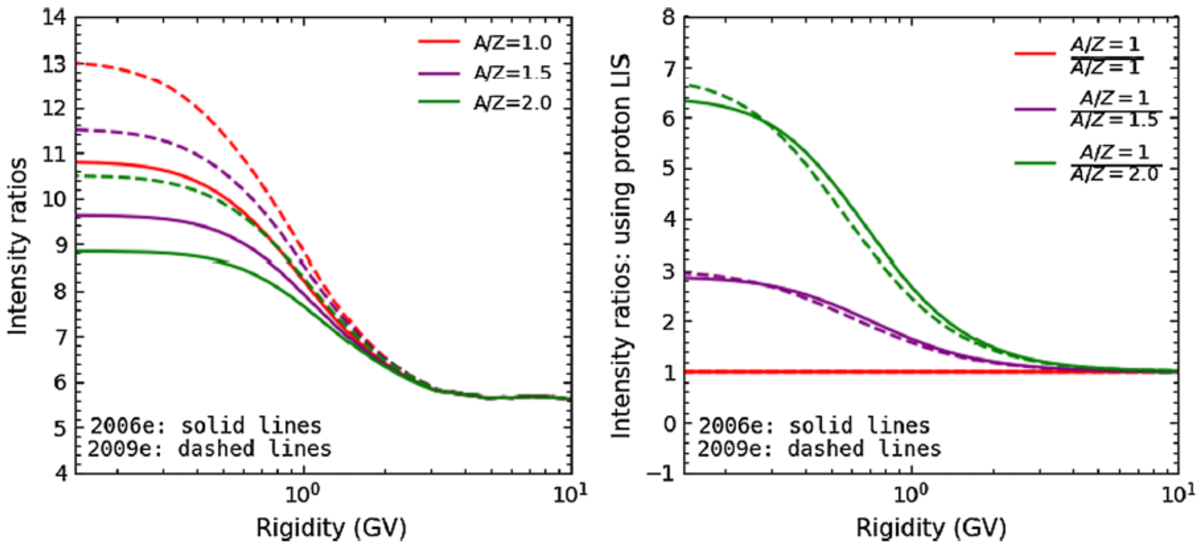

Figure 6.1: The computed intensity ratios based on different LIS's and A/Z values. The left panel shows the ratio of intensities, obtained with respect to their corresponding proton and $^4He_2$ LIS's specified at the HP, as a function of rigidity between 2006e (solid lines) and 2009e (dashed lines). (2006e and 2009e respectively corresponds to 2006b and 2009b in this work.) Three sets of ratios are shown: $A/Z = 1.0$ (red lines); second with $A/Z = 1.5$ (purple lines) and then with $A/Z = 2.0$ (green lines) are specified for both species to highlight the LIS contribution to the intensity ratio. In the right panel three sets of computed intensity ratios now obtained with the same exact proton LIS are plotted as a function of rigidity; red lines for spectra obtained with $A/Z = 1.0/A/Z = 1.0$; purple lines with $A/Z = 1.0/A/Z = 1.5$; green lines with $A/Z = 1.0/A/Z = 2.0$ to highlight the A/Z contribution to the intensity ratios. Again solid lines represent modulation conditions in 2006e and dashed lines in 2009e. Adapted from Ngobeni et al. [2020].

The P/He ratios has been a matter of active debate in solar modulation studies since Aguilar et al. [2018], using AMS02 observations, reported that it is not constant as a function of time at rigidities below 3 GV. This was followed up by the numerical computation of the time-dependence of the P/He first done by Corti et al. [2019] and more recently in more details by Ngobeni et al. [2020] and Song et al. [2021a, 2021b]. These studies established that the cause(s) of the non-constant ratio at lower rigidities is due to differences in their LIS's and A/Z.

Figure 6.1 illustrates the simulated effects on the intensity ratios of two CR species caused by differences in their LIS's (left panel) as compared to those due to differences in their A/Z (right panel) between 2006 and 2009. In the left panel both species assume their corresponding LIS's but have the same A/Z values, whereas in the right panel both species assume the same exact LIS but have different A/Z values. Separating these effects this way is indeed only possible with numerical modeling, and it is thus for illustrative purposes predicting maximum effects on intensity ratios. However, it can be clearly noted that the simulated effects on the intensity ratios caused by the differences in their LIS's and A/Z values are more pronounced at rigidity below 4 GV. Above this rigidity differences in intensity ratios due to both the LIS and A/Z are smeared out. Overall, Figure 6.1 illustrates that the predicted effects on P/He due to differences in their LIS's are dominant at all rigidities but those due to differences in their A/Z values are becoming increasingly noteworthy the lower the rigidity. For a detailed discussion on Figure 6.1 and the concept therein, see Ngobeni et al. [2020].

In this chapter, the global features of the modulation of GCR protons (P) and helium nuclei are studied simultaneously from solar minimum to maximum activity. (In the previous chapters the symbol P was used for rigidity but in this chapter it will refer to protons.) This is done more accurately with the accurate LIS's for both P and helium nuclei established in the previous chapters, and thus providing a unique opportunity to study in detail how differently CR species with dissimilar A/Z are modulated down to a few GV. Additionally, the computed results are used to understand how exactly the P/He ratio change with rigidity and time, together with the corresponding ratios $P/^3He_2$ and $P/^4He_2$. The end result of this chapter is the detailed reproduction of P/He ratio measured by PAMELA from 2006 to 2013, displaying both qualitative and quantitative agreement with the main observed features. The model predictions of this ratio are also extended to lower rigidities where PAMELA observations are unavailable.

6.2 The LIS's of proton, total He, $^3He_2$ and $^4He_2$

The left panel of Figure 6.2 depicts the computed P LIS (solid line) in comparison to $^4He_2$ (dashed line), $^3He_2$ (dashed-dotted) and the total He (dotted line) LIS's as a function of rigidity from 30 GV down to 0.14 GV. It can be noted from this panel that apart from the large difference in intensity levels between P and He LIS, their slopes are also different at low rigidities and also have spectral peaks at different rigidity values. For example, P peaks at 0.8 GV, whereas He peaks at 1.2 GV. These features greatly influence the difference in the total amount

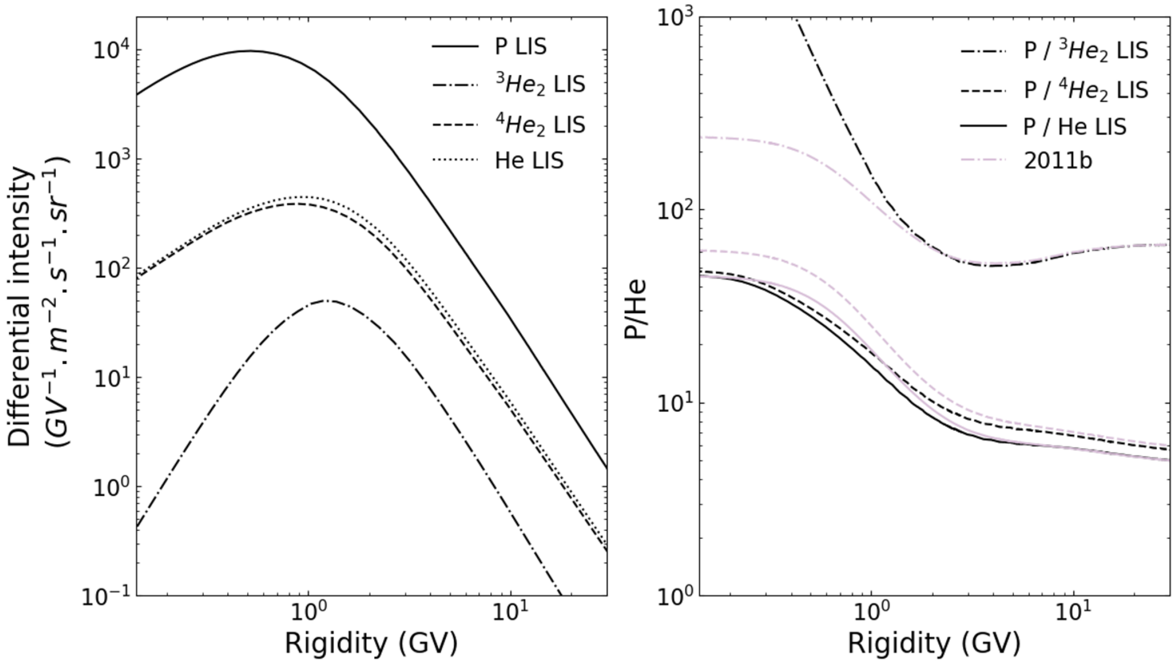

Figure 6.2: Left panel: The computed proton (P) (solid line), $^3He_2$ (dashed-dotted lines), $^4He_2$ (dashed lines) and total He (dotted lines) LIS's as a function of rigidity. Right panel: The corresponding ratios of the LIS's with respect to the proton LIS (black lines) and the modulated ratios for 2011b at 1 AU (grey lines).

of modulation at the Earth between these species for a given rigidity range and also the shape of their modulated spectra. For more on the procedure for determining the LIS's of various GCR species see Bisschoff et al. [2021] and Potgieter et al. [2021]. What is also of interest in the left panel is the visible contribution of $^3He_2$ to the total He at different rigidities, clearly subsiding with decreasing rigidity below 0.3 GV.

The right panel of Figure 6.2 emphasizes the difference between these LIS's by displaying the corresponding ratio of each of these helium nuclei LIS's with respect to P LIS together with the modulated ratio at the Earth as a function of rigidity. When comparing $P/^3He_2$ and $P/^4He_2$, it follows that $P/^3He_2$ reaches a local minimum around $\approx$ 3 GV, whereas for $P/^4He_2$ such minimum is not evident. Therefore, this indicates that above 3 GV the LIS for P increased relatively more than that of $^3He_2$ with increasing rigidity, while at the same rigidity decreasing relatively more than $^4He_2$ LIS. This aspect has been discussed in detail in Ngobeni et al. [2020] and may reveal interesting information about the propagation of these nuclei in the interstellar medium. It is also interesting to note that the contribution of $^3He_2$ to the total He increases the differences between the modulated $P/^4He_2$ and P/He at the Earth at rigidity below $\approx$ 4 GV when compared to their LIS ratios. As already mentioned, this indicates further that separating the modeling effects of both He isotopes is important in explaining simultaneously the $^3He_2/^4He_2$ and P/He ratios.

6.3 Simultaneous modulation of P and He nuclei

6.3.1 Computed P LIS, $^3He_2$, $^4He_2$ and total He spectra as a function of rigidity

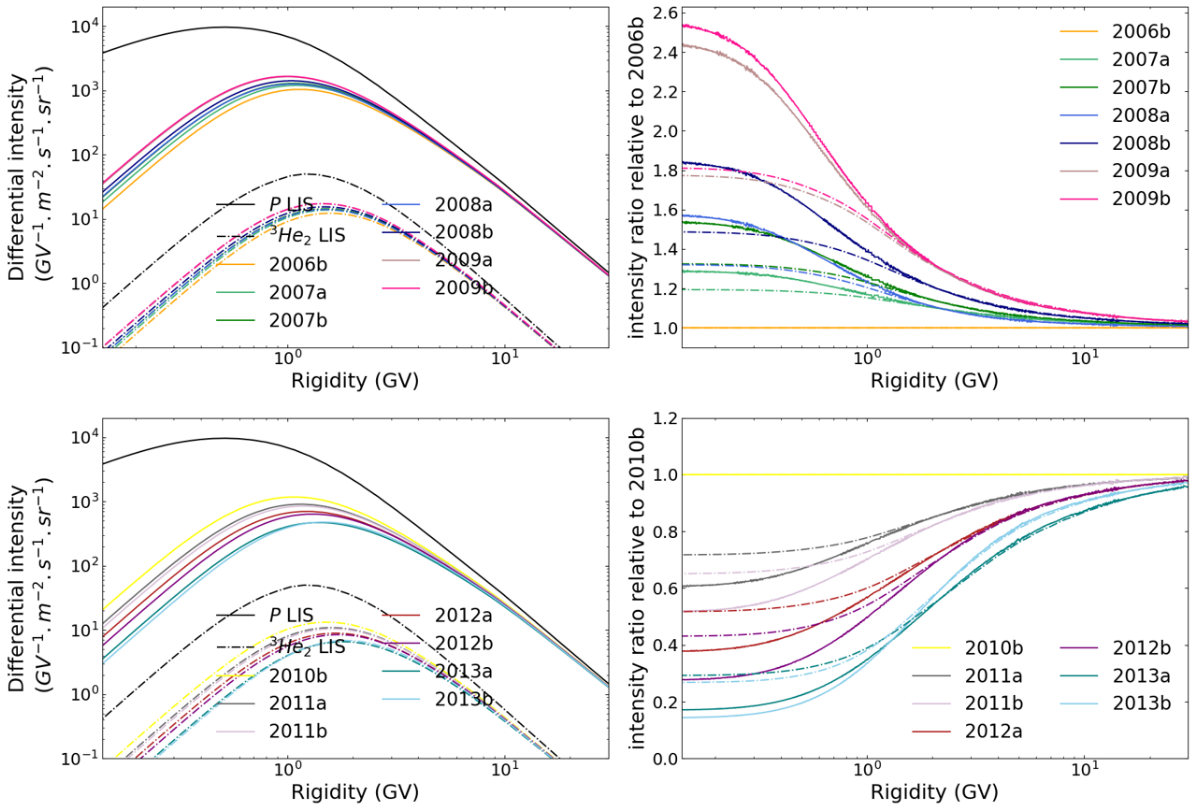

Figure 6.3: Left panel shows the LIS's for P (black solid line) and $^3He_2$ (dashed-dotted lines) together with the computed modulated differential intensity (coloured solid lines) as a function of rigidity at the Earth for the solar minimum period of 2006 to 2009 (top row) and from 2010 to 2013 (bottom row). Right panel shows the corresponding computed intensity ratios for proton (solid lines) and $^3He_2$ (dashed-dotted lines) relative to 2006b (top row) and 2010b (bottom row).

The LIS's for P (black solid lines) and $^3He_2$ (black dashed lines) are shown in the left panel of Figure 6.3, together with the computed modulated spectra for P (coloured solid lines) and $^3He_2$ (coloured dashed-dotted lines) as a function of rigidity at the Earth from 2006 to 2009 (top) and 2010 to 2013 (bottom). The right panel of Figure 6.3 shows how the computed intensities increased for both P and $^3He_2$ relative to 2006b (top) and decreased relative to 2010b (bottom) as function of rigidity. Noteworthy is that for the same set of modulation parameters and diffusion coefficients, the P computed intensities increased relatively more than $^3He_2$ below $\approx$ 3.0 GV as solar modulation changed from 2006b to 2009b. For example, at 0.14 GV P increased by a factor of more than $\approx$ 2.5 in 2009b relative to 2006b while at the same time $^3He_2$ intensities increased by a factor of $\approx$ 1.8 at the same rigidity. Above $\approx$ 3.0 GV, the differences in relative increases are small to become negligible with increasing rigidity. Evidently, the adiabatic energy changes, resulting in the flattening of the intensity ratios at lower rigidities, set in at much higher rigidities for $^3He_2$ than P intensities. Therefore, the $^3He_2$ did not undergo similar spectral changes to that of P from 2006b to 2009b at lower rigidities. However, from 2010b to 2013b P intensities decreased relatively more than $^3He_2$ intensities below $\approx$ 3 GV, showing that P intensities are more sensitive to changes in solar modulation conditions than $^3He_2$ at these rigidities. These differences between P and $^3He_2$ are the consequence of how the combined interplaying modulation mechanisms in the heliosphere affect the modulated spectra based on their A/Z and specifically on the shape of their LIS's at lower rigidities.

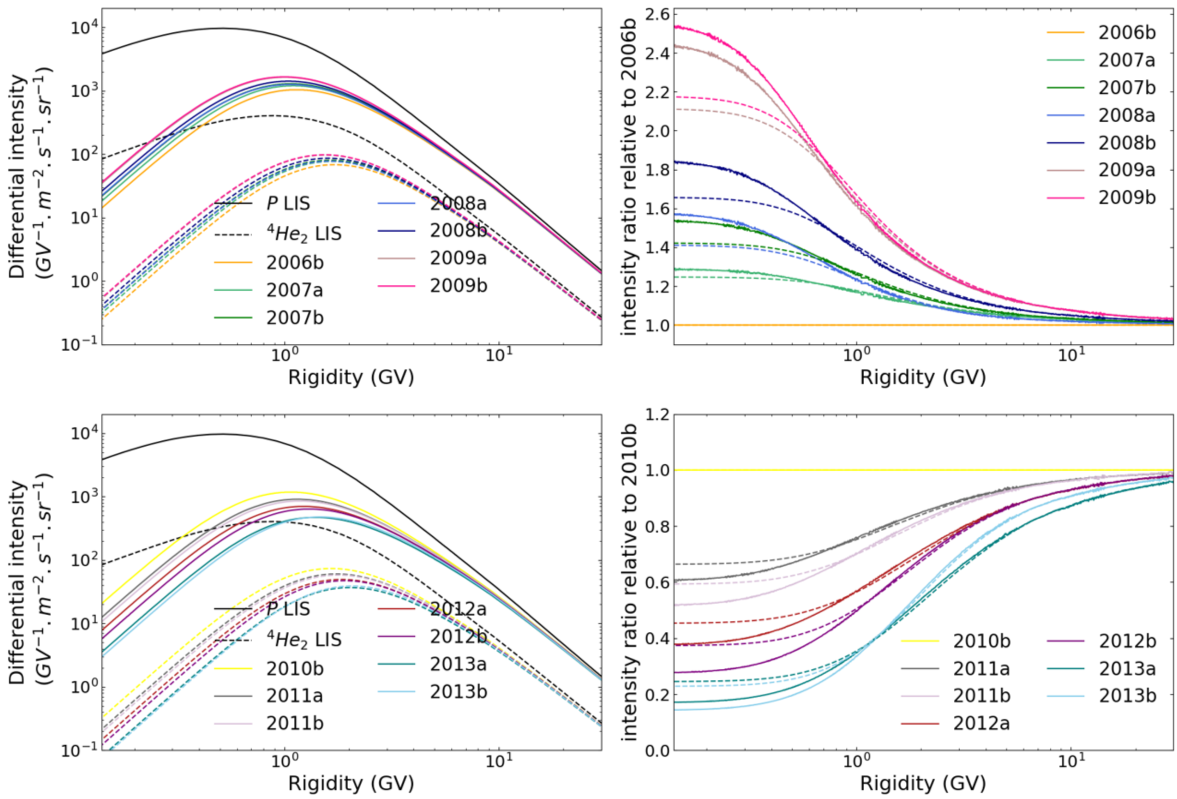

Figure 6.4: Similar to Figure 6.3 but now showing the computed P (solid lines) and $^4He_2$ (dashed lines) differential intensities.

Figure 6.4 is similar to Figure 6.3, but now showing the LIS for P (black solid lines) in comparison with that of $^4He_2$ (black dashed lines) in the left panel, together with their corresponding computed modulated spectra as a function of rigidity at the Earth from 2006 to 2009 (top) and 2010 to 2013 (bottom). The right panel of Figure 6.4 shows how the computed rigidity spectra for both P and $^4He_2$ unfolded relative to their 2006b (top) and 2010b (bottom) values. What is striking in the right panel of this figure is that below $\approx$ 1.0 GV P intensities increased more than $^4He_2$ intensities between 2006 and 2009, whereas at rigidities between $\approx$ 1.0 GV and $\approx$ 5.0 GV $^4He_2$ intensities increased noticeably more than P intensities. This noticeable change in relative intensity increases with rigidity between P and $^4He_2$ is in contrast to the relative increases between P and $^3He_2$ shown in Figure 6.3. For increasing solar activity, between 2010 and 2013, $^4He_2$ intensities decreased noticeably more at rigidities between ≈ 1.0 GV and ≈ 5 GV than P intensities, whereas below ≈ 1.0 GV $^4He_2$ intensities decreased less when compared to P intensities. Above ≈ 5 GV both P and $^4He_2$ intensities unfolded in a similar manner.

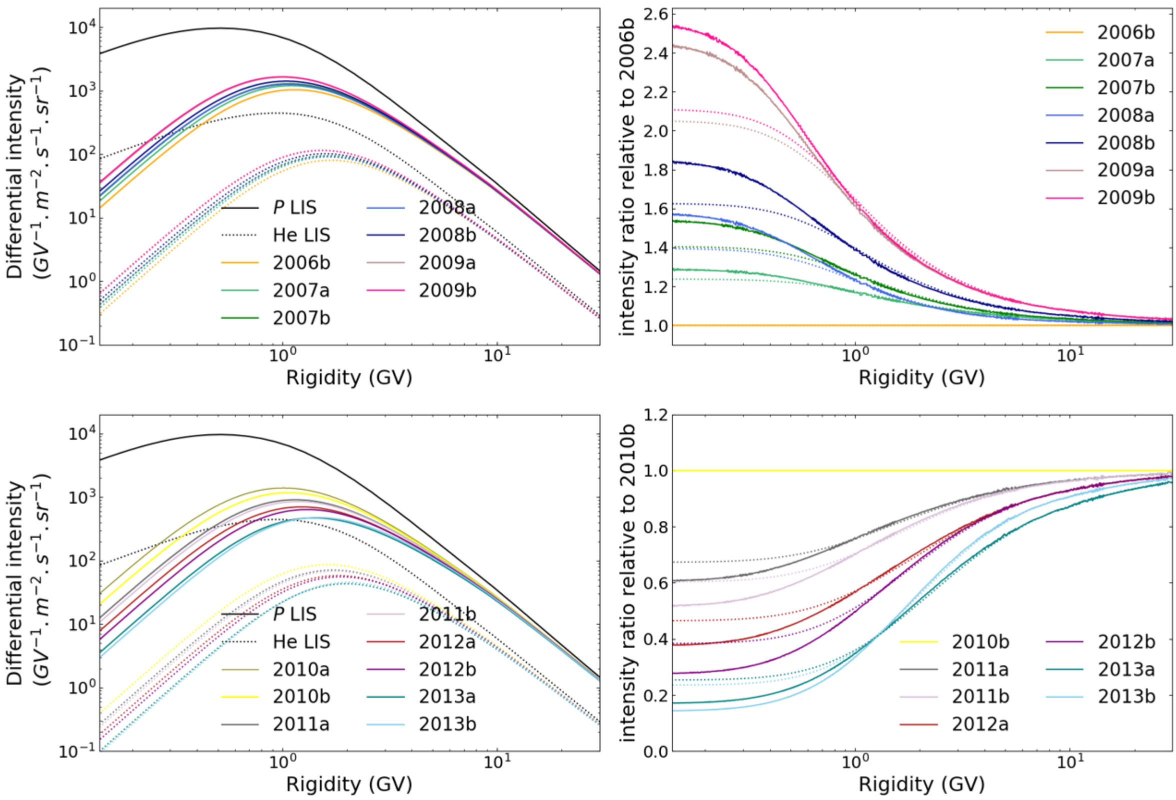

Figure 6.5: Simillar to both Figures 6.3 and 6.4 but now showing the computed P (solid lines) and total He (dotted lines) differential intensities.

The left panel of Figure 6.5 depicts the computed modulated P and total He spectra in relation to their LIS's as a function of rigidity between 2006 and 2009 (top) and between 2010 and 2013 (bottom), respectively. It is worth repeating to mention that the total He modulation in this figure is obtained by adding up the modulated spectra and LIS's for $^3He_2$ and $^4He_2$ shown in Figures 6.3 and 6.4, respectively. Therefore, the effects discussed in the mentioned figures are now combined in Figure 6.5. Comparing P and He spectra as done in this figure shows that the spread in the modulated spectra for both P and He due to changing solar activity becomes wider below the rigidity where the characteristic peak in intensity is reached. The peak in the computed intensity for P in 2009 and 2013 is at ≈ 1.0 GV and ≈ 1.5 GV, whereas for He is at ≈ 1.6 GV and ≈ 2.4 GV, respectively. Therefore, the P/He ratio as a function of time is expected to exhibit changes below ≈ 2.5 GV in response to changing solar activity that differ to that at higher rigidities. Fortunately PAMELA observations of P/He ratios are available at these rigidities for an interesting comparison with numerical modeling.

The right panel of Figure 6.5 gives the modulated intensity ratios of P (solid lines) and total

He (dashed lines) from 2006 to 2009 (top) and from 2010 to 2013 (bottom) relative to their respective 2006b (top) and 2010b (bottom) spectra as a function of rigidity, and show how adiabatic energy losses shape the spectral slopes of the modulated spectra to have spectral indices not varying much for P and total He at low rigidities. Clearly, the difference between the computed relative intensities of the two species grows significantly with decreasing rigidity below $\approx$ 1.0 GV but subsides at rigidities above $\approx$ 5.0 GV. Quantitatively, the largest relative changes in intensity for both P and He occurs at lower rigidities, similar to that for $^3He_2$ and $^4He_2$, but with different values based on their respective LIS's. It is also noted in this panel that the computed P intensities continue to increase (decrease) noticeably more than He below $\approx$ 1.0 GV between 2006 and 2009 (2010 and 2013), illustrating that adiabatic energy losses become evident at different rigidities for P and total He, as indicated by when the spectral indices of the modulated spectra at these low rigidities remain essentially unchanged with decreasing rigidity.

It should be pointed out that the computations shown in Figures 6.3, 6.4 and 6.5 were obtained using the same set of modulation parameters, DCs and drift coefficient, which is considered as essential for a consistent approach to the numerical modeling of GCR nuclei. This is of importance for solar modulation studies since the information gained from these results acts as indicators of the fundamental properties of the SW and magnetic turbulence (e.g., Shalchi [2020]) throughout the heliosphere as related to the modulation conditions from 2006 to 2009 and 2010 to 2013.

6.3.2 Computed proton, $^3He_2$, $^4He_2$ and total helium spectra as a function of time

Figure 6.6 depicts the quantitative and qualitative time-dependent modulation of the computed P and $^3He_2$ spectra at rigidity values between 1.06 GV and 3.69 GV on the left panel and the corresponding intensity ratios relative to 2006b on the right panel. It is evident in this figure that P and $^3He_2$ intensities display similar time-trend, but with some relative variations in amplitude. This is highlighted in the right panel of this figure, showing that P intensities changed more compared to $^3He_2$ at rigidities below $\approx$ 2.43 GV especially during solar minimum conditions. However, towards solar maximum conditions variations in the unfolding of the intensities of this two GCR species above $\approx$ 1.61 GV became quantitatively more or less the same.

Figure 6.7 is similar to Figure 6.6 but illustrates the difference between the computed P and $^4He_2$ intensities as a function of time from 2006 to 2013 at rigidities between 1.06 GV and 3.69 GV. It can be noted that the P and $^4He_2$ intensity ratios relative to 2006b, apart from the fact that $^4He_2$ intensities relative to 2006b were higher than P intensities during solar minimum conditions at the displayed rigidities, these ratios and their spectra do not show any significant quantitative differences when compared to the P and $^3He_2$ intensity ratios shown in Figure 6.6.

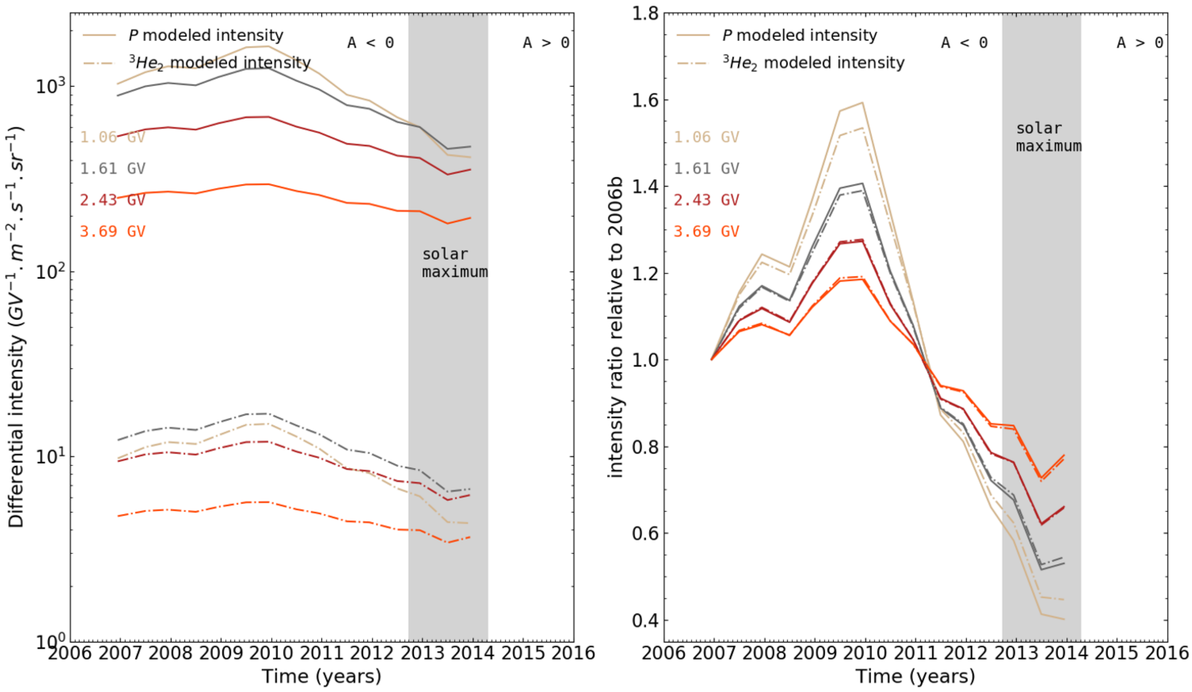

Figure 6.6: Computed P (solid lines) and $^3He_2$ (dashed-dotted lines) intensities as a function of time left panel) at four selected rigidities ranging between 1.06 GV to 3.69 GV together with their corresponding intensity ratios relative to 2006b (right panel). The polarity epochs; A $<$ 0 and A $>$ 0 before and after the period of maximum solar activity are also indicated.

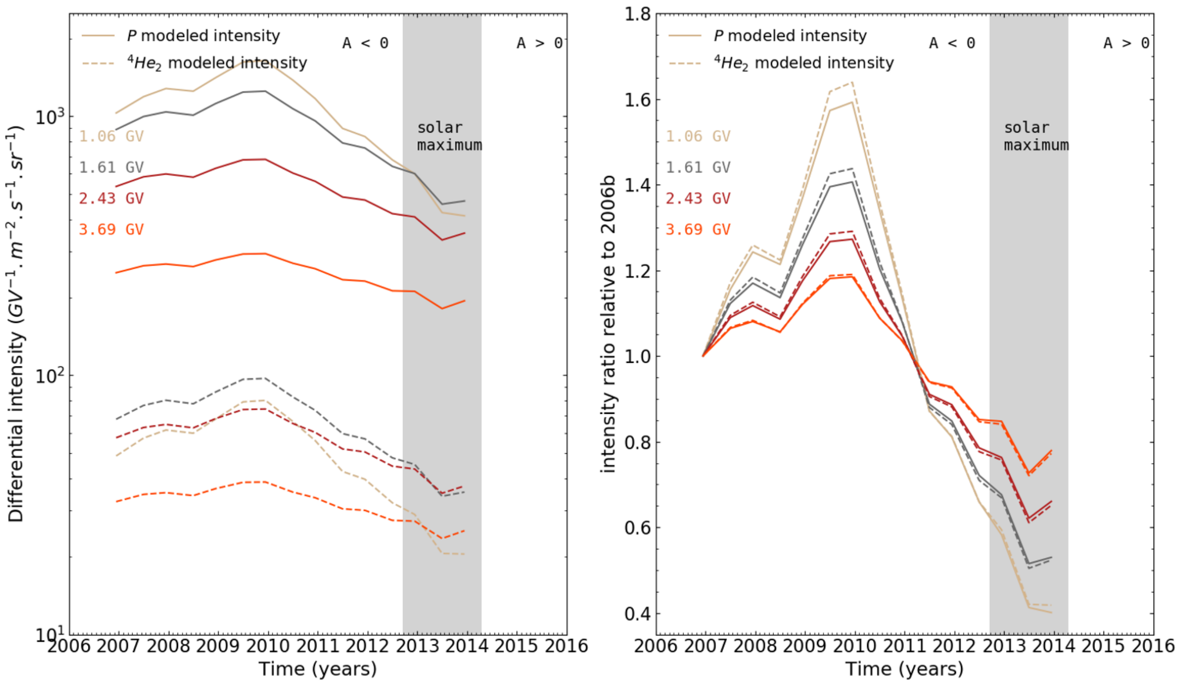

Figure 6.7: Similar to Figure 6.6 but now showing the computed proton (solid lines) and $^4He_2$ (dashed-dotted lines) intensities.

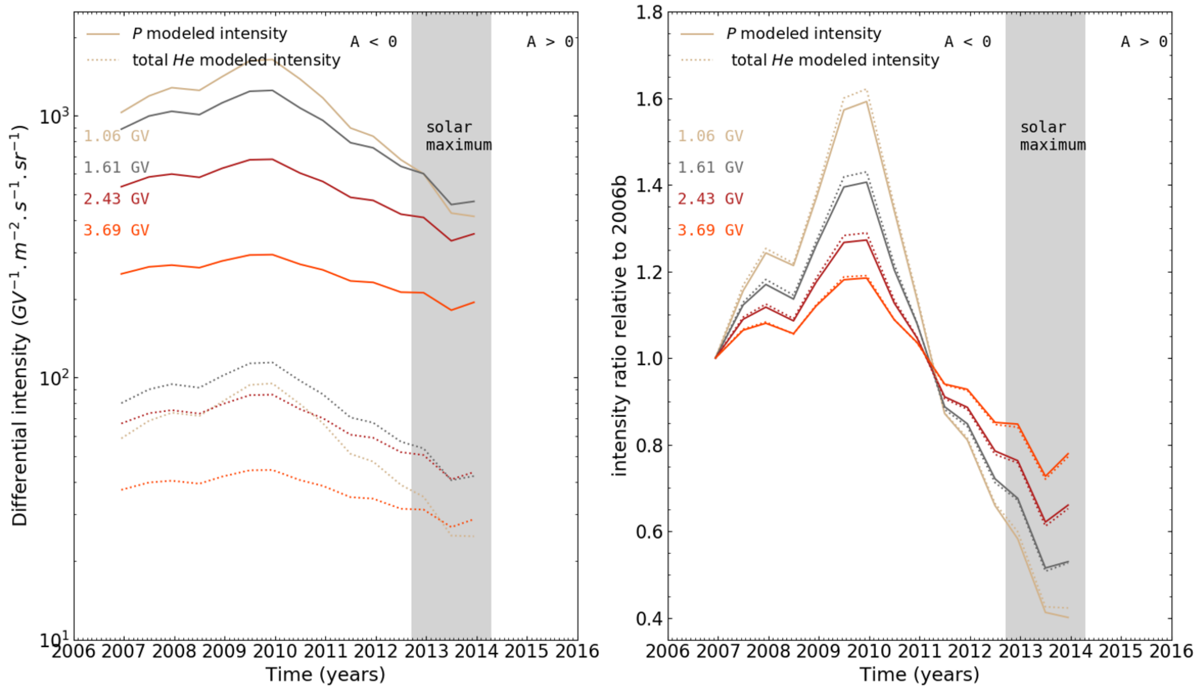

Figure 6.8: Similar to Figures 6.6 and 6.7 but now showing the computed proton (solid lines) and total He (dotted lines) intensities.

Figure 6.8 is similar to Figure 6.7 but now showing the computed P and total He intensities together with their ratios relative to 2006b as a function of time. Regarding the P and total He intensity and ratios relative to 2006b as a function of time, it can be seen that apart from small quantitative changes especially at lower rigidities, these ratios do not show any significant qualitative differences when compared to the $^4He_2$ intensity ratios shown in Figure 6.7.

With all the modeled variations in the time dependencies of P and helium nuclei intensities, total He and its isotopes, an interesting time dependence for P/He ratio at lower rigidities is expected and this is evaluated in the next section.

6.4 Proton to helium ratios

6.4.1 Proton to helium ratios as a function of rigidity

Separating the computed intensity ratios of $P/^4He_2$ and $P/^3He_2$ allows for an investigation of how exactly the overall P/He ratio changed from 2006b to 2009b and 2010 to 2013 at various rigidities of interest as solar activity changes. This is shown in Figure 6.9, here the computed intensity and LIS ratios $P/^3He_2$ (left panel) and $P/^4He_2$ (right panel) are depicted in comparison with P/He from 2006 to 2009 (top) and 2010 to 2013 (bottom) as a function of rigidity. It can be readily noticed, on the presented scale, that the modulated P/He, $P/^3He_2$ and

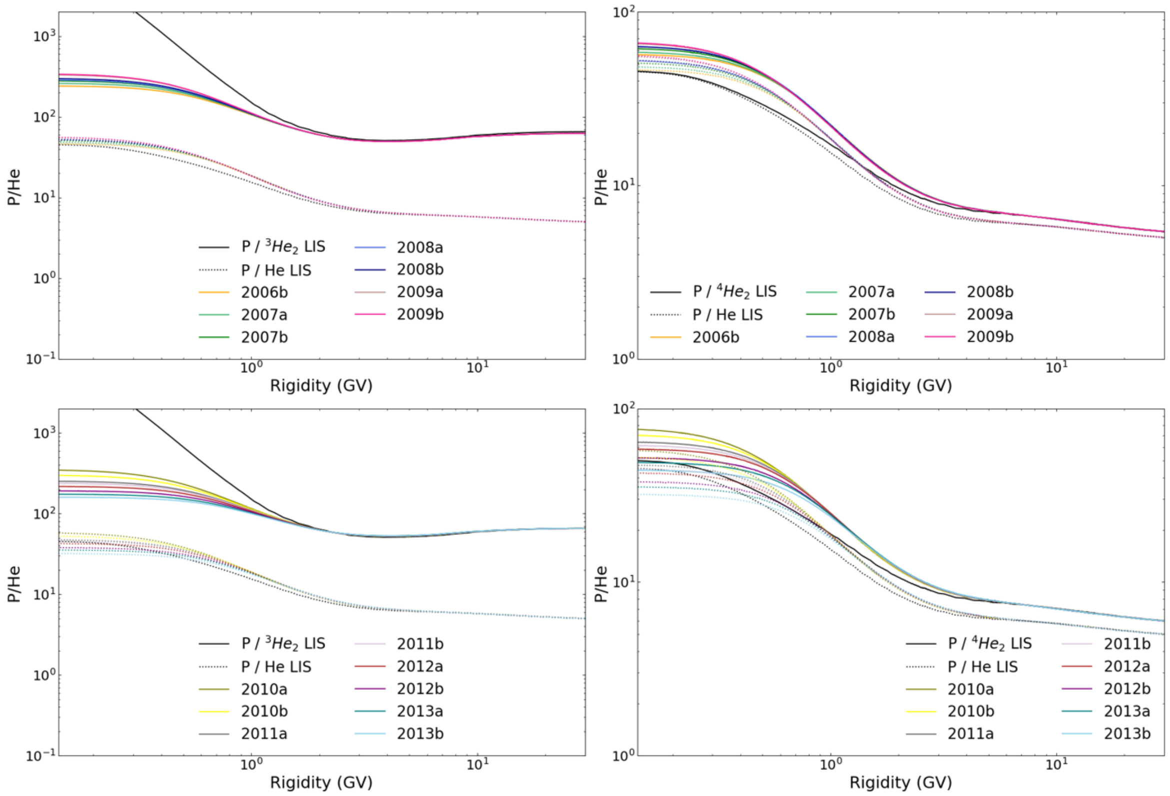

Figure 6.9: Left panel: A comparison of $P/^3He_2$ and P/He ratios along with the ratios of their LIS's computed from 2006 to 2009 (top) and 2010 to 2013 (bottom) as a function of rigidity. Right panel: Similar to the left panel but now showing the ratio of $P/^4He_2$ compared to P/He.

$P/^4He_2$ at lower rigidities (below ≈ 1.0 GV) display time dependence in response to changing solar activity that is different between 2006 and 2009 as compared to that between 2010 and 2013. From 2006 to 2009 these modulated ratios increase noticeably at rigidities below ≈ 0.6 GV, whereas from 2010 to 2013 a clear decrease in these ratios is noted at rigidities below ≈ 1.0 GV but more so the lower the rigidity. However, above ≈ 5 GV all the three modulated ratios closely follow their corresponding LIS ratios but deviate progressively from these values with decreasing rigidity, and eventually flattens off when both P and helium nuclei spectra go into the adiabatic energy regime. This deviation with respect to the LIS ratio at lower rigidities is quite pronounced for $P/^3He_2$ compared to both $P/^4He_2$ and P/He due to differences in their respective LIS's.

The significance of including the modeling effects of $^3He_2$ when computing P/He ratios for comparison with Spacecraft observations is displayed in the right panel of Figure 6.9. Here the computed P/He and $P/^4He_2$ are compared with each other. This panel shows that excluding the modeling effects of $^3He_2$ result in the overestimation of the P/He ratio at all rigidities, confirming what is already mentioned that the inclusion of $^3He_2$ modulation effects in the numerical model is crucially important in understanding exactly how P/He changes with rigidity; an aspect that has been discussed in detail in Ngobeni et al. [2020, 2021a, 2021b] . Clearly, $P/^3He_2$ displays a different rigidity dependence compared to $P/^4He_2$ because of the differences in their respective LIS's, not because of any fundamental difference in the solar modulation of these helium nuclei and P. Because at high enough rigidity the three major diffusion and the drift coefficients are the same in terms of rigidity for these GCRs as illustrated in Chapter 3. Overall, the computed P/He ratios depicted in Figure 6.9 display three modulation regimes caused by a complex interplay between diffusion, drifts and adiabatic energy losses.

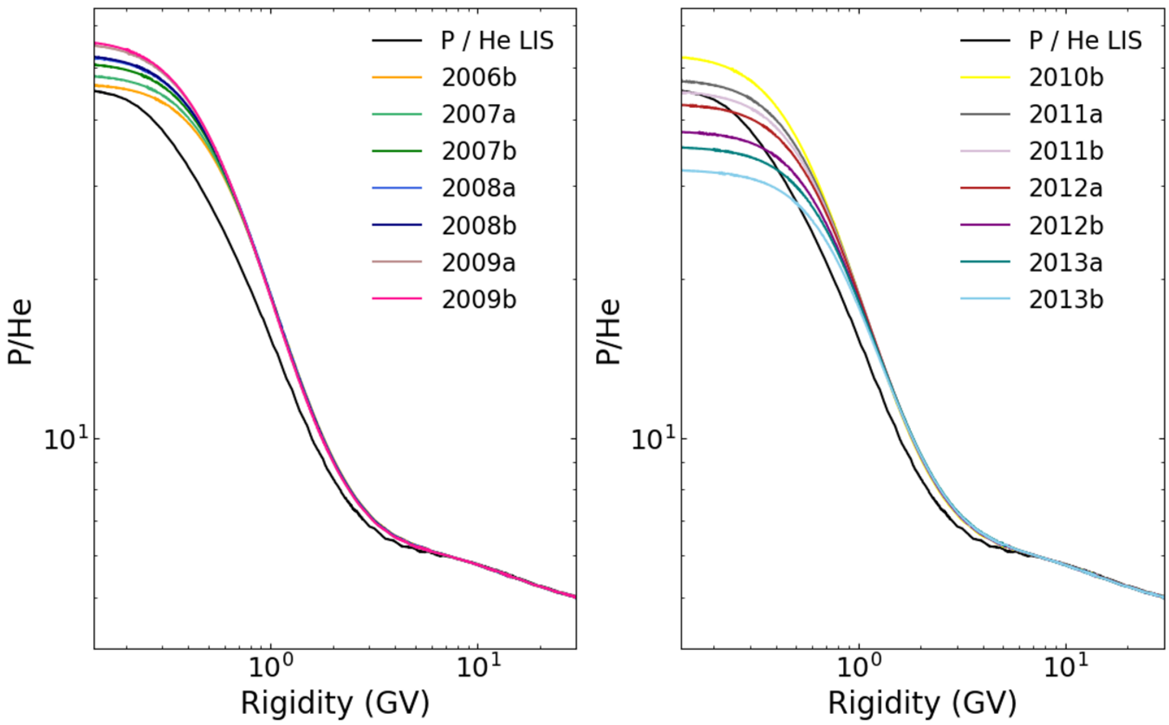

Figure 6.10: The computed P/He ratio as a function of rigidity from 2006 to 2009 (left) and 2010 to 2013 (right).

Figure 6.10 depicts P/He ratios as a function of rigidity from 2006 to 2009 (left) and 2010 to 2013 (right). The essence of this figure is to highlight the modulational effects of the computed P/He ratios as a function of rigidity with changing solar activity. It is clearly shown on both panels of Figure 6.10 that the computed P/He ratios vary more with time during inclining than declining solar activity. Furthermore, it can be noted that at rigidities between $\approx$ 0.6 GV and $\approx$ 1.0 GV the P/He ratio time trend changes when compared to that at the corresponding lower rigidities between 2006 and 2009 and 2010 and 2013, respectively. The next section focuses on the computed time dependence of P/He ratio at different rigidities.

6.4.2 Proton to He nuclei ratio as a function of time

Shown in Figure 6.11 is the $P/^3He_2$, $P/^4He_2$ and P/He ratios normalized relative to 2006b as a function of time at four different rigidities ranging between 1.61 GV and 7.36 GV from 2006 to 2013. This figure highlights the time variation in these ratios at the indicated rigidities. Evidently, the time variation of P/He closely follows that of $P/^4He_2$ in all panels. This remains the case even though $P/^3He_2$ is much higher than $P/^4He_2$ at all rigidities. What is striking is that at 1.61 GV, all three ratios have significant time dependences but $P/^3He_2$ is in anti-correlation with that of $P/^4He_2$ and P/He, with the former decreasing significantly after 2010 and the later increasing to reach a maximum during solar maximum activity period. Above 1.61 GV the time trends of the three ratios remain similar and all attain their maximum values during solar maximum activity period, except at 7.36 GV where relative changes in $P/^3He_2$ can still be noted while $P/^4He_2$ and P/He remain independent of time from 2006 to 2013.

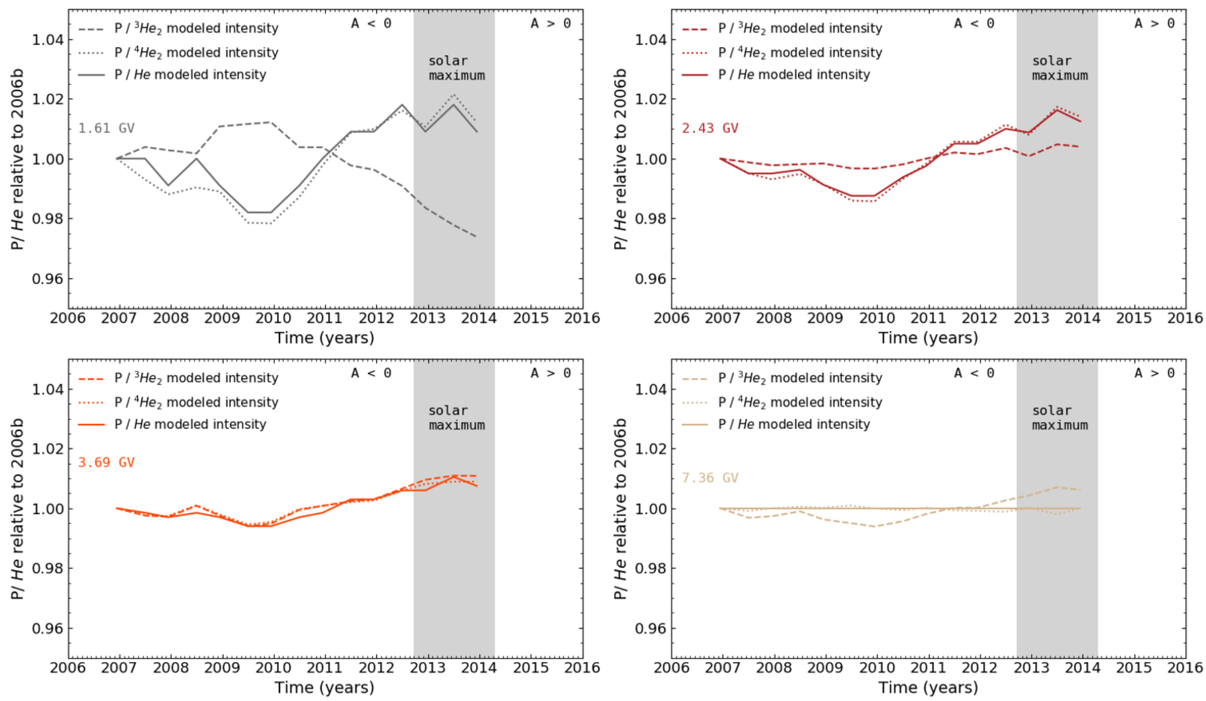

Figure 6.11: Computed $P/^3He_2$, $P/^4He_2$ and P/He ratios as a function of time relative to 2006b at rigidities ranging from 1.61 GV to 7.36 GV. The polarity epochs, A $<$ 0 and A $>$ 0, before and after the period of maximum solar activity are also indicated.

The different time trends in $P/^3He_2$, $P/^4He_2$ and P/He at 1.61 GV relative to 2006b warrants a more focussed investigation of these ratios at rigidities below 1.0 GV. This is shown in Figure 6.12 as a function of time at rigidities between 0.14 GV and 0.92 GV. Clearly all the three ratios in this figure have similar time trends at these rigidities, although the $P/^3He_2$ appears to reach its maximum at earlier time than $P/^4He_2$ and P/He, increasing sharply from 2006b to around the end of 2009 and the beginning of 2010, then afterwards decreasing rapidly from 2010 until

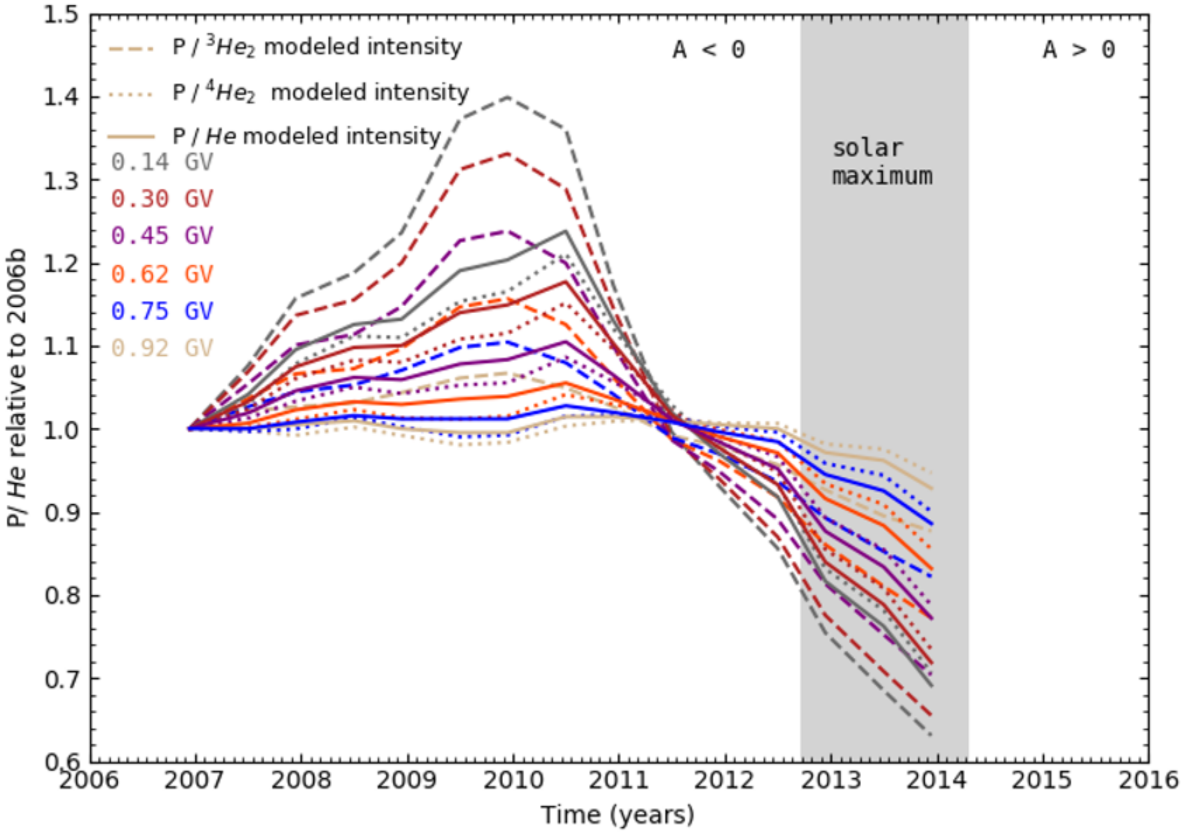

Figure 6.12: $P/^3He_2$, $P/^4He_2$ and P/He ratios as a function of time relative to 2006b computed at lower rigidities ranging from 0.14 GV to 0.92 GV where PAMELA observations are not available.

the end of 2013. Figure 6.12 shows that contrary to the higher rigidity part of P/He discussed in Figure 6.11, the computed lower rigidity part indicate a decrease as a function of time from the solar minimum at the end of 2009 up to the maximum solar activity period at the end of 2013. This opposite behaviour in the P/He ratio between low and high rigidity part has been observed by PAMELA and discussed in detail in Marcelli et al. [2022]. Furthermore, the computed P/He ratio at lower rigidities is more sensitive to changes in solar activity as noted in Figure 6.12 that it increased faster during solar minimum conditions and decreased faster during solar maximum conditions the lower the rigidity. Next the effects of different level of drifts on P/He ratios is illustrated.

In the 3D numerical model used in this study the drift coefficient, κ_{A0}, is changed time dependently as given in Table 4.1. Figure 3.19 illustrated that CR species with the same charge-sign have different κ_{A0} at lower rigidities due to β. Therefore, it remains to be seen how different values of this coefficient modify the P/He ratio at these rigidities. This is achieved in the model by keeping all the other modulation parameters the same but only change the value of κ_{A0}. This aspect is illustrated in Figures 6.13 - 6.15 by showing the computed $P/^3He_2$, $P/^4He_2$ and P/He ratios, respectively, as a function of time obtained from two scenarios corresponding to different values of κ_{A0}. The dashed lines correspond to ratios obtained with κ_{A0} = 0 (no drifts) and the dotted lines with κ_{A0} = 1.0 (full drifts) throughout the period under investigation. Here, the effects of different values of κ_{A0} are illustrated with emphasis on the resulting differences in the three ratios of the modulated intensities. Comparing the three figures illustrate that when κ_{A0} decreases from 1.0 to 0.0 at the Earth, in general the computed ratios of $P/^3He_2$, $P/^4He_2$ and P/He all increase at all rigidities in the A $<$ 0 cycle, except for $P/^3He_2$ at 1.61 GV. This demonstrates that drift effects indeed can modify the P/He ratio in the equatorial plane during this cycle. It worth mentioning that in A $<$ 0 cycle P, $^3He_2$ and $^4He_2$ drift into the inner heliosphere mainly along the HCS and out along the solar poles. So that in this cycle no-drift models can lead to high values of P/He while full-drift models lead to lower values.

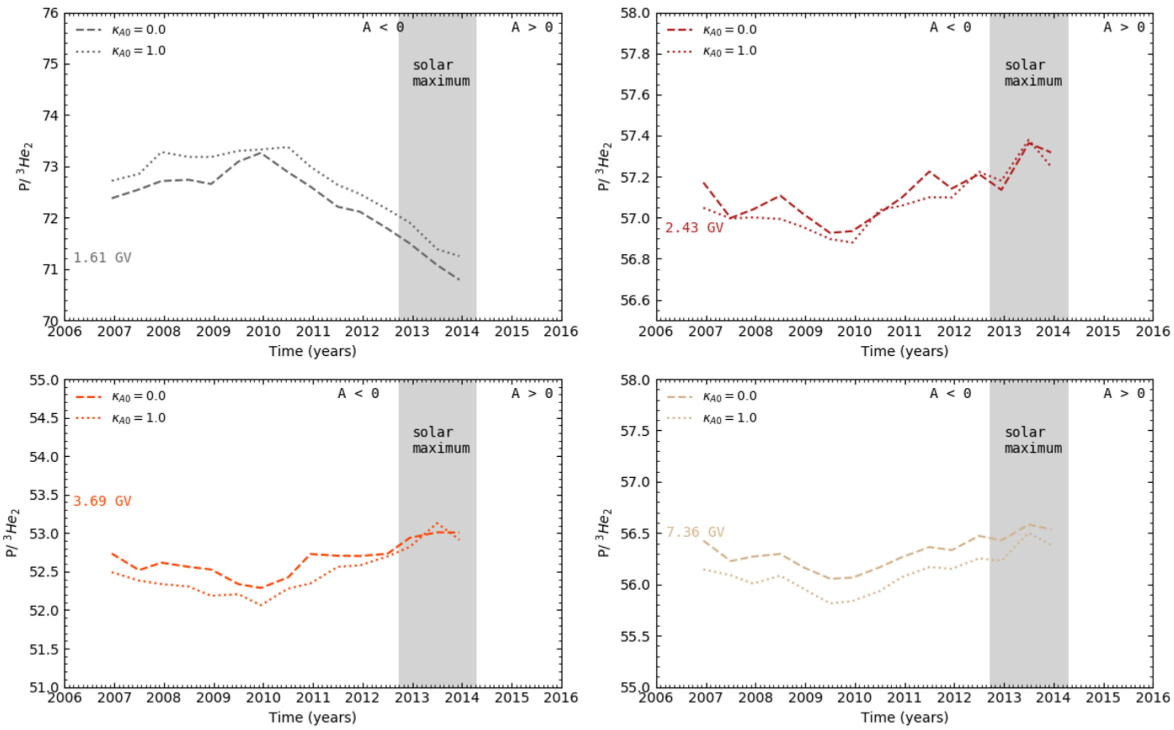

Figure 6.13: The computed $P/^3He_2$ obtained from two different scenarios of κ_{A0} with the dashed lines obtained with κ_{A0} = 0 (no drifts) and the dotted lines with κ_{A0} = 1.0 (full drifts) assumed. The shaded region indicates a period of the Sun's magnetic field reversal where the HMF polarity is not well-defined.

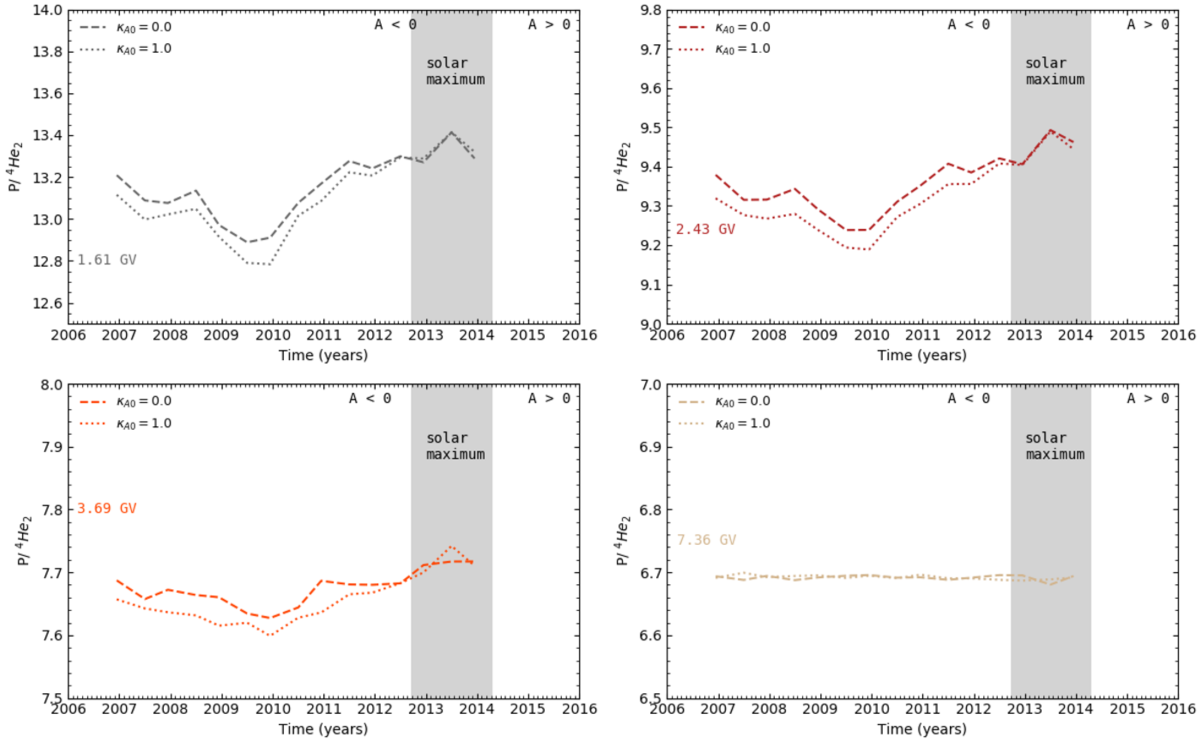

Figure 6.14: Similar to 6.13 but now showing the computed $P/^4He_2$.

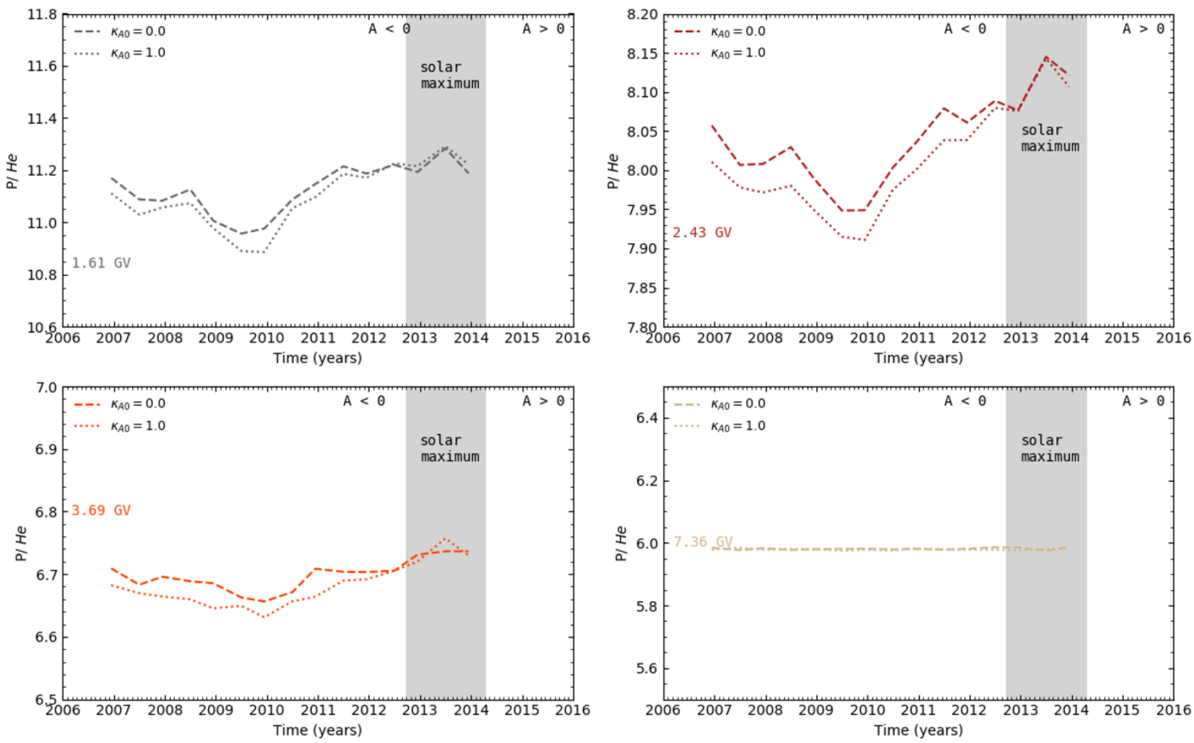

Figure 6.15: Similar to both 6.13 and 6.14 but now showing the computed P/He.

6.5 Computed P/He ratios in comparison with PAMELA observations

6.5.1 The P/He ratio as a function of rigidity

Figure 6.16 shows the computed P/He ratio (lines) in comparison with PAMELA observations (symbols) as a function of rigidity from 2006 to 2009. The three coloured solid lines in each panel correspond to the three model scenarios given in Figures 4.12 and 4.13. The purple lines represent values of the rigidity slopes of the DCs given in Table 4.1 for the full time dependences in the model, whereas the blue lines represent the slopes of the DCs when all time dependent parameters in the model are kept constant at their 2006b values and only α and B are changed with time from 2006b to 2013b. While for the red lines the full time dependences in the model are assumed but with a single rigidity power law (DC $\propto$ rigidity$^{1.0}$) at all rigidities and at all times. Also shown in each panel is the ratio of their LIS's (black lines). In general the value and shape of the observed P/He ratios at all rigidities are reproduced quite well with the numerical modulation model for all the selected time periods. Furthermore, it is interesting to note that above $\approx$ 5.0 GV both the rigidity dependence of the ratio of the modulated spectra and that of the LIS ratios follow closely the PAMELA observations independent of the assume modulation conditions. This indicates that the observed P/He ratio taken by PAMELA at the Earth essentially reveals the difference in the rigidity dependence of the LIS's for both P and total He already above $\approx$ 5.0 GV, providing evidence about the difference in their origin and propagation in the interstellar medium. Concerning the three investigative scenarios of the rigidity slopes of the DCs, differences are only noticeable at lower rigidities below the PAMELA rigidity thresh-hold. Such that the available observations of P/He ratio between 2006 and 2009 are not suitable to arrive at the conclusion regarding the rigidity slope of the DCs. However, it was already shown in Chapter 4 that in fact the unfolding of the observed spectra from 2006 to 2009 is more suitable to study the time evolution of the slopes of the DCs even during this period of unusually low modulation in the A < 0 magnetic cycle (see also a discussion by Ngobeni et al. [2021b]).

Figure 6.17 is similar to Figure 6.16 but now showing P/He ratios from 2010 to 2013, representing increasing solar activity period. Similarly, the numerical computations reproduce PAMELA observations reasonably well at all rigidities of interest. However, differences in the three scenarios concerning the rigidity slopes have now shifted to higher rigidities but unfortunately still below the smallest rigidity value of P/He observed by PAMELA. It is worth mentioning that studies done by Song et al. [2021b] revealed that the rigidity dependence of the DCs (MFPs) may vary significantly with time such that it is possible that the lower rigidity part may even have larger slopes than the higher rigidity part. This indicates that a time dependence in the rigidity slopes of the DCs is required to reproduce the observed P/He before solar maximum conditions and afterwards. This is the same conclusion reached by Ngobeni et al. [2021b] but using the computed $^3He_2/^4He_2$ ratio compared to AMS02 observations. Unfortunately the modeling shown in Figures 6.16 and 6.17 end in 2013 as restricted by the availability of PAMELA observation. However, this study will be extended in future to include both AMS02 and PAMELA observations through the complete solar maximum conditions and afterwards in the declining solar activity in the A $>$ 0 cycle.

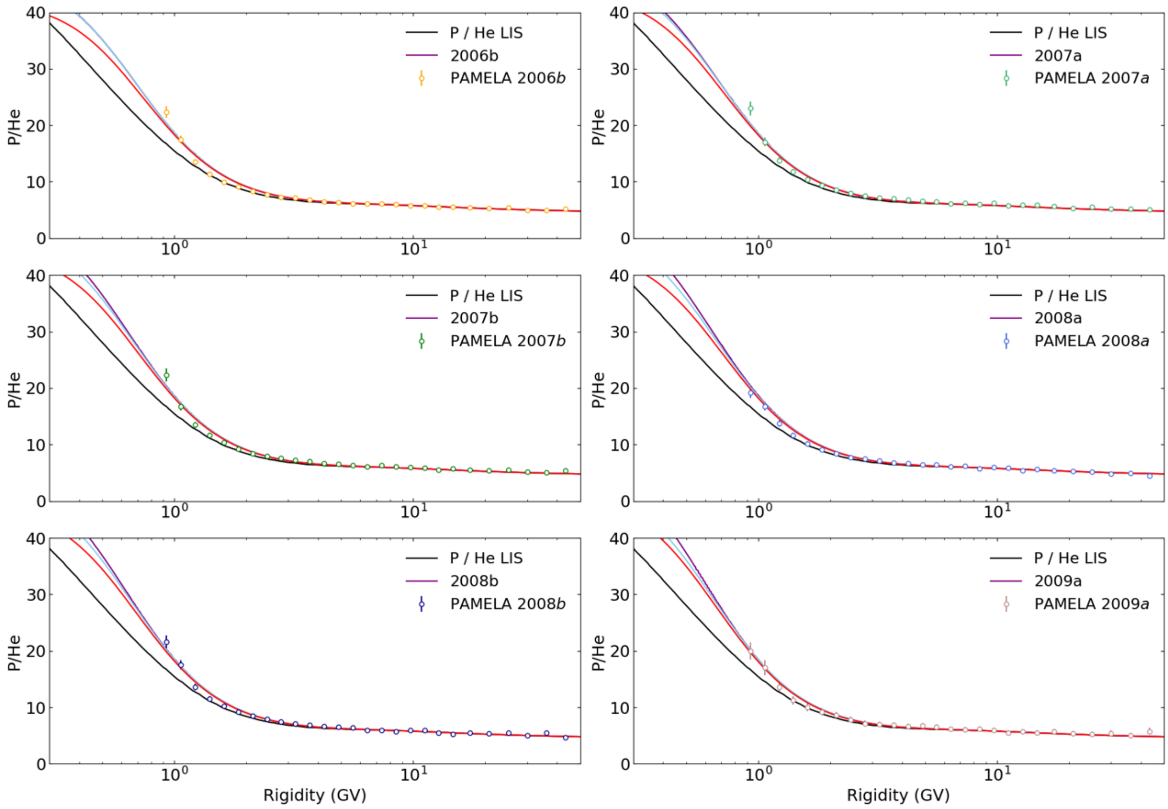

Figure 6.16: The computed P/He ratios (coloured lines) as a function of rigidity for six time periods between 2006b to 2009a and observed ratios (with uncertainties depicted by error-bars). The three different ratios shown correspond to the three scenarios of the same colour of the rigidity slopes of DCs shown in Figures 4.12 and 4.13. The corresponding P/He LIS ratio is given by the black lines in each panel. PAMELA P/He observations are taken from Marcelli et al. [2020].

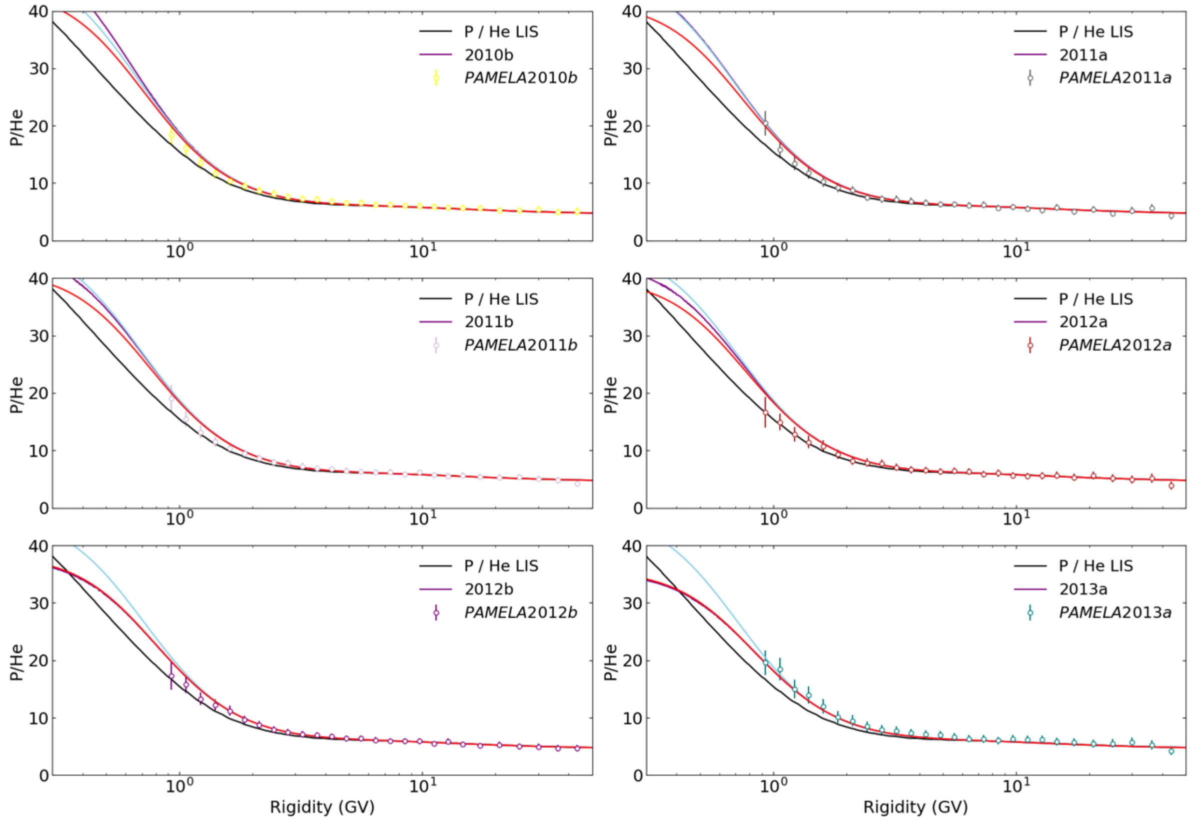

Figure 6.17: Similar to Figure 6.16 but now showing P/He ratios from 2010 to 2013. PAMELA P/He observations are taken from Marcelli et al. [2022].

6.5.2 The P/He ratio as a function of time

Figure 6.18 depicts the computed P/He ratio in comparison with PAMELA observations for four selected rigidities ranging between 1.61 GV and 7.36 GV as a function of time. The three computed scenarios are already described in Figures 6.17 and 6.16. It can be noted in this figure that there is reasonable compatibility between the computed and PAMELA observed ratios at all rigidities of interest. For example, the computed P/He ratios follow the same time profile as the observed ratios, that is, slightly decreasing between 2006 and 2009, in correlation with the decreasing solar activity in the A < 0 cycle solar minimum period, but gradually increasing from 2009 to reach a maximum around the end of 2013 during solar maximum conditions for rigidity below 3.69 GV. Above 3.69 GV the ratio is consistent with a constant value in time (see also Corti et al. [2019], Song et al. [2021b], Ngobeni et al. [2021b]). It can also be noted that the deviations in the three scenarios about the rigidity slope of the DCs are more visible at lower rigidities and subside with increasing rigidity. Overall the computed P/He ratio display both qualitative and quantitative agreement with the main observed features.

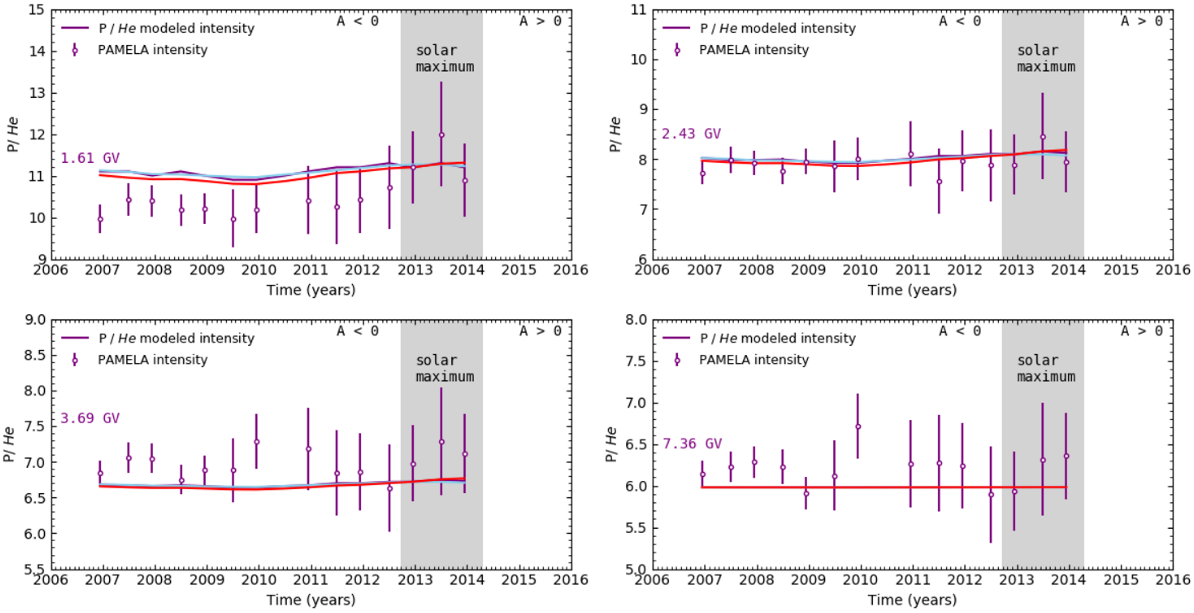

Figure 6.18: P/He ratios at various rigidities between 1.61 GV and 7.36 GV as a function of time. Observed ratios from PAMELA, reported by Marcelli et al. [2020, 2022], are given by the coloured symbols with uncertainties depicted by error-bars, the computed ratios from the model are given by the coloured solid lines corresponding to the three scenarios of the rigidity slopes of the DCs also shown in Figures 6.16 and 6.17 for the time period indicated. The shaded region indicates a period where the HMF polarity is not well-defined, and the HMF polarity indicated by A $<$ 0 and A $>$ 0.

6.6 Summary and conclusion

This chapter was focused on reproducing the P/He ratio observed by PAMELA from the solar minimum activity period beginning in 2006 to the solar maximum activity up to the end of 2013. This was done successfully by modeling P and He nuclei ($^3He_2$, $^4He_2$ and total He) simultaneously, shown in Figures 6.2 - 6.8, both as a function of time and rigidity using their more accurate LIS's established in the previous chapters. This made it possible to study the rigidity and time trends of $P/^3He_2$ and $P/^4He_2$ in Figures 6.9 - 6.12, which is considered crucially important for the understanding of the mostly studied and reported P/He ratios. It was found that apart from the large difference in intensity levels between P, $^3He_2$ and $^4He_2$ LIS's, their slopes are also different at low rigidities and also have spectral peaks at different rigidity values. Consequently, for the same set of modulation parameters and diffusion coefficients, the computed modulated intensities of the three CR species changed differently with changing solar activity, mostly at rigidities below $\approx$ 5.0 GV, when normalized relative to their 2006b and 2010b values. Therefore, the $P/^3He_2$ was found to display a different trend in terms of rigidity compared to $P/^4He_2$ at these rigidities, mainly due to these differences in their LIS's. This results in adiabatic energy losses also becoming evident at different rigidities for the three species. However, above $\approx$ 5.0 GV the spectra P, $^3He_2$, $^4He_2$ and total He unfolded in a similar manner with time independent of the assumed solar modulation. The contribution of $^3He_2$ to the total He was found to increase the differences between the modulated $P/^4He_2$ and P/He at the Earth at all rigidities. This is taken to further indicate that separating the modeling effects of both He isotopes is important in explaining simultaneously the observed $^3He_2/^4He_2$ and P/He ratios.

An investigation of how different values of the drift coefficient modify the $P/^3He_2$, $P/^4He_2$ and P/He ratios was carried out in Figures 6.13 - 6.15 by comparing the ratios obtained with no-drift (κ_{A0} = 0.0) and full-drift (κ_{A0} = 1.0) assumed in the model. It was found that, in general except for $P/^3He_2$ at 1.61 GV, the three computed ratios all increase at all rigidities in the A $<$ 0 cycle when no-drift is assumed compared to full-drift solutions. However, the difference between the two solutions was found to be too small to be observable by PAMELA with large error bars in the P/He ratios. Therefore, AMS02 with smaller P/He error bars may be more adequate to perform this kind of investigation.

Concerning the comparison of the model computations with the PAMELA observations of P/He ratios shown in Figures 6.16 - 6.18, it was found that the value and shape of the observed P/He ratios at all rigidities are reproduced quite well with the numerical modulation model for all the selected time periods. Furthermore, above $\approx$ 5.0 GV the rigidity dependence of the ratio of the modulated spectra and that of their LIS ratios is found to follow closely the PAMELA observations independent of the assumed solar modulation conditions. This indicates that the observed P/He ratio taken by PAMELA at the Earth essentially reveals the difference in the rigidity dependence of the LIS's for P and total He already above $\approx$ 5.0 GV, providing evidence about the difference in their origin and propagation in the interstellar medium. At rigidities $\leqslant$ 3.69 GV, the computed P/He ratios was also found to follow the same time profile as the observed ratios, i.e., slightly decreasing between 2006 and 2009, in correlation with the decreasing solar activity in the A $<$ 0 cycle, but gradually increasing from 2009 to reach a maximum value around the end of 2013 during solar maximum conditions. Above this rigidity both the computed and the observed ratios are found to be consistent with a constant value in time similar to conclusions reached by Corti et al. [2019], Song et al. [2021b] and Ngobeni et al. [2021b]. Extending the model computations to lower rigidities revealed an opposite behaviour in the P/He ratio as a function of time between low and high rigidity. This opposite behaviour in P/He ratio has also been confirmed recently by observations (Marcelli et al. [2022]). This interesting time dependence in the P/He ratio is found to be the consequence of how the combined interplaying modulation mechanisms in the heliosphere affect the modulated spectra based on their A/Z and particularly on the shape of their LIS's.

The next chapter gives a brief summary of the dissertation and the main conclusions of this work.

Chapter 7

Summary and conclusions

This work focused on illustrating how differently GCR species with a dissimilar A/Z, in particular galactic proton and total He nuclei, are modulated at the Earth when solar activity increased from minimum to maximum conditions between 2006 and 2013. To achieve this objective, the comprehensive 3D drift model developed by Vos [2016] based on Parker's transport equation (Parker [1965]) was used and modified to distinguish dominant modulation processes that GCR species of different A/Z experienced with increasing solar activity (for proton A/Z = 1.0, while total He nuclei consists of two isotopes, $^4He_2$ with A/Z = 2.0 and $^3He_2$ with A/Z = 1.5). The computed numerical modeling results were compared with GCRs measurements from PAMELA. This required that, first, the LIS's of both proton and total He nuclei (both $^3He_2$ and $^4He_2$) were established by applying GALPROP models as described by Bisschoff et al. [2019], then refined and compared to the existing set of accurate observations as a function of both kinetic energy per nucleon and rigidity. The achieved compatibility between GALPROP LIS's, for both proton and total He nuclei, and Voyager observations taken outside the solar cavity indicated that in general these LIS's can be utilized as input spectra at the HP for the detailed study of modeling proton and total He nuclei at the Earth. Then an investigative study was done using the 3D model to establish the set of modulation parameters, diffusion and drift coefficients that reproduced PAMELA proton observations between 2006 and 2013. To assure that the modulation parameters are not changed in an *ad hoc* and inconsistent manner just for the purpose of simply fitting a particular observational data, the same exact set of modulation parameters, diffusion and drift coefficients that reproduced PAMELA proton observations were utilized for the modeling of total He nuclei modulation, with the only difference between proton and total He nuclei remaining their LIS's and A/Z. Due to the isotopic mixing of $^3He_2$ and $^4He_2$, the modeling effects of $^3He_2$ and $^4He_2$ were explicitly distinguished, and then combined to describe the modeling effects of total He nuclei. The total He modeling results were also compared with PAMELA He observations between 2006 and 2013. Comparing the modeled results of both proton and total He nuclei with PAMELA observations led to the detailed study of P/He ratio as a function of rigidity and time from solar minimum to maximum activity periods in order to explain the cause(s) of the observed non constant P/He at rigidities below $\approx$ 3.0 GV (Aguilar et al. [2018], Corti et al. [2019], Song et al. [2021a], Marcelli et al. [2022]). The different conclusions are summarised next:

In **Chapter 1** a brief introduction and layout of this dissertation was given.

Chapter 2 briefly introduced relevant aspects and concepts required to understand heliospheric physics and cosmic ray modulation. This included the classification of CRs, the magnetic variable Sun, the heliosphere, the SW and TS, various modifications of the HMF, and HCS. This chapter ended with a brief description of different spacecraft missions relevant to this study, of which included PAMELA, Voyager, and AMS02.

The TPE, which accounts for all four major modulation processes that CRs encounter in the heliosphere, together with the spatial and rigidity dependence of all elements of the diffusion tensor K constructed by Vos [2016] were given in 3D in **Chapter 3**. This included those coefficients in the ϕr and $\phi\phi$ directions which are overlooked in 2D numerical models. A basic theory on drifts was also provided, covering weak scattering and modified drift phenomena, together with HCS drifts. This chapter established that diffusion coefficients in the ϕr and $r\phi$ directions have the same rigidity and spatial dependencies, hence it is considered that $\kappa_{\phi r}$=$\kappa_{r\phi}$. Furthermore, it was shown that at rigidities $< \approx$ 4 GV CR particles with smaller A/Z values result in larger DCs as compared to those with larger A/Z values due to their dependence on β. However, when considering the MFPs the dependence on A/Z is eliminated at all rigidities.

A comprehensive 3D numerical model developed by Vos [2016], which contains the essentials of the TPE described in **Chapter 3**, was applied in **Chapter 4** to study the modulation of CR proton observed by PAMELA from 2006 to 2013. The effects of changing the rigidity slopes of DCs were investigated using three scenarios and it was shown that to reproduce PAMELA observations, the rigidity slopes of the DCs (MFPs) below 4 GV should assume a significant time dependence between 2006 and 2013 while remaining almost constant above 4 GV between 2006 - 2009 and 2010 - 2013. From this investigation the following were established: (i) allowing only B and HCS α to change as a function of time can not reproduce the observed PAMELA spectra at all rigidities for every selected time period; (ii) the DCs $\approx P^1$ is not a reasonable assumption when considering the time evolution of the spectra and; (iii) PAMELA proton observations between 2006 and 2013 are better reproduced by the 3D model when B and HCS α are continuously adjusted with time along with the value and rigidity slopes of the DCs and the drift coefficient.

Chapter 5 was focused on reproducing the total He spectra observed by PAMELA at the same period as protons. This was done with the same set of modulation parameters, diffusion and drift coefficients that were used to reproduce PAMELA proton observations in **Chapter 4**, with the only differences remaining their LIS's and A/Z. Because total He has two isotopes, the modeling of these isotopes were done separately using their different LIS's and appropriate A/Z values. These LIS's were described by Bisschoff et al. [2019] but slightly modified at higher rigidities to match AMS02 $^3He_2/^4He_2$ ratios from Aguilar et al. [2019]. The modification was successfully carried out by multiplying the GALPROP $^3He_2$ LIS by an energy dependent function given in Equation (5.1). The approximate parameterized expressions of the LIS's of both $^3He_2$ and $^4He_2$ are given as a function of kinetic energy/nucleon in Equations (5.2) and (5.3), respectively. A comparative study on modulation of $^3He_2$ and $^4He_2$ was done and it was established that at lower rigidities $^4He_2$ intensities responds more to solar activity changes than $^3He_2$. This is a clear consequence of how adiabatic energy losses affect these species differently, with that of $^3He_2$ beginning at much higher rigidities than $^4He_2$. Consequently, $^3He_2$ did not undergo similar spectral changes when compared to that of $^4He_2$ from 2006 to 2009 and also from 2010 to 2013 at rigidities below 3.0 GV. This resulted in the computed $^3He_2/^4He_2$ ratio at these rigidities to correlate with solar activity, such that it reached minimum values during solar minimum and maximum values during solar maximum conditions. For comparison with PAMELA He observations, the numerical modulation of total He was obtained by summing up the computed spectra of the two helium isotopes. It was shown that the numerical model reproduced PAMELA He observations reasonably well using the same set of modulation parameters that were used for protons. This chapter established that GRC proton and He are modulated by the same mechanisms inside the heliosphere and that to properly model the total He effects in the heliosphere it is important to distinguish the modeling effects of $^3He_2$ and $^4He_2$.

Chapter 6 was focused on reproducing the P/He ratio observed by PAMELA from the solar minimum activity period beginning in 2006 to the solar maximum activity up to the end of 2013. This was done successfully by modeling P and He nuclei ($^3He_2$, $^4He_2$ and total He) simultaneously both as a function of time and rigidity using their more accurate LIS's established in **Chapters 4** and **5**, respectively. This made it possible to also study the rigidity and time trends of $P/^3He_2$ and $P/^4He_2$, which is considered crucially important for the understanding of the P/He ratios. It was found that apart from the large difference in intensity levels between P, $^3He_2$ and $^4He_2$ LIS's, their slopes are also different at low rigidities and also have spectral peaks at different rigidity values. Consequently, for the same set of modulation parameters, diffusion and drift coefficients, the computed modulated intensities of the three CR species changed differently with changing solar activity, mostly at rigidities below $\approx$ 5.0 GV. Therefore, the $P/^3He_2$ was found to display a different trend in terms of rigidity compared to $P/^4He_2$ at these rigidities, mainly due to these differences in their LIS's. However, above $\approx$ 5.0 GV the spectra of P, $^3He_2$, $^4He_2$ unfolded in a similar manner with time independent of the assumed solar modulation conditions. The contribution of $^3He_2$ to the total He was found to increase the differences between the modulated $P/^4He_2$ and P/He at the Earth at all rigidities. This is taken to further indicate that separating the modeling effects of both

He isotopes is important in explaining P/He ratios.

An investigation of how different values of the drift coefficient modify the $P/^3He_2$, $P/^4He_2$ and P/He ratios was carried out by comparing the ratios obtained with no-drift (κ_{A0} = 0.0) and full-drift (κ_{A0} = 1.0) assumed in the model. It was found that, in general except for $P/^3He_2$ at 1.61 GV, the three computed ratios all increased at all rigidities in the A $<$ 0 cycle when no-drift is assumed compared to full-drift solutions. However, the difference between the two solutions was found to be too small to be observable by PAMELA with large error bars in the P/He ratios. Therefore, AMS02 with smaller P/He error bars may be more adequate to perform this kind of investigation.

Lastly the comparison of the model computations with the PAMELA observations of P/He ratios was done, and it was found that the value and shape of the observed P/He ratios at all rigidities were reproduced quite well with the numerical modulation model for all the selected time periods. Furthermore, above $\approx$ 5.0 GV the rigidity dependence of the ratio of the modulated spectra and that of their LIS ratios was found to follow closely the PAMELA observations independent of the assumed solar modulation conditions. This indicates that the observed P/He ratio taken by PAMELA at the Earth essentially revealed the difference in the rigidity dependence of the LIS's for P and total He already above $\approx$ 5.0 GV, providing evidence about the difference in their origin and propagation in the interstellar medium. At rigidities below $\approx$ 3.69 GV, the computed P/He ratios was also found to follow the same time profile as the observed ratios, i.e., slightly decreasing between 2006 and 2009 in correlation with the decreasing solar activity in the A $<$ 0 cycle, but gradually increasing from 2009 to reach a maximum value at the end of 2013 during solar maximum conditions. Above this rigidity both the computed and the observed ratios were found to be consistent with a constant value in time similar to conclusions reached by Corti et al. [2019], Song et al. [2021b] and Ngobeni et al. [2021b]. Extending the model computations to lower rigidities revealed an opposite behaviour in the P/He ratio as a function of time between low and high rigidity. This opposite behaviour in P/He ratio has also been confirmed recently by observations (Marcelli et al. [2022]). The interesting time dependence in the P/He ratio was found to be the consequence of how the combined interplaying modulation mechanisms in the heliosphere affect the modulated spectra based on their A/Z and particularly on their LIS's.

Avenues of further research related to this study are:

- Repeating the study of P/He ratios at the same time period but comparing the modeling results with both PAMELA and AMS02 observations.

- Studying the influence of also the hydrogen isotopic mixing to P/He.

- Investigating the effects of different magnetic field modifications on P/He.

- Investigating the modulation of CR electrons, positrons, and antiprotons to understand differences that exist between CR matter and anti-matter modulation in the heliosphere.

References

Adriani, O., Barbarino, G. C., Bazilevskaya, G. A., Bellotti, R., Boezio, M., Bogomolov, E. A., et al. (2011). PAMELA measurements of cosmic-ray proton and helium spectra. *Science*, *332*(6025), 69–72.

Adriani, O., Barbarino, G. C., Bazilevskaya, G. A., Bellotti, R., Boezio, M., Bogomolov, E. A., et al. (2013). Time dependence of the proton flux measured by PAMELA during the 2006 July-2009 December solar minimum. *Astrophys. J.*, *765*(2), 91.

Adriani, O., Barbarino, G. C., Bazilevskaya, G. A., Bellotti, R., Boezio, M., Bogomolov, E. A., et al. (2016). Measurements of cosmic-ray hydrogen and helium isotopes with the PAMELA experiment. *Astrophys. J.*, *818*(1), 68.

Adriani, O., Barbarino, G. C., Bazilevskaya, G. A., Bellotti, R., Boezio, M., Bogomolov, E. A., et al. (2017). Ten years of PAMELA in space. *La Rivista del Nuovo Cimento*, *40*(10), 473–522.

Aguilar, M., Alberti, G., Alpat, B., Alvino, A., Ambrosi, G., Andeen, K., et al. (2013). First result from the alpha magnetic spectrometer on the international space station: precision measurement of the positron fraction in primary cosmic rays of 0.5–350 GeV. *Phys. Rev. Lett.*, *110*(14), 141102.

Aguilar, M., Cavasonza, L. A., Alpat, B., Ambrosi, G., Arruda, L., Attig, N., et al. (2018). Observation of fine time structures in the cosmic proton and helium fluxes with the alpha magnetic spectrometer on the international space station. *Phys. Rev. Lett.*, *121*(5), 051101.

Aguilar, M., Cavasonza, L. A., Ambrosi, G., Arruda, L., Attig, N., Bachlechner, A., et al. (2019). Properties of cosmic helium isotopes measured by the alpha magnetic spectrometer. *Phys. Rev. Lett.*, *123*(18), 181102.

Aslam, O. P. M., Bisschoff, D., Ngobeni, M. D., Potgieter, M. S., Munini, R., Boezio, M., & Mikhailov, V. V. (2021). Time and charge-sign dependence of the heliospheric modulation of cosmic rays. *Astrophys. J.*, *909*(2), 215.

Aslam, O. P. M., Bisschoff, D., Potgieter, M. S., Boezio, M., & Munini, R. (2019). Modeling of heliospheric modulation of cosmic-ray positrons in a very quiet heliosphere. *Astrophys. J.*, *873*(1), 70.

Bartusiak, M. (1994). Sounds of the Sun. *American Scientist*, *82*, 61–68.

Battiston, R. (2020). High precision cosmic ray physics with AMS-02 on the international space station. *La Rivista del Nuovo Cimento*, *43*, 319-384.

Bieber, J. W., Matthaeus, W. H., Shalchi, A., & Qin, G. (2004). Nonlinear guiding center theory of perpendicular diffusion: General properties and comparison with observation. *Geophys. Res. Lett.*, *31*(L10805), 1–4.

Bieber, J. W., Matthaeus, W. H., Smith, C. W., Wanner, W., Kallenrode, M.-B., & Wibberenz, G. (1994). Proton and electron mean free paths: The Palmer consensus revisited. *Astrophys. J.*, *420*, 294-306.

Biermann, L. (1951). Kometenschweife und solare Korpuskularstrahlung. *Zs. f. Ap.*, *29*, 274-286.

Bisschoff, D., Aslam, O. P. M., Ngobeni, M. D., Mikhailov, V. V., Boezio, M., Munini, R., & Potgieter, M. S. (2021). On the Very Local Interstellar Spectra for Helium, Positrons, Antiprotons, Deuteron, and Antideuteron. *Phys. Atomic Nuclei*, *84*, 121 - 1127.

Bisschoff, D., Potgieter, M. S., & Aslam, O. P. M. (2019). New very local interstellar spectra for electrons, positrons, protons, and light cosmic ray nuclei. *Astrophys. J.*, *878*(1), 59.

Boezio, M., Munini, R., Bonvicini, V., Mocchiutti, E., Vacchi, A., Zampa, G., et al. (2017). The PAMELA experiment: A cosmic ray experiment deep inside the heliosphere. *PoS (ICRC2017)*, *1091*.

Burger, R. A., & Hattingh, M. (2001). Effect of Fisk type heliospheric magnetic fields on the latitudinal transport of cosmic rays. *In Proceedings of the 24-th International Cosmic Ray Conference*, *9*, 3698–3701.

Burger, R. A., Potgieter, M. S., & Heber, B. (2000). Rigidity dependence of cosmic ray proton latitudinal gradients measured by the Ulysses spacecraft: Implications for the diffusion tensor. *J. Geophys. Res.*, *105*, 27447-27455.

Burlaga, L., Ness, N., & Stone, E. (2013). Magnetic field observations as Voyager 1 entered the heliosheath depletion region. *Science*, *341*(6142), 147–150.

Burlaga, L. F., Ness, N. F., Acuña, M. H., Lepping, R. P., Connerney, J. E. P., & Richardson, J. D. (2008). Magnetic fields at the solar wind termination shock. *Nature*, *454*, 75–77.

Busching, I., & Potgieter, M. S. (2008). The variability of the proton cosmic ray flux on the Sun's way around the galactic center. *Adv. Space Res.*, *42*, 504–509.

Casadei, D., & Bindi, V. (2004). The origin of cosmic ray protons and electrons. *Astrophys. J.*, *612*, 262.

Cliver, E. W., & Herbst, K. (2018). Evolution of the Sunspot Number and Solar Wind B B time series. *Space Sci. Rev.*, *214*(2), 1–31.

Corti, C., Potgieter, M. S., Bindi, V., Consolandi, C., Light, C., Palermo, M., & Popkow, A. (2019). Numerical modeling of galactic cosmic-ray proton and helium observed by AMS-02 during the solar maximum of solar cycle 24. *Astrophys. J.*, *871*(2), 253.

Cummings, A. C., Stone, E. C., Heikkila, B. C., Lal, N., Webber, W. R., Jóhannesson, G., et al. (2016). Galactic cosmic rays in the local interstellar medium: Voyager 1 observations and model results. *Astrophys. J.*, *831*(1), 18.

Decker, R. B., Krimigis, S. M., Roelof, E. C., Hill, M. E., Armstrong, T. P., Gloeckler, G., et al. (2005). Voyager 1 in the foreshock, termination shock and heliosheath. *Science*, *309*, 2020–2024.

Dresing, N., Gómez-Herrero, R., Heber, B., Klassen, A., Malandraki, O., Dröge, W., & Kartavykh, Y. (2014). Statistical survey of widely spread out solar electron events observed with STEREO and ACE with special attention to anisotropies. *Astron. Astrophys.*, *567*, A27.

Earl, J. A. (1974). The diffusive idealization of charged-particle transport in random magnetic fields. *Astrophys. J.*, *193*, 231–242.

Engelbrecht, N. E., & Di Felice, V. (2020). Uncertainties implicit to the use of the force-field solutions to the Parker transport equation in analyses of observed cosmic ray antiproton intensities. *Physical Review D*, *102*(10), 103007.

Fahr, H. J., Kausch, T., & Scherer, H. (2000). A 5-fluid hydrodynamic approach to model the solar system-interstellar medium interaction. *Astron. Astrophys.*, *357*, 268-282.

Ferreira, S. E. S. (2002). *The heliospheric transport of galactic cosmic rays and Jovian electrons* (PhD thesis). Potchefstroom University for CHE, South Africa.

Ferreira, S. E. S., Potgieter, M. S., Burger, R. A., & Heber, B. (2000). Modulation effects of anisotropic perpendicular diffusion on cosmic ray electron intensities in the heliosphere. *J. Geophys. Res.*, *105*, 18305-18314.

Ferreira, S. E. S., Potgieter, M. S., & Scherer, K. (2007). Transport and acceleration of anomalous cosmic rays in the inner heliosheath. *J. Geophys. Res.*, *112*(A11101), 1-11.

Fiandrini, E., Tomassetti, N., Bertucci, B., Donnini, F., Graziani, M., Khiali, B., & Conde, A. R. (2021). Numerical modeling of cosmic rays in the heliosphere: Analysis of proton data from AMS-02 and pamela. *Physical Review D*, *104*(2), 023012.

Fichtner, H. (2001). Anomalous cosmic rays: Messengers from the outer heliosphere. *Space Sci. Rev.*, *95*, 639-754.

Fisk, L. A. (1996). Motion of the footpoints of heliospheric magnetic field lines at the Sun: Implications for recurrent energetic particle events at high heliographic latitudes. *J. Geophys. Res.*, *101*, 15547-15553.

Giacalone, J., & Jokipii, J. R. (1999). The transport of cosmic rays across a turbulent magnetic field. *Astrophys. J.*, *520*, 204-214.

Gleeson, L., & Axford, W. (1967). Cosmic rays in the interplanetary medium. *Astrophys. J.*, *149*, L115.

Gurnett, D., Kurth, W., Burlaga, L., & Ness, N. (2013). $In\ situ$ observations of interstellar plasma with Voyager 1. *Science*, *341*(6153), 1489–1492.

Haasbroek, L. J. (1997). *The transport and acceleration of charged particles in the heliosphere* (PhD thesis). Potchefstroom University for CHE, South Africa.

Haasbroek, L. J., Potgieter, M. S., & Wibberenz, G. (1995). Long-term cosmic-ray modulation along the Ulysses trajectory: A numerical simulation. *In Proceedings of the 24-th International Cosmic Ray Conference*, *4*, 768–771.

Hansteen, V. H., & Leer, E. (1995). Coronal heating, densities, and temperatres and solar wind. *J. Geophys. Res.*, *100*, 21577–21593.

Hasselmann, K., & Wibberenz, G. (1970). A note on the parallel diffusion coefficient. *Astrophys. J.*, *162*, 1049–1051.

Hattingh, M. (1998). *The modulaion of galactic cosmic rays in a three-dimensional heliosphere* (PhD thesis). Potchefstroom University for CHE, South Africa.

Heber, B., & Potgieter, M. S. (2006). Cosmic rays at high heliolatitudes. *Space Sci. Rev.*, *127*, 117–194.

Hoeksema, J. T. (1992). Large-scale structure of the heliospheric magnetic field: 1976-1991. *in Solar Wind Seven Colloquium*, 191-196.

Jokipii, J. R. (1966). Cosmic-ray propagation. I. Charged particles in a random magnetic field. *Astrophys. J.*, *146*, 480-487.

Jokipii, J. R., & Kóta, J. (1989). The polar heliospheric magnetic field. *Geophys. Res. Lett.*, *16*, 1-4.

Jokipii, J. R., & Kóta, J. (1995). The maximum energy of anomalous cosmic rays. *In Proceedings of the 24-th International Cosmic Ray Conference*, *4*, 718–721.

Jokipii, J. R., Levy, E. H., & Hubbard, W. B. (1977). Effects of particle drift on cosmic-ray transport. I. General properties, application to solar modulation. *Astrophys. J.*, *213*, 861-868.

Jokipii, J. R., & Thomas, B. T. (1981). Effects of drift on the transport of cosmic rays IV. Modulation by a wavy interplanetary current sheet. *Astrophys. J.*, *243*, 1115-1122.

Khabarova, O., Malandraki, O., Malova, H., Kislov, R., Greco, A., Bruno, R., et al. (2021). Current sheets, plasmoids and flux ropes in the heliosphere. *Space Sci. Rev.*, *217*(3), 1–97.

Kobayashi, T., Komori, Y., Yoshida, K., & Nishimura, J. (2004). The most likely source of high-energy cosmic-ray electron in supernova remnants. *Astrophys. J.*, *601*, 340-351.

Kopp, A., Raath, J.-L., Fichtner, H., Potgieter, M., Ferreira, S., & Heber, B. (2021). Cosmic-ray transport in heliospheric magnetic structures. III. implications of solar magnetograms for the drifts of cosmic rays. *Astrophys. J.*, *922*(2), 124.

Kóta, J., & Jokipii, J. R. (1983). Effects of drift on the transport of cosmic rays. VI - A three-dimensional model including diffusion. *Astrophys. J.*, *265*, 573–581.

Kóta, J., & Jokipii, J. R. (1999). Cosmic-ray modulation and the structure of the heliospheric magnetic field. *In Proceedings of the 26-th International Cosmic Ray Conference*, *7*, 9–12.

Krimigis, S. M., Decker, R. B., Roelof, E. C., Hill, M. E., Armstrong, T. P., Gloeckler, G., et al. (2013). Search for the exit: Voyager 1 at heliosphere's border with the Galaxy. *Science*, *341*, 144-147.

Langner, U. W. (2004). *Effects of termination shock acceleration on cosmic rays in the heliosphere* (PhD thesis). Potchefstroom University for CHE, South Africa.

le Roux, J. A., & Potgieter, M. S. (1992). The simulated features of heliospheric cosmic-ray modulation with a time-dependent drift model. IV - The role of heliospheric neutral sheet deformation. *Astrophys. J.*, *397*, 686–693.

le Roux, J. A., Potgieter, M. S., & Ptuskin, V. S. (1996). A transport model for the diffusive shock acceleration and modulation of anomalous cosmic rays in the heliosphere. *J. Geophys. Res.*, *101*, 4791–4803.

Leighton, R. B. (1969). A magneto-kinematic model of the solar cycle. *Astrophys. J.*, *156*, 1–26.

Lenni, A., Boezio, M., Munini, R., Menn, W., Marcelli, N., Potgieter, M. S., et al. (2021). Study of the solar modulation for the cosmic ray isotopes with the PAMELA experiment. *PoS (ICRC2021)*, *1310*.

Li, H., Wang, C., & Richardson, J. (2008). Properties of the termination shock observed by Voyager 2. *Geophys. Res. Lett.*, *35*(19).

Longair, M. S. (1990). Cosmic rays and the galactic radio background emission. In N. E. Kassim & K. W. Weiler (Eds.), *In low frequency astrophysics from space* (p. 227-236). Berlin, Heidelberg: Springer.

Luo, X., Potgieter, M. S., Feng, X., Shen, F., & Zhang, M. (2021). A numerical study of the effects of a Corotating Interaction Region on cosmic proton and helium transport. *PoS (ICRC2021)*, *1353*.

Luo, X., Zhang, M., Feng, X., Potgieter, M. S., Shen, F., & Bazilevskaya, G. (2020). A numerical study of the effects of corotating interaction regions on cosmic-ray transport. *Astrophys. J.*, *899*(2), 90.

Manuel, R. (2013). *Time–dependent modulation of cosmic rays in the outer heliosphere* (PhD thesis). North-West University (Potchefstroom Campus), South Africa.

Manuel, R., Ferreira, S., & Potgieter, M. (2015). The effect of a dynamic inner heliosheath thickness on cosmic-ray modulation. *Astrophys. J.*, *799*(2), 223.

Marcelli, N., Boezio, M., Lenni, A., Menn, W., Munini, R., Aslam, O. P. M., et al. (2020). Time dependence of the flux of helium nuclei in cosmic rays measured by the PAMELA experiment between 2006 July and 2009 December. *Astrophys. J.*, *893*(2), 145.

Marcelli, N., Boezio, M., Lenni, A., Menn, W., Munini, R., Aslam, O. P. M., et al. (2022). Helium fluxes measured by the PAMELA experiment from the minimum to the maximum solar activity for solar cycle 24. *Astrophys. J. Lett.*, *925*(2).

Marquardt, J., Heber, B., Potgieter, M. S., & Strauss, R. D. (2018). Energy spectra of carbon and oxygen with HELIOS E6-radial gradients of anomalous cosmic ray oxygen within 1 AU. *Astron. Astrophys.*, *610*, A42.

Martucci, M., Munini, R., Boezio, M., Di Felice, V., Adriani, O., Barbarino, G. C., et al. (2018). Proton fluxes measured by the PAMELA experiment from the minimum to the maximum solar activity for solar cycle 24. *Astrophys. J. Lett.*, *854*(1), L2.

Matthaeus, W. H., Qin, G., Bieber, J. W., & Zank, G. P. (2003). Nonlinear collisionless perpendicular diffusion of charged particles. *Astrophys. J.*, *590*, L53-L56.

McComas, D. J., Elliot, H. A., Gosling, J. T., Reisenfield, D. B., Skoung, R. M., Goldstein, B. E., et al. (2002). Ulysses' second fast latitude scan: Complexity near solar maximum and the reformation of polar coronal holes. *Geophys. Res. Lett.*, *29*, 1-4.

McComas, D. J., Rankin, J. S., Schwadron, N. A., & Swaczyna, P. (2019). Termination shock measured by Voyagers and IBEX. *Astrophys. J.*, *884*(2), 145.

Mewaldt, R. (1986). ^{3}He in galactic cosmic rays. *Astrophys. J.*, *311*(2), 979–983.

Mitchell, J. J., Cairns, I. H., Müller, H.-R., & Zank, G. P. (2005). Prediction of the timing of the 2–3 kHz radio emission within the solar cycle. *Geophys. Res. Lett.*, *32*(7).

Moraal, H. (1990). Proton modulation near solar minimum periods in consecutive solar cycles. *In Proceedings of the 21st International Cosmic Ray Conference*, *6*, 140-143.

Moraal, H. (2013). Cosmic-ray modulation equations. *Space Sci. Rev.*, *176*(1-4), 299–319.

Myers, Z. D., Seo, E. S., Abe, K., Anraku, K., Imori, M., Maeno, T., et al. (2003). Cosmic ray ^{3}He and ^{4}He spectra from BESS 98. *In Proceedings of the 28th International Cosmic Ray Conference*, *4*, 1805.

Ngobeni, M. D., Aslam, O. P. M., Bisschoff, D., Ndiitwani, D. C., Potgieter, M. S., Boezio, M., et al. (2021a). Combined heliospheric modulation of galactic protons and helium nuclei from solar minimum to maximum activity related to observations by PAMELA and AMS-02. *PoS(ICRC2021)*, *1337*.

Ngobeni, M. D., Aslam, O. P. M., Bisschoff, D., Potgieter, M. S., Ndiitwani, D. C., Boezio, M., et al. (2020). The 3D numerical modeling of the solar modulation of galactic protons and helium nuclei related to observations by PAMELA between 2006 and 2009. *Astrophys. Space Sci.*, *365*.

Ngobeni, M. D., & Potgieter, M. S. (2015). Modelling the effects of scattering parameters on particle-drift in the solar modulation of galactic cosmic rays. *Adv. Space Res.*, *56*, 1525–1537.

Ngobeni, M. D., Potgieter, M. S., Aslam, O. P. M., Bisschoff, D., Ramokgaba, I. I., & Ndiitwani, D. C. (2021b). Numerical modeling of the solar modulation of Helium isotopes in the inner heliosphere. *PoS(ICRC2021)*, *1338*.

Ngobeni, M. D., Potgieter, M. S., Aslam, O. P. M., Bisschoff, D., Ramokgaba, I. I., & Ndiitwani, D. C. (2022). Simulations of the solar modulation of Helium isotopes constrained by observations. *Adv. Space Res.*, *69*, 2330-2341.

Nkosi, G. S. (2006). *A study of cosmic ray anisotropies in the heliosphere* (Masters dissertation). North-West University (Potchefstroom Campus), South Africa.

Nndanganeni, R. R. (2012). *Modelling of galactic cosmic ray electrons in the heliosphere* (Masters dissertation). North–West University (Potchefstroom Campus), South Africa.

Nndanganeni, R. R. (2016). *Modeling of electrons in the heliosphere* (PhD thesis). North-West University (Potchefstroom Campus), South Africa.

Nndanganeni, R. R., & Potgieter, M. S. (2016). The energy range of drift effects in the solar modulation of cosmic ray electrons. *Adv. Space Res.*, *58*(3), 453–463.

Opher, M., Drake, J. F., Zieger, B., & Gombosi, T. I. (2015). Magnetized jets driven by the Sun: the structure of the heliosphere revisited. *Astrophys. J. Lett.*, *800*(2), L28.

Parker, E. N. (1958). Dynamics of the interplanetary gas and magnetic fields. *Astrophys. J.*, *128*, 664-676.

Parker, E. N. (1961). Sudden expansion of the corona follow a large solar flare and the attendant magnetic field and cosmic effects. *Astrophys. J.*, *133*, 1033-1014.

Parker, E. N. (1965). The passage of energetic charged particles through interplanetary space. *Planet. Space Sci.*, *13*, 9-49.

Pesses, M. E., Jokipii, J. R., & Eichler, D. (1981). Cosmic ray drift, shock wave acceleration, and the anomalous component of cosmic rays. *Astrophys. J.*, *246*, L85-L88.

Phillips, J. L., Balogh, A., Bame, S. J., Goldstein, B. E., Gosling, J. T., Hoeksema, J. T., et al. (1994). Ulysses at 50^o south: constant immersion in the high-speed solar wind. *Geophys. Res. Lett.*, *21*, 1105-1108.

Phillips, J. L., Bame, S. J., Barnes, A., Barraclough, B. L., Feldman, W. C., Goldstein, B. E., et al. (1995). Ulysses solar wind plasma observations from pole to pole. *Geophys. Res. Lett.*, *22*, 3301-3304.

Picozza, P., Galper, A., Castellini, G., Adriani, O., Altamura, F., Ambriola, M., et al. (2007). PAMELA– a payload for antimatter matter exploration and light-nuclei astrophysics. *Astroparticle Phys.*, *27*(4), 296–315.

Pogorelov, N. V., Fichtner, H., Czechowski, A., Lazarian, A., Lembège, B., le Roux, J. A., et al. (2017). Heliosheath processes and the structure of the heliopause: modeling energetic particles, cosmic rays, and magnetic fields. *Space Sci. Rev.*, *212*(1), 193–248.

Potgieter, M., & Vos, E. (2017). Difference in the heliospheric modulation of cosmic-ray protons and electrons during the solar minimum period of 2006 to 2009. *Astron. Astrophys.*, *601*, A23.

Potgieter, M. S. (2000). Heliospheric modulation of cosmic ray protons: Role of enhanced perpendicular diffusion during periods of minimum solar modulation. *J. Geophys. Res.*, *105*(A8), 18295–18303.

Potgieter, M. S. (2013). Solar modulation of cosmic rays. *Liv. Rev. Solar Phys.*, *10*, 1-66.

Potgieter, M. S., Aslam, O. P. M., Bisschoff, D., & Ngobeni, M. D. (2021). A perspective on the solar modulation of cosmic anti-matter. *Physics*, *3*(4), 1190–1225.

Potgieter, M. S., & le Roux, J. A. (1992). The simulated features of heliospheric cosmic-ray modulation with a time-dependent drift model. I. General effects of the changing neutral sheet over the period 1985-1990. *Astrophys. J.*, *386*, 336–346.

Potgieter, M. S., Vos, E. E., Boezio, M., De Simone, N., Di Felice, V., & Formanto, V. (2013). Modulation of galactic protons in the heliosphere during the unusual solar minimum of 2006 to 2009. *Solar Phys.*, *281*, 391-406.

Raath, J. L. (2015). *A comparative study of cosmic ray modulation models* (Masters dissertation). North–West University (Potchefstroom Campus), South Africa.

Raath, J. L. (2020). *A stochastic approach to the modelling of cosmic rays in the heliosphere* (PhD thesis). North-West University (Potchefstroom Campus), South Africa.

Reimer, O., Menn, W., Hof, M., Simon, M., Davis, A. J., Labrador, A. W., et al. (1998). The cosmic-ray ^{3}He/^{4}He ratio from 200 MeV per nucleon- 1 to 3.7 GeV per nucleon- 1. *Astrophys. J.*, *496*(1), 490.

Richardson, J. D., Kasper, J. C., Wang, C., Belcher, J. W., & Lazarus, A. J. (2008). Cool heliosheath plasma and deceleration of the upstream solar wind at the termination shock. *Nature*, *454*, 63–66.

Richardson, J. D., Wang, C., & Paularena, K. I. (2001). The solar wind: From solar minimum to solar maximum. *Adv. Space Res.*, *27*, 427-479.

Ross, E., & Chaplin, W. J. (2019). The behaviour of galactic cosmic-ray intensity during solar activity cycle 24. *Solar Phys.*, *294*(1), 1–17.

Ruderman, M. S. (2000). Absolute and convective instability of tangential discontinuities in viscous fluids: Application to heliopause. *Astrophys. Space Sci.*, *274*(1), 327–341.

Scherer, K., & Fichtner, H. (2014). The return of the bow shock. *Astrophys. J.*, *782*(1), 25.

Schou, J., Antia, H. M., Basu, S., Bogart, R. S., Bush, R. I., Chitre, S. M., et al. (1998). Helioseismic studies of differential rotation in the solar envelope by the solar oscillations investigation using the michelson doppler imager. *Astrophys. J.*, *505*(1), 390.

Shalchi, A. (2006). Extended nonlinear guiding center theory of perpendicular diffusion. *Astron. Astrophys.*, *453*, L43–L46.

Shalchi, A. (2010). A unified particle diffusion theory for cross-field scattering: Subdiffusion, recovery of diffusion, and diffusion in three-dimensional turbulence. *Astrophys. J. Lett.*, *720*, L127-L130.

Shalchi, A. (2020). Perpendicular transport of energetic particles in magnetic turbulence. *Space Sci. Rev.*, *216*(2), 1–134.

Shalchi, A., & Schlickeiser, R. (2004). The parallel mean free path of heliospheric cosmic rays in composite slab/two-dimensional geometry. I. the damping model of dynamical turbulence. *Astrophys. J.*, *604*(2), 861.

Shen, Z.-N., Qin, G., Zuo, P., & Wei, F. (2019). Modulation of galactic cosmic rays from helium to nickel in the inner heliosphere. *Astrophys. J.*, *887*(2), 132.

Shen, Z.-N., Qin, G., Zuo, P., Wei, F., & Xu, X. (2021). Numerical modeling of latitudinal gradients for galactic cosmic-ray protons during solar minima: Comparing with Ulysses observations. *Astrophys. J.*, *256*(1), 18.

Simpson, J. A., Anglin, J. D., Balogh, A., Bercovitch, M., Bouman, J. M., Budzinski, E. E., et al. (1992). The Ulysses cosmic ray and solar particle investigation. *Astron. Astrophys.*, *92*, 365–399.

Simpson, J. A., Hamilton, D., Lentz, G., McKibben, R. B., Mogro-Campero, A., Perkins, M., et al. (1974). Proton and electrons in Jupiters's magnetic field : Results from the university of Chicago experiment on Pioneer 10. *Science*, *183*, 306-309.

Smith, C. W., & Bieber, J. W. (1991). Solar cycle variation of the interplanetary magnetic field spiral. *Astrophys. J.*, *370*, 435-441.

Smith, E. J. (2011). Solar cycle evolution of the heliospheric magnetic field: The Ulysses legacy. *J. Atmos. Solar-Terrestrial Phys.*, *73*, 277–289.

Smith, E. J., Marsden, R. G., Balogh, A., Gloeckler, G., Geiss, J., McComas, D. J., et al. (2003). The Sun and heliosphere at solar maximum. *Science*, *302*(5648), 1165–1169.

Snodgrass, H. B. (1983). Magnetic rotation of the solar photosphere. *Astrophys. J.*, *270*, 288-299.

Snyman, J. L. (2007). *Modelling of the heliosphere and cosmic ray transport* (Masters dissertation). North–West University (Potchefstroom Campus), South Africa.

Song, X., Luo, X., Potgieter, M. S., Liu, X. M., & Geng, Z. A. (2021b). A numerical study of the solar modulation of galactic protons and Helium from 2006 to 2017. *Astrophys. J.*, *257*(2), 48.

Song, X., Luo, X., & Xu, W. (2021a). Study galactic cosmic ray modulation with AMS-02 observation. *Pos(ICRC2021)*, *1354*.

Soon, W., Connolly, R., & Connolly, M. (2015). Re-evaluating the role of solar variability on northern hemisphere temperature trends since the 19th century. *Earth-Science Reviews*, *150*, 409–452.

Steenberg, C. D., & Moraal, H. (1996). An acceleration/modulation model for anomalous cosmic ray hydrogen in the heliosphere. *Astrophys. J.*, *463*, 776–783.

Sternal, O., Engelbrecht, N. E., Burger, R. A., Ferreira, S. E. S., Fichtner, H., Heber, B., et al. (2011). Possible evidence for a Fisk-type heliospheric magnetic field. I. Analyzing Ulysses/KET electron observations. *Astrophys. J.*, *741*, 1-12.

Stone, E. C., Cummings, A. C., McDonald, F. B., Heikkila, B. C., Lal, N., & Webber, W. R. (2005). Voyager 1 explores the termination shock region and the heliosheath beyond. *Science*, *309*, 2017–2020.

Stone, E. C., Cummings, A. C., McDonald, F. B., Heikkila, B. C., Lal, N., & Webber, W. R. (2008). An asymmetric solar wind termination shock. *Nature*, *454*, 71–74.

Stone, E. C., Cummings, A. C., McDonald, F. B., Heikkila, B. C., Lal, N., & Webber, W. R. (2013). Voyager 1 observes low-energy galactic cosmic rays in a region depleted of heliospheric ions. *Science*, *341*, 150-153.

Strauss, R. D., & Potgieter, M. S. (2010). Modeling anomalous cosmic ray oxygen gradients over successive solar cycles. *J. Geophys. Res.*, *115*(A12).

Strauss, R. D., & Potgieter, M. S. (2014a). Is the highest cosmic-ray flux yet to come? *Solar Phys.*, *289*, 3197–3205.

Strauss, R. D., & Potgieter, M. S. (2014b). Where does the heliospheric modulation of galactic cosmic rays start? *Adv. Space Res.*, *53*, 1015–1023.

Strauss, R. D., Potgieter, M. S., Büsching, I., & Kopp, A. (2012). Modelling heliospheric current sheet drift in stochastic cosmic ray transport models. *Astrophys. Space Sci.*, *339*(2), 223–236.

Strauss, R. D., Potgieter, M. S., Kopp, A., & Büsching, I. (2011). On the propagation times and energy losses of cosmic rays in the heliosphere. *J. Geophys. Res.*, *116*(A12).

Teufel, A., & Schlickeiser, R. (2002). Analytic calculation of the parallel mean free path of heliospheric cosmic rays. I. Dynamical magnetic slab turbulence and random sweeping slab turbulence. *Astron. Astrophys.*, *393*, 703–715.

Teufel, A., & Schlickeiser, R. (2003). Analytic calculation of the parallel mean free path of heliospheric cosmic rays. II. Dynamical magnetic slab turbulence and random sweeping slab turbulence with finite wave power at small wavenumbers. *Astron. Astrophys.*, *397*, 15–25.

Thomas, B. T., & Smith, E. J. (1980). The Parker spiral configuration of the interplanetary magnetic field between 1 and 8.5 AU. *J. Geophys. Res.*, *85*(A12), 6861–6867.

Tomassetti, N., Barão, F., Bertucci, B., Fiandrini, E., & Orcinha, M. (2019). Numerical modeling of cosmic-ray transport in the heliosphere and interpretation of the proton-to-helium ratio in solar cycle 24. *Adv. Space Res.*, *64*(12), 2477–2489.

Tomassetti, N., Orcinha, M., Barão, F., & Bertucci, B. (2017). Evidence for a time lag in solar modulation of galactic cosmic rays. *Astrophys. J. Lett.*, *849*(2), L32.

Usoskin, I. G. (2017). A history of solar activity over millennia. *Liv. Rev. Solar Phys.*, *14*(1), 1–97.

van den Berg, J., Strauss, D. T., & Effenberger, F. (2020). A primer on focused solar energetic particle transport. *Space Sci. Rev.*, *216*(8), 1–57.

Vogt, A., Engelbrecht, N. E., Heber, B., Kopp, A., & Herbst, K. (2022). Numerical and experimental evidence for a new interpretation of residence times in space. *Astron. Astrophys.*, *657*, A39.

Vogt, A., Engelbrecht, N. E., Strauss, R. D., Heber, B., Kopp, A., & Herbst, K. (2020). The residence-time of jovian electrons in the inner heliosphere. *Astron. Astrophys.*, *642*, A170.

Vogt, A., Heber, B., Kopp, A., Potgieter, M. S., & Strauss, R. D. (2018). Jovian electrons in the inner heliosphere-proposing a new source spectrum based on 30 years of measurements. *Astron. Astrophys.*, *613*, A28.

Vos, E. E. (2012). *Cosmic ray modulation processes in the heliosphere* (Masters dissertation). North-West University (Potchefstroom Campus), South Africa.

Vos, E. E. (2016). *Modelling charge-sign dependent modulation of cosmic rays in the heliosphere* (PhD thesis). North-West University (Potchefstroom Campus), South Africa.

Vos, E. E., & Potgieter, M. S. (2015). New modeling of galactic proton modulation during the minimum of solar cycle 23/24. *Astrophys. J.*, *815*(2), 119.

Vos, E. E., & Potgieter, M. S. (2016). Global gradients for cosmic-ray protons in the heliosphere during the solar minimum of cycle 23/24. *Solar Phys.*, *291*(7), 2181–2195.

Wang, J. Z., Seo, E. S., Anraku, K., Fujikawa, M., Imori, M., Maeno, T., et al. (2002). Measurement of cosmic-ray hydrogen and helium and their isotopic composition with the BESS experiment. *Astrophys. J.*, *564*(1), 244.

Wang, Y. M. (2011). Semiempirical models of the slow and fast solar wind. *Space Sci. Rev.*, *172*, 123-143.

Wei, W., Shen, F., Yang, Z., Zhao, L., Wang, Y., Zuo, P., & Zhang, J. (2019). Modeling solar energetic particle transport in 3D background solar wind: Influences of the compression regions. *J. Atmospheric and Solar-Terrestrial Phys.*, *182*, 155–164.

Whang, Y. C., Burlaga, L. F., Wang, Y. M., & Sheeley, N. R. (2004). The termination shock near 35^o latitude. *Geophys. Res. Lett.*, *31*(L03805), 1–4.

Acknowledgements

In no particular order, I would like to acknowledge and thank the following individuals and organizations:

- Heavenly Father for always leading and guiding through everything and in everything, for also empowering me with a sound mind and understanding.
- Gratitude to my supervisor, Dr. Donald Ngobeni, for his excellent supervision,support, motivation and for being a constant source of information.
- Dr Chris Ndiitwani, my assistant supervisor, for teaching me the inner workings of the numerical scheme, outlining the techniques related to calculating the 27-day averages for both the HMF and tilt, and for the modulation discussions.
- Mrs I. Venter, for her assistance with the language editing of this dissertation.
- The Department of Physics at the North-West University (Mahikeng Campus) for the use of their facilities.
- The North-West University bursary offices for the partial financial support (Master's bursary) and the South African National Research Foundation for awarding me a fully funded postgraduate scholarship for the study period.
- My family, for the love and support. My late brother, Thapelo Ramokgaba, for always being an ambassador for education; pushing me to strive for academic excellence, and encouraging me to follow my passion.